A Herbig disk view of planet formation

Proefschrift

Lucas Marinus Stapper

geboren te Amsterdam, Nederland
in 1997

Promotores:

Prof. dr. E. F. van Dishoeck

Prof. dr. M. R. Hogerheijde   Universiteit Leiden

Universiteit van Amsterdam

Promotiecommissie:

Prof. dr. I. A. G. Snellen

Prof. dr. S. F. Portegies Zwart

Prof. dr. C. Dominik   Universiteit van Amsterdam

Prof. dr. J. P. Williams   University of Hawaii

Dr. M. Benisty   Université Côte d'Azur

Cover design: Cover designed by the author. ALMA Herbig disk observations of their dust emission in orange and gas CO (isotopologue) emission in blue. The gas is a factor of 2 smaller compared to the dust. A size of 200 au in dust is indicated by the bar on the front cover. All data is freely available on the ALMA archive.

On Earth, humankind can step onto another continent, and without a thought, destroy the kindred civilizations found there through warfare and disease. But when they gaze up at the stars, they turn sentimental and believe that if extraterrestrial intelligences exist, they must be civilizations bound by universal, noble, moral constraints, as if cherishing and loving different forms of life are parts of a self-evident universal code of conduct. I think it should be precisely the opposite: Let's turn the kindness we show toward the stars to members of the human race on Earth and build up the trust and understanding between the different peoples and civilizations that make up humanity.

The Three Body Problem, Liu Cixin

Table of contents

Chapter 1

Introduction

From being subjects of mythology thousands of years ago, to helping us take our first steps towards understanding the universe around us: planets have played a significant role in our cultures and in our understanding of the universe since time immemorial. Particularly in the last few decades, modern technological progress has advanced astronomy in major ways. Not only are probes visiting planets in our Solar system, more than 5500 extrasolar planets have been confirmed to date. This enormous variety of exoplanets presents a challenge when it comes to understanding how planets form. The key in understanding this planet formation puzzle lies in protoplanetary disks, the nurseries of new exoplanets.

1.1 Star and planet formation

Star and planet formation is a complicated topic, spanning large ranges in space and time. Before a planetary system as we know it has formed, at least four different stages and millions of years have already passed.

The star formation cycle starts in a dense molecular cloud (see Fig. 1.1). This cloud mainly consists of gas, and some dust, with a typical gas-to-dust ratio of 100. Once dense and cold enough, the cloud starts to contract under its own gravity and collapse as it reached its so-called Jeans' mass. During this process, the density increases with a few orders of magnitude, from 10^2 hydrogen nuclei cm^{-3} to 10^6 cm^{-3} (Benson & Myers 1989). For the gas to be able to contract the temperature needs to stay low, around 10-15 K, which is aided by molecules radiating the heat away. The stages of star-formation have been formalized into four classes based on the slope of the infrared spectral energy distribution of the object,

$$\alpha_{\mathrm{IR}} = \frac{d \log \lambda F_\lambda}{d \log \lambda}.$$ (1.1)

The first three classes, Class I-III, were defined by Lada (1987), and later an earlier class, Class 0, was added by Andre et al. (1993), see Fig. 1.1. In between the Class I
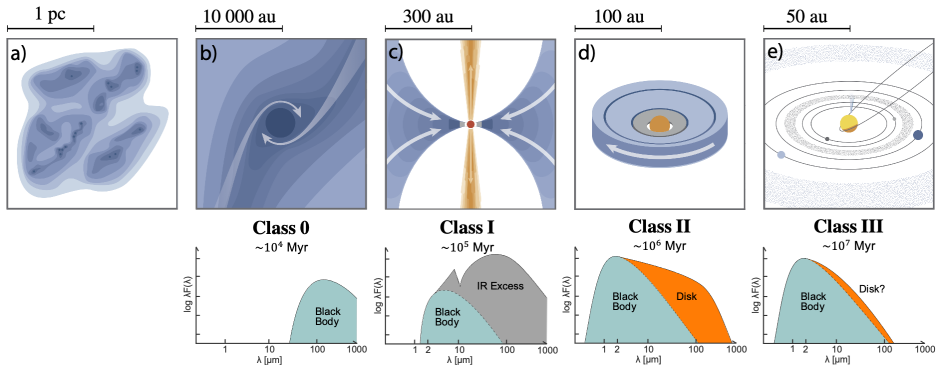
Figure 1.1: Star formation stages. **a)** Dense cores in interstellar molecular clouds. **b)** The cores start to collapse due to gravity, forming a protostellar core. This is a Class 0 object, and emits at long wavelengths. **c)** A protostar forms, still accreting from the remnant cloud, forming an accretion disk due to conservation of angular momentum. The emission from this Class I object consists of a star with additional IR excess from a disk and envelope. **d)** The remnant cloud dissipates and a disk is left over, a Class II object. The emission is dominated by the star and the disk. **e)** Eventually the primordial gas dissipates and a Class III object is left over, where stellar emission dominates. The typical size of the object is shown on top of the panels. Figure adapted from Öberg & Bergin (2021) and Magnus Persson.

and Class II stages, a flat spectrum source has also been defined (Greene et al. 1994).

Class 0 objects are still embedded in their envelope, making it difficult to observe the protostar at the center. Still, there is evidence of rotating gas disks in these young objects (e.g., Tobin et al. 2012; Murillo et al. 2013), which form due to conservation of angular momentum. The high accretion rates result in rapid evolution, and these embedded objects are therefore difficult to observe: protostars were first discovered through outflows of winds and jets (e.g., Snell et al. 1980; Codella et al. 2014; Bally 2016). When the envelope starts to dissipate, the star begins to be detectable and the object has transitioned to the Class I stage. As the disks of Class I objects are more massive than the successive classes, planet formation may already start at this stage (Tychoniec et al. 2020). Indeed, Class I objects show clear signs of disks with some already having visible substructures (ALMA Partnership et al. 2015; Sheehan & Eisner 2018; Segura-Cox et al. 2020). Once the envelope has dissipated and only a disk is left over, the Class II stage is reached. The disks of Class II objects, also called protoplanetary disks, have been subject of many detailed studies (e.g., Williams & Cieza 2011; Andrews 2020; Manara et al. 2023; Miotello et al. 2023), and are the focus of this thesis. Eventually, most of the disk has dissipated, either accreted onto the star, blown away by a disk wind, or formed into planets, and a debris disk is left over (Hughes et al. 2018). Planet formation is far from over in debris disks, as at this stage processes such as collisions and scattering between protoplanets (e.g., the Nice model, Tsiganis et al. 2005) are likely happening regularly. The dust and gas in

debris disks are thought to be secondary of nature, produced via these violent collisions (Hughes et al. 2018). When most of the disk has dissipated, a Class III object remains.

The pre-main sequence stars around which protoplanetary disks reside are often split into low and intermediate mass stars. The lower mass stars are called T Tauri stars, which have stellar masses lower than $\sim 1.5\ M_\odot$ and spectral types down to M. The disks around intermediate mass stars, further discussed in Sec. 1.4 and the focus of this thesis, reside around stars with a mass of ~ 1.5 to 8-10 $M_\odot$ with spectral types ranging from F to B (see Brittain et al. 2023, and Section 1.4). The disks around pre-main sequence intermediate mass stars are called Herbig disks.

1.2   Protoplanetary disks

1.2.1   Gas evolution

During the different stages mentioned in the previous section, disk evolution plays an important role. The evolution of the gas is thought to occur via two mechanisms: viscous evolution and/or driven by a magnetohydrodynamical (MHD) wind, see Fig. 1.2.

As the Keplerian rotation decreases with the square root of the radius, different annuli of the disk rotate with different velocities and the annuli shear against each other (Lynden-Bell & Pringle 1974). This process carries the angular momentum outwards, increasing the radius of the disk, while most of the material of the inner disk drifts inwards and is accreted by the star. This shear depends on the viscosity of the disk and is parameterized into the α-parameter (Shakura & Sunyaev 1973). Viscosity is assumed to be associated with turbulence in the disk, though this is not known with certainty, originating from for instance (magneto)hydrodynamical instabilities (e.g., MRI, Balbus & Hawley 1991; VSI, Nelson et al. 2013; see also
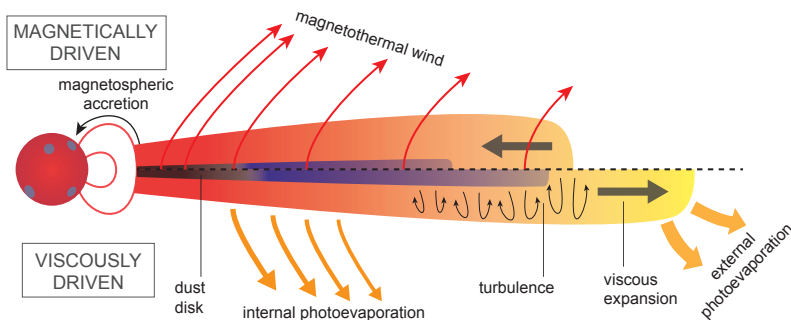
Figure 1.2: Schematic of the two main mechanisms thought to drive the evolution of the protoplanetary disk. While magnetically driven winds (top half) transport angular momentum away from the disk, decreasing the disk size, viscous evolution (bottom half) redistributes the angular momentum over the disk, increasing the disk size. Figure from Manara et al. (2023).

Bae et al. 2023 and Lesur et al. 2023). Based on this prescription the surface density of the disk can be described as

$$\Sigma_{\text{gas}} = \frac{(2 - \gamma)M_{\text{disk}}}{2\pi R_c^2} \left(\frac{R}{R_c}\right)^{-\gamma} \exp\left[-\left(\frac{R}{R_c}\right)^{2-\gamma}\right], \qquad (1.2)$$

if the viscosity ν is assumed to vary radially with the powerlaw $\nu \propto R^\gamma$ (Hartmann et al. 1998). Other parameters include the disk mass M_{disk}, and the characteristic radius R_c, which is the radius at which the the exponential taper of the surface density profile takes over from the powerlaw part of the equation. As the turbulence is thought to be the driving factor behind viscous evolution, many works have tried to measure it. As of writing, the viscous parameter α is measured to be relatively low, in the order of 10^{-3}-10^{-5} (e.g., Flaherty et al. 2015, 2020; Villenave et al. 2022; Jiang et al. 2024), though some works estimate it to be higher (Hughes et al. 2011; Paneque-Carreño et al. 2024). Hence, it is still unknown what the main driver of the viscosity in disks is. Additional physical processes can be added, such as external or internal photoevaporation, which will influence the disk lifetime compared to an exclusively viscously evolving disk (see e.g., Rosotti et al. 2017).

Rather than the transport of angular momentum in the disk, MHD disk winds remove the angular momentum from the disk by using a magnetic field inherent to the disk. Recently, Tabone et al. (2022a) have parameterized the MHD disk evolution similar to the viscous case with an α_{DW}. With this parameterization, Tabone et al. (2022b) show that the fast dispersal and the correlation between the disk mass and accretion rate of the disks in Lupus can be reproduced with MHD disk winds (more on disk population studies, see Section 1.3). As material, and thus angular momentum, is removed from the disk, the disk radius stays the same or decreases with time (Trapman et al. 2022). Hence, the radius of the disk is one of the main observational signatures to distinguish MHD driven or viscous driven evolution.

1.2.2 Obtaining the gas mass

Besides the evolution of the gas in the disk, the total gas mass of the protoplanetary disk is also one of the most important open questions in the field of planet formation. Directly tracing the total disk mass is difficult; the most common molecule H_2 does not have a dipole moment, and its low-energy rotational levels are weak quadrupole transitions, which are faint at the low temperatures of the disk outer regions. The isotopologue of H_2, hydrogen deuteride (HD), however, does have a small dipole moment which allows for dipole transitions. The first rotational transition of HD $J = 1 - 0$ can be excited around 100 K and emits at 112 μm. This transition has only been detected with the *Herschel Space Observatory* for three disks (Bergin et al. 2013; McClure et al. 2016). For Herbig disks there are also a dozen of upper limits based on the HD measurements (Kama et al. 2016, 2020). Unfortunately, the *Herschel Space Observatory* ceased operations in 2013.

Therefore, (combinations of) other molecules need to be used as tracers for the total gas mass in disks. The most logical step is to use the second most abundant
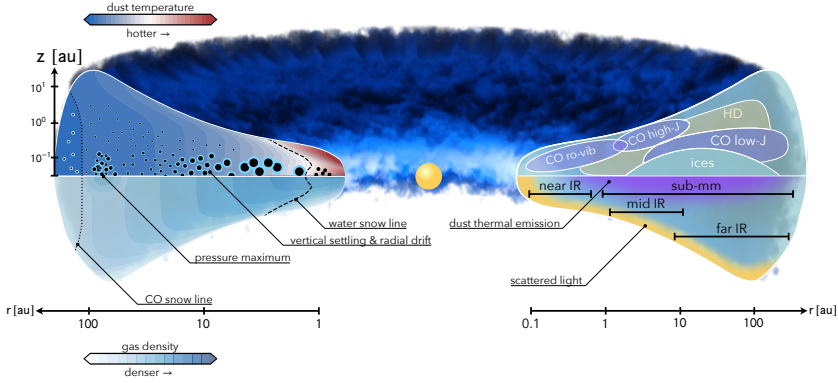
Figure 1.3: Schematic view of a protoplanetary disk. The left side of the figure shows the temperature and density structure of a disk. As the distance from the star increases, the temperature decreases, resulting in different molecules freezing out and giving rise to the snow lines (water close in, CO farther out). Dust grains grow via collisions, settle towards the midplane, and drift inwards due to gas drag. Pressure maxima in the disk can halt the radial drift at different radii. The right side shows the different parts of the disk which can be traced by different detection methods. The millimeter dust is observed at 10s of au near the midplane. Low rotational transition CO emission lines are emitted at higher regions of the disk. To trace the inner disk or the upper regions of the disk one needs to go towards IR wavelengths. Figure from Miotello et al. (2023).

molecule: carbon-monoxide (CO). Indeed, many works have used CO, or one of its many isotopologues (^{13}CO, C^{18}O, C^{17}O, ^{13}C^{18}O, ^{13}C^{17}O), to determine the total mass either by scaling the luminosity of the CO isotopologue using an excitation temperature and an abundance ratio (e.g., Hughes et al. 2008; Loomis et al. 2018; Miley et al. 2018), or using thermochemical models to obtain a disk mass by relating the luminosity of the disk to a particular model disk mass (Williams & Best 2014; Miotello et al. 2014, 2016). Other methods to obtain a disk mass include combining CO measurements with N$_2$H$^+$ (Trapman et al. 2022) or [OI] (Kamp et al. 2010) to try to solve degeneracies in the models such as the carbon abundance and the temperature of the disk.

To use carbon monoxide as a tracer of the total disk mass, two main processes need to be taken into account: photodissociation and freeze-out. Both processes impact the abundance of CO and therefore need to be treated carefully to obtain a gas mass from the CO emission. Photodissociation of CO occurs via the absorption of UV photons, as an energy of 11.09 eV is necessary, and proceeds through discreet lines into an excited electronic state. Therefore, at high enough column densities, CO can self-shield, as the UV absorption lines become optically thick. For rarer isotopologues such as ^{13}CO and C^{18}O self-shielding also occurs, in addition to the molecules mutually shielding each other as their UV absorption lines overlap

(Visser et al. 2009; Miotello et al. 2014). The self-shielding of each molecule is reached at different column densities in the disk, and therefore layers of different isotope ratios arise in the disk.

At a dust temperature of around 20 K, CO freezes out onto grains (Bisschop et al. 2006). This reduces the total amount of CO in the gas-phase, and therefore the brightness of the emission from the disk. However, even when taking the freeze-out into account, CO is found to be less bright than expected, resulting in low disk masses and gas-to-dust ratios of around 10 (e.g., Pascucci et al. 2016; Long et al. 2017; Miotello et al. 2017). Processes such as ice chemistry turning CO into molecules such as CO_2 and CH_4 (or more complex molecules such as CH_3OH) are therefore likely to be fundamental in understanding the CO emission (Bosman et al. 2018; Agúndez et al. 2018). Indeed, taking these processes into account results in an order of magnitude higher gas-to-dust ratios (Deng et al. 2023). Additionally, the CO ice can be locked into larger bodies in the midplane, removing it from the gas reactions higher up in the disk (Du et al. 2015; Krijt et al. 2018). In warm disks such as those around the more luminous Herbig stars the freeze-out of CO is much less relevant (Kama et al. 2020; Sturm et al. 2022; Miotello et al. 2023). For some Herbig disks evidence even suggests that no CO snow line is present (e.g., HD 100546, Kama et al. 2016). Therefore, CO can be used as a gas mass tracer in Herbig disks.

Lastly, both the freeze-out and photodissociation of CO results in CO being abundant between two boundaries in the vertical direction of the disk (see Fig. 1.3). The upper boundary set by the photodissociation from UV photons from the central star or an external field, while the lower boundary is set by the freeze out in the cold midplane of the disk (Aikawa et al. 2002), see Fig. 1.3.

For the modeling of the gas and chemistry of protoplanetary disks, multiple codes have been developed over the years, such as ProDiMo (Protoplanetary Disk Modeling, Woitke et al. 2009), and DALI (Dust And LInes, Bruderer et al. 2012; Bruderer 2013; Bruderer et al. 2014). For DALI, detailed CO chemical networks have been developed, including isotopologue specific photodissociation, mutual- and self-shielding, and freeze-out (Miotello et al. 2014, 2016). The isotopologue ratios are initiated with the ISM abundances (Wilson & Rood 1994). DALI then obtains the disk gas and dust thermal structure, and the abundances of each molecule in the disk by doing the following steps (see also Bruderer et al. 2012). First, using a specific density structure, see eq. (1.2), and a stellar spectrum, DALI obtains the dust temperature and UV radiation field in the disk. Then, the chemical network is run using the dust temperature as a first guess to the gas temperature, resulting in molecular abundances. Subsequently, the excitation of the molecules is calculated using non-LTE methods, providing the cooling rates. The gas temperature is then obtained from the balance between heating and cooling processes. This new gas temperature is then used to recalculate the chemistry and the molecular excitations. This process is iterated until they converge. DALI has been used in many different studies. From disk specific modeling (e.g., van der Marel et al. 2016; Leemker et al. 2021, 2022), to population studies (e.g., Miotello et al. 2016, 2017; Kama et al. 2020; Trapman et al. 2019).

1.2.3   Vertical structure of the disk

The gas can be used to trace other processes as well, especially with the velocity resolution of ALMA. CO emission profiles can reveal the kinematics in disks, showing minute changes in the 10s of m s^{-1} caused by possible embedded planets (e.g., Pinte et al. 2018b, 2019; Izquierdo et al. 2022; Wölfer et al. 2023). Similarly, the vertical height can be traced by using the isovelocity curves of the gas emission (Pinte et al. 2018a). As the gas is pressure supported, the gas will follow the rotation of the disk elevated from the midplane, resulting in a cone shape. From this shape the emission height can be inferred. This technique has been used to show clear vertical stratification of different molecules in the disk (e.g., Paneque-Carreño et al. 2023). The focus of this technique has mostly been on the CO isotopologues, with ^{12}CO, ^{13}CO, and C^{18}O $J = 2 - 1$ emitting from layers at an aspect ratio of $\sim 0.2 - 0.3$ and lower depending on the rarity of the isotopologue and where the emission line becomes optically thick (e.g., Law et al. 2021, 2022, 2023). Additionally, the vertical thermal structure of the disk can be inferred from the brightness temperature of the different layers (Law et al. 2021).

1.2.4   Dust evolution and planet formation

While the gas is evolving, the dust is too. As the dust will eventually form the (cores of) planets, this evolution is just as important as the evolution of the gas. The dust will settle vertically, drift radially, collide with other particles, and possibly be trapped in the disk (see Fig. 1.3). One of the most important findings by ALMA in the last decade is the presence of dust rings and other structures in protoplanetary disks. After the first confirmation of rings in HL Tau in 2015 (ALMA Partnership et al. 2015), others were soon to follow. The ALMA large program 'Disk Substructures at High Angular Resolution Project' (DSHARP, Andrews et al. 2018a) has shown a plethora of structures in the brightest disks. The disks show clear signs of dynamical processes occurring in them: ranging from rings and gaps (Andrews et al. 2018a), large cavities (Pineda et al. 2019; Benisty et al. 2021), crescents (Dong et al. 2018; Kraus et al. 2017; van der Marel et al. 2013), to spirals (Pérez et al. 2016). Many barriers need to be overcome to eventually form planets, but the timescale of planet formation is short, as disks disperse after only < 10 Myr (Haisch et al. 2001; Hillenbrand 2005). Still, we know that planets do form in disks: besides the thousands of detected exoplanets, which had to form somewhere, direct detections of young protoplanets in disks have been made as well (PDS 70, Keppler et al. 2018; Haffert et al. 2019; AB Aur, Currie et al. 2022; HD 169142, Hammond et al. 2023).

The dust evolution starts with small micron-sized dust coupled to the gas. This dust can be observed in scattered light (see Fig. 1.3, and for a recent overview Benisty et al. 2023). The gas is pressure supported resulting in a sub-Keplerian rotation velocity, which the small micron-sized dust follows. Based on the scattered light, these micron-sized particles have been inferred to be both low- and high-porosity aggregates, possibly linked to planets in the disk stirring up the more compact grains from the midplane (Ginski et al. 2023; Tazaki et al. 2023). If these grains are growing by sticking together, they need to overcome the bouncing

barrier (Zsom et al. 2010), which may be possible outside the snowline where
the dust particles are more sticky due to an icy layer. Eventually, these small
dust grains start to grow to centimeter or even decimeter sized particles, called
pebbles, and decouple from the gas. Still, difficulties remain for overcoming the
subsequent fragmentation barrier, where particles start to fragment instead of
stick when colliding (e.g., Booth et al. 2018). A more direct mechanism to form
planetesimals is via gravitational collapse triggered by the streaming instability
(Youdin & Goodman 2005), due to the particles settling down in the midplane
(Johansen et al. 2014), practically skipping the different barriers. The problem of
radial drift may still remain however, which is caused by the pebbles experiencing
a headwind due to the sub-Keplerian velocity of the pressure-supported gas. This
headwind slows down the particle and it drifts inwards, which, based on dust
evolution models, can happen on timescales of only a few 100 years (Pinilla et al.
2022b). To overcome this loss of grains, a pressure maximum is needed, where
the particles will drift towards and be trapped. To make such a dust trap, many
different mechanisms have been put forward. For example planets may directly
form via gravitational instabilities in the outer disk (Boss 1997; Kratter et al.
2010), which will then generate spirals trapping the dust, and create dust traps of
their own (e.g., Bae et al. 2017), kickstarting the dust growth for other planets.
Other possible origins include snowlines (e.g., Zhang et al. 2021) or MHD zonal
flows (e.g., Hu et al. 2022).

Eventually planetesimals will form, which then need to grow towards young
protoplanets. The two main mechanisms proposed for this are planetesimal accre-
tion and pebble accretion. For planetesimal accretion, the process is governed by
gravity, as the planetesimals themselves are decoupled from the gas (Lissauer 1993;
Kokubo & Ida 1996; Drążkowska et al. 2023). When the random velocities between
the planetesimals is much smaller than the escape velocity, gravitational focusing
dominates and a runaway growth starts. This will stop when the planet embryo is
massive enough to dynamically stir the smaller planetesimals (Drążkowska et al.
2023). Unfortunately, the efficiency of planetesimal accretion drops with the sepa-
ration from the star. Forming a massive planetary core outside the snowline takes
therefore too long compared to the disk lifetime (Ida & Lin 2004). Pebble accre-
tion may be a solution to this, where the planetesimal accretes smaller particles,
pebbles, to grow (Visser & Ormel 2016; Johansen & Lambrechts 2017). As this
process is assisted by the gas drag, material from a substantially larger radius can
be accreted onto the planetesimal, making this process orders of magnitude faster
than planetesimal accretion. But a large enough reservoir of pebbles is needed
to be able to do so (Ormel 2017). Once the planetary core has been sufficiently
built up, gas accretion starts. Consequently, the Bondi radius (the radius at which
the sound speed of the gas equals the escape velocity of the embryo) extends and
even more gas is accreted. A run-away growth period occurs, leading to a giant
exoplanet forming (e.g., Pollack et al. 1996).

1.2.5   Obtaining the dust mass

The amount of dusty material as building blocks of planets is thus an important factor in the formation of exoplanets. To obtain a measure of the dust mass in a disk, often a relatively simple formulation is used (Hildebrand 1983),

$$M_{\mathrm{dust}} = \frac{d^2 F_\nu}{\kappa_\nu B_\nu(T_{\mathrm{dust}})},$$
(1.3)

which assumes the dust to be optically thin. Here, the continuum millimeter flux F_ν is scaled to a dust mass M_{dust} via the distance d and by assuming a particular dust temperature T_{dust} and the Planck curve at that temperature B_ν. The dust temperature is often assumed to be 20 K for T Tauri disks (e.g., Andrews & Williams 2005), but the temperature can also be scaled with the luminosity of the central star (Andrews et al. 2011). The dust opacity κ_ν is assumed to be a powerlaw of the form (Beckwith et al. 1990)

$$\kappa_\nu = \kappa_0 \left(\frac{\nu}{\nu_0}\right)^\beta = 10 \ \mathrm{cm}^2 \ \mathrm{g}^{-1} \times \left(\frac{\nu}{10^3 \mathrm{GHz}}\right)^\beta,$$
(1.4)

such that at a typical frequency of 230 GHz in Band 6 with ALMA, assuming the powerlaw index β to be equal to 1, the dust opacity is 2.3 cm^2 g^{-1}. However, β is not necessarily equal to 1, as it is related to the growth of the dust in the disk. Lower values are associated with dust growth. To obtain an estimate of the powerlaw index, observations at different wavelengths are needed. For example Tazzari et al. (2016) obtained $\beta = 0.5$ for the inner disk, and $\beta = 1.7$ for the outer disk (consistent with the ISM value of 1.8, Draine 2006) by combining VLA, SMA, and CARMA observations. Similar disk averaged values of $\beta = 0.5$ were found by Tychoniec et al. (2020) and Tazzari et al. (2021). Another uncertainty in obtaining a dust estimate is the assumption of optically thin emission. This may not be true, and dust masses may be underestimated by an order of magnitude, based on dust radiative transfer modeling using RADMC-3D (Dullemond et al. 2012; Liu et al. 2022) and MCFOST (Pinte et al. 2006, 2009; Kaeufer et al. 2023).

1.3   Disk population studies

In the past decade ALMA and other millimeter arrays have given the opportunity to obtain large samples of millimeter observations of protoplanetary disks, specifically to obtain their dust mass and radius. This section will summarize those results, after introducing two millimeter interferometers mainly used in this thesis.

1.3.1   Observing planet formation with millimeter interferometers

Interferometers are a collection of telescopes, or antennas, which combine their inputs into a single image. This effectively results in a telescope with a resolution

proportional to the largest separation (or baseline) between the antennas. As radio waves are combined, the array of antennas samples a Fourier transform of the sky brightness. These samples are called visibilities. As not all space between the telescopes is covered, there is a finite sampling of the visibilities. This results in artifacts in the 'dirty' image, due to the so-called point-spread function of the telescope, which need to be deconvolved out of the dirty image to obtain a cleaned image of the sky brightness.

The Netherlands has been at the forefront in radio astronomy for decades by building arrays such as the Westerbork Synthesis Radio Telescope (WSRT), and the Low-Frequency Array (LOFAR). For planet formation however, we need to look at millimeter wavelengths, as planet-forming disks radiate at these wavelengths. While for radio telescopes the Dutch weather is not a big problem, for shorter wavelengths dryer conditions are required. One of the world leading observatories is therefore located in the Atacama desert in the Andes mountain range in Chile at a height of 5000 m above sea level: the Atacama Large Millimeter/submillimeter Array (ALMA). ALMA is an international partnership between Europe, North America, east Asia, and the Republic of Chile. The array consists of 66 antennas, of which 54 have a diameter of 12 meters, and 12 have a diameter of 7 meters. Part of ALMA is the so-called Atacama Compact Array (ACA), which consists of 16 closely separated antennas: the 12 7-meter antennas together with 4 12-meter antennas. The antennas can be arranged into different configurations, changing their baselines from 150 meters all the way to 16 kilometers. The largest separations can give milli-arcsecond (mas) resolution at the highest frequencies observed. Additionally, ALMA has a high velocity resolution as well, being able to resolve emission lines at a velocity resolution of only 50 m s^{-1}.

Another millimeter interferometer, though less often used for planet formation than ALMA, is the Northern Extended Millimeter Array (NOEMA). This telescope is located on Plateau de Bure in the French Alps at a height of 2500 meters. NOEMA is operated by the Institut de Radioastronomie Millimetrique (IRAM) which is supported by institutes in France, Germany, and Spain. This array consists of 12 15-meter antennas. At its most extended configuration the baselines can range out to 1.7 kilometers. The main strength of NOEMA is its large bandwidth. Its upper and lower side-band are 8 GHz wide, making it particularly useful for molecular emission line surveys. In addition, while the spatial resolution and sensitivity do not match that of ALMA, it can be nicely used for photometric surveys as its beam size (resolution) matches with the size of planet-forming disks in the nearby star-forming regions, optimizing the sensitivity for those kinds of observations.

The unique features of both telescopes allow for large surveys of planet-forming disks in relatively short integration times. In particular ALMA has revolutionized star and planet formation since the telescope saw its first light in 2011. It has been used extensively to obtain large samples of disks (nearly 2000 in total) around pre-main sequence stars in nearby low-mass star-forming regions such as Lupus, Taurus, Chamaeleon, and Upper Sco, and high-mass star-forming regions such as Orion.

Figure 1.4: The 12 meter antennas of the Atacama Large Millimeter/submillimeter Array (ALMA, top), and the 15 meter antennas of the Northern Extended Millimeter Array (NOEMA, bottom). Credit: ESO/C. Malin, and IRAM.

1.3.2   Findings from population studies

Protoplanetary disk population studies have greatly advanced our understanding of planet formation in the past decade. Different relationships between parameters have been found, which will be discussed here. A recent review by Manara et al. (2023) has collected the data of seven nearby star-forming regions, see Fig. 1.5. These star-forming regions include: Ophiuchus (Cieza et al. 2019; Williams et al. 2019), Taurus (combination of ALMA and SMA observations, e.g., Andrews et al. 2013, see Manara et al. 2023 for more details), Lupus (Ansdell et al. 2016, 2018; Sanchis et al. 2020), Chamaeleon I (Pascucci et al. 2016; Long et al. 2018), Chamaeleon II (Villenave et al. 2021), Upper Scorpius (Carpenter et al. 2014; Barenfeld et al. 2016; van der Plas et al. 2016), and Corona Australis (Cazzoletti et al. 2019). Besides these nearby star forming regions, Orion has been subject of many studies as well. One of the largest surveys to date is of L1641/L1647 (SODA, van Terwisga et al. 2022; van Terwisga & Hacar 2023), consisting of 873 disks in total (see also Grant et al. 2021). Other regions surveyed in Orion include σ Orionis (Ansdell et al. 2017), λ Orionis (Ansdell et al. 2020), NGC 2024 (van Terwisga et al. 2020), the Orion Nebula Cluster (ONC, Eisner et al. 2018), and the Orion Molecular Cloud-2 (van Terwisga et al. 2019). This section will shortly summarize some of the relationships found for the disk dust mass from these population studies, for a more comprehensive overview see Manara et al. (2023).

1.3.2.1   Dust mass versus stellar mass and age

One of the main findings from disk populations is the relationship between the stellar mass and the disk dust mass. Before ALMA, this relationship was already reported by Andrews et al. (2013) for the Taurus region. Since then, many other population studies done the same for other regions. The left panel of Figure 1.5 shows the disk dust and stellar masses of seven star-forming regions as collected by Manara et al. (2023).

Combining all surveys into one figure does not immediately show that there is a trend between the dust mass and stellar mass. However, when looking at each region separately, this relationship is well established by now. When fitting a powerlaw through the relation, $M_{\text{dust}} \propto M_{\text{star}}^{\alpha}$, the powerlaw index α was found to range from 1.7±0.2 for the 1-2 Myr old Taurus region to 2.4±0.4 for the 5-11 Myr old Upper Sco region, with in between values of α for regions with intermediate ages (Ansdell et al. 2017). These relationships have also been added to the left panel of Fig. 1.5. Around the relationship a spread of 0.6-0.9 dex is present, likely related to the initial formation conditions of the disks as this spread is present for all ages (Manara et al. 2023).

While tentative, the relationship between the stellar mass and the disk dust mass seems to steepen over time: the higher mass disks retain their disk mass for longer. While this particular relationship has not been subject of many modeling studies, the steepening of the relationship may be due to the effect of dust traps stopping radial drift (Pinilla et al. 2020). As the dust is stopped at larger radii, the emission area is larger and thus the recovered disk mass is higher. Still, the overall mass budget in millimeter sized grains clearly decreases in time, see Figure 1.6. This is likely due to disk dispersal, or grain growth and/or evolution (Manara et al. 2023). Though trends with age must be looked at carefully, as contamination due
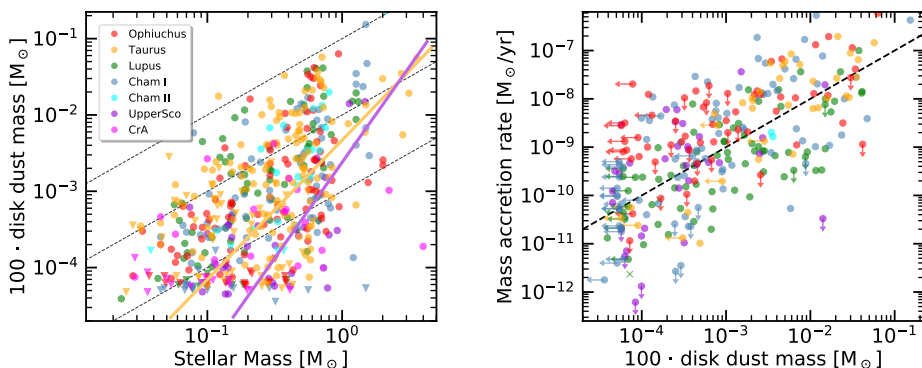
Figure 1.5: Relationships found based on the disk populations done with ALMA. The left panel shows the disk dust mass, stellar mass relationship, with the relationships for Taurus and Upper Sco from Ansdell et al. (2017) overplotted. The right panel presents the mass accretion rate against the disk dust mass. Both panels are from Manara et al. (2023).
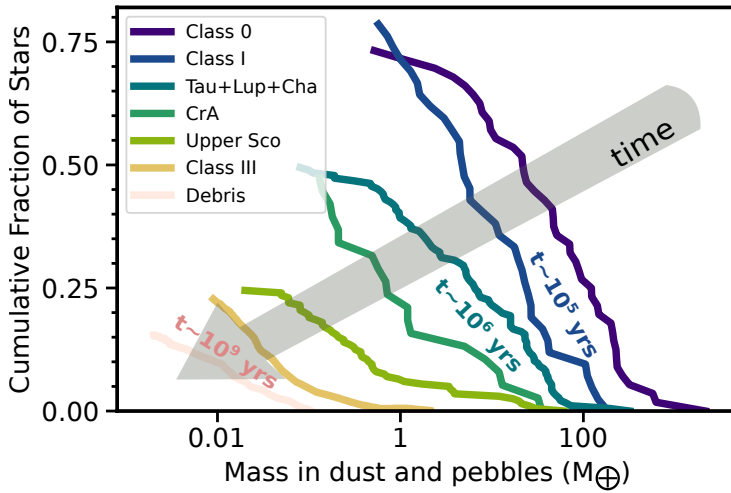
Figure 1.6: Dust mass cumulative distribution from Class 0 objects to debris disks from Drążkowska et al. (2023). There is a clear decrease in total disk mass, and fraction of stars with a disk, seen over time.

to the complex history of the region may happen (e.g., Krolikowski et al. 2021).

1.3.2.2   Versus disk dust radius

A relationship between the disk dust radius and the disk luminosity (or disk mass) has been found as well (Andrews et al. 2010; Tripathi et al. 2017; Tazzari et al. 2017, 2021; Hendler et al. 2020; Sanchis et al. 2021). The relationship is generally found to be sub-linear with a slope of ~ 0.5 (ranging from 0.4-0.6) in Lupus, Chamaeleon I, Ophiuchus, and Taurus, while for Upper Sco a shallower slope of ~ 0.2 was found (Hendler et al. 2020). One interpretation of this relationship is the presence of optically thick substructures in the disks (Tripathi et al. 2017; Andrews et al. 2018b; Zormpas et al. 2022). As the dust radial drift is stopped by the substructures, the emission size of the disk stays large.

A difference between the dust and (CO) gas radius has been found as well. While appealing, the difference cannot solely be related to radial drift. The optical depth of the dust continuum and gas lines differ: the continuum emission will be below the detection limit at smaller radii compared to the optically thick CO emission (Guilloteau & Dutrey 1998; Facchini et al. 2017; Trapman et al. 2019). A combination of optically thick gas emission and radial drift is indeed necessary to explain the ratio of ~ 2 between the gas radius and dust radius found for the disks in Lupus (Ansdell et al. 2018).

1.3.2.3   Versus stellar accretion rate

The relationship between the accretion rate and dust mass is well established and much more similar between different star forming regions compared to the stellar mass dust mass relationship, see the middle panel of Fig. 1.5. The accretion rate $\dot{M}_{acc}$ increases close to linearly with disk dust mass, which is expected from viscous evolution models (Manara et al. 2016; Rosotti et al. 2017). The spread of the relationship is distributed around the $M_{\mathrm{disk}}/\dot{M}_{\mathrm{acc}} = 1$ Myr line. From viscous evolution, this spread is expected to decrease with time, as the high and low accretors are decreasing in disk mass at different rates. This is however not observed in Upper Sco (Manara et al. 2020), but can be solved by taking into account that many of these disks are radial drift dominated and are therefore compact and some of the mass is not accounted for (Sellek et al. 2020). Other factors impacting the relationship between the stellar accretion and disk dust mass are for instance stellar irradiation and photo-evaporation (Rosotti et al. 2017), giant planets (Manara et al. 2019a), and binarity (Zagaria et al. 2022). Lastly, while the relationship is expected from viscous evolution, MHD disk winds can also explain the seen relationship and corresponding spread (Tabone et al. 2022b).

1.3.3   Comparisons to exoplanets

As large numbers of disks and exoplanets start to be gathered, comparisons between the two can be done. These comparisons have shown that the amount of dust present in Class II disks is less than what is necessary to build the exoplanetary systems observed (Manara et al. 2018; Tychoniec et al. 2020), though a careful consideration of the detection biases in the exoplanet population suggests that it is more similar (Najita & Kenyon 2014; Mulders et al. 2021). This can be reconciled by letting planets already form early on in the lifetime of the disk. Tychoniec et al. (2020) show that in Class 0 and I objects there is enough mass for the seen planet population to be formed. Indeed, recent observations show that dust substructures are already present in Class I objects (e.g., ALMA Partnership et al. 2015; Sheehan & Eisner 2018; Segura-Cox et al. 2020). van der Marel & Mulders (2021) demonstrate that the fraction of structured disks is strongly dependent on stellar mass, and that the occurrence rate of giant exoplanets is the same as the frequency of structured disks. This suggests a relation between giant exoplanets and the structures seen in disks. Furthermore, planets smaller than Neptune are anti-correlated with stellar mass, and are likely related to the non-structured disks (Mulders et al. 2015; van der Marel & Mulders 2021). These more compact disks are more likely to form Super-Earths due to a higher pebble flux (Lambrechts et al. 2019).

1.4   Planet formation around intermediate mass stars

The population studies discussed above have given important insights into the evolution of disks around pre-main sequence stars. However, as the stellar mass increases fewer stars reside in each star-forming region, at most only a couple

of intermediate mass stars are present in each. Therefore a dedicated study on intermediate mass stars is missing, which this thesis aims to solve.

1.4.1   What are Herbig stars?

Herbig Ae/Be stars were first observed in the seminal paper of George Herbig (Herbig 1960), who selected 26 Ae and Be stars which lie in obscured regions and illuminate nearby luminosity, trying to find stars with masses ranging from 3 $M_\odot$ to 20 $M_\odot$. Since then, the definition of a Herbig star has evolved. Herbig Ae/Be stars are defined as having spectral types B, A, and F, hydrogen emission lines (hence the "e"), and an infrared excess (The et al. 1994; Malfait et al. 1998; Waters & Waelkens 1998; Vieira et al. 2003; Brittain et al. 2023). The stellar masses range from 1.5 $M_\odot$ to 10 $M_\odot$, with the upper limit set by the stellar mass for which a non-obscured pre-main sequence phase is still expected (Brittain et al. 2023). The lower limit on the stellar mass on the other hand is set by the coolest (i.e., latest spectral type) star which is thought to reach the zero age main sequence as an A9 star. Therefore, as the star evolves towards the main sequence, there are stars which look like T Tauri stars but are of intermediate mass. These stars are called Intermediate Mass T Tauri stars and have spectral types of F0 to K3 and stellar masses ranging from 1.5 to 5 solar masses (Calvet et al. 2004; Valegård et al. 2021).

Thanks to ESA's Global Astrometric Interferometer for Astrophysics (Gaia) space observatory (Gaia Collaboration et al. 2016), the parallaxes to stars have been accurately obtained for more than 1.5 billion stars. By using the accurate parallaxes from Gaia data release 2 (Gaia Collaboration et al. 2018a), Vioque et al. (2018) obtained the distances and stellar parameters such as the stellar luminosities, masses, and ages of 252 Herbig stars. More recently, Gaia early data release 3 parallaxes (Gaia Collaboration et al. 2021) have also been used (Guzmán-Díaz et al. 2021). Based on these works, there are a total of 31 Herbig stars known within 225 pc and 87 Herbig stars within 450 pc (Guzmán-Díaz et al. 2021). However, these sets of Herbig stars are likely to be influenced by historical biases. Hence, Vioque et al. (2022) added 128 new Herbig stars based on new optical spectroscopy data, mostly residing at distances larger than 600 pc, making the total number of known Herbig stars to be around 360. Machine learning may identify even more (Vioque et al. 2020). In addition to the Herbig stars, the Gaia astronometric data have also been used to obtain a total of 49 Intermediate Mass T Tauri stars (Valegård et al. 2021). While being the precursors of Herbig stars, these stars need to be included for a complete view of disks around pre-main sequence intermediate mass stars.

Herbig stars are Class II objects, this is mainly due to part of its definition: the hydrogen emission lines necessitate that the Herbig stars are accreting and optically visible and therefore a mostly unobscured disk needs to be present. Removing this definition and only looking at the pre-main sequence intermediate mass stars which have an infrared excess (down to debris disk levels) reveals that a significant fraction of these stars have only debris disks left (Iglesias et al. 2023). Even though Herbig stars are relatively old, with a median age of a Herbig Ae star being 6 Myr, large and massive disks are still the norm (see Section 1.4.3).

Work towards a complete inventory of all intermediate mass pre-main sequence stars and their disks is therefore highly needed.

1.4.2   Stellar properties of Herbig stars

Herbig stars are the bridge between low and high mass star formation. Due to their higher stellar mass compared to T Tauri stars, there are stark differences with respect to their stellar and disk evolution. Herbig stars are more luminous and have higher effective temperatures, which result in Herbig stars having a higher UV radiation field, impacting the chemistry differently (see, e.g., Jonkheid et al. 2007, Miotello et al. 2016). This higher UV emission for example results in warmer disks resulting in less chemically complex carbon-bearing molecules (Bosman et al. 2018; Agúndez et al. 2018). Their higher mass also means that their evolution towards the main sequence occurs quicker when compared to T Tauri stars. This is especially the case for Herbig Be stars. Based on near infrared excess Vioque et al. (2018) found that the disks surrounding the Be stars are typically smaller for stars with a mass more than 7 $M_\odot$ than their lower mass counterparts, which is likely due to their stronger UV emission. Herbig Be stars are also found to be more clustered compared to the lower mass Ae stars (Vioque et al. 2023). As Herbig Be stars generally reside at larger distances from Earth, in combination with the fact that many of them are still surrounded by leftover cloud remnants, means that interferometer observations are needed to study them, which are still lacking (Brittain et al. 2023).

Accretion rates of Herbig stars are determined in the same way as is done for T Tauri stars. However, the accretion tracers are generally at UV wavelengths, where the Herbig star is brighter than a T Tauri star, making the contrast between the accretion luminosity and the stellar photosphere for Herbig stars smaller. This leads to a minimum accretion rate of $\sim 10^{-9}$-10^{-8} $M_\odot$ yr^{-1} (e.g., Mendigutía et al. 2011; Fairlamb et al. 2017; Wichittanakom et al. 2020; Grant et al. 2022). Some tracers of the accretion luminosity are for example Hα (Wichittanakom et al. 2020) and Brγ (Grant et al. 2022). Based on the line luminosity of these tracers the accretion luminosity can be determined via a linear relationship between the two, where the slope and intercept are different for each tracer (e.g., Fairlamb et al. 2017).

Once the accretion luminosity is determined one can obtain a mass accretion rate by assuming that the material is falling from infinity via

$$\dot{M}_{acc} = \frac{L_{acc} R_\star}{G M_\star},$$ (1.5)

where L_{acc} is the accretion luminosity, $R_\star$ and $M_\star$ are respectively the stellar radius and mass, and G is the gravitational constant. The accretion onto T Tauri stars is thought to occur via the magnetic field lines of the star's magnetic field (e.g., Hartmann et al. 2016). As the outer layers of these lower mass stars are convective, a magnetic field is generated which truncates the disk, the gas from the disk free-falls along the field lines resulting in the kinetic energy being changed into UV luminosity. This is called the magnetospheric accretion (MA) paradigm.

However, as higher mass stars are expected to have radiative envelopes, which do not generate a magnetic field, MA may not be applicable for Herbig stars. Still, it seems like that it can be applied to Herbig stars, especially to Herbig Ae stars, as the relationship only changes from that of the T Tauri stars above a stellar mass of 4 $M_\odot$ (e.g., Wichittanakom et al. 2020). Magnetic fields have been detected towards a few Herbig stars (Alecian et al. 2013; Hubrig et al. 2015; Mendigutía 2020), which may be fossil in nature (Brittain et al. 2023).
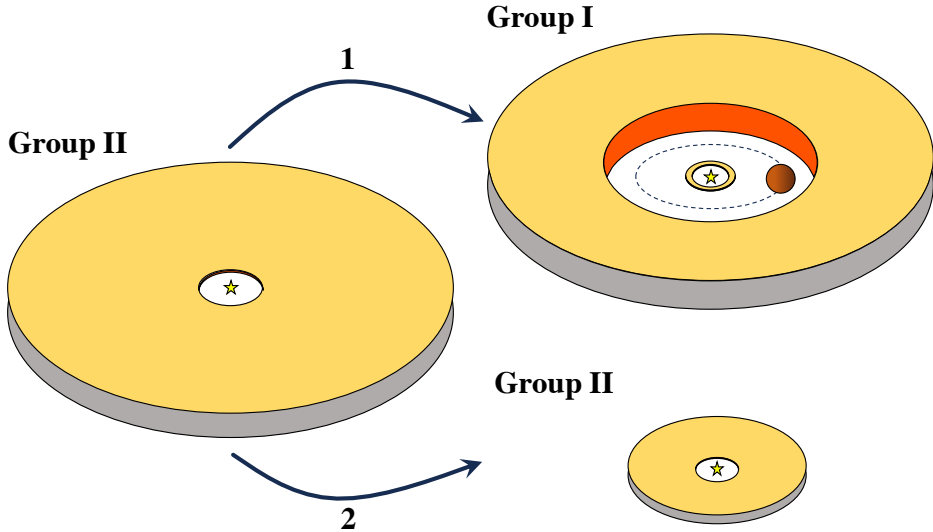
1.4.3   Evolution of Herbig disks

Disks around Herbig stars have been the focus of many in-depth studies. One of the main properties of Herbig disks is the so-called Meeus group, first identified by Meeus et al. (2001). Based on the mid-to-far-infrared spectral energy distribution (SED) of 14 Herbig stars measured with ISO, Meeus et al. (2001) divided the Herbig disks into two separate groups: group I for which the near- and mid-infrared continuum could be described by a power-law and a blackbody, while the group II disks can be reconstructed with only a power-law. Sub-groups were implemented as well, where the 'a' suffix was added when solid state bands are present, and a 'b' suffix was added if those were not visible. Other works have quantified this definition by either using IRAS 12-60 μm color (van Boekel et al. 2005), or an IR flux ratio (Khalafinejad et al. 2016).

The interpretation of these groups has stayed relatively similar since they were defined. Meeus et al. (2001) themselves interpreted the two groups as being either flared (group I) or flat (group II) disks. This results in an increase in far-IR emission, and thus FIR excess, for the group I disks, as the outer parts of the disk are illuminated by the star. On the other hand, as the group II disk is flat, the outer disk is not irradiated leading to no FIR excess. Dullemond & Dominik (2004a) modeled the SED of group I and group II disks and showed that the flaring of the disk can explain the seen dichotomy in Herbig disks. Later, Honda et al. (2012) proposed that the group I disks are disks with an inner cavity depleted of material, which results in large inner walls contributing to the mid and far-infrared excess.

Based on mid-infrared imaging, Maaskant et al. (2013) refined this view by proposing that Herbig disks start as a full flaring disk which eventually either form a gap, resulting in a group I disk, or flatten, resulting in a group II disk. Depending on the location of the gap size, the region from which the solid state bands originate are either completely depleted or heavily irradiated resulting in the corresponding 'a' and 'b' sub-classification. This would also mean that if a group II disk were to create an inner cavity, there would be an influx of group II disks towards the group I disks (Maaskant et al. 2013; Menu et al. 2015).

The last few years some major refinements have been made to this idea. As both resolved continuum dust emission with ALMA and scattered light imaging with SPHERE became available, Garufi et al. (2017) noted that there are large group II Herbig disks in sub-millimeter continuum, while barely or not visible in scattered light. Group II disks can also be small and flat, resulting in the same SED classification. An interplay between the inner and outer disk was found by

Figure 1.7: Proposed evolution of Herbig disks. First a full disk forms. Due to an puffed up inner disk the outer disk is shadowed, leading to a group II classification. Once a giant planet has formed in the outer disk, radial drift is stopped and an inner cavity forms, now depleted of dust (1). The inner rim of the disk is illuminated by the central star giving rise to a group I classification. In some disks a giant exoplanet does not form in the outer disk, leading the disk to shrink over time and stay classified as a group II (2).

Garufi et al. (2022): if the size of the disk seen in scattered light is small, but the NIR excess is large, the group II disk is shadowed by the inner disk, but if the disk does not have a large NIR excess, the group II disk is simply small. On the other hand, group I disks are generally large in both continuum emission and scattered light, with a clear gap visible in the continuum emission. If an inner disk is present in a group I disk this can shield the inner cavity from UV radiation and CO can survive (Banzatti et al. 2018).

Hence, the following intriguing picture arises. A full disk forms around a star, in which planets are forming. As the inner disk can still be puffed up, the outer disk is not irradiated by the central star. Once a massive planet forms, the radial transport of solids is stopped at the inner edge of the outer ring. The inner disk clears out due to radial drift and an empty inner cavity is formed; the outer disk now gets irradiated by the central star. On the other hand, if a massive planet does not form, the disk shrinks over time as all of the mass is accreted onto the star. The large group II disks could therefore still be able to evolve towards a group I classification by emptying an inner cavity. Similar scenarios have been proposed based on the morphology of disks around lower mass stars (van der Marel et al. 2018; Cieza et al. 2021).

It should be noted that the complexity needed to explain the group I and

group II classification should possibly incite us to rethink this classification. As high resolution observations of Herbig disks are now available, group I disks show deep cavities, while group II disks do not, with some exceptions. A redefinition would therefore simply be that group I disks are those with a cavity, or the transitional disks, while the group II disks are those without. More high resolution observations, especially for the more compact disks, are therefore highly needed.

1.4.4   Planet formation leftovers

After the Class II phase of the Herbig disks has passed, a debris disk is left over. Debris disks need to be sustained by collisional processes, and are therefore also known as secondary disks (Hughes et al. 2018). Debris disks around intermediate mass (AB-type) stars are found to have a higher detection rate of CO at millimeter wavelengths compared to later (FGK) spectral type stars (Lieman-Sifry et al. 2016). Though, a large range in upper limits is found, many at a similar level as the detections around AB-type stars (Matrà et al. 2015; Hughes et al. 2018). Both the origin of the gas (either primordial or second-generation) and the reason why there is a higher detection rate around intermediate mass stars is still heavily debated (Hughes et al. 2018). Additionally, a large fraction of the pre-main sequence intermediate mass stars with an infrared-excess are debris disks (Iglesias et al. 2023).

Going to the final result of planet formation, the exoplanets themselves, many thousands of exoplanets have been found to date and show a dependence on stellar mass. A large fraction of exoplanets consist of smaller planets such as super-earths residing around lower mass stars (e.g., Mulders et al. 2015), and, as discussed previously, may be related to the compact non-substructured disks. On the other
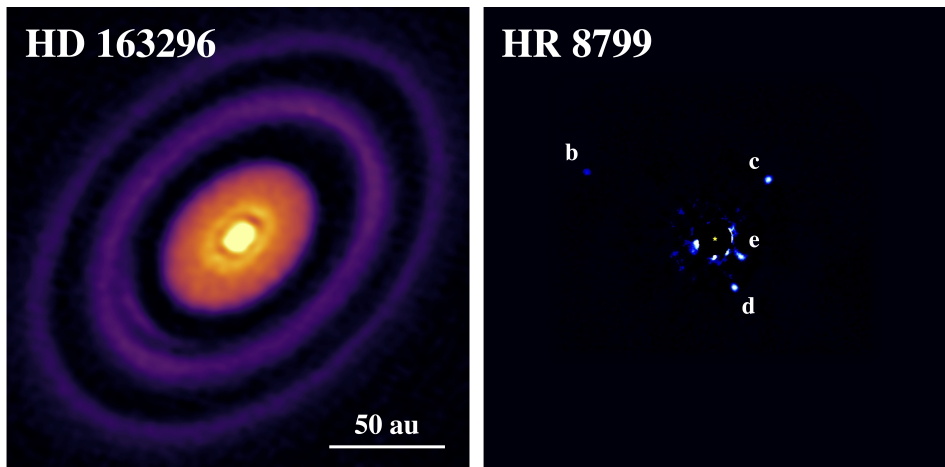
Figure 1.8: The spatial scales of the HD 163296 Herbig disk and the HR 8799 planetary system are remarkably similar (Andrews et al. 2018a; Marois et al. 2008, 2010). We may be witnessing the birth of a similar planetary system as HD 8799 in HD 163296.

hand, the occurrence rate of giant planets increases with stellar mass and is highest around intermediate mass stars (1.5-2 $M_\odot$, e.g., Johnson et al. 2007, 2010; Reffert et al. 2015; Nielsen et al. 2019). As mentioned before, the number of disk substructures is likely related to this (van der Marel & Mulders 2021), although this does invoke planet migration to occur for giant planets from the outer regions of the disk inwards. Yet, direct observations of exoplanets further away from their host star show that giant planets around intermediate mass stars such as HR 8799 (Marois et al. 2008, 2010), β Pic (Lagrange et al. 2010), and 51 Eri (Chauvin et al. 2017), are common (Vigan et al. 2021). The spatial scale of the HR 8799 system, consisting of four giant planets (7-10 $M_{\rm jup}$) at tens of au in separation, is very similar to that of HD 163296 (see Fig. 1.8). Observing planet formation occurring in the disk itself is more difficult, but over the last few years methods (in)directly detecting planets have started to be fruitful: PDS 70 (Keppler et al. 2018), AB Aur (Currie et al. 2022), HD 169142 (Hammond et al. 2023), HD 163296 (Izquierdo et al. 2022), HD 100546 (Booth et al. 2023a), AS 209 (Bae et al. 2022), and HD 97048 (Pinte et al. 2018b). Most of these detections are around intermediate mass stars.

These giant exoplanets are also influencing the elemental makeup of the central star itself. At least 33% of Herbig stars are found to be depleted in refractory elements, compared to 2% of all field stars (Folsom et al. 2012; also known as the λ Boötis phenomenon, Morgan et al. 1943). Herbig stars hosting group I disks are found to be depleted in refractory elements by 0.5 dex, but not in volatile elements, while Herbig stars hosting a group II disk are not depleted (Kama et al. 2015; Guzmán-Díaz et al. 2023). As group I disks are known to have large cavities (Fig. 1.7), this depletion of refractory elements of their host stars may point towards giant-planets forming in their disks.

Considering that current facilities are limited to detecting (proto)planets down to only a few Jupiter masses, Herbig disks are going to be one of the most important group of objects to hunt for giant planets and understand their formation. Systematic high spatial resolution studies are therefore urgently needed.

1.5 This thesis

The last decade, ALMA has observed complete star-forming regions, which almost primarily consist of T Tauri stars. As a consequence, a systematic study on disks surrounding higher-mass stars has mostly been ignored. This in spite of some of the most well-known and well-studied disks residing around Herbig stars. This thesis therefore focuses on the Herbig disks, and investigates how these compare to T Tauri disks. This thesis primarily aims to obtain a systematic view of the mass content in and radial extent of Herbig disks; both based on the dust and gas observations. This goal is primarily achieved with the use of archival data of the ALMA interferometer. The recent Gaia updated parallaxes have allowed for a much better determination of the Herbig star population, resulting in multiple works obtaining updated stellar parameters and distances for all known Herbig stars (e.g., Vioque et al. 2018; Guzmán-Díaz et al. 2021). Based on these works

all archival Band 6/7 ALMA data are obtained to determine the dust mass and radius from the continuum emission, gas mass and radius from the CO isotopologue emission, and compare the radial and vertical heights to infer evolutionary scenarios. The main work of this thesis is summarized in the following chapters.

Chapter 2 obtains the dust masses of Herbig disks, by obtaining archival Band 6 and Band 7 ALMA data of 36 Herbig disks. This results in a 64% complete sample out to 225 pc, and 38% complete out to 450 pc of the Vioque et al. (2018) sample. Comparing the obtained dust masses to those of the Lupus and Upper Sco star-forming regions, Herbig disks are found to be a factor of ~ 3 and ~ 7 more massive respectively. Moreover, while not all disks are resolved in these data, the Herbig dust disks are found to be larger in size compared to T Tauri disks. Differentiating between the group I and group II SED classification shows that the group I disks are more massive than the group II disks. As intermediate mass stars are associated with a high occurrence rate of giant planets, this difference in dust masses between the T Tauri and Herbig disks, and the differences between the group I and group II disks in the Herbig disk population itself, could be related to giant planet formation. As radial drift is stopped in the Herbig group I disks, the subsequent disk evolution then enlarges the differences between the T Tauri disks (or group I and group II disks) resulting in enlarging the inferred disk masses.

Chapter 3 focuses on the gas masses of Herbig disks, which is in effect the total disk mass and important for setting the stage of planet formation in disks. Multiple techniques have been developed to determine the total mass of a disk in the past years, one of which is with the use of the CO isotopologues ^{13}CO and $C^{18}O$. While for T Tauri stars CO has been shown to be frozen out and reprocessed into other molecules, resulting in apparent low gas masses, Herbig disks are expected to be much warmer, and hence the total mass can be determined by using CO. This chapter gathers the ^{12}CO, ^{13}CO, and $C^{18}O$ observations of 35 Herbig disks, consisting of ALMA archival data and new NOEMA observations. Using the thermochemical code Dust And LInes (DALI), the luminosity of the CO isotopologues can be related to the total disk mass. It is found that the Herbig disks are optically thick in both the ^{13}CO and $C^{18}O$ isotopologues, resulting in lower limits on the total disk mass for most of the 22 disks in which the two isotopologues are detected. Combining with the dust masses from Chapter 2, the gas-to-dust ratios are found to be consistent with 100 (the canonical interstellar matter value) or higher. Over multiple orders of magnitude in dust mass, the gas-to-dust ratio is two orders of magnitude higher compared to those found for T Tauri disks with similar techniques, indication the importance of the chemical conversion of CO in colder T Tauri disks.

Chapter 4 presents the first complete survey of Herbig disks in a single star-forming region. A total of 35 Herbig disks are identified in the Orion region, of which this chapter presents 25 new NOEMA observations and an additional 10 ALMA archival data. These data are used to obtain an unbiased view of the dust masses around Herbig disks. A median dust mass of 11.7 $M_\oplus$ is found, hence

around 50% of the Herbig disks are more massive than 10 $M_\oplus$ while this is only the case for less than 25% of the T Tauri disks in Orion. Comparing these dust masses to those found in Chapter 2, a slight bias towards higher disk masses is found for the disks observed with ALMA compared to those in Orion. Moreover, due to the higher dust masses specifically at the lower UV-irradiated regions, a steeper relation between the dust mass and UV irradiation is found compared to T Tauri disks.

Chapter 5 combines the dust masses from Chapter 2 together with accretion rates of Herbig disks to obtain the disk mass accretion rate relationship for Herbig disks. This fundamental property has been well-established for T Tauri disks, and is a key diagnostic in constraining the disk lifetime. For a total of 32 Herbig disks both parameters are known, and while the accretion rates are largely flat around 10^{-7} $M_\odot$ yr^{-1}, the dust masses differ over three orders of magnitude in dust mass. Specifically around the high dust mass end the Herbig disks follow the established T Tauri disk relationship. The problem arises from the 12 outliers at low dust mass high accretion rates, for which a disk lifetime of less than 0.01 Myr is inferred, most of which are group II sources. As Herbig stars need a high accretion rate to be identified as such, these objects have likely been identified in part by this bias. Multiple solutions are proposed, from optically thick dust emission, to overestimating the accretion rate due to disk winds contributing to the Brγ line. Still, the data suggests that group II disks are on the verge of dissipation, which may be due to efficient radial drift in these disks as they were not able to form dust traps in the outer disk like group I disks.

Chapter 6 explores the interpretation of group I disks being vertically extended, while group II disks are flat or self-shadowed by directly tracing the emission height of eight Herbig disks in ^{12}CO. All four group I disks are found to be vertically extended, while the four group II disks are either vertically extended or compact (< 200 au in size) and flat. These findings agree with previous works, suggesting that group II disks can be either shadowed, but still large, or small and flat. The two group II disks which are found to be vertically extended (MWC 480 and HD 163296) may be precursors of group I disks, which will eventually form a cavity and the outer disks starts to be irradiated. The two flat disks (AK Sco and HD 142666) may have undergone significant settling because of the advanced age of the disks.

Chapter 7 looks into the disks of the precursors of Herbig stars, the Intermediate mass T Tauri (IMTT) disks. Obtaining ALMA archival data of 34 IMTT disks, the dust and gas masses are obtained using the techniques from Chapters 2 and 3. The IMTT disks are found to have the same dust and radius distributions as the Herbig disks. Furthermore, no differences in dust mass are found between the group I and group II disks, which further substantiates the hypothesis proposed in Chapter 2 where group I disks have formed a giant exoplanet stopping radial drift, while the group II disks have not and slowly drift towards smaller and more optically thick disks. Based on these findings, it is concluded that most disks around intermediate mass pre-main sequence stars converge quickly to small disks

unless prevented by a massive exoplanet.

The following main conclusions can be constructed based on the chapters of this thesis:

1. Herbig disks are massive, both in dust and gas (*Chapters 2-4, 7*).

2. The Herbig dust masses are more massive compared to T Tauri disks, especially when taking the advanced age of the Herbig disks into account compared to the younger T Tauri disks (*Chapters 2, 4*).

3. Herbig disks are larger in size compared to T Tauri disks (*Chapter 2*).

4. For the warmer Herbig disks CO freeze-out is not significant, in contrast to the colder T Tauri disks, resulting in CO being a good disk mass tracer in these disks (*Chapter 3*).

5. Herbig disks are found to have high accretion rates independent of disk dust mass, which is in contrast to T Tauri disks for which a positive correlation is found (*Chapter 5*).

6. The group I, group II classification of Herbig disks may need to be redefined, now that resolved high-resolution millimeter observations are available (*Chapters 2, 6*).

7. Giant planet formation is impacting the evolution of Herbig disks. The high disk masses and large radii (*Chapters 2, 3, 7*), the quick or slow dissipation of the disk (*Chapters 2, 5*), the significant differences compared to T Tauri disks (*Chapters 2, 4*), and the similarities between the disks around Herbig stars and the disks around their precursors the IMTT stars (*Chapter 7*), are all pointing towards giant planet formation occurring in these disks.

1.6   Future outlook

The future of Herbig stars and disks is bright. Following on the Chapter 2 results, a push towards obtaining a full set of millimeter observations of Herbig disks is now starting to be fruitful. In the near future a full dust mass study on all known Herbig disks within 750 pc will be possible. This will increase the number of Herbig disks with millimeter observations by a factor of more than 5 compared to the study done in Chapter 2. This will give great insights into the population of Herbig disks, with numbers comparable to many T Tauri disk dominated star-forming regions. The additional ALMA 2030 upgrades will allow for deeper observations in shorter integration times, and cover more molecular lines in a single observation, which is ideal for large population studies of disks.

In the coming years, a large part of the community will focus on observing protoplanets (in)directly in disks. As recent observations have shown, many of the directly and indirectly observed protoplanets in disks are around Herbig stars. As intermediate mass stars have a high occurrence rate of giant exoplanets, in

combination with a Jupiter mass sensitivity of the current observatories, Herbig disks will be at the forefront of understanding the formation and evolution of giant exoplanets in the foreseeable future. One should also not forget the compact Herbig disks, which are in desperate need to have high resolution ALMA observations, to both obtain a measure of their size and search for substructures. These disks likely form Super-Earths due to the higher pebble flux. Upcoming large telescopes such as the Extremely Large Telescope (ELT) will therefore be important in observing the inner regions of these disks and look for lower mass planets. This necessitates obtaining high resolution and deep ALMA observations of all Herbig disks.

For tracing the total mass in Herbig disks, rare CO isotopologues such as $^{13}C^{17}O$ will be important. With ALMA these should be detectable in a large fraction of the Herbig disk population within an hour of integration time. While HD is still thought to be one of the best disk mass tracers, there will not be any observatories which will be able to observe the $J = 1 - 0$ line soon. One of the planned far-infrared probes, the Space Infrared Telescope for Cosmology and Astrophysics (SPICA), has unfortunately been discontinued. Still, for Herbig disks there are a dozen HD upper limits available to combine with the rare CO isotopologues. Regarding the dust, the upcoming Square Kilometer Array (SKA, Ilee et al. 2020) and the Next Generation Very Large Array (ngVLA) will revolutionize our understanding of cm-sized grains (provided that processes such as free-free emission can be accounted for), and give insights into if the disks are optically thick.

Especially for probing the group I and group II dichotomy in Herbig disks, tracing the inner disk will be of importance. The James Webb Space Telescope (JWST) is already revolutionizing our understanding of the inner disk chemistry of mostly T Tauri disks, as nearby Herbig disks are too bright. Still, the influence of the outer disk on the composition of the inner disk will be interesting to test in the context of the two groups. Later on, ELT will advance this further. Regarding scattered light imaging, the Spectro-Polarimetric High-contrast Exoplanet REsearch (SPHERE) instrument on the Very Large Telescope (VLT) is close to being decommissioned, but the improved contrast of SPHERE+ will especially be important for the bright Herbig stars, to probe the smaller or shadowed disks in the population.

Lastly, and more practically, as also mentioned in Brittain et al. (2023), the definition of what a Herbig star is may need to be reassessed. The current definition includes only pre-main sequence intermediate mass stars with hydrogen emission line features, likely biasing the population to high accretors. Ideally the definition should include all pre-main sequence stars with stellar masses of $1.5 - 10$ M$_\odot$.

Concluding, there is much to be looking forward to the coming years, not only in the field of Herbig stars and disks, but in the general field of planet formation.

PART I

Surveying the Herbig disk
population

The mass and size of Herbig disks as seen by ALMA

L. M. Stapper, M. R. Hogerheijde, E. F. van Dishoeck, R. Mentel

Abstract

Context: Many population studies have been performed over the past decade with the Atacama Large millimeter/submillimeter Array (ALMA) to understand the bulk properties of protoplanetary disks around young stars. The studied populations have mostly consisted of late spectral type (i.e., G, K & M) stars, with relatively few more massive Herbig stars (spectral types B, A & F). With GAIA-updated distances, now is a good time to use ALMA archival data for a Herbig disk population study and take an important step forward in our understanding of planet formation.

Aims: The aim of this work is to determine the masses and sizes of all Herbig dust disks observed with ALMA to date in a volume-limited sample out to 450 pc. These masses and sizes are put in the context of the Lupus and Upper Sco T Tauri disk populations.

Methods: ALMA Band 6 and Band 7 archival data of 36 Herbig stars are used, making this work 64% complete out to 225 pc, and 38% complete out to 450 pc also including Orion. Using stellar parameters and distances, the dust masses and sizes of the disks are determined via a curve-of-growth method. Survival analysis is used to obtain cumulative distributions of the dust masses and radii.

Results: Herbig disks have a higher dust mass than the T Tauri disk populations of Lupus and Upper Sco by factors of ~ 3 and ~ 7 respectively. In addition, Herbig disks are often larger than the typical T Tauri disk. Although the masses and sizes of Herbig disks extend over a similar range to those of T Tauri disks, the distributions of masses and sizes of Herbig disks are significantly skewed toward higher values. Lastly, group I disks are more massive than group II disks. An insufficient number of group II disks are observed at sufficient angular resolution to determine whether or not they are also small in size compared to group I disks.

Conclusions: Herbig disks are skewed towards more massive and larger dust disks compared to T Tauri disks. Based on this we speculate that these differences find their origin in an initial disk mass that scales with the stellar mass, and that subsequent disk evolution enlarges the observable differences, especially if (sub)millimeter continuum optical depth plays a role. Moreover, the larger disk masses and sizes of Herbig stars could be linked to the increasing prevalence of giant planets with host star mass.

2.1   Introduction

Many population studies of protoplanetary disks in various star-forming regions have been carried out in recent years with the Atacama Large millimeter/submillimeter Array (ALMA). These demographic studies have led to new insights into disk evolution by finding relations between stellar mass and disk mass (e.g., Andrews et al. 2013; Barenfeld et al. 2016; Ansdell et al. 2016; Pascucci et al. 2016), and between disk radius and disk mass (Andrews et al. 2013, 2018b; Tripathi et al. 2017; Tazzari et al. 2021). On the other side of the planet formation process, exoplanet demographics show a trend where higher mass stars (1 $M_\odot$ and higher) are more often associated with planets more massive than 100 $M_\oplus$ than stars with lower stellar masses (e.g., Johnson et al. 2007, 2010; Wittenmyer et al. 2020; Fulton et al. 2021). The increasing number of observed exoplanets and disks allows for connections to be made between the beginning and ending stages of planet formation (e.g Mulders et al. 2021), improving our understanding of the relations found in both disk and exoplanet demographics.

The increase in occurrence rate of giant exoplanets around more massive main sequence stars coincides with the frequency of substructure in disks —as seen in the (sub)millimeter continuum emission— in the form of rings and gaps (van der Marel & Mulders 2021), suggesting a connection between the two. One pathway for these structures to form is via planets forming inside these disks, creating pressure bumps preventing the radial drift of dust (e.g., Birnstiel et al. 2010) and influencing the overall evolution of a disk (Pinilla et al. 2020; Cieza et al. 2021). The relationships found between stellar mass, disk mass, and disk extent might explain the observed increase in occurrence rate of massive planets with stellar mass and orbital radius (Andrews et al. 2013). This introduces an enticing scenario in which the more massive disks produce gas giant planets at greater distances, creating structured disks, while the less massive disks shrink over time because of radial drift (Cieza et al. 2021; van der Marel & Mulders 2021). Indeed, the more massive disks seem to retain their disk mass for longer, steepening the stellar mass–dust mass relation over time (Pascucci et al. 2016; Ansdell et al. 2017), while on the contrary, the dust radii in the 5–11 Myr-old Upper Sco star-forming region (SFR) were found to be significantly smaller than those in the younger 1–3 Myr-old Lupus region (Barenfeld et al. 2017; Ansdell et al. 2018), suggesting an evolution towards smaller disks.

However, as expected from the initial mass function (e.g., Kroupa 2001; Bastian et al. 2010), these disk population studies mainly consist of T Tauri stars and lack coverage of more massive pre-main sequence (PMS) stars (cf. top panel of Fig. 2.1 and Table 2.A.1). These more massive stars, known as Herbig Ae/Be stars (Herbig 1960; Waters & Waelkens 1998), typically have masses between 2 $M_\odot$ and 12 $M_\odot$, are optically visible and have, by definition, an excess in infrared (IR) light because of a disk surrounding them. Infrared excess is used to classify their spectral energy distributions (SED) into group I and group II disks (Meeus et al. 2001). This division was based on whether the SED could be described by a single power law at mid- to far-IR wavelengths or if an additional blackbody component was necessary. Lastly, due to the PMS evolutionary tracks being horizontal for
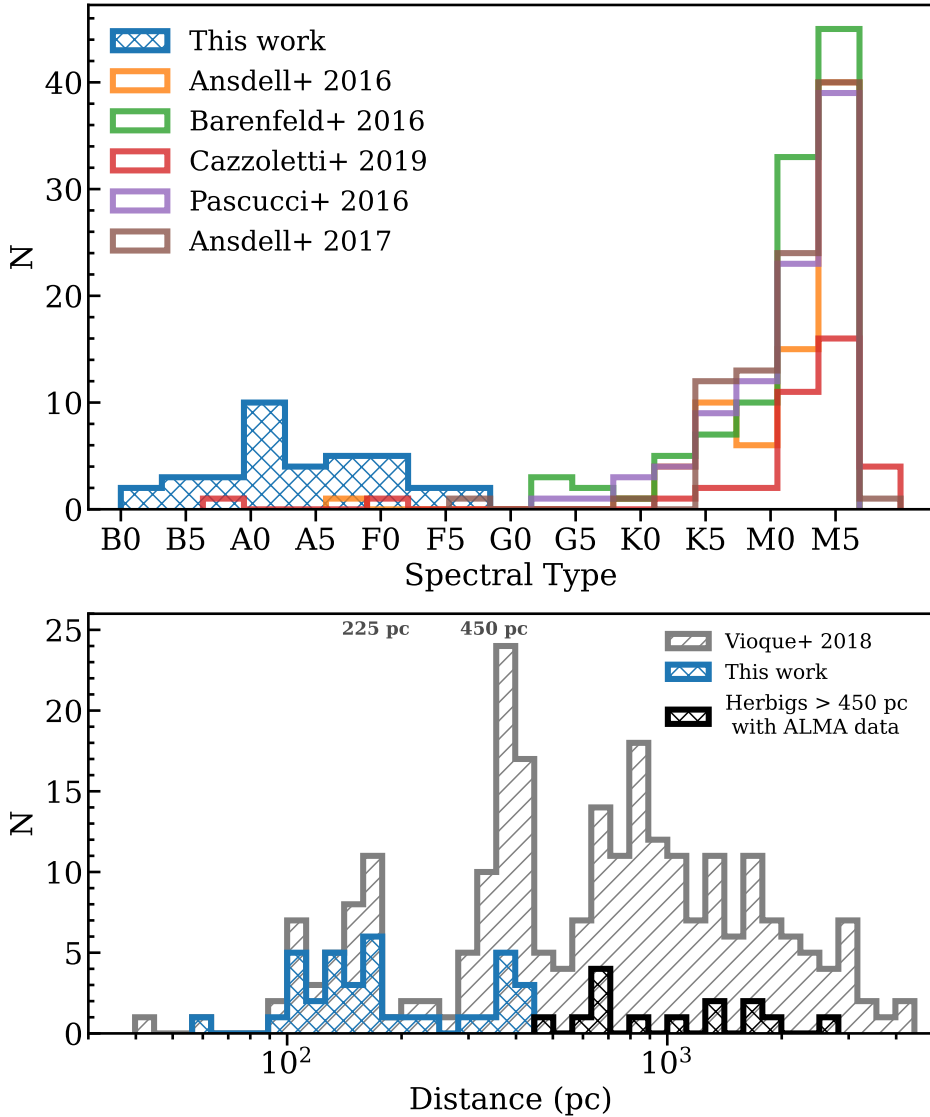
Figure 2.1: Top: Histogram of spectral types of five different population studies together with the full sample of this work. The population studies included are: Lupus (Ansdell et al. 2016), σ Orionis (Ansdell et al. 2017), Upper Sco (Barenfeld et al. 2016), Corona Australis (Cazzoletti et al. 2019), and Chamaeleon I (Pascucci et al. 2016). **Bottom:** Histogram of the distances of the 252 Herbig disks as defined by Vioque et al. (2018) and the full sample used in this work. The black histogram shows the Herbig disks beyond 450 pc for which ALMA data are available. The shaded areas indicate the two different cutoffs used in this work.

early-spectral-type stars, stars which end up with a spectral type A will first be F- or even G-type stars. Therefore, Herbig Ae stars are relatively old. To counteract this, research into intermediate-mass T Tauri stars —which precede Herbig Ae stars— has been done (recently e.g., Valegård et al. 2021) and the definition of Herbig Ae/Be stars is often expanded to include F-type stars (e.g., Chen et al. 2016; Vioque et al. 2018).

While T Tauri stars are abundant throughout star-forming regions, less than 300 Herbig stars are known to date (The et al. 1994; Carmona et al. 2010; Chen et al. 2016; Vioque et al. 2018, 2020; Guzmán-Díaz et al. 2021), which include stars with spectral types ranging from B to F. Before ALMA, dust mass studies of disks around Herbig stars (hereafter: Herbig disks) have been done with other facilities such as the NRAO Very Large Array (VLA) and the IRAM Plateau de Bure (e.g., Alonso-Albi et al. 2009) and while recent work by van der Marel & Mulders (2021) does include all Herbig disks associated with nearby SFRs (but does not include isolated Herbig disks), there has not yet been a dedicated population study of Herbig disks observed with ALMA. Nevertheless, a significant portion of the nearby Herbig disks have been observed with ALMA over the years in a variety of programs and these data are used in the present work for a first systematic look at Herbig disks with ALMA.

In this study, we use a more complete sample of Herbig disks compared to any other survey done before. Distances from GAIA parallaxes and newly determined stellar properties (Vioque et al. 2018) allow for a well-defined sample. What is the typical extent and mass of a Herbig disk? Do the dust disk mass and extent follow the expected stellar mass–dust mass relationship? Do Herbig disks fall within the posed scenario in which larger disks form giant planets further out, while smaller disks decrease in size over time? Are there any differences between the dust mass and extent and the groups defined by Meeus et al. (2001) based on their SEDs? To answer these questions, we determine the dust mass and extent of Herbig disks with ALMA archival data in a volume-limited sample and compare these parameters with their T Tauri counterparts from previous population studies. Section 2.2 shows the selection process of the sample used in this work. Section 2.3 sets out how the data are retrieved and how the integrated (sub)millimeter flux and size was determined. Section 2.4 describes the results of the dust mass and extent measurements and compares these to the Lupus and Upper Sco SFRs. In Sect. 2.5 we discuss the implications on the stellar mass–dust mass and disk radius–dust mass relations and look at the Meeus et al. (2001) group dichotomy. Section 2.6 summarizes our conclusions.
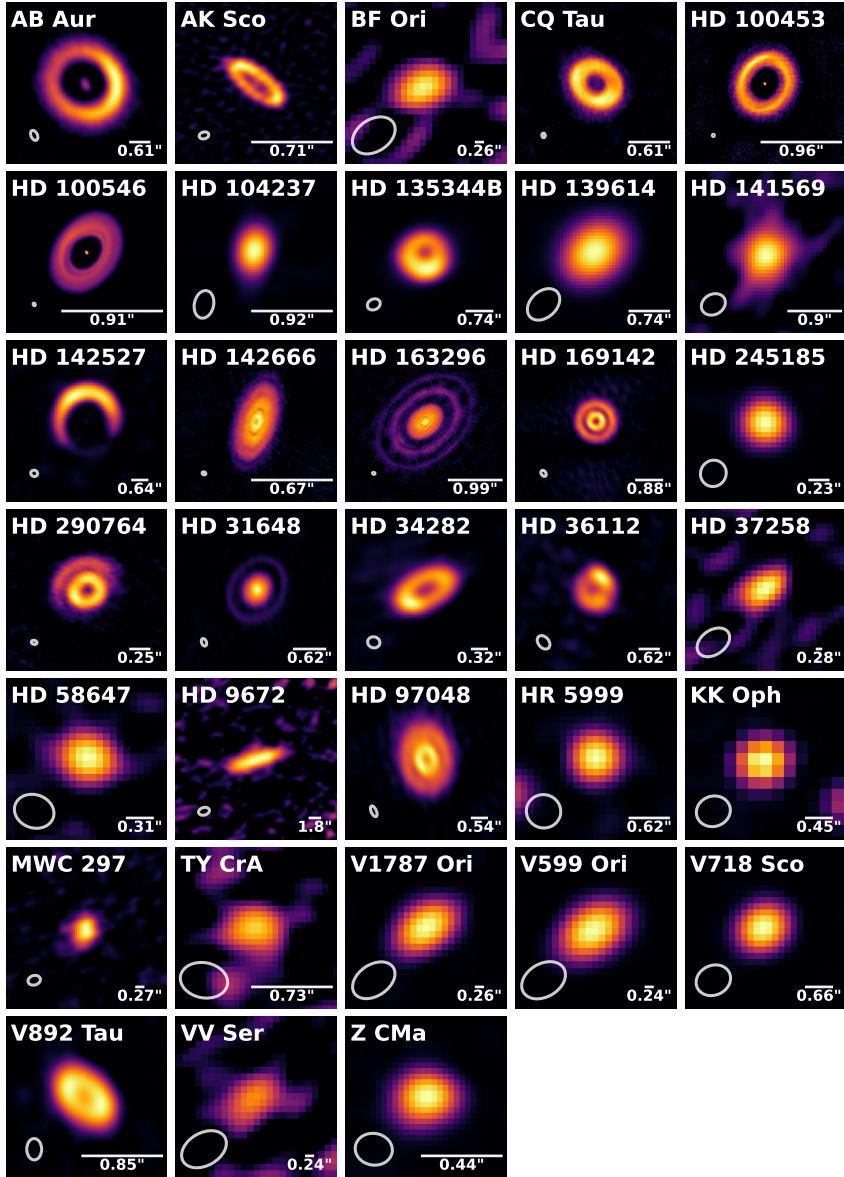
Figure 2.2: ALMA Band 6 and 7 continuum images of all objects. The size of the beam is shown in the bottom left of each plot and a scale bar of 100 au in size together with the angular scale in arcseconds is shown in the bottom right. Each image is normalized with an asinh stretch to make the fainter details of the disk more visible. HD 53367, HD 176386 and R CrA, which are not detected, are not shown.

Table 2.1: Coordinates and spectral types of the Herbig stars used in this work and the calculated Band 6 and 7 flux densities and dust masses of each Herbig disk.

Name	R.A.J2000 (h:m:s)	Decl.J2000 (deg:m:s)	Sp.Tp.	Group	$F_{cont.}$ (mJy)	M_{dust} ($M_\oplus$)	$R_{dust, 68\%}$ (au)	$R_{dust, 90\%}$ (au)	inc (°)	PA (°)	Ref.
AB Aur[α]	04:55:45.9	+30:33:04	A0	I	192.8	11.8±1.2	186±15	225±34	23.2	99	1, i, β
AK Sco	16:54:44.9	−36:53:19	F5	II	26.1	6.1±0.6	42±3	53±15	71	39	2, ii, β
BF Ori	05:37:13.3	−06:35:01	A7	II	0.8	1.1±0.1	<233	<311	–	–	3, β
CQ Tau[α]	05:35:58.5	+24:44:54	F5	I	144.0	44.2±4.8	62±4	76±18	35	35	4, iii, β
HD 100453	11:33:05.6	−54:19:29	A9	I	141.1	17.5±1.8	39±2	44±6	38	128	5, iv, β
HD 100546	11:33:25.4	−70:11:41	A0	I	399.6	38.0±3.9	35±2	41±4	43	131	6, v, β
HD 104237[α]	12:00:05.1	−78:11:35	A0	II	88.9	10.5±1.1	<59	<98	–	–	5, β
HD 135344B	15:15:48.5	−37:09:16	F8	I	539.7	35.2±3.8	81±10	109±31	11	28	7,vi, β
HD 139614	15:40:46.4	−42:29:54	A9	I	197.2	41.7±4.3	<65	<97	–	–	6, β
HD 141569	15:49:57.8	−03:55:16	A2	II	3.4	0.36±0.04	<139	<232	–	–	6, β
HD 142527	15:56:41.9	−42:19:23	F6	I	1048.1	214.9±22.1	208±9	236±33	27	71	8, vii, β
HD 142666	15:56:40.0	−22:01:40	F0	II	118.6	25.1±2.6	40±3	52±11	60	109	6, viii, β
HD 163296	17:56:21.3	−21:57:22	A1	II	541.3	46.7±5.0	71±6	101±16	45	137	4, ix, β
HD 169142[α]	18:24:29.8	−29:46:49	F1	I	203.7	22.9±2.4	71±7	140±77	13	5	6, x, β
HD 176386[α]	19:01:38.9	−36:53:27	B9	II	<0.32	<0.06	–	–	–	–	9, γ
HD 245185	05:35:09.6	+10:01:52	A0	I	34.6	41.5±7.6	<76	<126	–	–	10, β
HD 290764	05:38:05.3	−01:15:22	F0	I	210.1	90.3±11.8	119±16	167±28	30	154.6	5, xi, β
HD 31648[α]	04:58:46.3	+29:50:37	A5	II	253.0	70.9±7.7	58±18	107±49	37	122	4, xii, β
HD 34282	05:16:00.5	−09:48:35	B9.5	I	99.0	86.8±9.7	189±18	260±77	60	150	11, xiii, β
HD 36112[α]	05:30:27.5	+25:19:57	A8	I	70.7	18.8±2.0	90±17	123±50	21	65	5, xiv, β
HD 37258[α]	05:36:59.3	−06:09:16	A3	II	1.8	2.4±0.4	<326	<435	–	–	3, β
HD 53367[α]	07:04:25.5	−10:27:16	B0	?	<0.81	<0.05	–	–	–	–	12
HD 58647[α]	07:25:56.1	−14:10:44	B9	II	1.9	1.0±0.1	<75	<126	–	–	13, β
HD 9672[α]	01:34:37.9	−15:40:35	A1	II	4.1	0.13±0.01	315±39	473±111	81	161	13, xv, β
HD 97048	11:08:03.3	−77:39:18	A0	I	711.4	155.9±16.0	182±19	245±69	41	85	14, xvi, β
HR 5999	16:08:34.3	−39:06:18	A7	II	26.5	4.0±0.4	<48	<81	–	–	15, β

Table 2.1: Continued.

Name	R.A._J2000 (h:m:s)	Decl._J2000 (deg:m:s)	Sp.Tp.	Group	$F_{\rm cont.}$ (mJy)	$M_{\rm dust}$ ($M_\oplus$)	$R_{\rm dust,\,68\%}$ (au)	$R_{\rm dust,\,90\%}$ (au)	inc (°)	PA (°)	Ref.
KK Oph$^\alpha$	17:10:08.1	-27:15:19	A6	II	27.7	17.4±2.5	<88	<88	–	–	16, δ
MWC 297	18:27:39.5	-03:49:52	B1.5	I	288.7	65.7±9.6	<169	<253	–	–	17, β
R CrA$^\alpha$	19:01:53.7	-36:57:09	B5	II	<65.8	<13.2	–	–	–	–	18, ϵ
TY CrA$^\alpha$	19:01:40.8	-36:52:34	B9	I	0.67	0.10±0.01	<27	<34	–	–	5, β
V1787 Ori$^\alpha$	05:38:09.3	-06:49:17	A5	I	14.8	24.2±2.9	<313	<391	–	–	5, β
V599 Ori	05:38:58.6	-07:16:46	A8.9	I	55.9	75.0±8.6	<328	<410	–	–	19, β
V718 Sco	16:13:11.6	-22:29:07	A5	II	49.5	11.9±1.3	<69	<114	–	–	20, β
V892 Tau$^\alpha$	04:18:40.6	+28:19:15	A0	I	285.4	76.1±8.3	40±4	52±13	54.5	52.1	21, xvii, ζ
VV Ser	18:28:47.9	+00:08:40	B5	II	2.3	2.3±0.3	<239	<399	–	–	22, β
Z CMa$^\alpha$	07:03:43.2	-11:33:06	B5	I	29.3	7.6±6.4	<28	<41	–	–	23, β

Notes. All distances are obtained from Vioque et al. (2018). The luminosities, stellar masses, and ages were obtained from Wichittanakom et al. (2020) except the objects marked with an α of which these parameters were obtained from Vioque et al. (2018). The objects in italics are from the Vioque et al. (2018) low-quality parallax sample, and the others are from the high-quality sample. The error on the continuum flux is 10% of the given value. *Spectral type references:* (1) Mooley et al. (2013), (2) Houk (1982), (3) Tisserand et al. (2013), (4) Mora et al. (2001), (5) Vieira et al. (2003), (6) Gray et al. (2017), (7) Coulson & Walther (1995), (8) Houk (1978), (9) Torres et al. (2006), (10) Gray & Corbally (1998), (11) Houk & Swift (1999), (12) Tjin A Djie et al. (2001), (13) Houk & Smith-Moore (1988), (14) Irvine & Houk (1977), (15) Bessell & Eggen (1972), (16) Carmona et al. (2007), (17) Drew et al. (1997), (18) Gray et al. (2006), (19) Hsu et al. (2013), (20) Carmona et al. (2010), (21) Skiff (2014), (22) Guzmán-Díaz et al. (2021), (23) Covino et al. (1984). *Inclination and position angle references:* (i) Tang et al. (2017), (ii) Czekala et al. (2015), (iii) Ubeira Gabellini et al. (2019), (iv) Benisty et al. (2017), (v) Pineda et al. (2019), (vi) Stolker et al. (2016), (vii) Kataoka et al. (2016), (viii) Rubinstein et al. (2018), (ix) de Gregorio-Monsalvo et al. (2013), (x) Fedele et al. (2017), (xi) Kraus et al. (2017), (xii) Liu et al. (2019), (xiii) van der Plas et al. (2017a), (xiv) Isella et al. (2010), (xv) Hughes et al. (2017), (xvi) van der Plas et al. (2017b), (xvii) Long et al. (2021). *Meeus group references:* (β) Guzmán-Díaz et al. (2021), (γ) Boersma et al. (2009), (δ) Juhász et al. (2010), (ϵ) Acke & van den Ancker (2004), (ζ) Menu et al. (2015).

2.2   Sample selection

The sample in this work is based on the GAIA DR2 study of Herbig Ae/Be stars of Vioque et al. (2018) for which ALMA data are available. Previous population studies were limited to one SFR and consequently all stars have approximately the same distance, but the Herbig stars are distributed over the sky and therefore each has a different distance, which should be well determined. The newly determined GAIA distances and accurately derived stellar properties inspired us to do a population study on these objects.

Vioque et al. (2018) obtained a sample of 218 objects classified as Herbig stars with high-quality parallax measurements from GAIA DR2 (Gaia Collaboration et al. 2018b). In addition, 34 Herbig stars were classified as belonging to a low-quality parallax measurement sample. We take the stellar properties (mass, age) from Vioque et al. (2018), who determine these from comparison to isochrones in the HR-diagram (see Table 1 of Vioque et al. (2018) for an overview of the values we adopted). The bottom panel of Fig. 2.1 shows the distribution of a total of 252 Herbig stars over distance. The first peak at a distance of $\sim$ 200 pc consists of the nearby star-forming regions. The second peak at a distance of $\sim$ 400 pc is the Orion star-forming complex, after which —at much larger distances— the distribution goes up again due to a fast increase in volume. Due to incompleteness, the number of sources decreases again at large distances. From this figure, two natural cutoff distances emerge to define our sample and a subsample of all Herbig disks. One cutoff distance is at 450 pc. This distance includes the Orion star-forming complex and has a relatively good sampling of Herbig disks observed with ALMA compared to the full sample of disks given by Vioque et al. (2018). After 450 pc, this sampling becomes quite sparse (see the bottom panel of Fig. 2.1). The other cutoff distance is at 225 pc, which excludes Orion, but includes the nearby star-forming regions, and has a more complete sampling. Using a limit of 450 pc (225 pc) leaves a total of 96 (39) Herbig stars as listed by Vioque et al. (2018) of which 42 (25) have ALMA archival data.

While classified as Herbig stars by Vioque et al. (2018), four objects with ALMA archival data are not included in our work: HD 143006 and BP Psc are left out because they have a G5 and G9 spectral type, respectively (Pecaut & Mamajek 2016; Torres et al. 2006), HD 135344 was not included as it is often mistaken for the B component of the binary (Sitko et al. 2012), and DK Cha because it is in the Class I phase (van Kempen et al. 2010; Spezzi et al. 2008). In addition, the data of HD 36982 and HD 50138 do not satisfy the data selection criteria: for a proper comparison with other surveys, only ALMA Band 6 and 7 are used (see §2.3.1 for further details on the selection criteria). While being at the boundary of the definition of Herbig stars, we retained several objects in the interest of obtaining a sample that is as complete as possible: HD 9672, HD 9672, Z CMa, HD 58647, MWC 297, HD 53367, and R CrA. For more details on the individual motivations, see Appendix 2.B. Lastly, this work contains a few disks that would be classified as more evolved debris disks, especially among the group II objects (e.g., HD 9672 and HD 141569). However, all objects in our work do meet the definition of Herbig stars and are therefore kept in the sample.

In summary, of the 42 objects from Vioque et al. (2018) within 450 pc that have ALMA archival data, 36 data sets were used in this research (see the blue distribution in the top panel of Fig. 2.1). This set of 36 Herbig disks is the full sample used in this work. The 25 out of 36 disks that are within 225 pc are referred to as the nearby sample. All 36 objects are listed in Table 2.1. The used data sets and their corresponding properties can be found in Table 2.C.1. Ultimately, the nearby sample (up to 225 pc) covers 64% (25/39 objects) of the total number of Herbig stars present within this distance, and 38% (36/96) of the full sample (up to 450 pc).

The distances of the full sample range from 57 pc to 429 pc with a median of 160 pc. The range in stellar mass is fairly narrow: 1.47 $M_\odot$ to 3.87 $M_\odot$ with MWC 297 being an outlier with 14.5 $M_\odot$. The median stellar mass is 2.0 $M_\odot$. The age is fairly advanced, ranging from 0.04 Myr (MWC 297) to 18.5 Myr (KK Oph) with a median of 5.5 Myr. As HD 53367, R CrA, and V892 Tau belong to the low-quality sample of Vioque et al. (2018), their masses and ages were not determined. Although B stars are over-represented in the overall sample of Vioque et al. (2018), our volume-limited sample is likely complete with respect to these spectral types and contains more A and F stars than B stars (especially early B stars, because none of these bright stars are likely missed at the close distances we are considering). The full sample is divided into 9 B-type, 20 A-type, and 7 F-type spectral type stars (see Table 2.1 for references). As mentioned in §2.1, Herbig Ae stars have horizontal PMS evolutionary tracks. Therefore, it is plausible that the sample used in this work consists of stars with relatively old ages. However, these selection effects are likely to be minimal both because the nearby sample is well covered and F-type stars are included. Lastly, there are 19 group I and 16 group II sources following the Meeus et al. (2001) classification (see Table 2.1 for references). The Meeus group for HD 53367 is undetermined.

2.3 Data and their reduction

2.3.1 Data retrieval

Most of the data were obtained as product data from the ALMA archive[1]. For the retrieval of the data, a few criteria were taken into account. First, the data have to be in Band 6 or Band 7 to both cover a similar wavelength range as previously done for population studies and to be able to compare the dust radii between Herbig disks and T Tauri stars with data taken in different bands (dust radii in Band 6 and 7 are comparable in size Tazzari et al. 2021). In addition, this minimizes the effects of dust evolution (grain growth and radial drift) that impacts different grain sizes differently; by using the same bands, we sample the same grain sizes. Second, the data with the highest resolution were often chosen —except if the largest recoverable scale was too small— to minimize the chance of resolving out large-scale structures. Lastly, if the first two criteria left multiple

---

[1]https://almascience.eso.org/asax/

data sets to choose from, the data set with the highest continuum sensitivity was chosen.

All ALMA product data are imaged and calibrated using the standard ALMA pipeline, ensuring uniform data for all objects and thus well-suited product data for use in this work. However, some of the data were not directly available as a product. We therefore reduced the data of HD 37258, HD 176386, and TY CrA ourselves. The reduction of all three data sets was done in the `Common Astronomy Software Applications` (CASA) application version 5.7.0 (McMullin et al. 2007). To increase the sensitivity of the continuum image and ultimately be able to adequately determine the dust mass of the disk, natural weighting was used for all three data sets. Because of a truncation error when setting the observation coordinates, the coordinates of HD 176386 and TY CrA are shifted resulting in an offset of the sources of up to $15''$ east of the phase centre (Cazzoletti et al. 2019). The phase centre was therefore shifted to the correct source positions. For all three datasets, the signal-to-noise ratio (S/N) was deemed to be too low for self calibration to be applied. For the pipeline products, self calibration would likely have increased the S/N of the images, but would not significantly affect the total flux (which are all well above the S/N limit) and the inferred radii.

Figure 2.2 shows the images of all detected disks. In general, the obtained set of data products consists of a large range of spatial resolutions. All images in which substructure is visible are considered to be resolved; for the remaining disks a Gaussian was fitted using the `CASA imfit` task. For all of these disks, the FWHM major axis found deviated by up to a few percent from the beam major axis and was therefore considered to be unresolved. Consequently, out of the 36 data sets, 17 are resolved. The resolution of the resolved data ranges from $0.02''$ to $1.7''$ with a median of $0.2''$. The resolution of the unresolved data ranges from $0.2''$ to $8''$ with a median of $0.7''$. Three data sets are taken in Band 7 (275–373 GHz), while the other data sets are taken in Band 6 (211–275 GHz). The sensitivity ranges from an rms of 0.02 mJy beam^{-1} to 12.4 mJy beam^{-1} with a median of 0.31 mJy beam^{-1}. See Appendix 2.C for specific information for each data set. Lastly, the data of HD 53367 and HD 176386 are listed as non-detections, because continuum emission was only present at the 2.4σ and 1.6σ level respectively. For R CrA no emission is detected and is listed as an upper limit as well.

2.3.2   Determination of disk flux and size

The flux was measured using the same method as that adopted by Ansdell et al. (2016), who use aperture photometry where the radius of the aperture is determined by a curve-of-growth method. An aperture with a specific position angle and inclination was centered on the disk. For the resolved disks, these were retrieved from other works; see Table 2.1 for the values and references. For the unresolved disks, a circular aperture was used. The radius of this aperture was increased with a minimum step size set by the pixel size until the change in the total disk integrated flux by increasing the radius was smaller than five times the RMS noise. While the noise depends on the weighting scheme used, different robust parameters only minimally influenced the final found radius. This method gives

the maximum disk-integrated flux emitted by the disk and in addition returns the radius of the disk. To facilitate comparison with the results of Ansdell et al. (2016), we report $R_{90\%}$, the radius where 90% of the total flux is reached. We also report $R_{68\%}$, where 68% of the flux is reached, in order to allow comparison with other studies that report this value. Table 2.1 lists the dust masses and the 68% and 90% radii.

For unresolved disks, we use the curve of growth method as well, as opposed to the Gaussian fitting method used by Ansdell et al. (2016), because the difference between the two methods was found to be within 1%. Considering that a standard 10% flux calibration error has to be taken into account as well, these differences are deemed negligible.

2.4   Results

2.4.1   Dust masses

The (sub)millimeter continuum flux can be directly related to the dust mass assuming optically thin emission (Hildebrand 1983) using

$$M_{\mathrm{dust}} = \frac{F_\nu d^2}{\kappa_\nu B_\nu\left(T_{\mathrm{dust}}\right)},\tag{2.1}$$

where F_ν is the continuum (sub)millimeter flux as emitted by the dust in the disk and d the distance to the object. $B_\nu(T_{\mathrm{dust}})$ is the value of the Planck function at a given dust temperature T_{dust}. In many population studies, the dust temperature is taken to be a single constant value across the disk with $T_{\mathrm{dust}} = 20$ K (e.g., Ansdell et al. 2016; Cazzoletti et al. 2019) as found for the mean of the disks in the Taurus region (Andrews & Williams 2005).

Given the high luminosity of the Herbig stars, we explicitly take the higher expected dust temperatures into account. We used the approach by Andrews et al. (2013) to estimate the dust temperatures, where the mean dust temperature of the disk scales with the stellar luminosity as

$$T_{\mathrm{dust}} = 25 \text{ K} \times \left(\frac{L_*}{L_\odot}\right)^{1/4}.\tag{2.2}$$

As shown by Ballering & Eisner (2019), taking $T_{\mathrm{dust}} = 20$ K as well as assuming a luminosity-scaled dust temperature via Eq. (2.2) can lead to underestimation of the dust temperature by ~ 10 K. However, for Herbig disks, Eq. (2.2) leads to a less substantial underestimation of the temperature compared to the assumption of $T_{\mathrm{dust}} = 20$ K.

Following previous studies (e.g., Ansdell et al. 2016; Cazzoletti et al. 2019), the dust opacity at a given frequency κ_ν is given by a power law such that it equals $10 \text{ cm}^2\text{g}^{-1}$ at a frequency of 1000 GHz (Beckwith et al. 1990) which is scaled with an index of $\beta = 1$. While Tychoniec et al. (2020) found from combining VLA and ALMA data that the power-law index β is ~ 0.5, indicating growth of dust
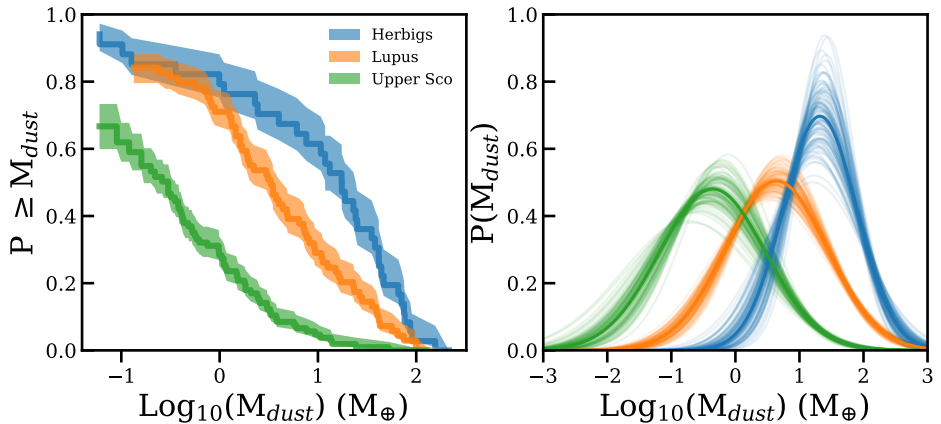
Figure 2.3: Left: Cumulative distribution functions of the dust masses contained inside the disks of our Herbig sample, Upper Sco (Barenfeld et al. 2016) and Lupus (Ansdell et al. 2016). **Right:** log-normal fit through the cumulative distributions. The solid line represents the best-fit distribution, while the light lines show a subsample of distributions from a bootstrapping method, showing the spread in possible fits.

Table 2.2: Log-normal distribution fit results for the dust mass cumulative distributions shown in Fig. 2.3. The M_{dust} parameters are given in $\log_{10}(M/M_{\oplus})$.

	$M_{\star}$ $(M_{\odot})$		M_{dust}	
	μ	σ	μ	σ
Herbigs	2.44	2.24	$1.32^{+0.05}_{-0.05}$	$0.57^{+0.07}_{-0.07}$
Lupus	0.42	0.48	$0.64^{+0.04}_{-0.05}$	$0.79^{+0.05}_{-0.04}$
Upper Sco	0.43	0.37	$-0.36^{+0.11}_{-0.14}$	$0.83^{+0.09}_{-0.07}$

particles (e.g., Natta et al. 2004; Ricci et al. 2010; Testi et al. 2014), for the purpose of comparing with previous population studies, we use $\beta = 1$ in this work.

Lastly, the errors on the dust masses as given in Table 2.1 are calculated by taking two sources of error into account. First, the 10% flux calibration and second, the error on the distance by averaging the upper and lower confidence intervals on the distance as given by Vioque et al. (2018). While previous studies did not take the error on the distance into account because all the stars reside in the same SFR, it is important in this study because the Herbig stars are distributed over a large range of distances.

2.4.2 The dust mass distribution

We derive the dust mass cumulative distribution function (CDF) using the `lifelines` Python package (Davidson-Pilon et al. 2021). `Lifelines` uses survival analysis to construct a cumulative distribution of the dust masses, as shown in the left panel

of Fig. 2.3. The `lifelines` package can take left-censored data into account (i.e., upper limits on the dust mass). The 1σ confidence intervals are shown as the vertical spread in the distribution, reflecting the number of samples in each bin. For a discussion on the completeness of the sample, see Appendix 2.D where three extra Herbig disks are added from JCMT/SCUBA (sub)millimeter observations.

To understand the differences as a function of stellar mass, the dust mass CDF of the Herbig disks is compared in the left panel of Fig. 2.3 with the dust mass CDFs of the young (1–3 Myr) Lupus (Ansdell et al. 2016) as well as with the older (5–11 Myr) Upper Sco (Barenfeld et al. 2016) star-forming regions obtained by assuming a dust temperature of 20 K.

In general, using a luminosity-dependent T_{dust} for the Lupus sample (with luminosities from Alcalá et al. 2014) marginally changes the distribution, with the mean mass increasing by only 4% and the median by 14%. We therefore retain the $T_{\mathrm{dust}} = 20$ K derived masses for consistency. HR 5999 is the only object in Ansdell et al. (2016) for which a temperature of 20 K would not be appropriate. This Herbig disk is also in our sample and we infer a dust disk mass of 4.0 $M_{\oplus}$ instead of 23.3 $M_{\oplus}$ as reported by Ansdell et al. (2016), because our determination uses $T_{\mathrm{dust}} \approx 67$ K which is more appropriate for an object of this luminosity (52 $L_{\odot}$).

The mean dust mass of the Herbig sample is 38 ± 5 $M_{\oplus}$. This is a factor of about three higher than the amount of dust in the disks in the Lupus star-forming region (15 ± 3 $M_{\oplus}$) and a factor of about seven higher than the dust masses in the disks in Upper Sco (5 ± 3 $M_{\oplus}$). We note that while the assumption of optically thin emission may be valid for T Tauri disks, this might not be the case for massive Herbig disks. However, if the Herbig disks are partially optically thick, the inferred mass from Eq. (2.1) would underestimate the true mass; correcting for this would even further increase the differences in dust mass between the Herbig sample and the Lupus and Upper Sco star-forming regions. Our finding that Herbig disks have a higher mass is therefore robust. These higher dust masses are consistent with the well-known stellar mass ($M_{\star}$)–dust mass (M_{dust}) relation (e.g., Andrews et al. 2013; Barenfeld et al. 2016; Ansdell et al. 2016; Pascucci et al. 2016, see §2.5.1 for further discussion on this). Following Williams et al. (2019), the right panel of Fig. 2.3 presents the result of fitting a log-normal distribution through the found cumulative distributions as shown in the left panel of Fig. 2.3 (for the best-fit parameters, see Table 2.2). The resulting distributions provide a more straightforward depiction of the means and standard deviations of the obtained CDFs. To account for the asymmetric errors on the CDFs obtained with the `lifelines` package, a bootstrapping method is used via sampling a split-normal distribution 10^5 times, with the left and right standard deviation of the split-normal distribution given by the upper and lower errors on the CDF. The solid line in the right panel of Fig. 2.3 is the best-fit log-normal distribution, while the fainter lines show the spread in possible fits. From Fig. 2.3 it is clear that the Herbig disks indeed contain more dust mass than both Lupus and Upper Sco. At the same time, the distribution of the older Upper Sco region is lower (more than one standard deviation) than both the Lupus and Herbig disks, which is likely due to its advanced age (approximately one-third of the disks in Upper Sco are more evolved class III objects Michel et al. 2021).
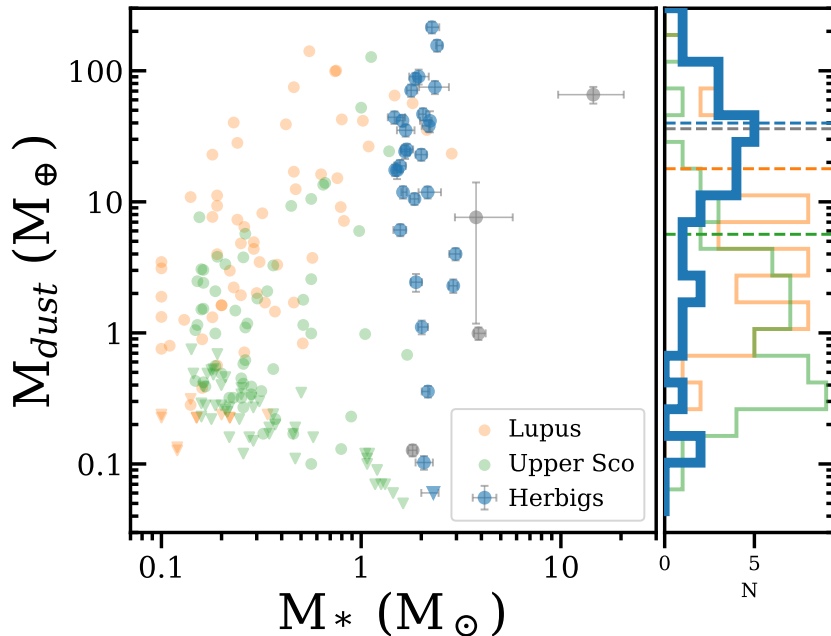
Figure 2.4: Stellar mass vs measured dust mass inside the disk. We show the dust masses of Upper Sco in green (Barenfeld et al. 2016), Lupus in orange (Ansdell et al. 2016), and the ALMA Herbig sample in blue. On the right a histogram is plotted of the distribution of the dust masses. The grey points are four of the six borderline stars (see Sect. 2.2). HD 53367 and R CrA are missing because no stellar mass is available from Vioque et al. (2018) or Wichittanakom et al. (2020).

The now clearly identified relation between stellar mass ($M_\star$) and dust mass ($M_{\rm dust}$) is consistent with this finding. Figure 2.4 plots the stellar mass against the dust mass for the Herbig, Lupus, and Upper Sco samples together with a histogram showing the distribution of the detected dust masses of each sample. While the mean dust mass of the Herbig disks is indeed higher than that of Lupus and Upper Sco, this figure shows that the range in dust mass is relatively similar in the two low-mass star-forming regions. The highest dust masses of Lupus and Upper Sco are 141 ± 21 $M_\oplus$ (Sz 82) and 127 ± 31 $M_\oplus$ (2MASS J16113134–1838259) respectively, while the highest mass in the Herbig sample is 215 ± 22 $M_\oplus$ (HD 142527), which is a factor of 1.5 higher. The biggest difference is in the distribution of the masses. The Herbig sample contains many more massive disks than the low-stellar-mass sources. Of the Herbig sample, $\sim 63\,\%$ of the disks have a mass of more than 10 $M_\oplus$. Compared to only $\sim 26\,\%$ of Lupus and $\sim 6\,\%$ of Upper Sco disks.

Figure 2.5 presents the age of the disks plotted against the dust mass. The ranges in detected dust masses and ages of the Lupus and Upper Sco SFRs are shown as well. The mean dust mass of the Herbig disks, shown by the horizontal
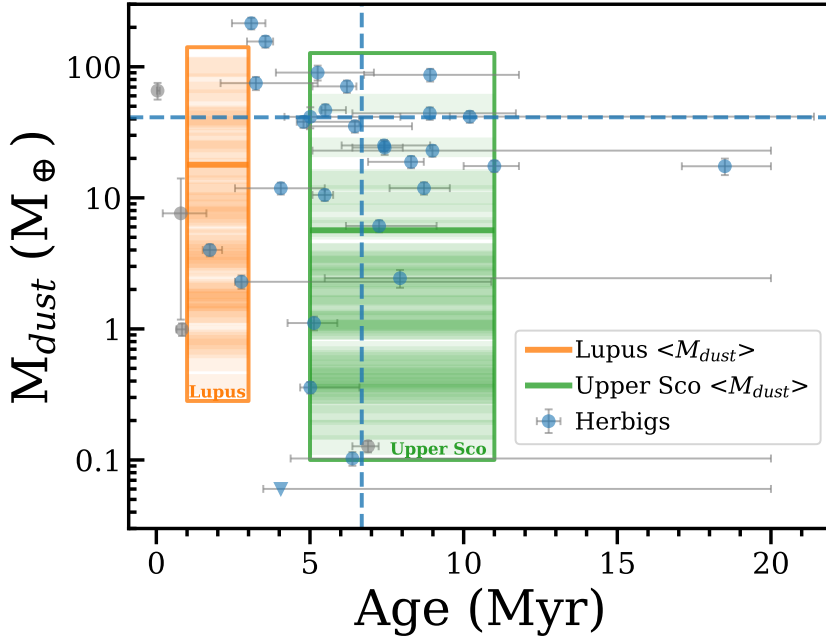
Figure 2.5: Disk dust mass vs the age of the star. The blue points are the ALMA Herbig sample and the grey points are the four out of six borderline stars (see Sect. 2.2). The range in dust mass and age of the Lupus and Upper Sco star-forming regions are shown as colored regions, where the gradient indicates the number of disks of a specific dust mass and the thick solid horizontal colored lines show the mean dust masses. The blue horizontal and vertical dashed lines show the respective mean values of the Herbig sample.

dashed line, is higher than the mean dust masses of both Lupus and Upper-Sco, as shown by the solid horizontal lines. Additionally, this plot shows that the mean age of the Herbig sample mostly overlaps with the Upper Sco region. This suggests that Herbig disks either retain their disk mass for longer, and/or that they are initially formed with higher dust masses following the $M_\star$–M_{dust} relation and thus still have a large disk mass after a few million years. This is discussed further in §2.5.1. Additionally, when removing the six borderline objects from the sample, the distribution as shown in the left panel of Fig. 2.3 does not change significantly. It is therefore unlikely that these targets are much different from the other Herbig disks.

2.4.3   Herbig disk dust radii

We also determined the Herbig disk dust radii at 68% ($R_{68\%}$) and 90% ($R_{90\%}$) of the total flux (see Table 2.1). Based on these measurements, the majority of the Herbig disks seem to be large compared to T Tauri disks. For the resolved disks,
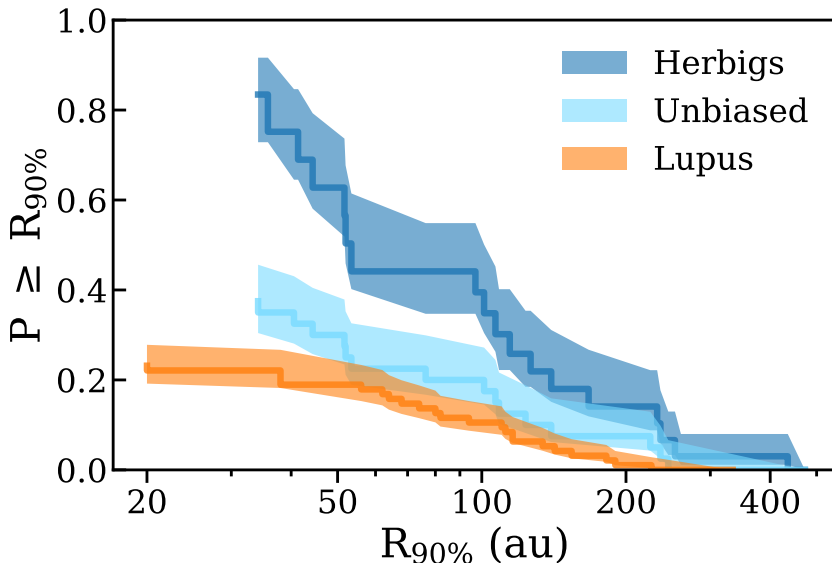
Figure 2.6: Cumulative distribution functions of the 90% dust radii of the Herbig and Lupus samples (Ansdell et al. 2018). The unbiased distribution is made by assuming that all unresolved and unobserved disks are smaller than or equal in size to the smallest disk present in the sample.

$R_{68\%}$ ranges from 35±2 au (HD 100546) to 315±39 au (HD 9672), with a median radius of 71±7 au (HD 169142). The minimum and maximum radius of $R_{90\%}$ is slightly larger at 41±4 au and 473±112 au for the same disks, with a median radius of 109±31 au (HD 135344B). We should stress that this is the *dust* radius and the *gas* radius is most likely a factor of a few larger (e.g., Ansdell et al. 2018; Trapman et al. 2019; Sanchis et al. 2021). Also, it is possible that there is some tenuous dust emission at larger radii, which was for example found for HD 100546 (Walsh et al. 2014; Fedele et al. 2021). But this would not strongly influence $R_{90\%}$.

The larger confidence intervals of $R_{90\%}$ are due to the curve-of-growth levelling off, making the range in which the flux is within its 10% error rather large. The errors on $R_{68\%}$ are on the other hand set by the discrete number of pixels in the image, where the pixel size is dictated by the resolution (synthesized beam). For the unresolved disks, the radius is constrained by the computed upper limits. The $R_{68\%}$ upper limits range from 27 au (TY CrA) up to 328 au (V599 Ori) and have a median of 82 au. The $R_{90\%}$ upper limits range from 34 au (TY CrA) up to 326 au (HD 37258) and have a median of 126 au (HD 245185).

For Lupus, 76% of all detected disks were unresolved (Ansdell et al. 2018). Using half of the FWHM beam size (0.25″/2) and a mean distance of 160 pc (Manara et al. 2018), the upper limit on $R_{90\%}$ for these unresolved disks is <20 au. Consequently, the mean $R_{90\%}$ dust radius is at most 42 au and the median at most 20 au. This is a factor of about three smaller compared to the median radius of the Herbig disks. For Upper Sco, the same is found: Barenfeld et al. (2017) measured

the dust radii of Upper Sco by fitting power-law models to the dust surface density. They do not report $R_{90\%}$ radii, and so we compare their $R_{68\%}$ radii that have a median of 14 au and a range of 5 au to 44 au with our median Herbig $R_{68\%}$ dust radii. The latter are found to be a factor of about five larger.

These low mean dust disk radii do not mean that no large T Tauri disks exist. Some T Tauri dust disks in Lupus do extend out to $R_{90\%} = 334$ au. This is clear in Fig. 2.6, which shows the cumulative distributions of the 90% flux cutoff radii of the Lupus and Herbig populations. For both distributions, the upper limits on the unresolved disks are taken into account. The range in dust radii is similar in both T Tauri (the Lupus sample) and Herbig disks, but the large number of small T Tauri disks skews the distribution to smaller radii compared to the Herbig sample. However, the distribution for the Herbig disks is an optimistic case because the unresolved disks are likely smaller than what is suggested by their upper limits, and therefore the distribution lies higher than it would if all disks were resolved. One can 'unbias' the distribution by assuming all unresolved and unobserved disks to have the same upper limit as the smallest disk. The 225 pc limited sample is used, as this one is the most complete. This unbiased distribution is shown in light blue. Using a two-sample Kolmogorov-Smirnov test from the `Scipy` package (Virtanen et al. 2020), we can reject the null hypothesis of the Lupus and Herbig dust radii to be drawn from the same underlying distribution based on a p-value of 9.5×10^{-5}. The unbiased distribution is found to be similar to the Lupus distribution because the same null hypothesis cannot formally be rejected based on a p-value of 5.6×10^{-2}. Changing to $R_{68\%}$ (with the radii of Lupus from Sanchis et al. 2021), we obtain similar results. Hence, we conclude that the measured Herbig dust radii are significantly larger than those of Lupus. The Herbig disk size distribution only becomes comparable to that in Lupus if all unresolved and all unobserved disks turn out to be as small as (or smaller than) 27 au (although Lupus also has undetected disks, which might be small, which are not taken into account here); in all other cases, Herbig disks are significantly larger than the disks in Lupus.

2.5 Discussion

2.5.1 The $M_\star$–M_{dust} relation

The $M_\star$–M_{dust} relation is one of the important conclusions from population studies in the past decade. By now, this relation is well established across a large variety of star-forming regions mostly containing lower mass stars (e.g., Andrews et al. 2013; Ansdell et al. 2016, 2017; Pascucci et al. 2016; Barenfeld et al. 2016). Our observations are in line with the increase in dust mass for increasing stellar mass. The exact relation does however depend on the considered stellar mass range. For the full sample used in this work, the range in stellar masses is rather narrow: 1.5 $M_\odot$ to 3.9 $M_\odot$, excluding MWC 297 with a mass of 14.5 $M_\odot$. As Fig. 2.4 shows, among this small range of stellar masses, there is a large spread in dust mass. This might be due to the diversity in age and birth environment present in the sample, which changes the amount of dust present in the disk and complicates
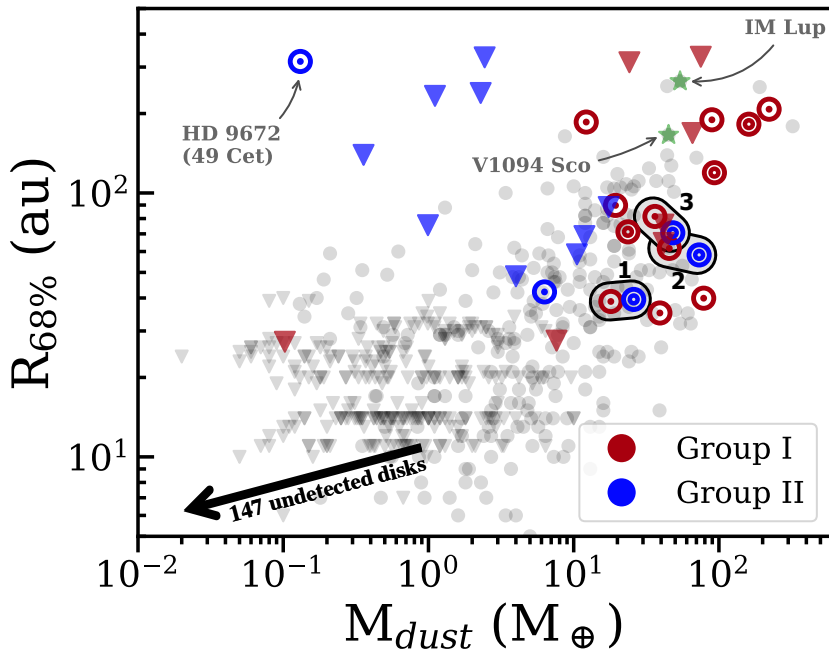
Figure 2.7: $R_{68\%}$ radius plotted against the dust mass for the full sample in this work. Unlike Fig. 2.6, we use $R_{68\%}$ values here for consistency with the work of van der Marel & Mulders (2021). The Herbig disks are divided into the Meeus et al. (2001) group I and II disks. disks with one ($\odot$) and two or more ($\circledcirc$) (visible) rings are indicated as well. The upper limits on the radius are plotted as triangles. The grey scatter points and radius upper limits are the T Tauri disks of van der Marel & Mulders (2021). The large arrow shows the range of upper limits on the undetected disks. Three pairs of Herbig group I and II disks are circled and numbered 1-3; these are further discussed in Sect. 2.5.4 and Fig. 2.10. For extra context, the positions of the large T Tauri disks IM Lup and V1094 Sco are shown as green stars (Ansdell et al. 2016, 2018; van Terwisga et al. 2018; Cleeves et al. 2016).

the comparison in terms of dust mass between the different distributions; this is further addressed in §2.5.2. Both the narrow range in stellar mass and the diversity in age and birth environment hide any trend which could be present within the sample. However, a general trend is visible when considered in a wider stellar mass range (i.e., combined with Lupus and Upper Sco); see the histograms in Fig. 2.4. The Herbig disks are more massive compared to the disks in Lupus and Upper Sco.

The $M_\star$–M_{dust} relation has also been found to steepen over time, mainly based on low-mass stars (e.g., Pascucci et al. 2016; Ansdell et al. 2017). The fact that the more massive disks seem to retain their disk mass for longer has been hypothesized to originate from inner holes and/or structures, which tend to be larger in more massive disks. Guzmán-Díaz et al. (2021) found that $\sim 28\%$ of Herbig Ae/Be disks can be considered to be transitional based on their SED (though uncertain because

it can be affected by for example inclination and extinction; half of transition disks in Lupus show no signature of a cavity in the SED van der Marel et al. 2018), which is more than the fraction of transitional disks in T Tauri stars as imaged with ALMA (van der Marel et al. 2018). Also, $\sim 34\%$ of Herbig Be stars tend to have larger inner disk holes, significantly higher compared to $\sim 15\%$ for Herbig Ae stars (Guzmán-Díaz et al. 2021, who estimated the inner disk hole sizes from the SED, i.e., sizes from 0.1 au out to 10 au, which samples smaller radii than the large cavities with ALMA at tens to hundreds of au). This is in accordance with an observed increase in structure with stellar mass (van der Marel & Mulders 2021). In our work there are two B-type stars with disks that have a dust mass higher than 10 $M_\oplus$. HD 34282 has a visible ring structure present in its disk, while R CrA has been observed with the largest beam size of the data used in this work so that no structures are visible. For the later spectral types, all resolved disks indeed show disk structures.

Figure 2.7 shows the dust masses and dust radii for all detected disks in this work and indicates whether the disk is unresolved or a ring ($\odot$) or multiple rings ($\circledcirc$) are visible. This plot shows that in general, the disks with visible structure are more massive with a mean of 57 ± 9 $M_\oplus$ compared to the unresolved disks with a mean of 19 ± 3 $M_\oplus$, a factor of two lower. The unresolved disks mainly consist of the Herbig disks coming from population studies by for example Cazzoletti et al. (2019). These disks are expected to be the least biased towards large and bright disks. It is therefore not unlikely that the 17 resolved disks ($\sim 47\%$ of the 36 disks) are more massive than the average Herbig disk. Still, the 225 pc limited sample contains 15 of the 17 resolved disks (HD 34282 and HD 290764 are at larger distances), all showing structure. This means that at least $\sim 60\%$ (15/25) of the disks likely contain structure. This is an important result, as van der Marel & Mulders (2021) show that there is a correlation between stellar mass and the presence of structure. These latter authors find that $\sim 63\%$ of disks around stars with masses $> 1.5 M_\odot$ are structured (i.e., transition and ringed disks), which agrees well with our findings. Additionally, the more massive disks (i.e., $\gtrsim 10$ $M_\oplus$) seem to be more extended and show more structure than lower mass disks (van der Marel & Mulders 2021). This also agrees with our findings here (which include a factor of about two more Herbig disks): the number of high-mass disks (64% (23/36) of the disks have $\gtrsim 10$ $M_\oplus$) does fall in line with the number of disks in which we see structure (15/25, $\sim 60\%$).

2.5.2 Scaling dust masses with $M_\star$

How does the Herbig disk mass distribution look if we remove the underlying $M_\star$–M_{dust} dependency calibrated primarily at lower $M_\star$? To obtain an $M_\star$ independent mass estimate, the dust masses are scaled with the $M_\star$–M_{dust} relation to the expected dust masses for a $1 M_\odot$ star using

$$M_{\mathrm{dust,\ scaled}} = \left(\frac{M_\star}{1 M_\odot} \right)^{-\alpha} \times M_{\mathrm{dust}}, \qquad (2.3)$$

where α is the slope of the power-law and $M_\star$ is in solar masses. The resulting
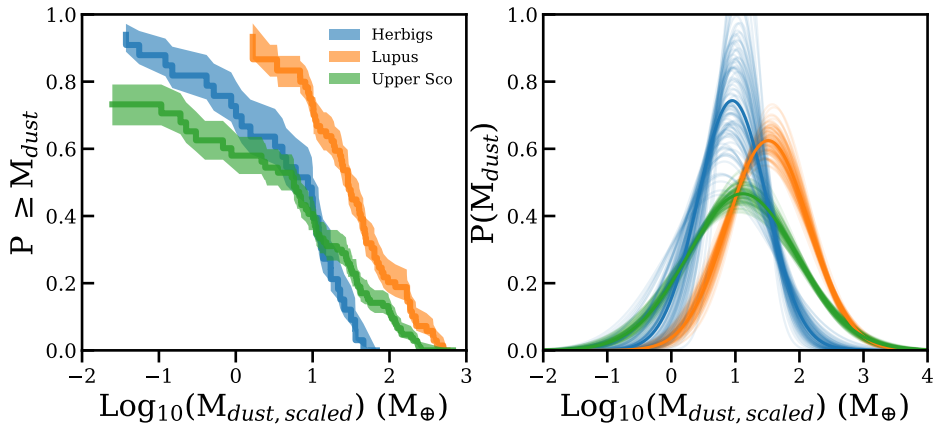
Figure 2.8: Left: Cumulative distributions of the dust masses scaled with the $M_\star$–$M_{\rm dust}$ relation to a $1 M_\odot$ star. **Right:** log-normal fit through the cumulative distributions. The solid line represents the best-fit distribution, while the light lines show a subsample of distributions from a bootstrapping method, showing the spread in possible fits.

CDFs can be found in the left panel of Fig. 2.8. For both Lupus and Upper Sco, the relations found by Ansdell et al. (2017) are used (respectively $\alpha = 1.8$ and $\alpha = 2.4$). For the Herbig sample, the relation found by Andrews et al. (2013) is used ($\alpha = 1.4$) because this study includes more Herbig stars compared to other studies (see Table 2.A.1). Scaling the dust masses removes the effect that the stellar mass has on the dust mass and mostly leaves the effects of age considering that dust temperature was already accounted for with Eq. (2.2) for the Herbig disks and a temperature of 20 K for the low-mass star-forming regions. Again, following the same approach as Williams et al. (2019), a log-normal distribution is fitted through the found CDFs; the fitted parameters are shown in Table 2.3. The best-fit log-normal distribution is shown in the right panel of Fig. 2.8.

For these scaled masses, the cumulative distribution of the Herbig disks moved towards lower dust masses because the stellar mass is above one solar mass. On the contrary, both Upper Sco and Lupus moved towards higher dust masses. The

Table 2.3: Log-normal distribution fit results for the scaled dust mass cumulative distributions shown in Fig. 2.8. The $M_{\rm dust}$ parameters are given in $\log_{10}(M/M_\oplus)$.

	$M_\star$ ($M_\odot$)		$M_{\rm dust,\ scaled}$	
	μ	σ	μ	σ
Herbigs	2.44	2.24	$0.95^{+0.07}_{-0.09}$	$0.54^{+0.12}_{-0.11}$
Lupus	0.42	0.48	$1.51^{+0.04}_{-0.04}$	$0.64^{+0.04}_{-0.04}$
Upper Sco	0.43	0.37	$1.11^{+0.04}_{-0.04}$	$0.86^{+0.05}_{-0.05}$

width of both the Upper Sco and Herbig disk distributions stayed similar (though the width of the Herbig disk distribution is not well constrained) because of the relatively narrow stellar mass distributions. Lupus has in contrast a broader stellar mass distribution, resulting in a narrower distribution after scaling the dust masses (see Table 2.2).

Applying the $M_\star$–$M_{\rm dust}$ relation unsurprisingly moves the mass distribution of the Herbig disks to the same values as found in Upper Sco and only slightly below the distribution found in Lupus. This scaling shows that the mass difference between the Herbig disks and the T Tauri disks can indeed be tied to a difference in stellar mass. Also, the larger disk sizes we find for the Herbig disks may hold further clues as to why this relation exists.

2.5.3   The $R_{\rm dust}$–$M_{\rm dust}$ relation

Following van der Marel & Mulders (2021), we speculate that the larger disk masses and sizes found for Herbig disks as compared to their T Tauri counterparts reflect the combined effect of inheritance and evolution. Our ansatz is that these findings originate from an initial disk mass that increases with stellar mass, and that subsequent disk evolution enlarges the differences as explained below, especially as these are obtained via (sub)millimeter continuum flux observations. It is a reasonable assumption that more massive cloud cores form more massive stars that are surrounded by more massive disks, if a constant fraction of the accreting material ends up in the disk. Although object-to-object variations will undoubtedly introduce a scatter around this relation, an overall scaling between the mass of the cloud core, the final mass of the star, and the mass of the disk is plausible.

A higher mass disk contains more material available for planet formation, and such planets can grow out to larger masses (e.g., Mordasini et al. 2012). This matches the observed trend that higher mass stars (1 $M_\odot$ and higher) are more often found to host planets more massive than 100 $M_\oplus$ compared to stars with lower stellar masses (e.g., Johnson et al. 2007, 2010; Wittenmyer et al. 2020; Fulton et al. 2021). Such planets can also be formed on larger orbits, because the required surface density is present at larger radii in a higher mass disk. This matches the presence of wide-orbit gas-giants around stars like HR 8799 (Marois et al. 2008, 2010) and β Pictoris (Lagrange et al. 2010), and (proto)planets in the disks like the ones around HD 100546 (Quanz et al. 2013, 2015) or HD 163296 (Isella et al. 2016; Zhang et al. 2018; Liu et al. 2018; Teague et al. 2018; Pinte et al. 2018b). Once planets are formed of sufficient mass, gaps can open up, as is commonly observed in many disks, and inward transport of material, especially dust, is halted (e.g., Zhu et al. 2012). This has two observable effects. First, it traps a detectable mass reservoir outside the gaps that leads to larger dust continuum disk sizes. Second, by preventing the dust from flowing inward, a larger fraction of the dust remains in outer disk regions, thus allowing a larger continuum flux (because the more spread out material remains optically thin, and so all dust mass contributes, or because optically thick material subtends a larger region on the sky) and larger inferred disk dust mass (Ballering & Eisner 2019). A relation has indeed been found between the continuum size and the luminosity in disks (Tripathi et al.

2017) and more recently, van der Marel & Mulders (2021) found a general increase in dust mass with dust extent. Figure 2.7 presents the $R_{68\%}$ and M_{dust} of the full sample of our work together with the 700 disks analyzed in van der Marel & Mulders (2021). The sample of van der Marel & Mulders (2021) mainly contains T Tauri disks, but does have $\sim 50\%$ of the Herbig disks which are in our work. Figure 2.7 clearly shows that in general the dust disk size and mass of Herbig disks are larger than those of the typical T Tauri disk, especially because $\sim 21\%$ of the T Tauri disks are not detected.

However, this does not mean that T Tauri stars cannot have disks that are large and massive: there are T Tauri disks that are as large and massive as a Herbig disk, but they make up a much smaller fraction of the total population. Figure 2.7 also shows the two largest disks in Lupus (V1094 Sco, K6-type, van Terwisga et al. 2018; IM Lup, M0-type, Cleeves et al. 2016), which are of similar size, but have a six times lower mass than the Herbig disks and are only 2% of the Lupus population. The mass difference may simply reflect the dust mass distribution of Herbig disks peaking at masses a factor of about 6 higher than the dust mass distribution for T Tauri stars.

HD 9672 (49 Ceti) is unusually large for its mass and a clear outlier in Fig. 2.7. Its close distance (57 pc) has helped in detecting this low-mass source and identifying it as an outlier. This raises the question of whether other undetected objects may be harboring extended, low-surface-brightness disks.

In contrast, if most or all of the dust has migrated radially inward to spatially unresolved disk regions, smaller disk sizes are inferred and, because inner disk regions will more easily become optically thick at (sub)millimeter wavelengths (for the same mass), lower continuum fluxes lead to lower inferred disk dust masses following Eq. (2.1). This is in line with the findings of Ballering & Eisner (2019), who show that the inferred disk mass from Eq. (2.1) of T Tauri disks in Taurus could underestimate the mass by a median factor of about two. Neglecting dust scattering on the other hand may lead to overestimation of the mass Zhu et al. 2019. Some of the Herbig disks in this sample might not have formed a gas giant planet at large separations, which would explain the lower dust masses of some of the disks. This illustrates that if higher mass stars are formed with on average higher mass disks, the change in observable consequences (i.e., continuum flux and therefore inferred mass) during the evolution of the disk is likely to amplify the original trend.

2.5.4   Group I and Group II

How do the dust mass and size correspond to other disk properties of our Herbig sample? One such property is the Meeus groups: group I and group II (Meeus et al. 2001). Different explanations for the origin of the two groups exist. Evolutionary arguments have been put forward, for example grain growth and/or settling causing group I to evolve into group II (Dullemond & Dominik 2004a,b, 2005). However, the finding that many group I sources have disks with gaps (e.g., Honda et al. 2012) caused Maaskant et al. (2013) to propose an evolutionary scenario where both groups are preceded by a primordial flaring disk. Nonetheless, Menu

et al. (2015) pointed out that there were group II sources with gaps as well (based on VLTI observations, referring to gaps on au scales, as opposed to tens of au for ALMA), giving rise to the idea that group I has an influx of evolving group II gapped disks.

Table 2.1 contains the groups in which each Herbig disk falls following the classification of Meeus et al. (2001). Figure 2.7 combines the dust mass and radius with the Herbig group classification and information on the structures visible in the disk. From this figure, it is apparent that the mean dust mass of the group I disks is larger than that of the group II disks. Using the same approach as before, the cumulative and fitted log-normal distributions of the group I and group II sources are shown in Fig. 2.9. The fitting results are listed in Table 2.4. While the number of disks for each distribution is small, this analysis clearly shows a higher mean dust mass for the group I objects compared to the group II objects. Moreover, the distribution of the group II objects is similar to the distribution of the disks in Lupus (see Fig. 2.9).

Table 2.4: Log-normal distribution fit results for the group I and group II dust mass cumulative distributions shown in Fig. 2.9. The M_{dust} parameters are given in $\log_{10}(M/M_{\oplus})$.

	$M_{\star}$ $(M_{\odot})$		M_{dust}	
	μ	σ	μ	σ
Group I	2.73	2.99	$1.57^{+0.06}_{-0.07}$	$0.34^{+0.08}_{-0.07}$
Group II	2.13	0.65	$0.61^{+0.15}_{-0.19}$	$0.68^{+0.18}_{-0.15}$
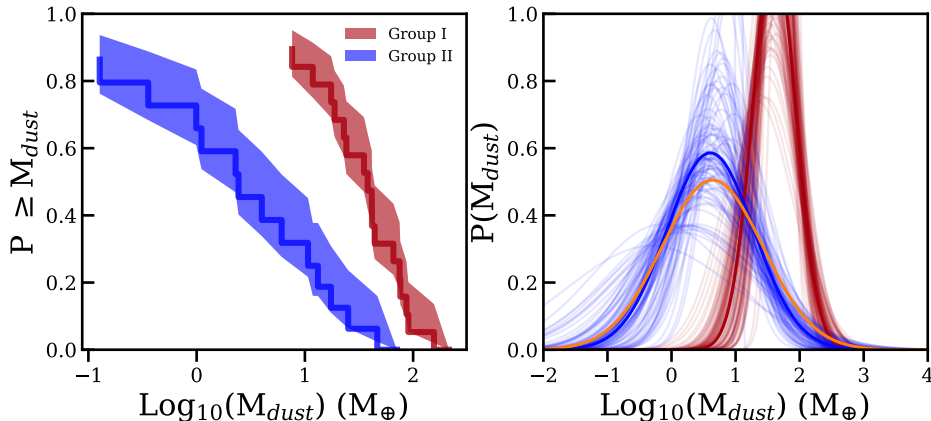
Figure 2.9: Left: Cumulative distributions of the dust masses of the group I and group II sources. **Right:** log-normal fit through the cumulative distributions. The solid line represents the best-fit distribution, while the light lines show a subsample of distributions from a bootstrapping method, showing the spread in possible fits. The orange log-normal distribution shows the best-fit distribution of Lupus shown in Fig. 2.3.
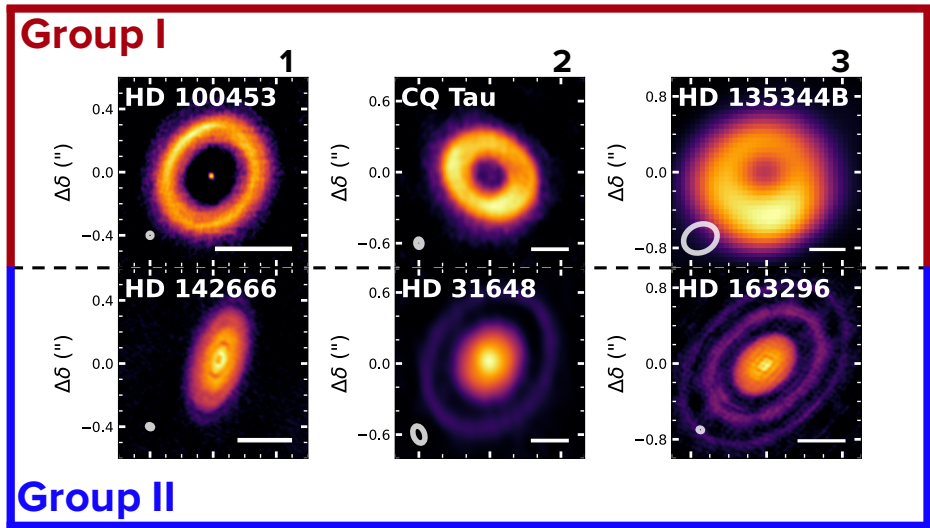
Figure 2.10: Three resolved disks for both group I and group II with similar extent and mass for each pair of disks. Each image is normalized with an asinh stretch to increase the visibility of the fainter details of the disk. A 50 au scale bar is shown to the bottom right of each image.

As many as 13 out of 19 group I disks are resolved, and they all show structure. The resolved group II disks are smaller than the group I disks, but there are group I disks with sizes very similar to several group II disks, and in these cases both the group I and II disks show structure (for a comparison see Fig. 2.10). While there are large upper limits for both group I and group II disks, there are a few much smaller and thus more stringent dust radius upper limits for both groups, showing that there are a few much smaller disks in either group. Based on the grey region showing where most of the disks lie (as studied by van der Marel & Mulders 2021) we predict that the five unresolved group II disks at $\sim 1\ \mathrm{M_\oplus}$ (BF Ori, HD 37258, HD 58647, HD 141569 and VV Ser) are going to be 10–30 au in size when resolved. While for four of these disks the size is unknown, from visibility modeling HD 141569 is thought to have an outer disk component out to 300 au, though it is much fainter than an inner disk component with a radius of 45 au (White & Boley 2018). If these disks are indeed ~ 10 au in size, a resolution of at least $0.02''$ is needed to resolve all five disks. This resolution is achievable with ALMA in the most extended array in Band 7.

In general, one ring is visible for most of the group I disks (9/12), while multiple rings are visible for most group II disks (3/5). Three of these resolved group II disks can be paired with group I disks of very similar size and mass (indicated by the numbered pairs 1-3 in Fig. 2.7). Figure 2.10 shows these six disks, three for each group, with similar sizes and masses for each pair. When putting these disks side-by-side, an intriguing trend appears. The group II disks are more compact,

and the bulk of their mass is close to the star. This is in contrast to the group I
disks, where mostly large rings are visible, with little mass close to the star. The
same is found in scattered light images (Garufi et al. 2017).

As we hypothesized in §2.5.3, the larger disks could be connected to the forma-
tion of gas-giant planets at large separations, which can open up gaps and inward
transport of material is halted. The difference between group I and group II disks
could be caused by this as well: group I disks were able to form gas giants at large
distances, while group II disks were not, only halting the radial drift at closer-in
distances. The group I disks keep much of the dust mass at larger radii, while
the inner part of the disk accretes onto the star, leaving a single large ring. This
agrees well with the evolutionary scenario posed by Menu et al. (2015) and Garufi
et al. (2017), who suggested that group II disks may evolve into group I disks. The
group II disks might form (giant) planets closer-in or later on, eventually creating
a gap and moving towards group I. This would also explain the two other resolved
group II disks not yet mentioned: AK Sco and HD 9672, both of which show one
ring and are rather old. Furthermore, Cieza et al. (2021) propose a similar evolu-
tionary scenario based on the brightest disks from the DSHARP (Andrews et al.
2018a) and ODISEA programs. Cieza et al. (2021) propose that disks first form
with shallow gaps, which become more pronounced once planets start to grow; the
dust is trapped at the inner edges of the rings while the inner dust disk dissipates,
creating a single-ringed disk. This matches well with what we see here.

Another possibility which should be mentioned is that close (sub)stellar binary
companions would have a similar effect on the disk by creating an inner hole (van
der Marel & Mulders 2021). All three group I sources shown in Fig. 2.10 are
known to be wide binaries (HD 100453 Chen et al. 2006; CQ Tau Thomas et al.
2007; HD 135344B Coulson & Walther 1995). While wide separation binaries are
unlikely to affect disk structure (Harris et al. 2012, but see Rosotti et al. (2020)
who suggest that the spirals in HD 100453 are caused by the companion), for
HD 135344B and CQ Tau there is indirect evidence from spirals that there could
be a massive companion carving the inner gap (van der Marel et al. 2016; Wölfer
et al. 2021). A similar scenario has also been suggested for AB Aur (Poblete et al.
2020) . In HD 142527, an M-dwarf has been found to reside in the disk (e.g.,
Lacour et al. 2016; Claudi et al. 2019), giving rise to asymmetric structures in the
disk (Garg et al. 2021). Hence, binarity at relatively close separations could also
possibly explain the differences between the group I and group II sources.

The fact that we detect more massive group I disks compared to group II could
then be a consequence of the spatial distribution of the dust in the disk. As Fig.
2.11 shows, the distribution of stellar masses is the same in group I and group II
objects and therefore, following the $M_\star$–M_{dust} relation, they should have a similar
range in dust masses. Nevertheless, the group II disks are smaller and are therefore
prone to being optically thick due to most mass being in the inner regions of the
disk (which is indeed what Fig. 2.10 shows), reducing the inferred dust mass in
the disk. Consequently, in disks without gaps, the stellar radiation is potentially
'trapped' close to the star because much more dust is present in these close-in
regions, leaving most of the disk colder and flatter, resulting in a group II-type
SED. As Fig. 2.9 shows, the distribution of the disks in Lupus overlaps well with
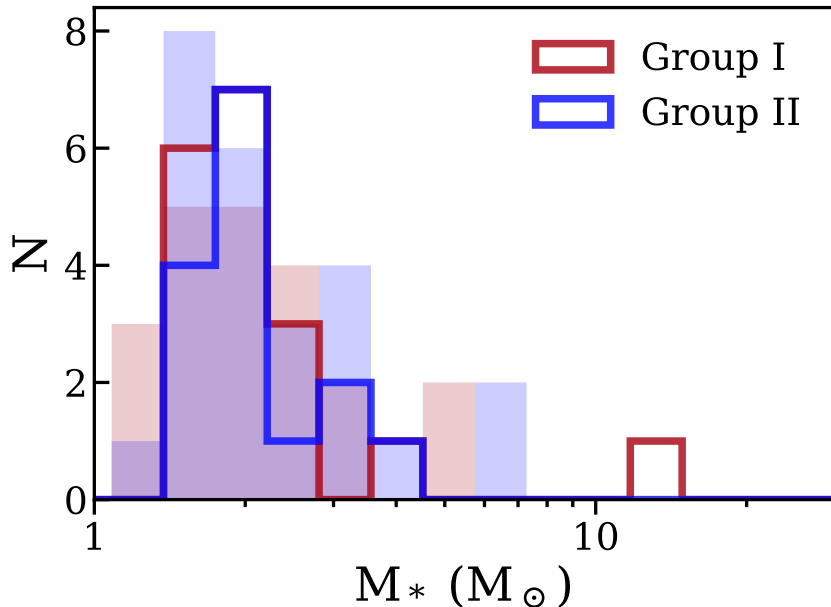
Figure 2.11: Stellar mass distribution of the group I and II objects used in this work. The shaded histogram shows the distribution of stellar masses for both the group I and group II objects not observed with ALMA within 450 pc.

the group II objects. This overlap could originate from group II Herbig disks being unable to form massive exoplanets at large distances, like T Tauri stars, reducing the inferred disk mass.

Lastly, in addition to the stellar masses being evenly distributed between the group I and II objects for both the observed and unobserved disks within 450 pc (see Fig. 2.11), $\sim 50\%$ of all Herbig disks within 450 pc belong to group I (Vioque et al. 2018) which is comparable to the 53% of the Herbig disks in our work. We therefore do not expect a change in the distributions presented in Fig. 2.9 if all disks are included in the distribution.

2.6 Conclusion

We present a first look at the distribution of dust mass and the extent of disks around Herbig stars by collecting ALMA archival data for 36 Herbig disks within 450 pc. Of these, 17 disks are resolved. Two Herbig disks are undetected. Excluding the Orion star-forming region, the completeness rate is 64%. We compare the results to previous population studies of Lupus (Ansdell et al. 2016, 2018) and Upper Sco (Barenfeld et al. 2016, 2017). Our results can be summarized as follows:

1. The mean dust mass of the Herbig sample is a factor of about three higher than the dust masses in Lupus and a factor of about seven higher than the

dust masses in Upper Sco. The Herbig disk masses are distributed over the same range as T Tauri disks, but are skewed towards higher masses.

2. Herbig disks are generally larger than T Tauri disks, although the largest Herbig disks are of similar size to the largest T Tauri disks.

3. The masses of the Herbig disks are as expected based on the $M_\star$–M_{dust} relation. After scaling the dust masses following this relation to a star of $1M_\odot$, the mean dust mass overlaps with the Upper Sco SFR, which has a similar age to the Herbig star sample used in this work.

4. Based on both larger and more massive disks, we speculate that these massive and large disks find their origin in an initial disk mass that increases with stellar mass, and that subsequent disk evolution enlarges the (observable) differences with disks around lower mass stars.

5. Group I objects are found to be both more massive and larger than group II objects. Additionally, the dust mass distribution of the group II disks is similar to that of the Lupus T Tauri disks. We argue that group II disks were unable to form massive companions or planets at (very) large radii and consequently much more dust is present at close-in regions compared to group I sources; this causes them to have masses and sizes similar to those of T Tauri disks, and they may trap stellar radiation at small radii, leaving most of the disk cold and flat, resulting in a group II-type SED.

This work shows that the evolution of Herbig disks may hold important clues about the formation of gas-giant planets. A complete ALMA study of a homogeneous sample of Herbig disks at similar resolutions and sensitivities is much needed in order to further investigate their formation.

Appendix

2.A   Previous disk population studies done with ALMA

Table 2.A.1 lists previous population studies done with ALMA and the number of Herbig stars (as listed in Vioque et al. 2018) present in each work.

Table 2.A.1: Some of the disk population studies done with ALMA. The approximate ages and mean distances are shown together with the total number of targets and the number of these targets that are Herbigs in each survey.

Region	Age (Myr)	Distance (pc)	N	Herbigs	Ref.
Taurus	2	140	210	3	1
Lupus	1–3	150	93	1	2
σ Orionis	3–5	385	92	0	3
λ Orionis	5	400	44	1	4
Upper Scorpius	5–11	145	106	0	5
Corona Australis	1–3	154	41	2	6
Ophiuchus	1	140	147	0	7, 8
OMC1	1	400	49	0	9
ONC	1	400	104	0	10
Lynds 1641	1.5	428	101	0	11
Chamaeleon I	2	160	93	0	12
IC 348	2–3	310	136	0	13
OMC 2	1	414	132	0	14
NGC 2024	0.5	414	179	0	15
This work	6.2±3.5	201±111	36	36	

Notes: An object is counted as an Herbig star if listed by Vioque et al. (2018). The given age and distance for this work are the mean ± standard deviation of the values given by Vioque et al. (2018). *References:* (1) Andrews et al. (2013), (2) Ansdell et al. (2016), (3) Ansdell et al. (2017), (4) Ansdell et al. (2020), (5) Barenfeld et al. (2016), (6) Cazzoletti et al. (2019), (7) Cieza et al. (2019), (8) Williams et al. (2019), (9) Eisner et al. (2016), (10) Eisner et al. (2018), (11) Grant et al. (2021), (12) Pascucci et al. (2016), (13) Ruíz-Rodríguez et al. (2018), (14) van Terwisga et al. (2019), (15) van Terwisga et al. (2020).

2.B   Details on individual boundary objects

2.B.1   HD 9672

HD 9672 (or better known as 49 Cet) has been classified both as an old debris disk and a Herbig star. Zuckerman & Song (2012) classified HD 9672 as a debris disk belonging to the 40 Myr old Argus association. However, the disk surrounding HD 9672 has been found to be relatively gas rich compared to other debris disks (Zuckerman et al. 1995; Moór et al. 2019). Moreover, the origin of both the dust and the gas is still unknown. It could be second-generation dust and gas generated by collisions between planetesimals, or inherited from the original cloud (Hughes et al. 2017). Because of this uncertainty, we decided to leave it in the sample.

2.B.2 Z CMa, HD 58647, MWC 297, and HD 53367

These four objects are quite massive, all belonging to the B spectral type which may be young massive objects instead of Herbig stars. Z CMa is a binary (Koresko et al. 1991) where the primary is a Herbig Be star (Whitney et al. 1993; van den Ancker et al. 2004) and the secondary is a FU Orionis variable (Hartmann et al. 1989). An asymmetric outflow is found in this system (Garcia et al. 1999; Baines et al. 2006). In HD 58647 outflows have been found as well (Kurosawa et al. 2016). MWC 297 has a large mass of ~ 14.5 M$_\odot$ (Vioque et al. 2018). While Vioque et al. (2018) estimate its age to be 0.04 Myr, MWC 297 has been characterized as being a main sequence star (Drew et al. 1997) surrounded by an evolved disk (Manoj et al. 2007). Lastly, HD 53367 is a binary star consisting of a massive (~ 20M$_\odot$) main sequence B0e star and a PMS secondary (~ 4M$_\odot$) (Pogodin et al. 2006). While classified as a Herbig star, even one of the original classified by Herbig (1960), it could also instead be a classical Be star (Pogodin et al. 2006).

2.B.2   R CrA

R CrA is still embedded in a dust envelope (Kraus et al. 2009) and is likely in an early evolution phase (Malfait et al. 1998). It also has outflows and jets (Rigliaco et al. 2019). This case is on the boundary of being a Herbig star, because it may be in an earlier stage than Herbig stars, and therefore we keep it in the sample.

2.C ALMA archival data

In this work, a total of 36 ALMA archival datasets have been used. Their continuum observing frequencies and corresponding Project IDs can be found in Table 2.C.1.

Table 2.C.1: The Project IDs of the data used in this work with the corresponding observation frequency of the continuum data.

Name	ν (GHz)	Beam ($''$)	RMS (mJy beam^{-1})	Project ID
AB Aur	343.51	0.32 × 0.20	0.40	2015.1.00889.S
AK Sco	233.00	0.09 × 0.06	0.17	2016.1.00204.S
BF Ori	233.01	1.49 × 1.03	0.34	2019.1.01813.S
CQ Tau	232.37	0.07 × 0.05	0.05	2017.1.01404.S
HD 100453	234.19	0.03 × 0.02	0.02	2017.1.01678.S
HD 100546	233.00	0.02 × 0.02	0.02	2018.1.01309.S
HD 104237	219.56	1.31 × 0.76	2.20	2015.1.01600.S
HD 135344B	340.98	0.37 × 0.29	2.09	2012.1.00870.S
HD 139614	232.01	0.68 × 0.48	3.55	2015.1.01600.S
HD 141569	229.00	1.39 × 1.05	0.08	2017.1.01545.S
HD 142527	231.90	0.27 × 0.24	1.55	2015.1.01353.S
HD 142666	232.60	0.03 × 0.02	0.03	2016.1.00484.L
HD 163296	232.60	0.05 × 0.03	0.06	2016.1.00484.L
HD 169142	232.50	0.22 × 0.15	0.27	2015.1.01301.S
HD 176386	224.14	0.43 × 0.32	0.20	2015.1.01058.S
HD 245185	248.00	0.31 × 0.30	0.24	2017.1.00466.S
HD 290764	344.30	0.07 × 0.05	0.15	2017.1.01607.S
HD 31648	218.00	0.15 × 0.09	0.33	2016.1.01164.S
HD 34282	234.19	0.25 × 0.22	0.29	2015.1.00192.S
HD 36112	232.01	0.47 × 0.33	0.55	2015.1.01600.S
HD 37258	233.01	1.84 × 1.24	0.27	2019.1.01813.S
HD 53367	225.51	0.48 × 0.39	0.14	2018.1.00814.S
HD 58647	225.51	0.47 × 0.39	0.14	2018.1.00814.S
HD 9672	232.50	1.69 × 1.16	0.09	2018.1.01222.S
HD 97048	233.70	0.38 × 0.18	0.91	2015.1.00192.S
HR 5999	232.01	0.53 × 0.51	0.67	2015.1.01600.S
KK Oph	232.01	0.58 × 0.51	0.66	2015.1.01600.S
MWC 297	217.51	0.42 × 0.31	3.81	2018.1.00814.S
R CrA	231.32	7.48 × 4.68	11.3	2018.A.00056.S
TY CrA	224.14	0.43 × 0.32	0.20	2015.1.01058.S
V1787 Ori	233.02	1.48 × 0.99	0.53	2019.1.01813.S
V599 Ori	233.02	1.42 × 1.00	1.54	2019.1.01813.S
V718 Sco	232.01	0.87 × 0.72	0.92	2015.1.01600.S
V892 Tau	242.68	0.23 × 0.16	1.28	2013.1.00498.S
VV Ser	239.35	1.43 × 0.97	1.03	2019.1.00218.S
Z CMa	224.26	0.20 × 0.17	0.22	2016.1.00110.S

2.D   Are there selection effects in our sample?

Section 2.4 found that Herbigs observed with ALMA are both larger and more massive than samples of disks in Lupus and Upper Sco. Are these Herbig disks in general indeed larger and more massive, or does the sample of Herbig disks observed with ALMA (i.e., the sample used in this work) mainly consist of more massive and larger disks?

Observations of individual objects in our sample were likely spurred by their
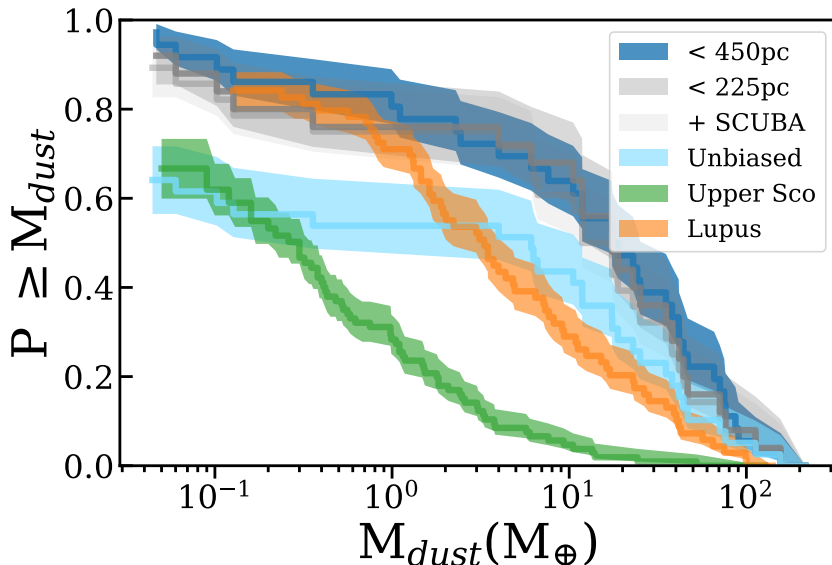
Figure 2.D.1: Cumulative distributions of the full Herbig sample (< 450 pc), the sample within 225 pc, the sample with the additional 3 JCMT/SCUBA data within 225 pc and the unbiased version of this distribution.

Table 2.D.1: Coordinates and spectral types of the Herbig stars used in this work observed with JCMT/SCUBA and the calculated flux densities and dust masses of each Herbig disk.

Name	R.A.$_{\text{J2000}}$ (h:m:s)	Decl.$_{\text{J2000}}$ (deg:m:s)	Sp.Tp.	Ref.	$F_{\text{cont.}}$ (mJy)	M_{dust} ($M_{\oplus}$)
HD 35187$^{\alpha}$	05:24:01.2	+24:57:37	A2	1	100.2	6.63 ± 0.75
HD 41511$^{\alpha}$	06:04:59.1	-16:29:04	A3	2	<0.91	<0.044
HD 150193	16:40:17.9	-23:53:45	B9.5	3	104.9	6.28 ± 0.66

Notes. All distances are obtained from Vioque et al. (2018). The luminosities, stellar masses, and ages were obtained from Wichittanakom et al. (2020) except the objects marked with an α of which these parameters were obtained from Vioque et al. (2018). *Spectral type references:* (1) Manoj et al. (2006), (2) Jaschek et al. (1991), (3) Levenhagen & Leister (2006).
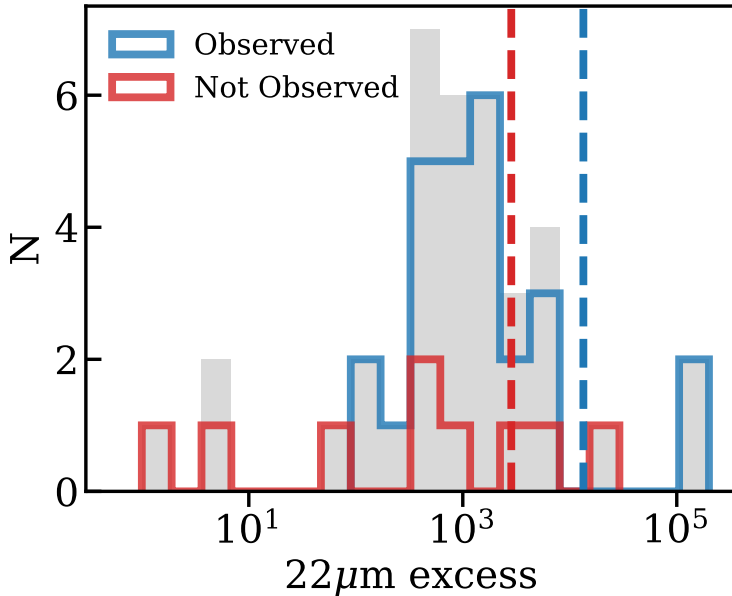
Figure 2.D.2: Distribution of WISE 22μm-excess for the Herbig disks at a distance < 225 pc. The mean 22μm-excess is shown with the dashed lines.

Table 2.D.2: Proposal IDs of the SCUBA data used in this work with the corresponding observation frequency of the continuum data.

Name	ν (GHz)	Instrument	RMS (mJy beam^{-1})	Proposal ID
HD 35187	347.79	SCUBA	17.37	m97bc36
HD 41511	352.71	SCUBA-2	0.36	M17BL002
HD 150193	347.38	SCUBA	16.23	m01bi09

brightness or the presence of structure in the disk either seen in scattered light or (sub)millimeter observations (e.g., Fukagawa et al. 2004, 2006; Doering et al. 2007; Tang et al. 2012; Quanz et al. 2013). While this may have biased our ALMA sample, a sufficiently large fraction of all Herbig disks (at least out to 225 pc) have ALMA archival data, even if we consider the unobserved disks to be small and too low in mass (which future ALMA observations may determine). The sample up to 225 pc, which excludes Orion, is 64% covered with ALMA (25/39 objects) compared to 38% (36/96) for the 450 pc distance sample. Figure 2.D.1 shows that the cumulative distribution does not significantly change when only using the more complete nearby sample (i.e., all Herbig disks observed with ALMA within 225 pc) compared to the full sample (i.e., all Herbig disks observed with ALMA within 450 pc). Both the most and least massive disks are within 225 pc and hence the overall cumulative distribution does not change significantly. Therefore, the general trend that the dust masses are larger compared to those of T Tauri

stars still holds. Of the 14 objects within 225 pc that have not been observed with ALMA, 3 have been observed with JCMT/SCUBA. For these three objects, SCUBA and SCUBA-2 data products[2] were used to determine the dust masses; see Table 2.D.1. Their continuum observing frequencies and corresponding Project IDs can be found in Table 2.D.2. These three datasets increase the percentage of observed disks to $\sim 72\%$ within 225 pc. Because of the large beam of JCMT/SCUBA ($\sim 14''$), the dust radii were not determined. HD 41511 is observed with SCUBA-2 and is not detected, so only an upper limit is given. The found dust masses are low: HD 35187, HD 41511, and HD 150193 are 6.63 ± 0.75 M$_\oplus$, < 0.044 M$_\oplus$, and 6.28 ± 0.66 M$_\oplus$ respectively. These three extra masses do not change the overall distribution much, although they provide anecdotal evidence that unobserved disks may indeed be smaller and less massive, see Fig. 2.D.1.

Assuming that all unobserved disks (so the left over 29%) have an upper limit on the detected mass as low as the lowest upper limit in the sample, we can see what the least favorable distribution would be if the unobserved disks turned out to have low masses. This 'unbiased' distribution is shown in Fig. 2.D.1 in light blue. It shows that the tail end of the cumulative dust mass distribution would still lie above the Lupus distribution and far above the Upper Sco distribution which has a similar age to the Herbig disks. However, this is most likely a worst-case scenario, because in terms of 22 μm emission tracing the warm inner disk, these objects do not stand out with respect to the detected sources. The 22μm excess of the disks within 225 pc with and without ALMA data are shown in Fig. 2.D.2. These IR excesses were obtained by Vioque et al. (2018) from the Wide-field Infrared Survey Explorer (WISE) which is an infrared all-sky survey and therefore contains observations of most of the Herbig disks that were not observed with ALMA. A two-sided t-test using the *SciPy* package (Virtanen et al. 2020) shows that the null hypothesis of both distributions being the same cannot be rejected (p-value=0.425). While the 22μm excess originates from inner parts of the disk, and no clear connection is present between this excess and the amount of dust, it does indicate that a disk is present around the star. We therefore do not expect the distribution to change significantly when including all Herbig disks within 450 pc as listed by Vioque et al. (2018). We therefore conclude that the derived mass distribution of Herbig disks is unlikely to deviate significantly from the real one, and that the thus-far unobserved targets are likely to retain at least some disk material. Future observations will need to establish this firmly.

---

[2]http://www.cadc-ccda.hia-iha.nrc-cnrc.gc.ca/en/jcmt/

Chapter 3

Constraining the gas mass of Herbig disks using CO isotopologues

L. M. Stapper, M. R. Hogerheijde, E. F. van Dishoeck, L. Lin, A. Ahmadi, A. S. Booth, S. L. Grant, K. Immer, M. Leemker, A. F. Pérez-Sánchez

Abstract

Context: The total disk mass sets the formation potential for exoplanets. Obtaining the disk mass is however not an easy feat, as one needs to consider the optical thickness, temperature, photodissociation, and freeze-out of potential mass tracers. Carbon-monoxide (CO) has been used as a gas mass tracer in T Tauri disks, but was found to be less abundant than expected due to the freeze-out and chemical conversion of CO on the surfaces of cold dust grains. The disks around more massive intermediate mass pre-main sequence stars called Herbig disks are likely to be warmer, allowing for the possibility of using CO as a more effective total gas mass tracer.

Aims: This work aims to obtain the gas mass and size of Herbig disks observed with ALMA and compare these to previous works on T Tauri disks and debris disks.

Methods: Using ALMA archival data and new NOEMA data of ^{12}CO, ^{13}CO, and $C^{18}O$ transitions of 35 Herbig disks within 450 pc, the masses were determined using the thermo-chemical code Dust And LInes (DALI). A grid of models was run spanning five orders of magnitude in disk mass, for which the model CO line luminosities could be linked to the observed luminosities. Survival analysis was used to obtain cumulative distributions of the resulting disk masses. These were compared with dust masses from previous work to obtain gas-to-dust ratios for each disk. In addition, radii for all three isotopologues were obtained.

Results: The majority of Herbig disks for which ^{13}CO and $C^{18}O$ were detected are optically thick in both. For these disks, the line flux essentially only traces the disk size and only lower limits to the mass can be obtained. Computing the gas mass using a simple optically thin relation between line flux and column density results in an underestimate of the gas mass of at least an order of magnitude compared to the masses obtained with DALI. The inferred gas masses with DALI are consistent with a gas-to-dust ratio of at least 100. These gas-to-dust ratios are two orders of magnitude higher compared to those found for T Tauri disks using similar techniques, even over multiple orders of magnitude in dust mass, illustrating the importance of the chemical conversion of CO in colder T Tauri disks. Similar high gas-to-dust ratios are found for Herbig group I and II disks. Since group II disks have dust masses comparable to T Tauri disks, their higher CO gas masses illustrate the determining role of temperature. Compared to debris disks, Herbig disks have gas masses higher by four orders of magnitude. At least one Herbig disk, HD 163296, has a detected molecular disk wind, but our investigation has not turned up other detections of the CO disk wind in spite of similar sensitivities.

Conclusions: Herbig disks are consistent with a gas-to-dust ratio of at least 100 over multiple orders of magnitude in dust mass. This indicates a fundamental difference between CO emission from Herbig disks and T Tauri disks, which is likely linked to the warmer temperature of the Herbig disks.

3.1   Introduction

The formation of exoplanets heavily depends on the amount of material present in a planet-forming disk. Hence, efforts have been made to determine the total disk mass and link this to planet formation occurring inside them. The most common disk mass tracer used is the millimeter dust continuum of the disk. Assuming the canonical gas-to-dust mass ratio of 100 (Bohlin et al. 1978), the total disk mass can be determined after making a few assumptions on the grain properties, most notably the grain emissivity (Beckwith et al. 1990). Many population studies on dust masses have been done with the Atacama Large Millimeter/submillimeter Array (ALMA) (see, e.g., Ansdell et al. 2016; Barenfeld et al. 2016; Pascucci et al. 2016; Eisner et al. 2018; Cazzoletti et al. 2019; Anderson et al. 2022; van Terwisga et al. 2022). These studies have shown clear trends regarding the disk mass with stellar mass (Ansdell et al. 2017; Manara et al. 2022), disk radius (Hendler et al. 2020), and stellar accretion rate (Testi et al. 2022). However, it is still unknown if the dust continuum does indeed trace the total disk mass, that is, gas and dust, directly. Recent works have shown that the dust can be optically thick, underestimating the total disk mass by an order of magnitude for the most massive disks (e.g., Liu et al. 2022; Kaeufer et al. 2023), and may even be optically thick at 3 mm (Xin et al. 2023).

An understanding of the total (gas) mass of the disk is therefore much needed (see Miotello et al. 2023 for a recent overview). The most abundant molecule in a planet-forming disk is H_2. However, its faint emission at the typically low temperatures (~ 20 K) present in a planet-forming disk do not make it a viable disk mass tracer. Hence, other more indirect tracers are necessary. One promising tracer is the H_2 isotopologue hydrogen deuteride (HD). Using thermo-chemical models, the HD emission can be used to determine the bulk mass of a disk (see e.g., Bergin et al. 2013; Schwarz et al. 2016; Trapman et al. 2017; Sturm et al. 2023). HD $J = 1 - 0$ observed with the *Herschel* Space Observatory has been detected in three disks resulting in gas mass measurements (Bergin et al. 2013; McClure et al. 2016), and a dozen non-detections in Herbig disks resulting in gas mass upper limits (Kama et al. 2016, 2020). However, after the end of the Herschel mission, there are no current facilities to observe the HD $J = 1 - 0$ line, so a different tracer is needed.

Carbon monoxide (CO) has been used extensively as a tracer of both the total gas mass and size of planet-forming disks. Especially its less common isotopologues ^{13}CO and $C^{18}O$ (e.g., Miotello et al. 2017; Long et al. 2017; Loomis et al. 2018), or even the rarer $C^{17}O$, $^{13}C^{17}O$ and $^{13}C^{18}O$ isotopologues (Booth et al. 2019; Booth & Ilee 2020; Loomis et al. 2020; Zhang et al. 2020b, 2021; Temmink et al. 2023), have been used as tracers of the bulk mass. Generally, two main methods are used to determine the gas mass from CO: simple scaling relations assuming an excitation temperature and optically thin emission (e.g., Loomis et al. 2018), and using thermo-chemical models (e.g., Miotello et al. 2014, 2016). It has been shown that in T Tauri disks the CO emission is much weaker than expected, which could be due to carbon- and oxygen-rich volatiles being locked up as ice resulting in chemical conversion into more complex ices (Bosman et al. 2018; Agúndez et al.

2018) and radial transport (Krijt et al. 2018), both of which lead to low CO fluxes and making CO less ideal to trace the bulk mass (see e.g., Ansdell et al. 2016, 2017; Pascucci et al. 2016; Miotello et al. 2017). Moreover, if CO is not abundant enough, it cannot self-shield, resulting in a drop in CO abundance due to UV photons dissociating the molecule (Visser et al. 2009). Alternatively, Miotello et al. (2021) show that the lack of CO emission can also be explained by compact gas disks for those disks that remain unresolved in ALMA observations. Because of the more luminous star, Herbig disks are expected to be warmer and thus less CO conversion should occur (Bosman et al. 2018). HD upper limits combined with dust based masses from Kama et al. (2020) do indeed imply that this is likely the case. Moreover, using literature values of gas-to-dust ratios Miotello et al. (2023) found that the CO depletion in Herbig disks is lower than for T Tauri disks. However, a general survey of Herbig gas masses is still lacking.

In addition to the gas mass, CO has also been used to trace the radius of the disk (Ansdell et al. 2017; Trapman et al. 2019). The outer disk radius can be used to distinguish between the two main evolutionary scenarios proposed for disks: viscous evolution and wind driven evolution (see for a recent overview Manara et al. 2022). The former results in an increasing outer radius with evolution, while the latter decreases the outer radius of the disk. Modeling has shown that this is also visible in CO emission (Trapman et al. 2022). In the Herbig disk HD 163296, a disk wind has been detected in ^{12}CO and ^{13}CO (Klaassen et al. 2013; Booth et al. 2021), suggesting a possible wind driven scenario operating in that Herbig disk. However, clear conclusions on which of the two scenarios is the main driver of evolution in disks is still missing. A survey is lacking here as well.

This work builds upon the previous work by Stapper et al. (2022) who obtained the dust masses of a comprehensive survey of Herbig disks observed with ALMA. We use their sample in addition to five observations done with the Northern Extended Millimeter Array (NOEMA) to obtain information on all Herbig disks with millimeter CO isotopologue observations. These CO observations are used to determine the gas masses in the same manner as Miotello et al. (2016), as well as gas disk radii. The obtained masses and radii are used to answer important questions in the field. The gas masses give us insights on whether there is less CO conversion in Herbig disks compared to T Tauri disks, and if CO can be used as an effective gas mass tracer in Herbig disks. The gas and dust radii can be used to investigate the efficiency of radial drift in Herbig disks, and the CO observations can be used to determine if there are any more wind signatures present in the available Herbig disk ALMA data. Also, comparisons to T Tauri and debris disks can be made.

This work is structured as follows. Section 3.2 details the selection of the sample and accompanying data reduction. Section 3.3 describes the DALI model grid parameters. The results are presented in Section 3.4, where the integrated-intensity maps of ^{12}CO, ^{13}CO and C^{18}O are presented in §3.4.1, the ^{12}CO radii are compared to the dust radii in §3.4.2, the luminosities of the observations and models are compared in §3.4.3 and the resulting gas mass estimates are shown in §3.4.4. We discuss these results in Section 3.5, where in §3.5.1.1 we investigate how to unravel the different masses of the disks using rare isotopologues, and introduce a new technique to compute the full mass of a disk using CO isotopologues in

§3.5.1.2. In §3.5.2 we compare the obtained masses to those of T Tauri disks in §3.5.2.1, between the group I and group II Herbig disks in §3.5.2.2, and to those of debris disks in §3.5.2.3. Lastly, in §3.5.3 we present results into finding disk winds in the data, and discuss the wind driven versus viscously driven evolution of Herbig disks using the obtained disk radii. Section 3.6 summarizes our conclusions.

3.2   Sample and data reduction

The sample used in this work is compiled by Stapper et al. (2022), who selected all Herbig disks from Vioque et al. (2018) with ALMA data within 450 pc. In this work, we update this sample by using the GAIA DR3 updated stellar parameters and distances from Guzmán-Díaz et al. (2021). We include HD 34282, KK Oph, V892 Tau and Z CMa from Vioque et al. (2018) as well, which are not included in Guzmán-Díaz et al. (2021).

A selection of the available data on the ALMA archive[1] was made which cover the ^{12}CO, ^{13}CO, and/or C^{18}O lines. In general, the $J = 2-1$ transition was chosen, except in cases where only the $J = 3-2$ transition was available. The data were chosen such that the largest angular scale is at least as large as the continuum disk size, as to not filter out larger scales. In cases where high resolution data were used (either due to a better sensitivity or no low resolution data were available), a uv-taper was applied, to taper the resolution to $\sim 0.1''$ to easier be able to determine the radius and integrated flux.

These selection criteria resulted in 30 disks for which at least one ^{12}CO, ^{13}CO or C^{18}O transition is available. R CrA is not included because it only has ACA (Atacama Compact Array) data available, which is prone to having contamination from nearby sources due to the much lower spatial resolution. Out of the 30 datasets, two (VV Ser and HD 245185) only have ^{12}CO observations available.

In addition to the ALMA archival data, we present observations made with the Northern Extended Millimeter Array (NOEMA) toward five Herbig disks which lie too far north for ALMA. These disks (BH Cep, BO Cep, HD 200775, SV Cep and XY Per) all lie at distances similar to Orion, ranging from 324 pc to 419 pc (Guzmán-Díaz et al. 2021). These data were calibrated using the IRAM facilities. Details on both the NOEMA and ALMA data and their project codes can be found in Table 3.A.1.

The data were imaged using the `Common Astronomy Software Applications` (CASA) version 5.8.0 (McMullin et al. 2007). The data were first self-calibrated using the continuum, which was made by combining all spectral windows and flagging the channels containing line emission. For the ALMA data, up to six rounds of phase-only self-calibration were computed, starting with a solution interval equal to the duration of a single scan. The solution intervals were shortened by a factor of two each round. For the NOEMA data, only one phase calibration round was used. After phase-only self-calibration, a single round of amplitude self-calibration was performed. Both the phase and amplitude calibrations were only applied if an increase of more than 2% in peak signal-to-noise ratio (S/N) was found, for

---

[1] https://almascience.eso.org/aq/

Table 3.1: Source parameters used for Keplerian masking and computing the gas radii.

Name	Distance (pc)	$M_\star$ ($M_\odot$)	$Log_{10}(L_\star)$ ($L_\odot$)	V_{sys} (km s^{-1})	V_{int} (km s^{-1})	PA (°)	Inc. (°)	Ref.
AB Aur	155.0	2.4	1.7	5.8	1.5	-36	23	Tang et al. (2017)
AK Sco	139.2	1.7	0.8	5.4	2.5	128	109	Czekala et al. (2015)
BH Cep	323.9	1.5	0.8	–	–	–	–	This work.
BO Cep	367.9	1.4	0.6	-11.6	2.0	-60	30	This work.
CQ Tau	148.6	1.5	0.8	6.2	1.5	-50	35	Wölfer et al. (2021)
HD 9672	57.1	1.9	1.2	2.8	2.5	73	81	Hughes et al. (2017)
HD 31648	155.2	1.9	1.2	5.1	1.5	148	37	Liu et al. (2019)
HD 34282	311.5	1.5	1.0	-2.4	1.0	65	60	van der Plas et al. (2017a)
HD 36112	155.0	1.6	0.9	6.0	1.5	-60	21	Isella et al. (2010)
HD 58647	302.2	4.1	2.5	–	–	–	–	
HD 97048	184.1	2.8	1.8	4.6	1.5	-176	41	Walsh et al. (2016)
HD 100453	103.6	1.6	0.8	5.2	1.5	-145	35	Rosotti et al. (2020)
HD 100546	108.0	2.1	1.3	5.6	1.5	-140	42	Pineda et al. (2019)
HD 104237	106.5	1.9	1.3	4.8	2.0	110	20	This work.
HD 135344B	134.4	1.5	0.7	7.1	1.5	-62	10	Cazzoletti et al. (2018)
HD 139614	133.1	1.6	0.8	6.8	1.5	-100	18	Muro-Arena et al. (2020)
HD 141569	111.1	2.1	1.4	6.4	2.0	-175	53	White et al. (2016)
HD 142527	158.5	2.2	1.4	3.6	1.5	26	27	Kataoka et al. (2016)
HD 142666	145.5	1.8	1.1	4.1	1.5	18	62	Huang et al. (2018)
HD 163296	100.6	1.9	1.2	5.9	2.0	-137	47	Huang et al. (2018)
HD 169142	114.4	1.6	0.8	6.9	0.8	-175	13	Fedele et al. (2017)

Table 3.1: Continued.

Name	Distance (pc)	$M_\star$ ($M_\odot$)	$\mathrm{Log_{10}}(L_\star)$ ($L_\odot$)	V_sys (km s^{-1})	V_int (km s^{-1})	PA (°)	Inc. (°)	Ref.
HD 176386	154.3	2.6	1.6	–	–	–	–	
HD 200775	352.4	7.0	3.4	–	–	–	–	
HD 245185	410.4	2.2	1.5	13.1	2.0	100	30	This work.
HD 290764	397.1	2.0	1.3	9.5	2.0	70	30	Kraus et al. (2017)
HR 5999	157.8	3.2	2.0	–	–	–	–	
KK Oph	221.1	1.5	0.7	–	–	–	–	
MWC 297	407.8	20.0	4.8	–	–	–	–	
SV Cep	340.3	2.0	1.3	–	–	–	–	
TY CrA	158.3	2.6	1.6	–	–	–	–	
V718 Sco	153.9	1.7	1.1	8.4	1.5	–	–	
V892 Tau	152.5	6.0	0.1	8.4	4.0	-60	55	Long et al. (2021)
VV Ser	403.4	3.6	2.3	–	–	–	–	
XY Per	419.2	3.7	2.3	–	–	–	–	
Z CMa	229.7	3.8	2.3	–	–	–	–	

Notes. The distances, masses and luminosities are from Guzmán-Díaz et al. (2021), except for KK Oph, V892 Tau and Z CMa which are from Vioque et al. (2018). The distance and luminosity of V892 Tau are also taken from Vioque et al. (2018), but the stellar mass is from Long et al. (2021). The PA and inclination references are given in the last column. The PA is defined as the angle in the clockwise direction between north and the blueshifted side of the disk. For three disks the position angle and inclination were determined by eye based on the ^{12}CO Keplerian mask. V_{sys} and V_{int} are respectively the system velocity of the disk and the internal velocity which is the range in velocities due to emission from different layers in the disk, as determined by the data.

Table 3.2: Integrated fluxes in Jy km s^{-1} and radii in au of ^{12}CO, ^{13}CO, and C^{18}O.

Name	^{12}CO			^{13}CO			C^{18}O		
	Flux (Jy km s^{-1})	$R_{\mathrm{gas,\,68\%}}$ (au)	$R_{\mathrm{gas,\,90\%}}$ (au)	Flux (Jy km s^{-1})	$R_{\mathrm{gas,\,68\%}}$ (au)	$R_{\mathrm{gas,\,90\%}}$ (au)	Flux (Jy km s^{-1})	$R_{\mathrm{gas,\,68\%}}$ (au)	$R_{\mathrm{gas,\,90\%}}$ (au)
AB Aur	52.35±0.30*	232±12	358±12	37.01±0.18	690±35	1118±35	7.50±0.11	370±35	678±40
AK Sco	2.18±0.05	78±4	114±5	0.68±0.04	66±6	97±18	0.27±0.02	52±5	69±11
BH Cep	–	–	–	<0.07	–	–	<0.07	–	–
BO Cep	–	–	–	1.22±0.08	<387	<525	0.35±0.07	<371	<529
CQ Tau	3.44±0.04	103±3	146±3	1.12±0.04	84±5	113±6	0.60±0.02	65±4	99±7
HD 9672	3.61±0.08	<285	<460	1.37±0.08	<285	<439	0.12±0.04	<231	<347
HD 31648	19.97±0.08	389±36	597±36	7.03±0.08	313±38	467±38	2.16±0.05	237±38	363±38
HD 34282	9.47±0.09	468±17	673±17	3.46±0.05	340±18	483±18	1.89±0.04	324±18	568±40
HD 36112	7.98±0.14	211±6	305±12	1.87±0.07	121±9	192±18	0.78±0.04	103±6	141±15
HD 58647	<0.03	–	–	<0.02	–	–	<0.02	–	–
HD 97048	27.40±0.14	389±45	596±45	15.93±0.11	433±48	615±48	8.41±0.08	366±48	512±48
HD 100453	2.40±0.03	51±5	78±5	0.91±0.02	38±5	56±5	0.37±0.01	39±5	59±10
HD 100546	63.56±0.12	230±6	322±6	13.13±0.08	187±6	256±6	3.35±0.06	127±9	236±16
HD 104237	2.43±0.06	<43	<64	0.64±0.03	<39	<59	0.37±0.03	<46	<69
HD 135344B	20.07±0.18*	158±10	219±10	8.86±0.08*	119±9	171±9	3.55±0.08*	86±9	125±9
HD 139614	–	–	–	2.82±0.05	<130	<179	1.12±0.04	<108	<151
HD 141569	18.43±0.12*	162±9	220±9	1.27±0.13	150±17	193±54	<0.07	–	–
HD 142527	27.14±0.10	542±30	793±30	11.88±0.07	334±31	491±31	3.91±0.04	271±31	368±31
HD 142666	4.05±0.03	136±6	186±6	1.51±0.06	<182	<260	0.64±0.04	<164	<236
HD 163296	51.99±0.09	348±13	496±13	16.98±0.07	287±14	400±14	5.96±0.04	228±14	324±14
HD 169142	18.93±0.05	232±8	347±8	6.37±0.04	156±9	230±9	2.93±0.02	129±9	169±9
HD 176386	<0.11	–	–	<0.10	–	–	<0.07	–	–
HD 200775	–	–	–	<0.09	–	–	<0.08	–	–
HD 245185	2.37±0.10	<221	<396	–	–	–	–	–	–
HD 290764	6.55±0.13*	271±11	386±14	2.95±0.05*	218±17	328±17	1.51±0.05*	188±18	277±23
HR 5999	<0.08	–	–	<0.08	–	–	<0.06	–	–

Table 3.2: Continued.

Name	^{12}CO			^{13}CO			C^{18}O		
	Flux (Jy km s^{-1})	$R_{\text{gas, 68\%}}$ (au)	$R_{\text{gas, 90\%}}$ (au)	Flux (Jy km s^{-1})	$R_{\text{gas, 68\%}}$ (au)	$R_{\text{gas, 90\%}}$ (au)	Flux (Jy km s^{-1})	$R_{\text{gas, 68\%}}$ (au)	$R_{\text{gas, 90\%}}$ (au)
KK Oph	–	–	–	<0.18	–	–	<0.07	–	–
MWC 297	<0.03	–	–	<0.05	–	–	<0.02	–	–
SV Cep	–	–	–	<0.08	–	–	<0.08	–	–
TY CrA	<0.10	–	–	<0.10	–	–	<0.07	–	–
V718 Sco	–	–	–	1.63±0.09	<106	<151	0.86±0.07	<113	<170
V892 Tau	16.18±1.87	171±30	242±126	3.92±0.20	128±9	191±18	0.86±0.10	90±15	123±43
VV Ser	<0.24	–	–	–	–	–	–	–	–
XY Per	–	–	–	<0.08	–	–	<0.08	–	–
Z CMa	<0.11	–	–	<0.06	–	–	<0.03	–	–

Notes. The fluxes with an asterisk are for the $J = 3 - 2$ transition, all others are for the $J = 2 - 1$ transition. The upper limits are estimated by using three times the noise in a single channel and multiplying this by the width of the channel and the square root of the number of independent measurements, assuming that the emission is coming from a range of 10 km s^{-1} in velocity and within a single beam. The error on the flux is estimated by multiplying the noise in an empty channel by the width of the channel and the square root of the number of independent measurements in the Keplerian mask and the area over which the integrated fluxes were computed. All integrated fluxes have an additional 10% calibration error.

which the rms was determined by excluding the disk emission and using the full field-of-view of the observation. Typically a factor of 1.8 was gained in peak S/N. Afterwards, the resulting calibration table was applied to the line spectral windows by using the `applycal` task in CASA. See Richards et al. (2022) for more information on self-calibration. After self-calibration each dataset was continuum subtracted using the `uvcontsub` task in CASA using a linear fit. For masking during the CLEAN process, hand-drawn masks were aided by the `auto-multithres`[2] option in `tclean` to automatically generate masks. For the resolved data, the data were cleaned using the `multiscale` algorithm in `tclean`. The used scales were 0 (point source), 1, 2, 5, 10 and 15 times the size of the beam in pixels ($\sim$5 pixels). The last three scales were only used if the disk morphology allowed for it. All unresolved data (which is, in addition to the NOEMA data, some of the ALMA data as well) were cleaned using the `hogbom` algorithm. For the ALMA data, every dataset was imaged using a Briggs robust weighting of 2.0, optimizing the S/N of the resulting image. For the NOEMA data, a Briggs robust weighting of 0.5 was used, due to its lower spatial resolution, without impacting the S/N. Finally, the resulting image cubes were primary beam corrected. All resulting image parameters can be found in Appendix 3.A in Table 3.A.1 which also lists the root-mean-square noise of the data. Additionally, the NOEMA continuum data are presented in Appendix 3.B.

The velocity integrated (moment 0) maps of the image cubes were obtained by using a Keplerian mask. We use the same implementation as Trapman et al. (2020) (also see Salinas et al. 2017; Ansdell et al. 2018). The used inclinations, position angles, system velocities and internal velocities (i.e., a range in velocity to take into account that emission is not geometrically thin and comes from different layers in the disk, extending the velocity range over which the mask is generated, see Appendix A in Trapman et al. 2020) can be found in Table 3.1. The internal velocity is for the majority of the disks set at 1.5 km s^{-1}, and generally provides an extra factor to improve the coverage of all emission by the Keplerian mask. The distances and stellar masses are taken from Guzmán-Díaz et al. (2021) or Vioque et al. (2018), obtained via evolutionary tracks on the HR-diagram, except for V892 Tau, for which we use the mass estimate from Long et al. (2021), because both Guzmán-Díaz et al. (2021) and Vioque et al. (2018) do not include a mass estimate. We note that other stars have dynamically estimates of their mass as well (e.g., AK Sco, Czekala et al. 2015; HD 169142, Yu et al. 2021; HD 163296, Teague et al. 2021; HD 34282 Law et al. 2023), but we do not include these to keep the stellar masses homogeneously derived for the complete sample. As all emission is included in the Keplerian masking, the stellar masses are not expected to impact our results. The references for the inclinations and position angles as obtained from continuum observations are given in Table 3.1. The position angles have been altered by hand by small amounts such that the Keplerian masks fit the channel maps well. By applying the Keplerian mask the moment 0 maps are made, see Figure 3.1. The integrated fluxes were determined using a curve-of-growth method, see Stapper et al. (2022) for more details. The final luminosity of

---

[2]The standard values given on `https://casaguides.nrao.edu/index.php/Automasking_Guide` were used.
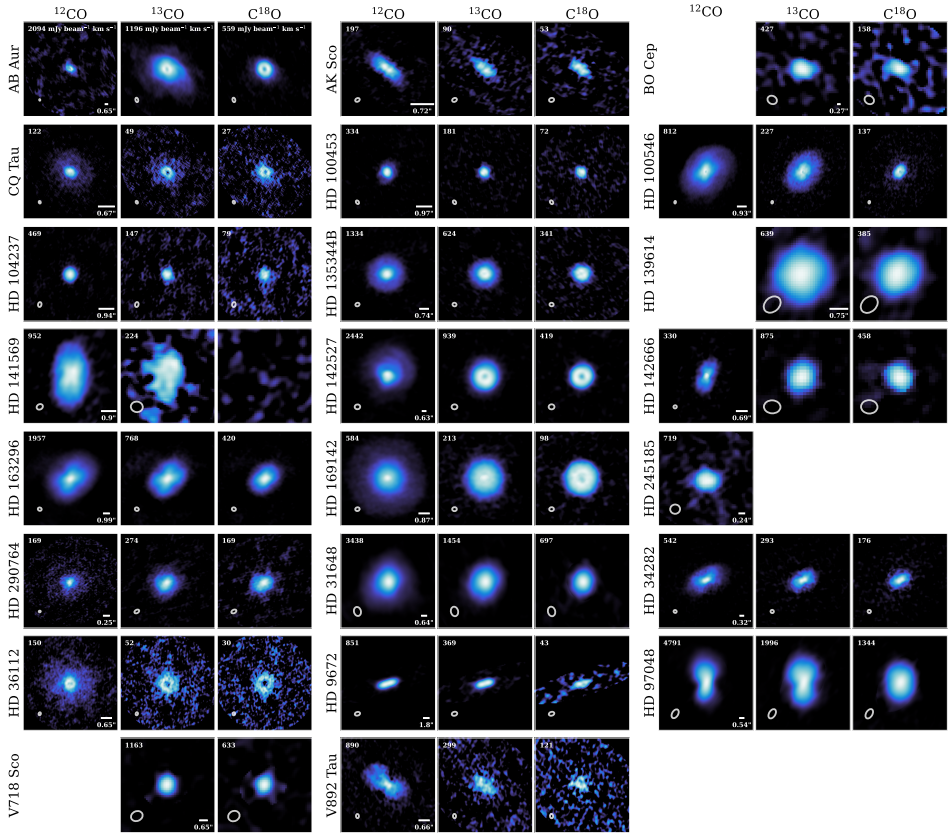
Figure 3.1: Keplerian masked velocity integrated-intensity maps of the 23 Herbig disks with at least one detection of ^{12}CO, ^{13}CO, or $C^{18}O$. For each disk, ^{12}CO, ^{13}CO, and $C^{18}O$ are given in the first, second, and third panel from left to right. If nothing is shown, the molecule is not covered. The bar in every first panel from the left indicates a size of 100 au with the corresponding angular size below. The size of the beam is indicated in the bottom left of each panel. A *sinh* stretch is used to make the fainter parts of the maps better visible. The minimum value is set to zero, and the maximum value in mJy beam^{-1} km s^{-1} is indicted on each panel in the top left corner. The disks with no detections in all three isotopologues are not shown here.

each line was computed by multiplying the integrated flux by a factor $4\pi d^2$ where d is the distance to the source in parsecs.

For the non-detections, the upper limits are estimated by using three times the noise in a single channel and multiplying this by the width of the channel and the square root of the number of independent measurements, assuming that the emission is coming from a range of 10 km s^{-1} in velocity and within a single beam. We note that this was also done for the binary XY Per (see Appendix 3.B). Similarly, the error on the integrated fluxes was estimated by multiplying the noise in an empty channel by the width of the channel and the square root of the number

of independent measurements in the Keplerian mask and the area over which the integrated fluxes were computed.

In addition to the integrated flux, the curve-of-growth method also gives the size of the disk. We compute the radii encircling 68% and 90% of the flux. We use a minimum error on the radius of 1/5 the size of the beam (i.e., the pixel size). Similarly, the errors on the dust radius from Stapper et al. (2022) are taken as 1/5 the size of the beam. Upper limits on the size of the disk are given if, after fitting a Gaussian to it with the CASA task `imfit`, the major or minor axes of the Gaussian are smaller than two times the beam. We note that for BO Cep, HD 104237 and HD 245185, while marginally resolved with only two beams along the minor axis, we estimate an inclination and position angle to cover all emission with the Keplerian mask. See the resulting values in Table 3.1. For the other unresolved disks, we either use the inclination and position angle of previous works (HD 9672, HD 142666, HD 139614) for the Keplerian mask or we use no Keplerian mask (V718 Sco). We include the inferred radii for these seven
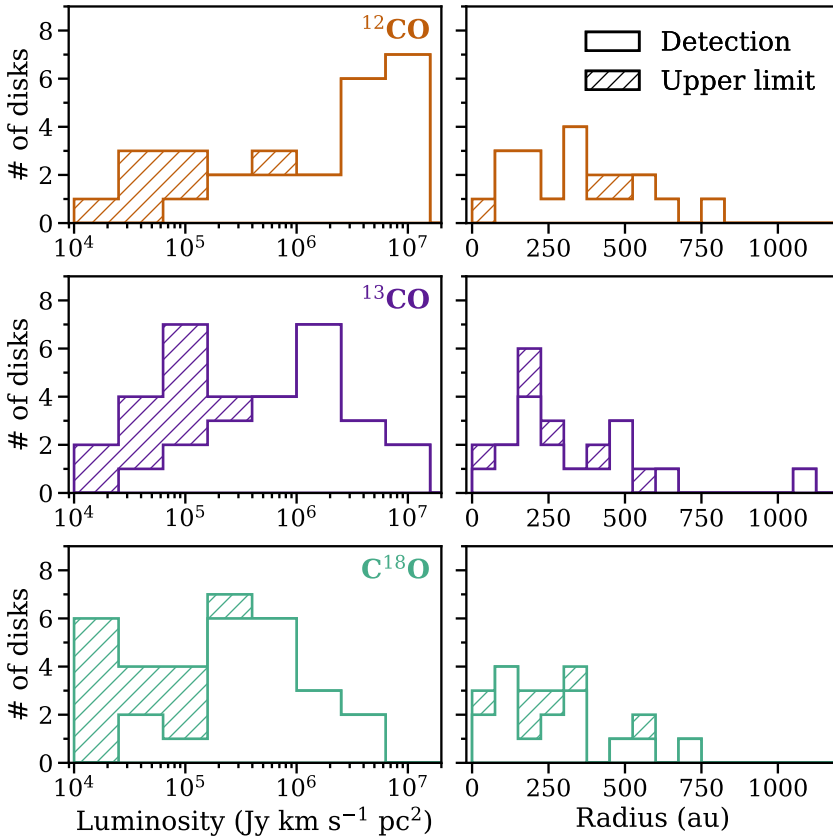
Figure 3.2: Summary of the luminosities and 90% radii for the ^{12}CO, ^{13}CO, and C^{18}O observations as presented in Table 3.2.

disks as upper limits in Table 3.2. Due to the many different projects imaged, the sample has a rather inhomogeneous distribution of spatial scales and sensitivities (see Table 3.A.1). All ^{13}CO and C^{18}O observations are from the same datasets, which is also the case for most ^{12}CO observations. The exceptions are: AB Aur, HD 135344B, HD 141569, HD 142666 and HD 290764, which have a different dataset for their ^{12}CO observations.

The fluxes and radii together with their errors are listed in Table 3.2. A summary of Table 3.2 of all luminosities and radii is shown in Figure 3.2.

3.3   Model setup

In this work a grid of `DALI` models (Dust And LInes, Bruderer et al. 2012; Bruderer 2013) is run to determine the gas masses of the Herbig disks based on the ^{13}CO and C^{18}O luminosities. `DALI` is a thermo-chemical code which solves for the gas and dust thermal structure of the disk by taking heating, cooling, and chemical processes into account. We use the CO isotopologue chemistry network by Miotello et al. (2016) evolved to 1 Myr, which is a simplified version of the network by Miotello et al. (2014). This network includes the ^{12}C, ^{13}C, ^{16}O, ^{18}O, and ^{17}O isotopologues, and processes such as isotope-selective photodissociation, fractionation reactions, self-shielding, and freeze-out.

`DALI` uses the simple parametric prescription proposed by Andrews et al. (2011) for the density structure. This density structure is motivated by the viscous accretion disk model, for which the solution follows an exponentially tapered power law (Lynden-Bell & Pringle 1974; Hartmann et al. 1998) given by

$$\Sigma_{\mathrm{gas}} = \Sigma_c \left(\frac{R}{R_c} \right)^{-\gamma} \exp \left[- \left(\frac{R}{R_c} \right)^{2-\gamma} \right], \qquad (3.1)$$

where Σ_c and R_c are respectively the surface density and critical radius and γ the power law index. The vertical distribution of the gas is given by a Gaussian distribution. The scale height angle of the gas is given by

$$h = h_c \left(\frac{R}{R_c} \right)^{\psi}, \qquad (3.2)$$

where ψ is the flaring index and h_c is the scale height at distance R_c. The physical scale height H is then equal to hR.

The models include small and large dust populations, for which the small dust follows the gas distribution and the large dust is settled vertically. The dust settling is set by the settling parameter χ. The gas-to-dust mass ratio in the disk is given by $\Delta_{g/d}$ and is set to the ISM value of 100.

In this work we use a range of parameters to run a grid of `DALI` models, see Table 3.3. All of these parameters combined make a total of 3600 models. Besides varying the gas mass of the models from 10^{-5} M$_\odot$ to $10^{-0.5}$ M$_\odot$ in steps of 0.5 dex, we also vary the parameters related to the vertical and radial mass distribution of the gas following eqs. (3.1) and (3.2). We expand the range of values used in

Table 3.3: Values of each DALI parameter used in this work.

Model Parameter	Range
Chemistry	
Chemical age	1 Myr
Volatile [C]/[H]	1.35×10^{-4}
Volatile [O]/[H]	2.88×10^{-4}
[PAH]	$10^{-2} \times$ ISM
ζ_{cr}	5.0×10^{-17} s^{-1}
Physical structure	
R_c	5, 10, 30, 60, 200 au
R_{subl}	0.2 au
$\text{Log}_{10}(M_{\text{gas}})$	{-5, -4.5, ..., -0.5} M$_\odot$
γ	0.4, 0.8, 1.5
h_c	0.05, 0.2, 0.4 rad
ψ	0.1, 0.2
Dust properties	
Dust populations	0.005–1 μm (small)
	1–1000 μm (large)
χ	0.2
$\Delta_{g/d}$	100
Stellar properties	
T_{eff}	10^4 K
L_{bol}	5, 10, 20, 50 $L_\odot$
L_X	10^{30} erg s^{-1}
$M_\star$	2.5 $M_\odot$
Observational geometry	
i	10°, 40°, 70°
d	100 pc

Miotello et al. (2016) by also including flat and compact disks, as these are likely present in the group II Herbig disks (Stapper et al. 2023), through h_c, ψ, and R_c. Therefore, the critical radius ranges from 5 to 200 au in steps of ~ 0.4 dex. The power-law index γ is set to 0.4, 0.8, and 1.5, which changes the steepness of the turnover in the surface density at large radii. Higher values of γ allow for the bulk of the mass to be distributed further out in the disk, effectively changing the size of the disk.

For the vertical distribution of the gas, we alter both the flaring index ψ and the scale height at the critical radius h_c. The range in ψ is kept the same as

Miotello et al. (2016) used, see Table 3.3. For the scale height h_c we use a larger range from a very flat disk with $h_c = 0.05$ rad, as very flat disks have been found to exist in the Herbig population (Law et al. 2021, 2022; Stapper et al. 2023), up to 0.2 rad and 0.4 rad for thicker disks. Flaring of the disk changes the (vertical) temperature structure of the disk and hence the emitting layer of the CO, which in turn changes the observed luminosity of the line.

To better accommodate for the range in stellar properties, we vary the stellar luminosity from 5 $L_\odot$ to 50 $L_\odot$ in steps of ~ 0.3 dex to include a similar range in luminosities present in our Herbig sample (not including the most luminous stars), as determined by Guzmán-Díaz et al. (2021). We keep the effective temperature $T_{\rm eff}$ at 10^4 K as this matches well with the effective temperatures of the sample, and we use the sublimation radius $R_{\rm subl}$ corresponding to a stellar luminosity of 10 $L_\odot$ (using the scaling relation by Dullemond et al. 2001) for all models, as the sublimation radius is much smaller than the scales we probe.

We kept the remaining parameters the same as Miotello et al. (2016). The PAH abundance is set to 1% of the ISM, with the ISM value being a PAH-to-dust mass ratio of 5% (Draine & Li 2007). The cosmic-ray ionization rate (ζ_{cr}) is set to 5.0×10^{-17} s^{-1}, and the X-ray luminosity (L_X) is set to 10^{30} erg s^{-1}. As noted in both Bruderer et al. (2012) and Miotello et al. (2016), L_X only has a minor influence on the CO pure rotational lines, which are the focus in this work.

The models have been run with 40 vertical cells and 42 log-spaced radial cells out to 1000 au. The highest mass models were radially sampled in 62 cells out to 1500 au. This sampling was found to be sufficient to yield line fluxes accurate to $< 5\%$. The grid extends vertically to ten times the scale height, as given by eq. (3.2).

For the built-in DALI ray-tracer, a distance of 100 pc is used and each model is ray-traced at inclinations of $10°$, $40°$ and $70°$, encompassing all inclinations in our sample (see Table 3.1). A total of six CO isotopologues are ray-traced: ^{12}CO, ^{13}CO, C^{18}O, C^{17}O, ^{13}C^{18}O, and ^{13}C^{17}O. The $J = 2 - 1$ and $J = 3 - 2$ transitions are ray-traced for each molecule (Yang et al. 2010; Schöier et al. 2005).

3.4   Results

3.4.1   Integrated-intensity maps

Figure 3.1 presents the integrated intensity maps of the disks in which any of the three CO isotopologues is detected: 20 out of 27 for ^{12}CO, 22 out of 33 for ^{13}CO, and 21 out of 33 for C^{18}O for our 35 sources. If nothing is shown, the molecule is not covered. As C^{18}O is covered but not detected, the integrated-intensity map of HD 141569 is presented as well, which is obtained by integrating over the same velocity range as done for the ^{12}CO and ^{13}CO emission. All other non-detections are not shown. For the majority of the disks, the transition used is $J = 2 - 1$, except for all lines in the HD 135344B and HD 290764 disks, and ^{12}CO in AB Aur and HD 141569, for which the $J = 3 - 2$ transition is imaged. For the detections, azimuthally averaged radial profiles are presented in Fig. 3.3 which have been
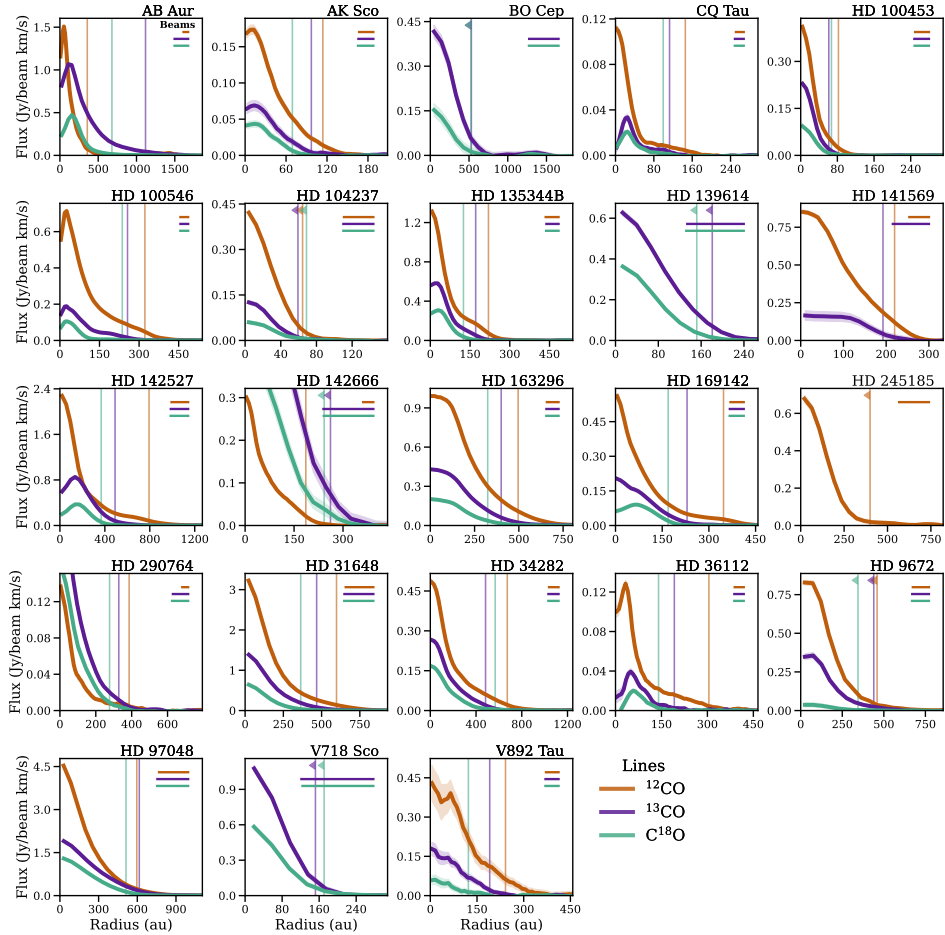
Figure 3.3: Azimuthally averaged radial profiles of the three CO isotopologues in all 23 Herbig disks in which at least one isotopologue is detected. The 1σ uncertainty interval is indicated by the shaded region in the same color as the profile. The vertical solid lines indicate the derived 90% radii for each line. An upper limit on the radius is indicated with a left facing arrow. The beam size is illustrated by the horizontal lines in the top right of each panel.

made using the inclinations and position angles listed in Table 3.1. Fig. 3.3 also presents the radii listed in Table 3.2.

In general we find that the size of the disk decreases with the abundance of the isotopologue. For the resolved disks the median ^{12}CO $R_{68\%}$ ($R_{90\%}$) radius is a factor of 1.3 (1.3) larger compared to ^{13}CO, and a factor of 1.8 (1.4) larger compared to C^{18}O. Hence, for C^{18}O the bulk of the emission is generally compact, but it can have more faint extended emission around the compact emission compared to ^{12}CO and ^{13}CO, resulting in a larger difference between the $R_{68\%}$ and

$R_{90\%}$ radii. The decrease with abundance of the isotopologues observed is caused by the smaller column density of the rarer CO isotopologue and isotope selective photodissociation, which lead to optically thin millimeter emission at larger radii reducing the amount of emission. Regarding the luminosity of the disk, we find a clearly decreasing trend with rarity of the isotopologue. Most ^{12}CO disks have a luminosity of at least 5×10^6 Jy km s^{-1} pc^2, while the ^{13}CO and C^{18}O disk luminosities are 2×10^6 Jy km s^{-1} pc^2 and 4×10^5 Jy km s^{-1} pc^2 respectively. As all three isotopologues are likely optically thick in our sample when detected, this decrease in luminosity is a result of a decrease in size of the detected disk, a reduction in temperature due to the emission from rarer isotopologues originating from deeper in the disk, and/or truncation by photodissociation.

The sizes of the ^{12}CO disks are seen to vary significantly. The smallest detected gas disks range from an $R_{90\%}$ of less than 64 au (HD 104237) out to 82 au (HD 100453). The HD 104237 disk is particularly small both in CO and continuum: we measure a continuum disk extent of less than 21 au, which is still unresolved (we use a higher spatial resolution dataset than Stapper et al. 2022, who had an upper limit of 139 au). Most of the ^{12}CO disks have a $R_{90\%}$ between 100-400 au (65%, 13/20; see Fig. 3.2). The median disk size lies close to the middle of this range at 335 au. The $R_{68\%}$ radius has a median of 226 au. The largest disk in ^{12}CO is HD 142527 which has a $R_{90\%}$ of 793 au, by far the largest disk in the sample. AB Aur is likely a very large disk in ^{12}CO as well, because of its ^{13}CO radius of 1118 au. But due to a small maximum recoverable scale a large part of the ^{12}CO disk is filtered out. A number of disks show large extended emission especially in ^{12}CO (but also for ^{13}CO and C^{18}O) where there is an initial peak and a much flatter emission "shoulder" toward larger radii. This part contributes to the integrated flux only slightly, and mainly increases the inferred radius of the disk, especially for the 90% radius. Hence, $R_{90\%}$ is the main tracer of the outer radius, and we primarily use this over the 68% radius, except when explicitly stated otherwise.

The ^{13}CO and C^{18}O sizes are generally smaller than the ^{12}CO sizes. As Fig. 3.2 shows, most of the ^{13}CO and C^{18}O emission is within 300 au in size. The range of the inferred radii is larger than for ^{12}CO, ranging from the smallest resolved ^{13}CO disk in the sample of 61 au, out to 1118 au in size for the largest disk. The most stringent upper limit obtained is similar as the smallest resolved disk, at 59 au, for HD 104237. There are also more upper limits on the ^{13}CO and C^{18}O radii compared to ^{12}CO due to four relatively low resolution datasets used not containing ^{12}CO.

Some disks suffer from foreground cloud absorption, such as HD 97048 and V892 Tau, as can be seen in Fig. 3.1 where emission along the minor axes of these disks seems to be absent. Especially the ^{12}CO emission of AB Aur and some of HD 97048 suffers from this, resulting in a smaller outer radius found for ^{12}CO compared to the other isotopologue(s). For ^{13}CO and C^{18}O the cloud absorption leaves much less of an imprint on the moment map, and these do not affect the obtained integrated fluxes and the radii significantly. Hence, we mainly use the ^{13}CO radius as a measure of the size of the disk. Several of the non-detections show foreground cloud emission: HD 176386, MWC 297, TY CrA and Z CMa.

For Z CMa emission from the disk is present at $V_{\mathrm{LSRK}} \sim 10$ km s^{-1}, but the foreground cloud emission makes it difficult to extract any information from this, and thus it is considered as an upper limit. For the other disks with foreground cloud emission no signature of a disk is visible in any of the isotopologues, possibly due to the cloud emission.

Due to the different datasets, their spatial resolution is different resulting in unresolved ^{13}CO and C^{18}O disks for HD 142666, and different sensitivities resulting in upper limits larger than the ^{12}CO disk. This is especially clear from the azimuthal averages in Fig. 3.3, where one can see that the inferred radii of ^{12}CO are indeed smaller than for the rarer isotopologues in these two disks. Lastly, for BO Cep, HD 104237, HD 142666, and V718 Sco we do find very similar outer radii for ^{13}CO and C^{18}O because the disk is unresolved. The other two disks with upper limits on their size, HD 139614 and HD 9672, are marginally resolved, especially along the major axes, resulting in a more significant difference between the ^{13}CO and C^{18}O radii.
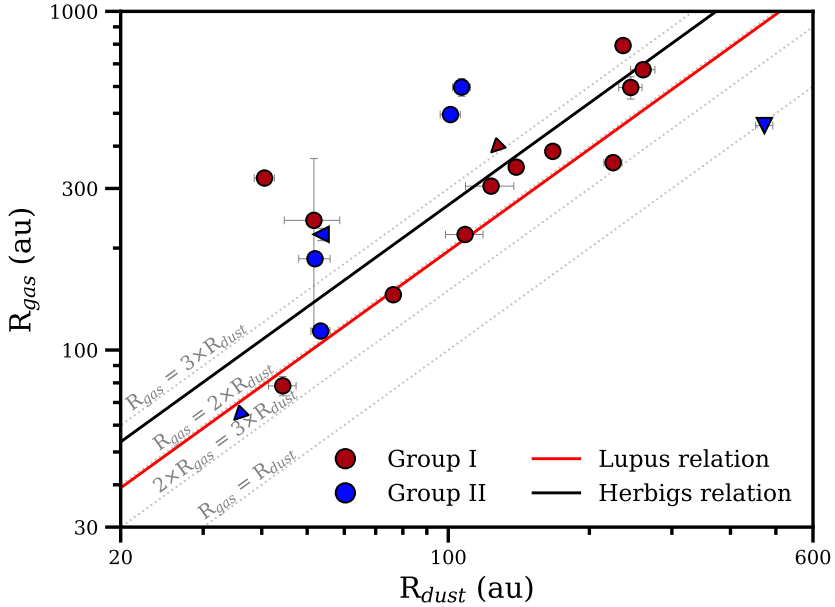
3.4.2 ^{12}CO radius versus dust radius

The ^{12}CO observations can be used to compare the gas radii of the Herbig disks with the dust radii from Stapper et al. (2022). Figure 3.4 presents the dust radius compared to the gas radius. In addition to HD 104237, a higher resolution dataset of HD 141569 has been used as well compared to Stapper et al. (2022), which further constrains the dust radius to less than 38 au for the 68% radius and 54 au for the 90% radius. In addition to the region in the plot which is radial drift dominated, the relation found for the disks in Lupus is also indicated (Ansdell et al. 2018). If the gas radius is larger, the disk is thought to be radial drift dominated (Trapman et al. 2019). Anything below this value can still be caused by optical depth effects.

All disks but one (HD 9672) have larger gas radii compared to their dust radii. Most disks lie along the same relation as found for Lupus, where the gas is two times the dust radius. However, a larger spread in ratios is present in the Herbig sample compared to the disks in Lupus. The black line in Fig. 3.4 indicates the relation for the resolved disks between the dust and gas radii for the $R_{90\%}$ radii. A simple fitting routine `curve_fit` is used from the `scipy` package to fit the scaling between the dust and gas radii. We find that for the $R_{90\%}$ radii, the ratio between the dust and gas radii is a factor of 2.7. The $R_{68\%}$ are consistent with this value. HD 9672 is the outlier in this sample, showing an equal size in both the dust and gas. The gas radius is slightly unresolved however, and this could make the gas radius even smaller. A comparison with debris disks is shown in Section 3.5.2.3.

These ratios are high compared to Lupus due to a few disks which are close to or within the regime where radial drift is necessary to explain the differences seen between the dust and gas radii (Trapman et al. 2019). This is the case for HD 100546, HD 142666, HD 163296, HD 31648 (MWC 480) and V892 Tau, all of which have gas disks a factor of more than four larger than their dust radius. This is consistent with other works of for instance MAPS (Zhang et al. 2021). A few disks have gas radii only slightly smaller than four times the dust radius,

Figure 3.4: Gas radii versus dust radii of the Herbig disks with detected ^{12}CO emission, both $R_{90\%}$. An upper limit on the gas radius or dust radius, or both, is marked with a triangle pointing in the corresponding direction(s). The colors indicate the Meeus et al. (2001) group of the disk: red is group I, blue group II. Lines for different R_{dust} to R_{gas} ratios are shown as well. The black line shows for the resolved disks the relation of the $R_{90\%}$ radii. Using $R_{68\%}$ does not alter the relation significantly. The yellow region indicates the region where the difference between the dust and gas radii cannot solely be explained by optical depth effects, and radial drift is necessary (Trapman et al. 2019). The red line corresponds to the relation found for the disks in Lupus (Ansdell et al. 2018).

HD 142527 and HD 245185. We note that HD 100546 has a very faint outer dust ring at 190 au (Walsh et al. 2014; Fedele et al. 2021), lowering the ratio to 1.7 instead of almost a factor of 8. Similarly, HD 163296 has a faint outer ring in both the DSHARP and MAPS data as well (Huang et al. 2018; Sierra et al. 2021). Hence, Fig. 3.4 could indicate around which disks a faint outer ring can be found, possibly linked to giant exoplanet formation happening in these disks.

3.4.3 ^{13}CO and C^{18}O luminosities

Figure 3.5 presents the resulting ^{13}CO and C^{18}O $J = 2 - 1$ line luminosities of the models in colors and observations in black (the same figure for the $J = 3 - 2$ transition can be found in Appendix 3.C). The size of the markers are scaled by the ^{13}CO 90% radius of the models and observations. The disks with upper limits on both ^{13}CO and C^{18}O are presented as the diagonal triangles. HD 141569, which has a C^{18}O upper limit, is shown as a downward pointing triangle. The top and
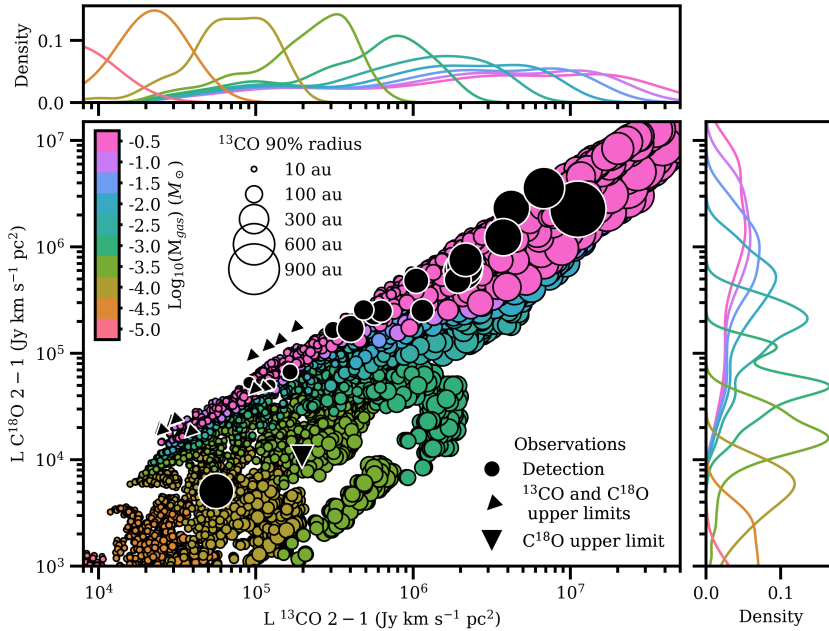
Figure 3.5: $C^{18}O$ luminosity versus ^{13}CO luminosity for the DALI models (colored circles) and the observations (black circles). The colors indicate the gas mass of the disk model. The size of the markers indicate the 90% radius of the ^{13}CO emission. Probability density curves of the models for each gas mass are shown along the x-axis in the top panel and along the y-axis in the right panel, i.e., most models of a particular gas mass reside around the peak of each curve.

right hand-side panels indicate the distribution of the models for the ^{13}CO and $C^{18}O$ luminosity respectively.

The two main deciding factors governing how luminous the disk is are the optical depth of the millimeter lines as seen from the observer and the self-shielding capacity of the CO isotopologues against UV (e.g., Visser et al. 2009). Additionally, these two factors depend on the distribution of the mass and the size of the disk (Trapman et al. 2019, 2020). If the disk is very compact a large range of masses can be 'hidden' behind the region where the gas becomes optically thick (Miotello et al. 2021). This results in a large degeneracy in possible luminosities for a single mass, as can be seen in Fig. 3.5. The only way to change the observed luminosity is to increase the emitting area as for optically thick emission, the intensity per unit area is constant, and thus increasing the radius of the disk. So a clear trend is present in the models where the smallest disks are at low ^{13}CO and $C^{18}O$ luminosities, while the largest disks are on the opposite side with high ^{13}CO and $C^{18}O$ luminosities due to an increase in radius.

Figure 3.6 presents this in another way: for the most massive disks an increase in radius results in an increase in luminosity. In addition, Appendix 3.D shows this for the other values of R_c and γ. This trend is also evident in the observations,
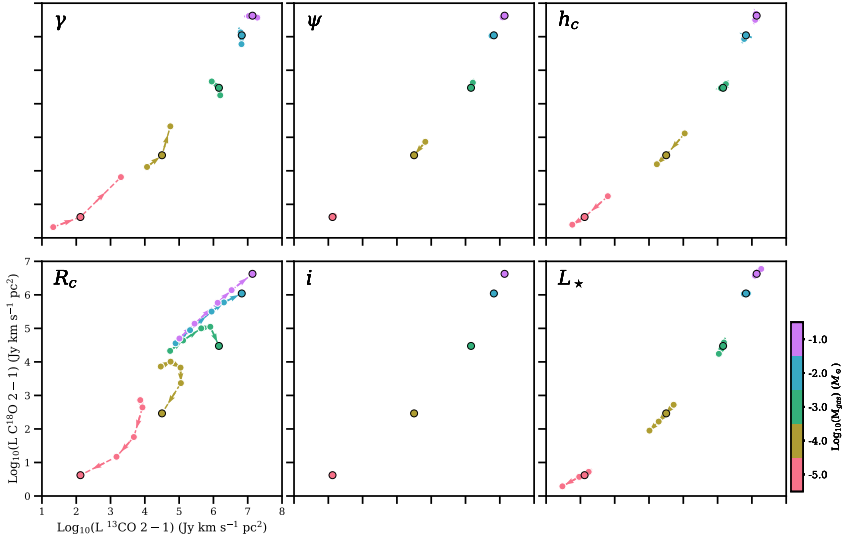
Figure 3.6: Overview of the different parameters explored in the DALI models and their effect on the luminosity of ^{13}CO and C^{18}O. The colors indicate the mass of the model. The arrows indicate in which direction the parameter increases in value (see Table 3.3). The black outlined circles are the same models for each mass in all panels. The black outlined models have the following parameters: $\gamma = 0.8$, $\psi = 0.2$, $h_c = 0.2$ rad, $R_c = 200$ au, $i = 10°$ and $L_\star = 10\ L_\odot$. In Appendix 3.D the same plot is shown, but with $\gamma = 0.4$ and $\gamma = 1.5$, and with $R_c = 5$ au, $R_c = 10$ au, $R_c = 30$ au, and $R_c = 60$ au, and for the $J = 3 - 2$ transition

where the largest disks such as AB Aur and HD 97048 are in the top right of Fig. 3.5 and the smallest disks such as HD 100453 and HD 104237 are in the bottom left. We can therefore conclude that most disks, apart from HD 9672 and HD 141569, are likely to be optically thick in both ^{13}CO and C^{18}O as for these disks both luminosities scale with the size of the disk.

The models with higher mass disks can also make larger disks due to the disk surface density being higher at larger radii. This results in a maximum ^{13}CO and C^{18}O luminosity for both the 10^{-1} M$_\odot$ and 10^{-2} M$_\odot$ models. The distributions presented in the top and right panels of Fig. 3.5 show that the 10^{-1} M$_\odot$ models can have luminosities up to $\sim 4 \times 10^7$ Jy km s^{-1} pc^2 for ^{13}CO and $\sim 10^7$ Jy km s^{-1} pc^2 for C^{18}O. Similarly, the 10^{-2} M$_\odot$ models have luminosities up to $\sim 2 \times 10^7$ and $\sim 2 \times 10^6$ Jy km s^{-1} pc^2 for ^{13}CO and C^{18}O, resulting in a region where the mass of the disks needs to be at least 0.1 M$_\odot$ to explain the observed luminosities.

For the lower mass disks, an interplay between the optical depth and self-shielding of the CO molecules sets the observed luminosities. Due to its larger abundance, ^{13}CO becomes optically thin further out in the disk than C^{18}O. For the 10^{-2} M$_\odot$ models, first an increase in radius results in an increase in luminosity in both isotopologues, but eventually C^{18}O becomes optically thin. Consequently,

an increase in radius does not increase the luminosity of $C^{18}O$, but it still does so for ^{13}CO, and the model moves horizontally with an increase in radius, also see the bottom left panel of Fig. 3.6. When the $C^{18}O$ is spread out even more, its self-shielding ability decreases and the $C^{18}O$ starts to photodissociate, decreasing its abundance and thus its luminosity. This results in the model moving down with an increase in radius in Fig. 3.6. Consequently, a maximum luminosity for $C^{18}O$ is set by photodissociation for disk masses $\lesssim 10^{-3}$ $M_\odot$. ^{13}CO is on the other hand still optically thick, and increasing the radius still increases its luminosity, until ^{13}CO starts dissociating as well, causing the models to curve toward lower luminosities in both isotopologues with increasing radius for $M_{disk} \lesssim 10^{-4}$ $M_\odot$.

Photodissociation of $C^{18}O$ is already the main driver for the luminosity of the lower mass models of almost all sizes, hence almost all models move horizontal or diagonally down to lower ^{13}CO luminosities. For the smallest models, while still being optically thin (or marginally optically thick) in $C^{18}O$, an increase in size can still result in an increase in luminosity if the photodissociation of the $C^{18}O$ does not yet dominate. Also in the $M_{disk} \lesssim 10^{-4}$ $M_\odot$ case the ^{13}CO becomes optically thin for the observer and photodissocation starts to lower its luminosity with an increase in radius. Going to the lowest mass models of 10^{-5} $M_\odot$ both ^{13}CO and $C^{18}O$ are (marginally) optically thin and photodissociation of both isotopologues reduce their luminosity with increasing radius.

Evidently, the mass and the radius of the disk have the biggest impact on the observables of the disk. The next most impactful parameter affecting the CO luminosity of the disk is γ in Eq. (3.1), which affects the overall distribution of the mass of the disk. A larger γ results in a higher surface density at the inner region and decreases the effect of the exponential taper in the outer region, which increases the size of the disk. γ especially impacts the lower mass models, see Fig. 3.6 and the extra Figures in Appendix 3.D. A larger γ makes the region where the $C^{18}O$ emission is coming from relatively constant in size and self-shielding occurs less than for smaller γ even for the largest R_c, while the ^{13}CO emission increases with increasing radius because of a larger emitting surface. Hence, the model moves horizontally in the bottom left panel of Fig. 3.D.6. For smaller γ at $C^{18}O$ can dissociate at large radii due to the lower surface density closer in and the luminosity decreases rapidly, as can be seen as the relatively large jump in luminosity from $R_c = 60$ au to 200 au for the 10^{-3} $M_\odot$ models in the bottom left panel of Fig. 3.6. This jump also causes the bimodal distribution present in the right panel of Fig. 3.5. This could have been alleviated by adding a value of γ between 0.8 and 1.5. For even lower masses an increase in γ results in less change in both ^{13}CO and $C^{18}O$ with an increase in radius due to more efficient self-shielding.

All remaining parameters affect the CO luminosity in the same direction as R_c, see Figs. 3.6, and 3.D.1 to 3.D.6. Changing h_c does not affect the more massive disks, because these are optically thick already. For the lower mass models increasing h_c has the main affect of increasing the volume of the disk, making the gas optically thin and reducing the abundance of both ^{13}CO and $C^{18}O$ due to photodissociation. Increasing the stellar luminosity decreases the abundance of both ^{13}CO and $C^{18}O$, hence the downward left movement of the models in Fig. 3.6.

For the higher mass disks the CO isotopologues are already shielded and the luminosity barely affects the overall abundance. Lastly, both ψ and the inclination do not affect the observed integrated ^{13}CO and C^{18}O luminosities considerably.

3.4.4   Obtaining the mass of the disk

As discussed in the previous section, Figure 3.5 shows that most observations are consistent with the highest possible masses based on their ^{13}CO and C^{18}O luminosities. However, at least for the observations detecting ^{12}CO, ^{13}CO, and C^{18}O, the mass range can be further constrained by using the observed size of the disk in the selected isotopologues.

3.4.4.1   Masses from detected emission

To obtain a measure of the mass of the disk, we select all models within a region around the observations in Fig. 3.5 based on the confidence intervals of the observations. There are two main sources of uncertainty that we take into account: a systematic uncertainty set by the calibration accuracy, and a statistical uncertainty set by the noise in the moment 0 map. We select all models which fall within 3σ from a line given by the 10% systematical uncertainty. For some of the more luminous targets the obtained uncertainty is relatively small and either no or very few models were found within the region confined by the two sources of uncertainty. If less than 200 models were found to fall within the given region of a disk, the closest 200 models were included, this occurred for 11 disks. Typically, the selected models deviated around 10% from the observed luminosity. For HD 141569 we take all models below the C^{18}O upper limit and within a 10% systematic uncertainty on the ^{13}CO luminosity because it dominates over the noise.

    After obtaining this set of models, selections based on the size of the disk and its inclination, and on the stellar luminosity can be made (see Tables 3.1 and 3.2). Given the lack of ^{12}CO observations for some of these disks, together with possible cloud contamination, we use the ^{13}CO $R_{90\%}$ as a disk size tracer. We select all models within a factor of 1.4 in size compared to the observations, as this is the factor by which the models are on average smaller than the observations in ^{13}CO, we discuss this further at the and of this section. Based on the radius, inclination, and stellar luminosity, the constraints on the disk mass can be tightened. Figure 3.7 presents the resulting range in possible disk mass values and the (logarithmic) mean mass of the models within that range, as shown by the light gray lines and darkblue diamonds respectively. The spread in mass of the selected models is given by the black lines. For the high-mass disks (on the right), that correspond to bright ^{13}CO emission, the masses are well constrained to be above $10^{-1.5}$ M$_\odot$. These stringent lower limits are mainly due to their large and well-known sizes. Our obtained disk masses can be found in Appendix 3.E.

    Figure 3.8 shows that the C^{18}O luminosity is sensitive to the gas mass when selecting models with the appropriate size based on our grid of models, each panel showing this for differently sized models in ^{12}CO. We note that this is the $R_{90\%}$
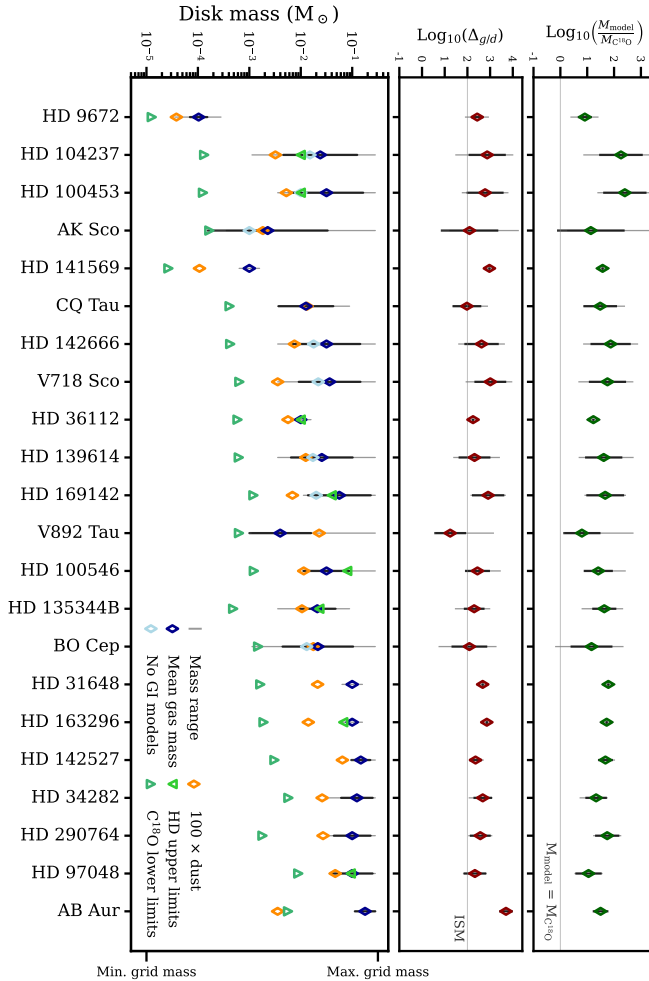
Figure 3.7: Gas masses of the Herbig disks detected in the CO isotopologues as selected from the models presented in Fig. 3.5. The disks are ordered from left to right by increasing ^{13}CO luminosity. The gray lines indicate the range in possible disk mass based on the disk parameters listed in Table 3.1, while the black lines indicate the standard deviation. The mean mass of these models is given as the dark blue diamond. After removing models which are potentially gravitationally unstable, the mean mass changes into the light blue diamond. The orange diamonds are taken from the dust masses of Stapper et al. (2022) multiplied by the canonical gas-to-dust ratio of 100. The HD upper limits from Kama et al. (2020) are shown as green downward pointing triangles. The $C^{18}O$ lower limits are directly obtained from the integrated flux. The middle panel shows the resulting gas-to-dust ratio based on the mass range and mean values, and the top panel shows the factor by which the mass could be underestimated when using $C^{18}O$ assuming optically thin emission.

radius, which should not be confused with R_c. This clearly shows that the size of the disk is an indicator of its mass as well. One cannot make disks larger than ~ 500 au without the disk mass being higher than $\sim 10^{-2}$ M$_\odot$. On the other hand, for the lower mass disks the tenuous ^{12}CO gas cannot self-shield in the outer regions anymore for the largest disks, reducing the measured size of the disk. Consequently, one obtains a better constraint on the disk mass of the largest disks in the sample.

For the smaller disks, more masses are compatible with the observed ^{13}CO and C^{18}O line luminosity due to the higher optical depth. This results in low lower limits on the gas mass from our models. For example AK Sco and HD 104237 have lower limits of $\sim 10^{-3.5}$ M$_\odot$ and $\sim 10^{-3}$ M$_\odot$ respectively. This is also evident from Figure 3.8, clearly showing that the different gas masses give similar C^{18}O luminosities for the smallest disks. For the smallest radius bin size a lower limit on the size of the disk can be given as well. Disks which are smaller than R$_{90\%}$=20 au in ^{12}CO and have a mass of more than 10^{-4} M$_\odot$ do not occur in our models.

To constrain the disk masses even more, one can include other parameters as well. For example, for AK Sco and HD 142666 the vertical extent of the disk from Stapper et al. (2023) can be exploited. We implement this in a simple way, where for the very flat disks AK Sco and HD 142666 we choose models with $h_c = 0.05$ rad. While this does not improve the overall range in possible disk masses (as h_c does not considerably change the overall luminosity, see Section 3.4.3), for both flat disks we can rule out either lower mass models for AK Sco or higher mass models for HD 142666. This difference is due to their relative position in Fig. 3.5.

For two low mass disks, HD 9672 and HD 141569, we can determine their disk mass within an order of magnitude. Based on their position in Fig. 3.5 (the two disks with the lowest C^{18}O luminosity or upper limits thereon), we can already see that the gas mass should be around 10^{-3}-10^{-4} M$_\odot$. No other models fall within the computed confidence intervals. We note that for HD 9672 we do not reproduce the size of the ^{13}CO disk well with the models. We comment more on this in Section 3.5.2.3. This results in a well determined disk mass of 10^{-4} M$_\odot$ for HD 9672 and 10^{-3} M$_\odot$ for HD 141569.

Based on the stellar mass of the Herbig stars, and the disk mass and disk outer radius of ^{12}CO from the models, we can determine if a specific model would be gravitationally unstable around the Herbig star using the relation

$$\frac{M_d}{M_\star} > 0.06 \left(\frac{f}{1}\right) \left(\frac{T}{10 \text{ K}}\right)^{1/2} \left(\frac{r}{100 \text{ au}}\right)^{1/2} \left(\frac{\text{M}_\odot}{M_\star}\right)^{1/2} \tag{3.3}$$

from Kratter & Lodato (2016), where T is the temperature of the disk, r the outer radius of the disk (given by the measured ^{13}CO R$_{90\%}$ radius) and $M_\star$ the mass of the star, we set the pre-factor f equal to 1. The temperature T is determined with the luminosity of the Herbig star via the relation by Andrews et al. (2013). For seven disks the radius of the disk combined with Eq. (3.3) is constraining enough to result in a lower mean disk gas mass by ruling out the potentially gravitationally unstable models. For the disks with radius upper limits especially, the compact
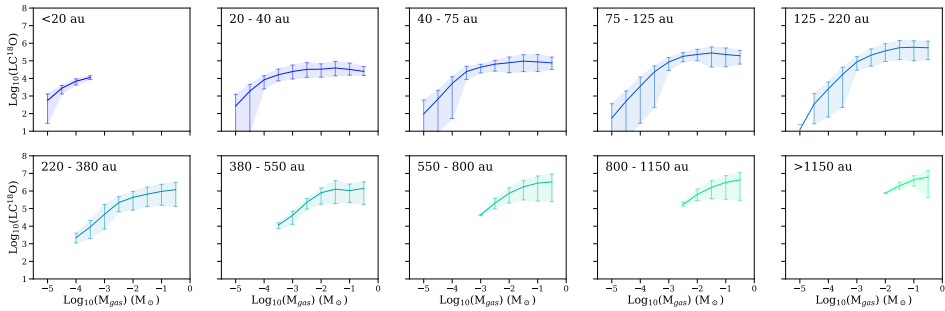
Figure 3.8: Range of $C^{18}O$ luminosities for different mass disks, selected for ^{12}CO $R_{90\%}$ radii from the DALI models presented in Fig. 3.5. The shaded area indicates the minimum and maximum values, and the solid line is the mean value.

high mass disks can be ruled out if assuming that these observed disks are not gravitationally unstable.

For eight of the Herbig disks, upper limits on the gas masses have been estimated from HD (Kama et al. 2020), see the downward facing triangles in Figure 3.7. In general, the gas masses we find are consistent with the HD upper limits. For HD 163296 and HD 36112, the HD upper limits are roughly equal to our gas mass estimates, suggesting that the observations might have been close to detecting HD. For HD 100453, HD 169142 and HD 97048 the mean gas masses of the models are higher than the HD upper limits, implying that these disks are not as massive as their size and ^{13}CO and $C^{18}O$ luminosities suggest. A combination of modeling the CO emission and HD upper limits could add additional constraints to the obtained gas masses.

Figure 3.7 also shows $100\times$ the dust mass from Stapper et al. (2022). For the five NOEMA targets we compute the dust masses in the same way as Stapper et al. (2022), see Appendix 3.B. The middle panel in Fig. 3.7 shows the resulting gas-to-dust ratio from the mean gas mass as the dark red diamonds and from the range in gas masses as the vertical gray line. The horizontal gray line indicates a gas-to-dust ratio of 100. For most disks we find that the total disk mass derived from the dust mass is consistent with a gas-to-dust ratio of 100. Some disks suggest a depletion of dust compared to the interstellar medium. Primarily for AB Aur the $100\times$ dust mass falls well below the gas mass range, giving a gas-to-dust ratio that is two orders of magnitude higher than the canonical value. For some of the other higher mass disks, such as HD 169142, the dust mass also suggests a depletion of dust compared to gas of a factor of a few. This apparent depletion of dust might be related to the dust being optically thick, we comment on this in §3.4.4.4. In general however, the dust mass does seem to indeed trace the total disk mass relatively well for Herbig disks, in contrast with the T Tauri disks.

Lastly, we note that the size of the models are generally smaller than those of the observations for the same flux in a particular CO isotopologue. When selecting all models within a factor of two of the observations, we find that the ^{12}CO, ^{13}CO, and $C^{18}O$ radii of the models are on average a factor 1.3, 1.4, and 1.9 times smaller

than the observed radii. This is likely due to the models being smooth, with no substructures present. The observations do show some gas structures which increase the emitting area of the disk, and also present weak emission extended structures which increase their 90% radius without much affecting the overall flux. Specifically gas cavities, the main gas structure seen in our data, are generally found to be smaller than continuum cavities (van der Marel et al. 2016; Leemker et al. 2022), and thus are likely not affecting the gas as much as it would to the continuum. Comparing our found gas masses to existing disk specific modeling efforts taking into account the structure of the disk show only differences of a factor of a few. For example the MAPS Herbig disks HD 163296 and HD 31648 were found to have gas masses of 0.14 $M_\odot$ and 0.16 $M_\odot$ respectively (Zhang et al. 2021), within a factor of a few from our derived masses (other examples include Tilling et al. 2012; Flaherty et al. 2015, 2020). Scaling the observed radii by the aforementioned factors does indeed not affect the inferred range in disk masses for a given disk. However, when using Fig. 3.8 one should keep this in mind when selecting which panel to use. Implementing gas and dust structures in the models exceeds the scope of this work, but future work could also consider the effect of these structures on the obtained dust and gas masses.

3.4.4.2   Mass lower limits from $C^{18}O$

In many works (see e.g., Hughes et al. 2008; Loomis et al. 2018; Miley et al. 2018; Booth & Ilee 2020), the disk mass has been estimated by using a flux scaling relation, assuming the emission is optically thin. This formula has been used to obtain a lower limit on the gas mass from ^{12}CO, ^{13}CO, and $C^{18}O$ flux. As we find that most Herbig disks are optically thick in $C^{18}O$, it is useful to obtain a measure of how much the total gas mass is underestimated when using $C^{18}O$ as a gas mass tracer. The total number of $C^{18}O$ molecules in the disk from the $C^{18}O$ flux can be calculated, assuming optically thin emission (see e.g., Loomis et al. 2018), with

$$n_{C^{18}O} = \frac{4\pi}{hc} \frac{F_\nu \Delta V d^2}{A_{ul} x_u},\tag{3.4}$$

where h, c, and A_{ul} are the Planck constant, speed of light, and the Einstein A coefficient for spontaneous emission respectively. x_u is the fractional population of the upper level, d the distance to the source, and $F_\nu \Delta V$ is the velocity integrated flux over the disk. Using a ratio between CO and H_2 of 2.7×10^{-4} (Lacy et al. 1994), and ratios of 77 and 560 of $^{12}C/^{13}C$ and $^{16}O/^{18}O$ in the local interstellar medium (Wilson & Rood 1994), in combination with a factor of 2.4 for the mean molecular weight, the total disk mass can be calculated. An excitation temperature is necessary to compute the population levels using the Boltzmann equation as well. We assume $T_{ex} = 40$ K which is higher than the $C^{18}O$ brightness temperatures of some of the Herbig disks (see e.g., Zhang et al. 2021), but is the same as other disks in our sample (e.g., HD 100546, HD 135344B, and HD 169142). We use the line properties (e.g., partition function values, A_{ul}, E_u, and g_u) from CDMS (Endres et al. 2016). Using the integrated $C^{18}O$ fluxes from Table 3.2, we obtain lower limits on the total gas mass of the disk, see Figure 3.7. The formula is also
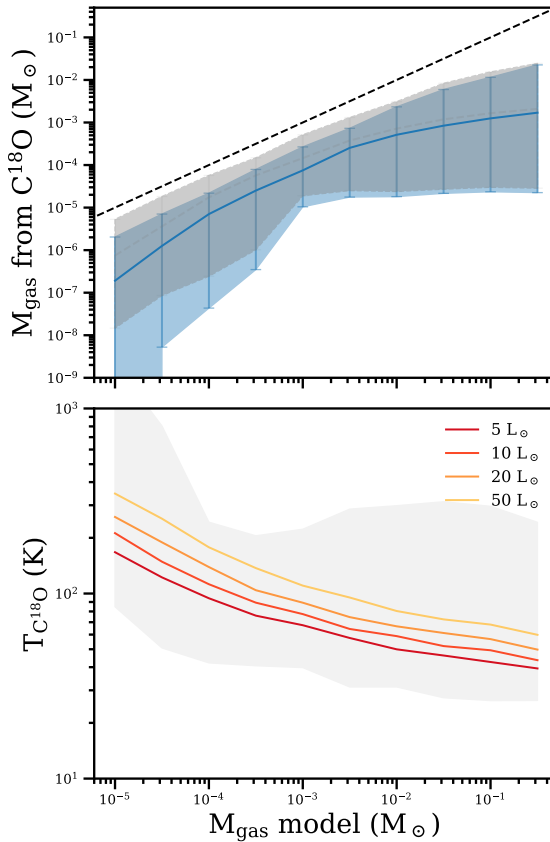
Figure 3.9: Gas mass of the models versus the retrieved gas mass from the $C^{18}O$ flux using Eq. (3.4), and the mass-weighted average of the temperature in the $C^{18}O$ emitting region. For the blue shaded region a temperature of 40 K is used, the gray shaded region uses the temperature of each model shown in the bottom panel. The shaded areas are the minimum and maximum values, with the mean value indicated by the solid line. The dashed line indicates the one-to-one correspondence between the two masses. The typical range in temperatures is indicated by the gray shaded region in the bottom panel.

applied to our models, a comparison can be found in Fig. 3.9 and the upper panel in Fig. 3.7.

Compared to the masses we find from the models, the masses obtained with Eq. (3.4) are a factor of 10-100 times lower, see Fig. 3.7. In the top panel of Figure 3.9, the blue shaded region indicates the retrieved masses using Eq. (3.4) with a temperature of 40 K compared to the true mass of the model. This large difference between the two is primarily due to two reasons. First, for the most massive disks, the $C^{18}O$ emission is optically thick which reduces the obtained disk gas mass. The disks for which the retrieved masses are closest to the true disk mass are also the largest disks, indicating that these are (marginally) optically thin. For the highest

mass disks, even the largest disks are not optically thin as the maximum retrieved mass bend toward relatively lower values. For the lowest mass disks on the other hand (e.g., HD 9672 and HD 141569) photodissociation becomes the dominant process reducing the CO abundance. Consequently, the mass of the disk is always underestimated when connecting $C^{18}O$ directly to the mass of the disk. As can be seen in both Figs. 3.7 and 3.9, the lowest mass disks have very low luminosities and retrieved masses due to photodissociation. The gray shaded area in the top panel of Fig. 3.9 are the retrieved masses after using the gas temperature in the emitting region of $C^{18}O$ where 90% of the emission is coming from as weighted by the mass in each cell, as indicated in the bottom panel. Both lower mass disks and smaller disks are warmer in the $C^{18}O$ emitting region, hence using a temperature of 40 K is not adequate. Especially for the lower mass disks this can underestimate the total disk mass with a factor of a few in addition to the lower CO abundance.

3.4.4.3   Upper limits

For the disks with upper limits on both isotopologues no selection can be made based on a region of luminosities in Figure 3.5 nor the size of the disk can be used. Using the dust radii of Stapper et al. (2022) in combination with the typical ratio of 2.7 between the gas and dust radii (see Section 3.4.2) does not add any constraints either as for all disks only upper limits on the dust disk size are known. Hence, a selection of all models within the quadrant confined by the upper limits is made. Figure 3.10 presents the resulting upper limits on the gas masses.

Based on the parameters in Table 3.1, a few constraints on the possible disk mass can be made. This is especially true for the ^{13}CO and $C^{18}O$ upper limits on the left side of Fig. 3.10, as these upper limits include models of all masses. While for the undetected or unresolved disks the inclination and radius do not give constraints, the luminosity gives enough constraints to lower the upper bound on some of the disks by multiple orders of magnitude, see Fig. 3.10. We find that HD 58647 and HR 5999 can have at most a mass of 10^{-4} M$_\odot$ to explain the non-detection in both ^{13}CO and $C^{18}O$. Interestingly, for both of these disks a higher dust mass is found, suggesting an increased abundance of dust compared to the ISM. For HD 176386 and TY CrA an upper limit of $10^{-3.5}$ M$_\odot$ is found. Z CMa has a higher upper limit of $10^{-2.5}$ M$_\odot$. The standard deviation, as given by the black lines in Fig. 3.10, show tighter constraints. For the other upper limits no constraints on the gas mass could be made, even after selecting for the source-specific parameters. However, we do note that the 10^{-1} M$_\odot$ models are by far outnumbered by lower mass models as most, but not all, high mass models can be excluded. This is reflected in the mean gas mass and standard deviation, as these are much lower than the maximum mass possible, see the dark blue diamonds and black lines in Fig. 3.10.

Based on the $C^{18}O$ upper limits, a maximum radius can be estimated for these disks. As Fig. 3.8 shows, an increase in size increases the luminosity of the disk. Hence, upper limits on the ^{12}CO radius can be determined for the disks with no detections. We find upper limits of 550 au (HD 58647, HD 176386, HR 5999, TY CrA and Z CMa) and 800 au (BH Cep, HD 200775, KK Oph, MWC 297 and
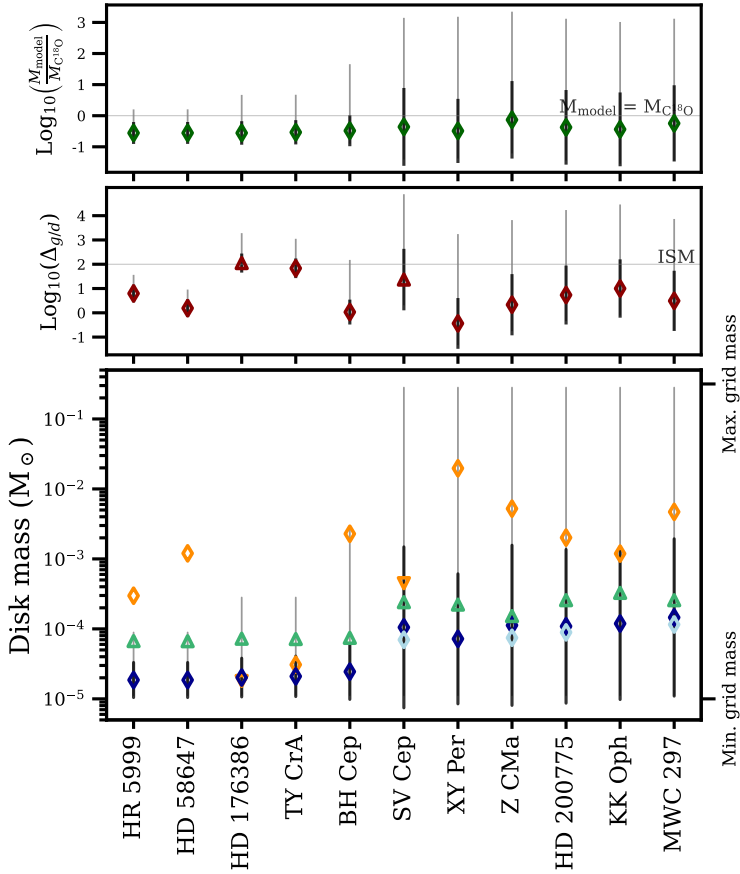
Figure 3.10: Same as Figure 3.7, but now for the disks with only upper limits on the ^{13}CO and $C^{18}O$ fluxes.

SV Cep). Besides non-detections, we also have four disks which have upper limits on their radius, for which we obtain an additional minimum radius to explain the found luminosities, as a decrease in size decreases the luninosity of the disk (see Fig. 3.8). BO Cep has at least a size of 125 au, and HD 139614 and V718 Sco have a size of at least 40 au. For HD 104237 we obtain the most stringent lower limit of 15 au.

Similarly, for HD 245185 and VV Ser, which only have ^{12}CO observations, the mass and radius can also be constrained. ^{12}CO is optically thick for lower disk masses, resulting in the same luminosities for multiple orders of magnitude in mass even for the largest disks. These luminosities can be used to obtain a lower limit on the mass and size of HD 245185. To explain the observed ^{12}CO emission, the disk needs to be at least 125 au in size and have a mass lower limit of 2×10^{-4} $M_\odot$. Due to the non-detection of ^{12}CO for VV Ser, the radius can be relatively well constrained to be less than 220 au in size using the ^{12}CO equivalent to Fig. 3.8.

Lastly, Grant et al. (2023) have shown that the relationship between the accretion rate $\dot{M}$ and dust disk mass is largely flat at $\sim 10^{-7}$ $M_\odot$ yr-1 over three orders of magnitude in dust mass. Hence, some disks have very short inferred disk lifetimes. Our gas mass estimates do not resolve this problem, as the inferred disk masses from our models are either low (see Fig. 3.10), or no observations are available.

3.4.4.4   Cumulative distributions

Figure 3.11 shows cumulative distributions of the dust masses from Stapper et al. (2022), together with the gas masses as found by the models and computed with Eq. (3.4). Following Stapper et al. (2022), we obtained the cumulative distributions using the `Python` package `Lifelines` (Davidson-Pilon et al. 2021). The shaded area indicates the 1σ confidence intervals. The dark blue distribution is made from the mean values in Figs. 3.7 and 3.10. The observed disks for which the range in model disk masses extends down to the lowest mass in our model grid are considered as an upper limit. The dust distribution in orange is obtained by using the dust masses from Stapper et al. (2022) in addition to the five NOEMA targets presented in this work (see Appendix 3.B). The green cumulative distribution is obtained from computing the gas using Eq. (3.4). The dust and gas distributions show a similar slope for the highest mass disks, indicating a relatively constant overestimate of the gas mass, or a constant underestimate of the dust mass. For lower mass disks, the distribution is set by the non-detections, resulting in a leveling-off at a $p \sim 0.7$ of the distribution reflecting the non-detection rate of 31% (11/35).

Using a bootstrapping method (see for details Stapper et al. 2022), a log-normal distribution is fit to the cumulative distributions to obtain a probability distribution, see the middle panel in Fig. 3.11. The fitting results are presented in Table 3.4. The best fit distributions are shown as the solid line. The fainter lines are included to demonstrate the range in possible fits. The dust distribution is slightly shifted toward lower masses when adding the five NOEMA targets, but the confidence intervals still overlap (in Stapper et al. (2022) μ=-2.18±0.05 and σ=0.53±0.07). We find that the mean of the 100× dust mass distribution lies

Table 3.4: Log-normal distribution fit results for the dust and gas mass cumulative distributions shown in Fig. 3.11. The values are in log base 10.

	$M_{\rm disk}$ $(M_\odot)$		$\Delta_{g/d}$	
	μ	σ	μ	σ
Dust ×100	$-2.25^{+0.05}_{-0.05}$	$0.61^{+0.06}_{-0.06}$		
$\overline{M}_{\rm gas,model}$	$-1.55^{+0.06}_{-0.07}$	$0.46^{+0.12}_{-0.10}$	2.70	0.76
$\overline{M}_{\rm gas,model}$ no GI	$-1.75^{+0.05}_{-0.06}$	$0.48^{+0.15}_{-0.18}$	2.50	0.78
Min. $M_{\rm gas,model}$	$-2.49^{+0.18}_{-0.20}$	$0.78^{+0.20}_{-0.17}$	1.76	0.98
$M_{\rm gas,C^{18}O}$	$-3.14^{+0.06}_{-0.07}$	$0.51^{+0.09}_{-0.08}$	1.11	0.79
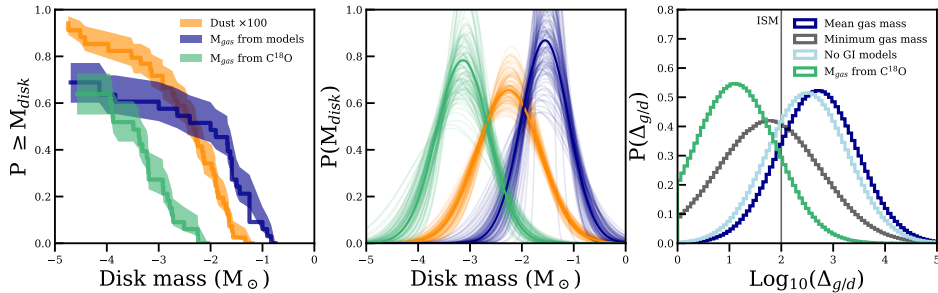
Figure 3.11: Cumulative distributions of the gas masses from Figs. 3.7 and 3.10 obtained from our models (dark blue) and obtained from the $C^{18}O$ flux (green), and dust masses $\times 100$ (orange) from Stapper et al. (2022). The corresponding probability distributions are shown in the middle panel, obtained by fitting a lognormal distribution to the cumulative distributions. The faint lines indicate the possible range in fits. Sampling from the gas and dust distributions a distribution of possible gas-to-dust mass ratios can be made, as shown in the right most panel.

~ 0.7 dex lower than the mean gas mass distribution, indicating that we do find more gas present than what would be assumed given $100\times$ dust mass in most Herbig disks. This was also the observed trend in Figs. 3.7 and 3.10. Removing the gravitational unstable disks only moves the gas masses slightly down and makes the distribution slightly wider, see Table 3.4. The distribution of the minimum gas masses from our models lies ~ 0.2 dex below the mean of the dust mass distribution. Hence, the gas mass is likely higher than this value, consistent with a gas-to-dust ratio of close to or above 100.

To test this, we can sample the distributions obtained by fitting to the cumulative distributions and obtain a gas-to-dust ratio distribution by dividing the resulting gas mass values by the dust masses. After taking 10^7 samples of each distribution, the gas-to-dust ratio distributions in the right panel of Fig. 3.11 are obtained. The canonical value of 100 for the gas-to-dust ratio falls within one standard deviation from the mean values of the different gas distributions obtained from our models. The mean of the gas-to-dust ratio made with the minimum gas mass values from the models differs an order of magnitude with the distribution using the mean gas masses. The gas-to-dust ratio distribution obtained from the gas masses based on the $C^{18}O$ flux is even lower at almost two orders of magnitude lower than those found by our models. This emphasizes the necessity of models to determine the disk mass, otherwise fundamental properties such as the gas-to-dust ratio can be severely underestimated.

Lastly, the higher than 100 gas-to-dust ratio may be originating from either optically thick dust or an increased size of dust grains in these disks. As more mass has grown into larger sized grains, the total mass visible at millimeter wavelengths decreases. The findings by Liu et al. (2022) and Kaeufer et al. (2023) show that an order of magnitude in mass can be hidden in the most massive disks. Taking multiple continuum wavelength dust observations into account our gas mass esti-

mates are indeed close to 100 times the dust mass (Sierra et al. 2021). Thus, this order of magnitude difference between $100\times$ the dust mass and the total disk mass is expected.

3.5 Discussion

3.5.1 Comparison between different CO mass tracers

3.5.1.1 Rare CO isotopologues

Because of the disks in Fig. 3.5 being optically thick in both ^{13}CO and C^{18}O, a different way to measure the different masses of the disks is necessary. To be able to properly do this, one needs to have a handle on the size of the disk and. have an optically thin tracer. Here the rare(r) isotopologues C^{17}O, ^{13}C^{17}O and ^{13}C^{18}O come into play.

Figure 3.12 shows the C^{17}O, ^{13}C^{18}O, and ^{13}C^{17}O $J = 3-2$ luminosities plotted against ^{12}CO $J = 2-1$ of the DALI models, as the observations we compare these to have these transitions available. The optically thick tracer on the horizontal axis gives an indication of the size of the disk, while the optically thinner tracer on the vertical axis gives an indication of the mass of the disk. The same trends (e.g., models of the same mass curve downward for an increase in radius) can be seen as found in Section 3.4.4. For ^{12}CO the smaller disks are now clearly separated into different areas of this parameter space. A clear stratification can be seen in the luminosities of the optically thinner isotopologues, where each mass has its own range in possible luminosities. However, even for these rare isotopologues, the most massive disks ($> 10^{-1.5}$ M$_\odot$) have very similar luminosities. This may be due to the dust opacity playing an important role in reducing the luminosity of the rare isotopologues, which mostly emit from a layer close to the midplane.

We can use observations of rare isotopologues to see if these can assist us in obtaining a better measure of the disk mass. We use the following lines: C^{17}O $J = 3 - 2$ for HD 100546 (priv.comm.), ^{13}C^{18}O $J = 2 - 1$ (Zhang et al. 2020a) and ^{13}C^{17}O $J = 3 - 2$ (Booth et al. 2019) for HD 163296, ^{13}C^{18}O $J = 3 - 2$ (Loomis et al. 2018) for HD 31648, and ^{13}C^{18}O $J = 3 - 2$ (Temmink et al. 2023) for HD 142527. We select the closest 100 models in luminosity around the observations as shown in Fig. 3.12, which reproduce the observed luminosities of the rare isotopologues to within 15%, except for the ^{13}C^{17}O $J = 3 - 2$ line of HD 163296 for which our models predict a factor of three lower luminosity. With these models we obtain ranges of possible disk masses very similar to the lower limits found with ^{13}CO and C^{18}O. For the highest mass models, the luminosities of the very rare isotopologues are still very similar for different mass disks.

However, for compacter lower mass disks ($\lesssim 10^{-2}$), for which no rare isotopologues have been observed yet, the luminosity would result in a well constrained gas mass. Figure 3.13 shows the luminosity of the ^{13}C^{17}O $J = 2 - 1$ transition for different mass disks, selected again for different sizes in ^{12}CO. This Figure shows that the gas mass of a disk, if resolved in ^{12}CO, can be constrained to within an order of magnitude given its ^{13}C^{17}O flux. An integration time of one hour with
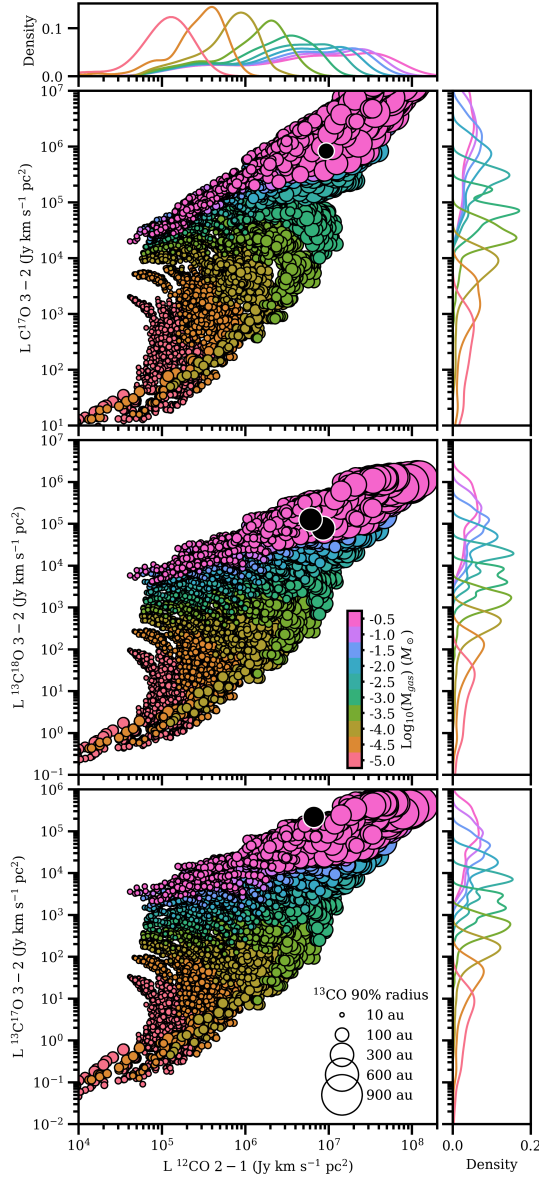
Figure 3.12: Similar to Fig. 3.5, but now with $C^{17}O$, $^{13}C^{18}O$ and $^{13}C^{17}O$ on the vertical axes and ^{12}CO on the horizontal axis. The black dots mark HD 100546 observations of $C^{17}O$ $J = 3 - 2$ (priv.comm.), HD 163296 observations of $^{13}C^{17}O$ $J = 3 - 2$ from Booth et al. (2019), HD 31648 observations of $^{13}C^{18}O$ $J = 3 - 2$ from Loomis et al. (2020), and HD 142527 observations of $^{13}C^{18}O$ $J = 3 - 2$ by Temmink et al. (2023). Similar to Fig. 3.5 probability density curves are shown along the vertical and horizontal axes to indicate where most of the models of a particular mass reside.
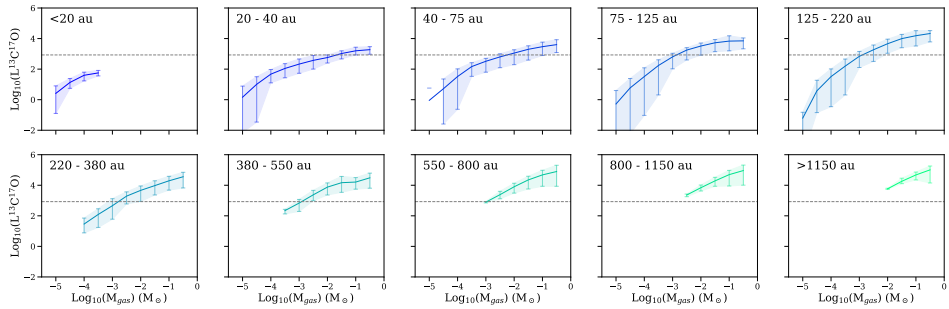
Figure 3.13: Same as Figure 3.8, but for $^{13}C^{17}O$ $J = 2 - 1$. The gray dashed line indicates a typical ALMA 3σ detection of 1 mJy km s^{-1} at a distance of 150 pc, which is achievable within an hour of integration time. The $J = 3 - 2$ transition can be found in Fig. 3.C.2.

ALMA typically gives a sensitivity of 1 mJy km s^{-1} which at 150 pc gives a luminosity of 8.5×10^2 Jy km s^{-1} pc^2. In Fig. 3.13 a 3σ detection is indicated with the dashed gray line. This shows that for the vast majority of disks, typically larger than ~ 300 au (Fig. 3.2) a detection is expected if the disk is more massive than 10^{-3} M$_\odot$ within an hour of observing time.

3.5.1.2   Peeling the disk 'onion'

As the previous section showed, an uncertainty of an order of magnitude is still present when determining the mass of the most massive disks. For some of those massive disks $^{13}C^{17}O$ is only marginally optically thin. Moreover, extrapolating the mass of the disk from the $^{13}C^{17}O$ emission which is mostly detected in the inner parts of the disk may not be accurate for the disk as a whole. Hence, this section explores how the disk gas surface density and mass can be constructed by considering, from the inner disk to the outer disk, a series of CO isotopologues with increasing abundance, from $^{13}C^{17}O$ or $^{13}C^{18}O$ to ^{12}CO. Until now we neglected processes such as radial drift which can enhance the CO/H ratio inside the CO snowline (Zhang et al. 2021), and depleting it outside. This technique is able to take this depletion into account.

The left panel of Figure 3.14 shows a disk model cut into sections of different CO isotopologues. The outer parts of the disk consist of the most abundant isotopologue, ^{12}CO. The closer to the star, the rarer the isotopologue to ensure that the tracer stays as optically thin as possible. The regions are determined by the $R_{90\%}$ radii of the isotopologues. The right panels show the abundance of the six CO isotopologues looked at in this work, together with their $\tau = 1$ lines and areas within which 50% and 95% of the emission is coming from.

Using Eq. (3.4) we compute the mass of each shell and add those together to obtain a measure of the mass of the disk. We obtain a total mass of 0.05 M$_\odot$ when combining the four regions shown in Fig. 3.14, which is a quarter of the mass of the model. This recovered mass comprises for 97% by mass out of $^{13}C^{18}O$, with
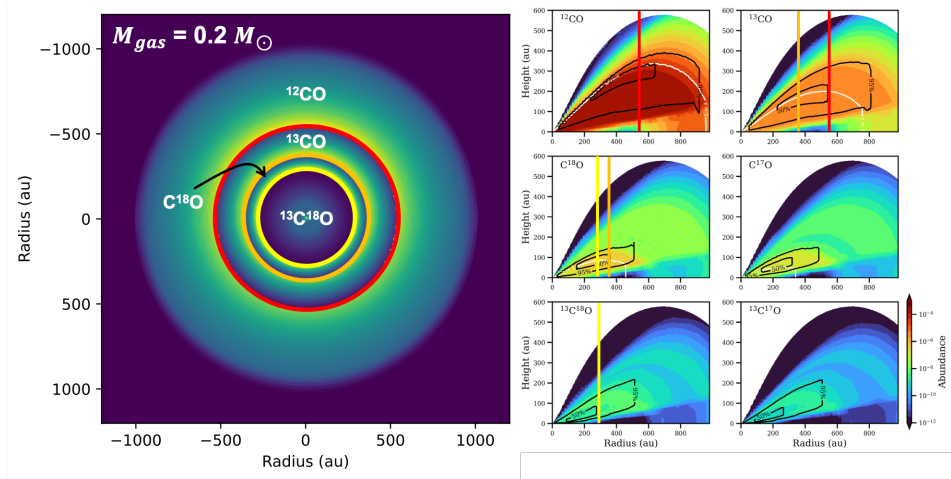
Figure 3.14: DALI model with a mass of 0.2 M$_\odot$. The disk is divided into rings based on the $R_{90\%}$ of the isotopologue. The rarest isotopologue (^{13}C^{18}O) is in the center, while ^{12}CO is in the outer ring. The six panels on the right show the abundance of the six ray-traced CO isotopologues. The vertical colored lines correspond to the colors of the circles on the left. The white lines indicate the $\tau = 1$ surface, and the black lines indicate where 50% and 95% of the emission is coming from.

the last 3% made up of ^{13}CO due to the larger emitting area. ^{12}CO does not contribute any significant amount due to either high optical thickness or weak emission at large radii. Changing the rarest isotopologue into ^{13}C^{17}O does not change the estimated mass, for it is still dominated by the rarest isotopologue.

Doing the same analysis on the HD 163296 and HD 142527 disks, using an excitation temperature of 40 K (based on the bottom panel of Fig. 3.9) and the rare isotopologue observations by Booth et al. (2019) and Temmink et al. (2023), a mass of respectively 0.05 M$_\odot$ and 0.18 M$_\odot$ were found. This is a factor of three lower than what has been found in MAPS for HD 163296 (Zhang et al. 2021), and based on the spiral present one would expect a factor of 1.5 higher disk mass for HD 142527 (Yu et al. 2019). However, these masses are consistent with those found using ^{13}CO and C^{18}O, see Figure 3.7.

In conclusion, rare isotopologues do trace the overall disk mass better than C^{18}O. However, more modeling of these rare isotopologues needs to be done to properly use them.

3.5.2 Comparison to other disk populations

3.5.2.1 T Tauri disks

Herbig disks are expected to be warmer than T Tauri disks, therefore causing less CO depletion due to freeze-out. Using the dust mass estimates from Ansdell et al. (2016) for Lupus and Pascucci et al. (2016) for Chameaeleon I together
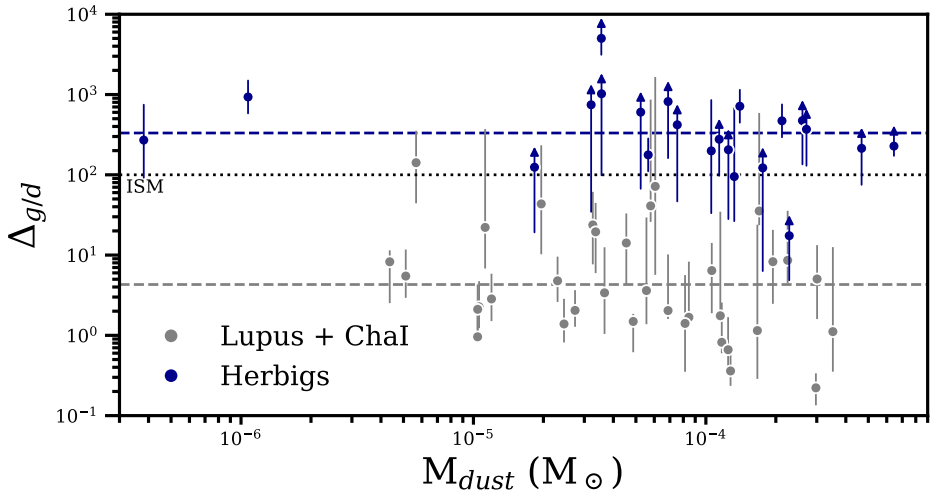
Figure 3.15: Gas-to-dust ratio of the Herbig disks compared to T Tauri disks in Lupus and Chamaeleon I (Ansdell et al. 2016; Pascucci et al. 2016; Miotello et al. 2017; Long et al. 2017). The corresponding horizontal dashed lines are the logarithmic mean values. The canonical value of 100 is indicated as the horizontal black dotted line.

with the gas mass estimates by Miotello et al. (2017) and Long et al. (2017) (who use the models from Miotello et al. 2016), gas-to-dust ratios of T-Tauri disks are obtained. Figure 3.15 shows these gas-to-dust ratios plotted against the inferred dust masses together with the gas-to-dust ratios obtained for the Herbig disks. This comparison is also done in Miotello et al. (2023), but we increase the number of Herbigs by more than a factor of two.

As was mentioned before, the mean gas-to-dust ratio of the Herbig disks lies above the canonical ISM value of 100, but many of the disks are still consistent with a gas-to-dust ratio of 100. The T Tauri disks on the other hand lie at least an order of magnitude below the gas-to-dust ratio of the ISM. Moreover, the data shown in Fig. 3.15 only includes detected disks. The many non-detections among the T Tauri disks suggests a lack of CO gas in these disks. The fact that orders of magnitude differences in the gas-to-dust ratio are found, over multiple orders of magnitude in dust mass, confirms the expectation that the warmer Herbig disks lack the CO-conversion processes that occur in the cold T Tauri disks.

3.5.2.2   Group I versus group II

Herbig disks can be separated into two different groups based on their spectral energy distribution (SED): group I have a rising SED in the far-infrared, while group II disks do not (Meeus et al. 2001). Stapper et al. (2022) showed a difference in disk dust mass between group I and group II disks, where the group II disks have a dust distribution very similar to T Tauri disks. Moreover, group I disks are generally large disks with large cavities (transition disks), while group II disks are
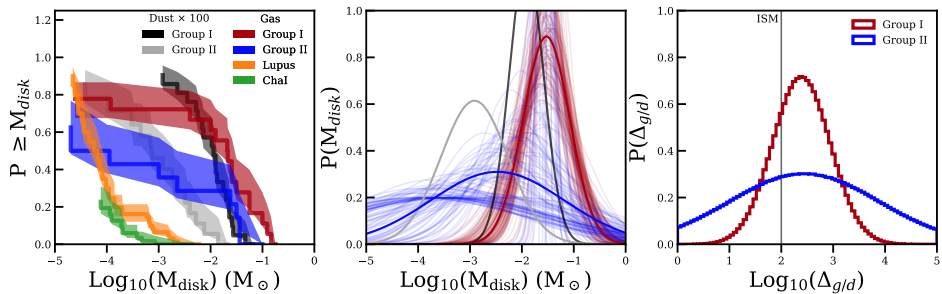
Figure 3.16: Cumulative distributions of the dust and gas masses of the Herbigs sepa-
rated into group I and group II. The dust distributions are shown in the left and middle
panel in dark gray for group I and light gray for group II. In addition, the gas distri-
butions from Lupus (orange) and Chamaeleon I (green) is shown (Miotello et al. 2017;
Long et al. 2017). The fitted probability distributions are shown in the middle panel.
The resulting gas-to-dust ratios are presented in the right panel.

Table 3.5: Log-normal distribution fit results for the dust and gas mass cumulative
distributions shown in Fig. 3.16. The values are in log base 10.

	M_{disk} $(M_\odot)$		$\Delta_{g/d}$	
	μ	σ	μ	σ
Group I				
Dust $\times 100$	$-1.91^{+0.05}_{-0.05}$	$0.33^{+0.06}_{-0.06}$		
$\overline{M}_{gas,model}$	$-1.53^{+0.08}_{-0.08}$	$0.45^{+0.10}_{-0.10}$	2.39	0.56
Group II				
Dust $\times 100$	$-2.91^{+0.14}_{-0.17}$	$0.65^{+0.16}_{-0.14}$		
$\overline{M}_{gas,model}$	$-2.47^{+0.85}_{-1.11}$	$1.29^{+0.71}_{-1.01}$	2.44	1.44

more compact (Stapper et al. 2022; Garufi et al. 2017).

Similar to the distributions in Fig. 3.11, we can obtain cumulative distributions
for the separate groups as well, see Fig. 3.16. Both the gas distributions in red
(group I) and blue (group II), and the dust distributions in dark gray (group I)
and light gray (group II) are shown. The dust mass distributions are relatively
well constrained, while the gas distributions much less so. The gas distributions
are shown in the left most panel in Fig. 3.16 for Lupus (orange; Miotello et al.
2017) and Chamaeleon I (green; Long et al. 2017).

Comparing the group I and group II disks, the group II disks are less massive
than the group I disks, which is consistent with their dust masses. The probability
distributions show an offset in the mean of the distribution of an order of magnitude
for both dust and gas (see Table 3.5). Hence, regardless of the differences in dust
and gas masses between the two groups, the relative gas-to-dust ratio remains the
same. As the right most panel of Fig. 3.16 shows, the mean of the gas-to-dust ratio
distributions are very similar (see Table 3.5). While Stapper et al. (2022) found

that the group II disks have a very similar dust mass distribution as T Tauri disks, compared to group I disks they have an order of magnitude lower dust mass. We find here that the gas distribution of the group II disks is shifted toward lower gas masses compared to the group I disks by the same factor (see Table 3.5). This further supports that the gas-to-dust ratio is disk mass independent and rather a result from differences in temperature compared to T Tauri disks.

Some group I disks have been found to have little to no CO depletion (e.g., HD 100546 Booth et al. 2023a, HD 169142 Carney et al. 2018; Booth et al. 2023b), while group II disks do in the outer disk (Zhang et al. 2021). As discussed in Stapper et al. (2022), group I disks show in general large cavities in millimeter emission, while group II disks are more compact. These differences in CO depletion between the two groups could indicate a much higher impact due to radial drift where most CO stayed in the outer disk for group I disks and the CO drifted inward for group II disks. This is further supported by observations of the metallicities of the hosting Herbig stars (Kama et al. 2015; Guzmán-Díaz et al. 2023), for which low metallicities generally coincide with group I disks. Hence, group I disks might be the formation sites of giant exoplanets stopping radial drift, stopping the enrichment of the host star, trapping CO in the outer disk, and creating the quintessential large cavity structure often associated with these disks. The fact that we find higher gas masses of group I disks compared to group II disks only further supports this hypothesis.

Regarding the sizes of the group I and group II disks, Brittain et al. (2023) report a comparison of the ^{13}CO and dust radii for 17 Herbig disks. They find that the group II disks are the smallest disks in both gas and dust and that in general the ratio between the dust and gas radii are consistent with the Lupus disks. Using ^{12}CO radii we do not report a similar difference between the two groups in gas observations (see Fig. 3.4) as most of the smallest disks lack any detection of ^{12}CO. Hence, this remains inconclusive. A uniform survey of Herbig disks would help in characterizing these differences.

3.5.2.3   Debris disks

Debris disks are the final stage of planet-forming disks and are sustained by collisional processes producing secondary dust (Hughes et al. 2018). In contrast to later spectral type stars, debris disks around A-type stars (i.e., the evolutionary successors of Herbig disks) are more common to be detected in CO gas compared to later spectral type stars (e.g., Moór et al. 2017, 2020). Whether this is primordial or secondary gas is still heavily debated (see for an overview Hughes et al. 2018). What has been found is that the amount of CO mass in the (debris) disks around A-type stars rapidly decreases between Herbig disks and debris disks around A-type stars (e.g., Moór et al. 2020). In this section we compare the CO masses found by Moór et al. (2020) and Cataldi et al. (2023) to the disk masses we obtained for Herbig disks.

Using the previously adopted CO isotopologue and CO/H_2 ratios, we compute the total disk mass from the CO mass estimates by Moór et al. (2017), see Figure 3.17. Moór et al. (2020) showed that most debris disks with an A spectral type
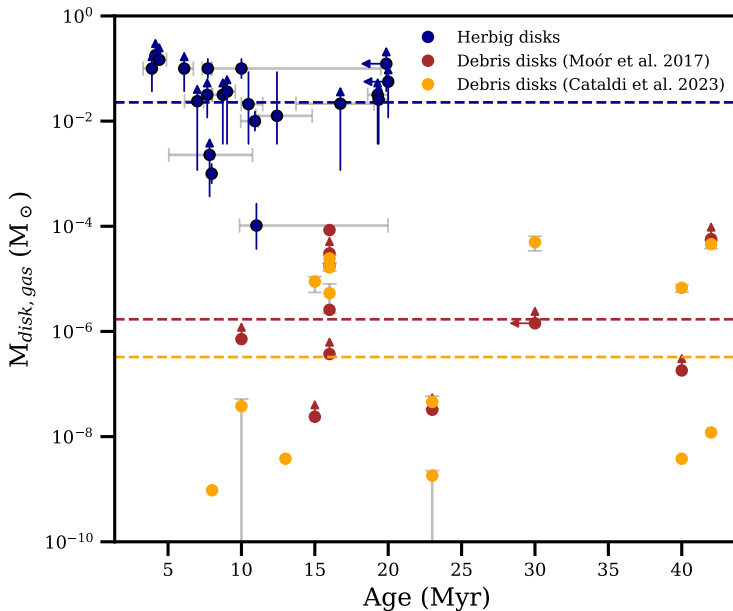
Figure 3.17: Comparison of the gas masses and ages of debris disks from Moór et al. (2017) and Cataldi et al. (2023) to our Herbig disk gas masses. The horizontal lines indicate the logarithmic means.

are two orders of magnitude less massive than Herbig disks in CO. Here we show that this difference may be even more dramatic, with a difference between the logarithmic means of the two population of four orders of magnitude. In Figure 3.17 we additionally show the LTE models from Cataldi et al. (2023) who modeled the CO and CI emission of 14 debris disks to obtain a CO mass in the disk. After converting these into total disk mass, large differences between the Herbig disks and the debris disks can be seen, as is the case for the masses from Moór et al. (2017). The fact that few disks are in between the Herbig disks and debris disks suggests that the disk needs to dissipate quickly over just a few million years.

Lastly we note that if the disk consists of second generation gas, the assumption of $CO/H_2=10^{-4}$ might not be correct and should rather be closer to one, but the assumption does give an upper limit on the gas mass in the disk. In the case of $CO/H_2=1$ the debris disk masses shown in Fig. 3.17 are even lower.

3.5.3 Viscous or wind driven evolution

Finally, we discuss the viscous versus wind driven evolution of disks. Wind signatures have been found in embedded disks but for later stage disks, in particular Herbig disks, direct evidence for a disk wind has only been found in HD 163296 in ^{12}CO and ^{13}CO (Klaassen et al. 2013; Booth et al. 2021). As our work has compiled all Herbig disks with CO observations available, we present in this section

the results of a search for wind signatures in other Herbig disks.

Following previous works (Klaassen et al. 2013; Booth et al. 2021), the search for wind signatures is done with visibility spectra. To ensure that the visibility spectrum is dominated by the large-scale structure of the wind, only the short baselines are selected. The 20% shortest baselines are used for the analysis, with two exceptions: AK Sco and HD 142666. Due to their relatively high resolution, a lower percentage is chosen such that all baselines smaller than respectively 80 and 100 meter are selected, corresponding to spatial scales of $\sim 2.0''$. To obtain the visibility spectra, the time and baselines are averaged to obtain a better S/N. The velocity is sampled from around -50 km s^{-1} to 50 km s^{-1} relative to the system velocities, so that all the possible disk wind channels can be covered (Pascucci et al. 2022).

No wind signatures have been found, either due to low-quality data or no presence of a disk wind. To assess this we obtain a measure of the noise from the visibility spectra of each disk scaled by the square-root of the velocity resolution relative to that of the HD 163296 observation. Using the estimate of the total mass of the disk wind from Booth et al. (2021) of 10^{-3} M$_\odot$ and the peak flux in their spectrum of 0.14 Jy in ^{13}CO, we can scale the upper limits of 5$\times$ the noise with the distance to the object relative to HD 163296 (see Table 3.1), assuming that CO/H$_2$ is not different in each disk wind. This results in an upper limit on the disk wind in Earth masses for each disk. Figure 3.18 presents the results.

The upper limits on the majority of the disks fall below the mass of the disk wind of HD 163296. Of these disks, a third have accretion rates lower than HD 163296 (see the red scatter points, from Guzmán-Díaz et al. 2021). This could result in the non-detections as a stronger disk wind induces a higher accretion rate. For these disks we can rule out the sensitivity of the data being the
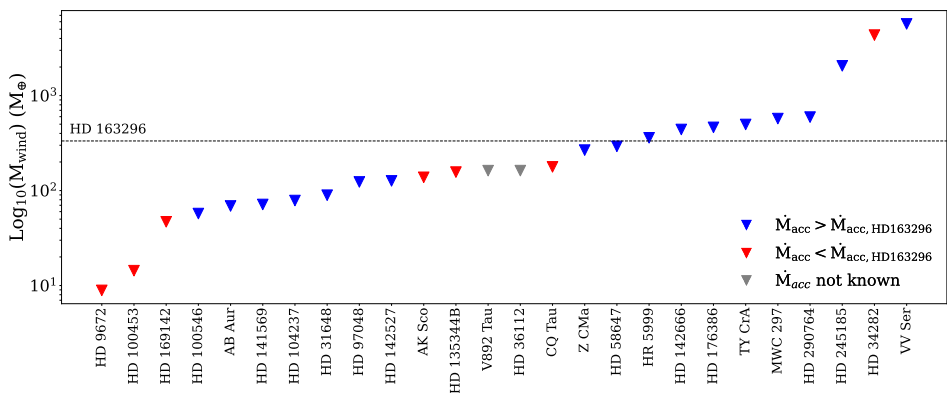
Figure 3.18: Upper limits on the disk wind mass. The mass of the disk wind of HD 163296 is shown as the dotted horizontal line (Booth et al. 2021). Disks which have an accretion rate higher or lower than that of HD 163296 are shown as blue or red respectively (Guzmán-Díaz et al. 2021). HD 34282 has a lower limit on its accretion rate. Disks with no accretion rate measured are shown in gray.
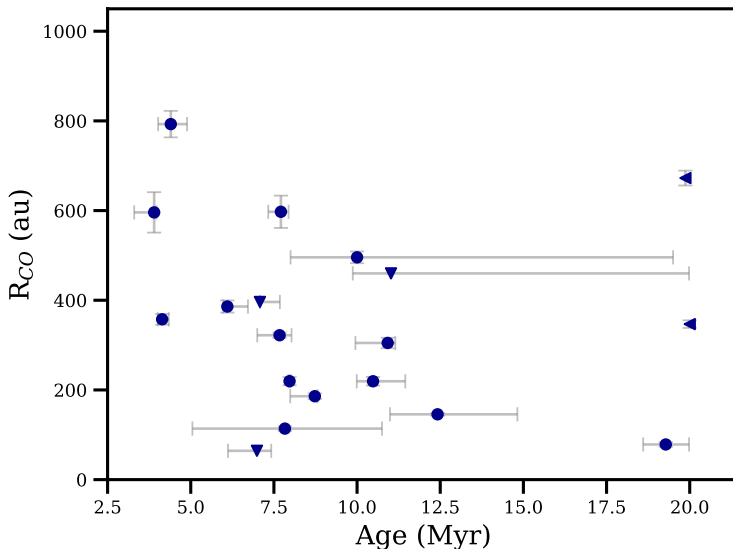
Figure 3.19: Gas radii ($R_{90\%}$) of the Herbig disks plotted against the age of the system (from Guzmán-Díaz et al. 2021). The downward facing triangles indicate an upper limit on the gas radius, an upper limit on the age is indicated as a left facing triangle.

main reason for not detecting a disk wind similar to that of HD 163296. On the other hand, nine disks have upper limits above the mass of HD 163296, which does indicate a lack of sensitivity and a disk wind similar to that of HD 163296 could possibly still be present.

Comparing these results to the gas masses found in Section 3.4.4, it is clear that only a few disks are likely more massive than HD 163296, most of which have a better upper limit on the disk wind mass than lower mass disks. For example HD 290764 and HD 245185 may be good candidates for deeper follow-up surveys of disk winds in Herbig disks due to their high gas mass and accretion rates, but relatively high upper limits. Another option would be HD 34282, which has a high disk mass but a lower accretion rate compared to HD 163296. Notably, Pegues et al. (2023) identify a tentative extended structure in ^{12}CO in HD 34282, while not seen in our data this further substantiates a follow-up. For some other disks such as HD 142666 longer and lower resolution observations to obtain better short baseline coverage and higher sensitivities would also be useful in order to confirm a lack of disk wind signatures.

Using the gas radii in combination with the ages from Guzmán-Díaz et al. (2021), we determine if the radii of Herbig disks evolve over their lifetime, and if so, whether a specific evolutionary scenario is favorable. Viscously evolving disks are expected to increase in size over time, while wind driven evolution results in a reduction of the size of the disk (e.g., Manara et al. 2022). Trapman et al. (2022) modeled the evolution of the CO radius in the wind driven case, showing that the size of the disk is indeed expected to decrease in this specific tracer. Though effects

of external photoevaporation are important to keep in mind (Trapman et al. 2023). Figure 3.19 shows the gas radius plotted against the age of the system. The Herbig disks younger than 12 Myr do seem to correspond well with the wind evolution shown by Trapman et al. (2022), the largest and highest mass disks decrease in size by a factor of ~ 4 between 2 and 10 Myr. For the three disks on the right hand side of Fig. 3.19, two (HD 34282 and HD 169142) only have upper limits on their age. However, other works do put these at younger ages of ~ 10 Myr (e.g., Vioque et al. 2018). Samples of older ages are missing, which is needed to constrain the specific evolutionary scenario. More sensitive observations of a larger sample are needed to make progress.

3.6   Conclusion

In this work we analyze the ^{12}CO ,^{13}CO and C^{18}O $J = 2-1$ or $J = 3-2$ emission in 35 Herbig disks, 30 with ALMA archival data and five new datasets observed with NOEMA. We compare the integrated line luminosities and R$_{90\%}$ radii of ^{12}CO and ^{13}CO with a large grid of `DALI` models (Bruderer et al. 2012; Bruderer 2013) to obtain a measure of the gas mass. We can conclude the following:

1. We detect ^{12}CO emission in 20 out of the 27 disks which have the line covered, for ^{13}CO in 22 disks out of 33 disks, and for C^{18}O in 21 disks out of 33 disks. In total, 15 disks are resolved in ^{12}CO, 16 in ^{13}CO, and 15 in C^{18}O. For all resolved disks, the ^{12}CO emission extends to larger radii compared to ^{13}CO, which in turn is larger than the C^{18}O disk.

2. The main model parameters affecting the luminosities of the ^{13}CO and C^{18}O lines in the models are the mass and size of the disk. In addition, the power-law index of the surface density affects the line luminosities due to changing the distribution of the mass in the disk. For the most massive disks we find that the effect of the stellar luminosity, the vertical distribution of the disk mass, and the inclination of the disk have negligible impact on the line luminosities. For low mass disks however, increasing the vertical distribution and stellar luminosity decreases the luminosity of the isotopologue lines by one to two orders of magnitude.

3. The two deciding processes influencing the line luminosity of the disk is are the line optical depth as seen from the observer and the self-shielding capacity of the CO isotopologues. Hence, one can make disks with similar luminosities with very different masses if the disk is optically thick in both ^{13}CO and C^{18}O. When enlarging the disk, first C^{18}O becomes optically thin and starts to photodissociate, reducing the C^{18}O line luminosity. At even larger sizes, ^{13}CO becomes optically thin as well and subsequently its luminosity reduces.

4. We find that most of the detected Herbig disks are optically thick in both ^{13}CO and C^{18}O. For almost all disks we can only find a lower disk mass which can reproduce the observed line luminosities. The R$_{90\%}$ size of the

disk is an essential observable to constrain the gas mass, as only the most massive disks can be large in ^{12}CO.

5. Comparing the gas masses to those obtained from the number of C^{18}O molecules with a simple CO/H$_2$ conversion shows that the disk mass is generally underestimated by at least an order of magnitude. This shows that to obtain the mass of a disk, modeling the disk is vital.

6. Combining the gas masses of the disks with the dust masses from Stapper et al. (2022), we find that Herbig disks are consistent with the canonical gas-to-dust ratio of 100. In general the ratio is even higher, which may be caused by a combination of dust optical depth and grain growth.

7. Comparing the gas radii with the dust radii from Stapper et al. (2022) we find a ratio of 2.7, higher compared to the disks in Lupus (a factor of 2.0, Ansdell et al. 2018). Still, the majority of the disks fall well below the factor of four, indicating that this difference may only be due to line optical depth effects rather than radial drift.

8. To distinguish different disk masses for optically thick disks, a combination of ^{12}CO tracing the size of the disk and ^{13}C^{17}O tracing the mass of the disk would make this possible for a large range in masses of disks. However, for the most massive disks dust opacity may inhibit tracing the disk mass with such a rare isotopologue.

9. Comparing the Herbig gas-to-dust ratios with those in T Tauri disks (Ansdell et al. 2016; Pascucci et al. 2016; Miotello et al. 2017; Long et al. 2017), we find that Herbig disks have a gas-to-dust ratio of almost two orders of magnitude higher over a range of multiple orders of magnitude in dust mass. Hence, this disparity could be caused by a fundamental difference in chemistry due to Herbig disks being much warmer, as proposed in previous works.

10. The gas and dust masses of the two different Meeus et al. (2001) groups are found both differ by an order of magnitude. This results in the same gas-to-dust ratios for both groups, even though group II disks have similar dust masses as T Tauri disks (Stapper et al. 2022). This further supports the idea that the gas-to-dust ratio is disk mass independent and that the lack of CO emission in T Tauri disks is not due to their lower mass disks, but rather a temperature difference compared to Herbig disks.

11. The total masses of debris disks are found to be at least four orders of magnitude lower than those of Herbig disks, indicating a rapid dissipation of the material in the disk within a few Myr. Full chemical modeling of debris disks is necessary to explore this further.

12. A search for disk wind signatures such as those found for HD 163296 (Booth et al. 2021) in the ^{12}CO data has resulted in no additional detections. Most disks have sufficiently sensitive data in which a disk wind analogous to that in HD 163296 would have been detected. This lack of disk wind may be in some of the disks related to a difference in accretion rate.

13. Comparing the gas radii to the age of the system we find that the data seem to support a disk wind driven evolution, but data of older age systems are lacking.

In conclusion, the warmer Herbig disks have significantly larger gas-to-dust mass ratios compared to the colder T Tauri stars, close to, or exceeding, the canonical value of 100.

Appendix

3.A Datasets used

In Table 3.A.1 the project codes of the used datasets are listed together with their spatial and velocity resolution and the line-free rms noise.

Table 3.A.1: Datasets and corresponding parameters for each Herbig disk. The rms noise is for a line-free channel at the given velocity resolution. When the CO isotopologue observations are coming from different projects, multiple project codes are listed. The ^{13}CO and project code columns are on the next page.

Name	^{12}CO Spat.res. ($''$)	Vel.res. (km s^{-1})	rms (mJy beam^{-1})	^{13}CO Spat.res. ($''$)	Vel.res. (km s^{-1})	rms (mJy beam^{-1})
AB Aur	0.39 × 0.28 (10°)	0.20	16.83			
				1.14 × 0.70 (14°)	0.20	5.67
AK Sco	0.15 × 0.11 (-63°)	1.00	1.35	0.16 × 0.12 (-63°)	1.00	1.53
CQ Tau	0.11 × 0.08 (18°)	0.32	1.53	0.12 × 0.09 (26°)	0.66	1.32
HD 100453	0.29 × 0.21 (40°)	0.20	3.26	0.31 × 0.23 (39°)	0.20	2.74
HD 100546	0.27 × 0.17 (-85°)	0.20	3.65	0.27 × 0.19 (-10°)	0.20	3.44
HD 104237	0.31 × 0.22 (-12°)	0.70	3.28	0.32 × 0.22 (-14°)	0.70	2.43
HD 135344B				0.34 × 0.30 (75°)	0.20	7.64
	0.36 × 0.29 (-68°)	0.20	11.79			
HD 139614				0.79 × 0.60 (-49°)	0.40	12.13
HD 141569	0.41 × 0.33 (-61°)	0.42	5.99			
				0.76 × 0.66 (82°)	0.40	15.19
HD 142527	0.93 × 0.81 (-85°)	0.20	6.35	0.97 × 0.84 (-87°)	0.20	6.68
HD 142666				1.05 × 0.82 (87°)	0.20	16.18
	0.21 × 0.20 (-70°)	0.32	2.27			
HD 163296	0.65 × 0.56 (71°)	0.20	3.63	0.68 × 0.59 (68°)	0.20	2.98
HD 169142	0.37 × 0.31 (-77°)	0.20	3.61	0.39 × 0.33 (88°)	0.20	3.67
HD 176386	0.40 × 0.30 (77°)	0.30	17.88	0.42 × 0.31 (79°)	0.30	17.33
HD 245185	0.42 × 0.39 (-85°)	0.70	8.05			
HD 290764	0.08 × 0.07 (-80°)	1.00	2.04			
				0.21 × 0.14 (-62°)	1.00	1.60
HD 31648	1.16 × 0.88 (15°)	0.20	7.35	1.22 × 0.92 (13°)	0.20	7.64
HD 34282	0.27 × 0.24 (68°)	0.20	4.50	0.28 × 0.27 (63°)	0.20	3.32
HD 36112	0.19 × 0.14 (-17°)	1.40	1.56	0.20 × 0.15 (-16°)	1.40	1.90
HD 58647	0.54 × 0.45 (73°)	0.20	6.03	0.64 × 0.54 (74°)	0.20	4.69
HD 9672	1.70 × 1.15 (-75°)	0.64	3.61	1.75 × 1.25 (-75°)	0.66	3.92
HD 97048	1.22 × 0.76 (-31°)	0.30	7.81	1.30 × 0.79 (-32°)	0.30	7.17
HR 5999	0.28 × 0.27 (87°)	0.40	12.62	0.29 × 0.29 (-82°)	0.40	12.86
KK Oph				0.77 × 0.68 (73°)	0.40	28.90
MWC 297	0.41 × 0.36 (71°)	0.20	7.29	0.43 × 0.38 (74°)	0.20	5.83
TY CrA	0.40 × 0.30 (78°)	0.30	17.60	0.42 × 0.31 (78°)	0.30	17.60
V718 Sco				1.01 × 0.82 (-67°)	0.40	10.52
V892 Tau	0.26 × 0.19 (4°)	0.32	21.12	0.27 × 0.19 (4°)	0.66	5.57
VV Ser	1.73 × 1.21 (-63°)	0.40	34.83			
Z CMa	0.22 × 0.20 (-78°)	0.20	5.55	0.23 × 0.21 (-79°)	0.20	6.15
BH Cep				1.10 × 0.82 (31°)	0.40	9.42
BO Cep				1.03 × 0.85 (64°)	0.40	11.31
HD 200775				1.09 × 0.85 (51°)	0.40	11.47
SV Cep				1.01 × 0.83 (71°)	0.40	10.83
XY Per				1.09 × 0.66 (8°)	0.40	10.33

Table 3.A.1: Continued.

C^{18}O			
Spat.res. ($''$)	Vel.res. (km s^{-1})	rms (mJy beam^{-1})	Project codes
			2012.1.00303.S*
1.14 × 0.71 (13°)	0.20	4.57	2019.1.00579.S
0.16 × 0.13 (-75°)	1.00	0.95	2016.1.00204.S
0.12 × 0.09 (25°)	0.67	0.91	2017.1.01404.S
0.30 × 0.22 (38°)	0.20	2.05	2015.1.00192.S
0.27 × 0.19 (-10°)	0.20	2.61	2016.1.00344.S
0.32 × 0.22 (-13°)	0.70	1.92	2017.1.01419.S
0.35 × 0.30 (84°)	0.20	10.43	2012.1.00158.S*
			2012.1.00870.S
0.81 × 0.60 (-47°)	0.40	8.03	2015.1.01600.S
			2012.1.00698.S*
0.72 × 0.67 (-66°)	0.40	10.91	2015.1.01600.S
0.98 × 0.85 (-88°)	0.20	4.92	2015.1.01353.S
1.04 × 0.85 (87°)	0.20	10.46	2015.1.01600.S
			2016.1.00484.L
0.69 × 0.59 (72°)	0.20	2.11	2018.1.01055.L
0.39 × 0.33 (-85°)	0.20	2.64	2016.1.00344.S
0.42 × 0.31 (78°)	0.30	14.01	2015.1.01058.S
			2017.1.00466.S
			2015.1.00986.S*
0.23 × 0.14 (-63°)	1.00	2.06	2017.1.01607.S*
1.22 × 0.92 (14°)	0.20	5.89	2016.1.00724.S
0.28 × 0.27 (59°)	0.20	2.46	2015.1.00192.S
0.20 × 0.15 (-16°)	1.40	1.28	2017.1.00940.S
0.65 × 0.55 (77°)	0.20	3.87	2018.1.00814.S
1.78 × 1.20 (-74°)	0.67	2.93	2018.1.01222.S
1.31 × 0.80 (-31°)	0.30	5.89	2015.1.00192.S
0.29 × 0.29 (-74°)	0.40	9.57	2015.1.00222.S
0.68 × 0.63 (-61°)	0.40	11.98	2015.1.01600.S
0.43 × 0.38 (75°)	0.20	4.65	2018.1.00814.S
0.42 × 0.31 (77°)	0.30	13.67	2015.1.01058.S
0.99 × 0.85 (-63°)	0.40	8.00	2015.1.01600.S
0.28 × 0.20 (5°)	0.67	3.93	2013.1.00498.S
			2019.1.00218.S
0.23 × 0.21 (-76°)	0.20	4.68	2016.1.00110.S
1.11 × 0.82 (32°)	0.40	9.61	S21AS
1.04 × 0.85 (61°)	0.40	10.77	S21AS
1.09 × 0.86 (51°)	0.40	11.24	S21AS
1.01 × 0.84 (70°)	0.40	10.69	S21AS
1.10 × 0.66 (8°)	0.40	10.44	S21AS

Notes. The Project codes with an asterisk are for the $J = 3 - 2$ transition, all others are for the $J = 2 - 1$ transition.

3.B   NOEMA continuum data

Figure 3.B.1 presents the continuum images of the five northern Herbig disks observed with NOEMA during the summer semester of 2021 (PI: Cridland, Booth; Project code: S21AS). XY Per was observed on the 17th of November 2021, for 3.4 hours. Both the bandpass and gain calibrator used was 3c84, while the flux calibrator was MWC349. BH Cep, BO Cep, HD 200775, and SV Cep were observed on the 18th of October, for 1.6 hours. The bandpass calibrator was 3C454.3, the gain calibrator was 2010+723, and the flux calibrator was MWC349. The observations were done in the C configuration, with nine antennas.

The data imaging was done using the `Common Astronomy Software Applications` (CASA) version 5.8.0 (McMullin et al. 2007). For the data one round of phase-only self-calibration was done. After applying the resulting calibration table to all spectral windows, the data were cleaned using the `hogbom` algorithm and imaged using the multifrequency synthesis spectral definition mode and a Briggs robust weighting of 0.5. The resulting beam and rms of each continuum observation can be found in Table 3.B.1. Four out of five Herbig disks have been detected. XY Per is a binary with the A component being a Herbig star.

The integrated fluxes and their corresponding dust masses obtained by following the same procedure as Stapper et al. (2022) can be found in Table 3.B.1. Because the disks are unresolved, the median upper limits on their size are 245 au and 373 au for the 68% and 90% radii respectively. Comparing the dust masses to the distribution found by Stapper et al. (2022), we find that only BO Cep is more massive than the mean dust mass, which is likely related to it being the only disk in our sample observed with NOEMA for which the ^{13}CO and C^{18}O isotopologues are detected. XY Per is slightly less massive than the mean dust mass from Stapper et al. (2022), but still well above the dust mass for which we still detect the CO isotopologues, which we do not detect in this disk possibly caused by the binary nature of this object. SV Cep and HD 200775 both have relatively low disk masses. Interestingly, in the mid-infrared HD 200775 was found to have diffuse emission going out to ~ 700 au ($2''$, corrected for the most recent
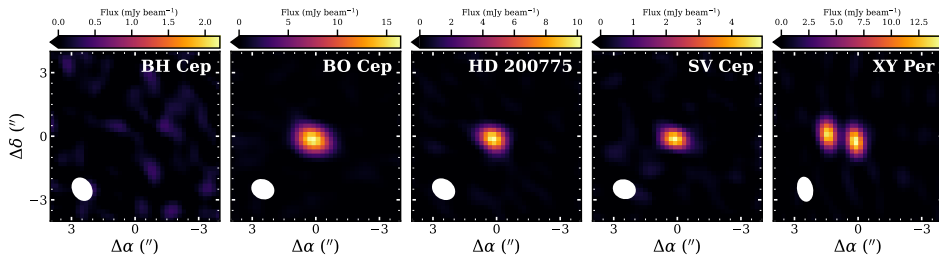
Figure 3.B.1: Continuum images of the five northern Herbig disks observed with NOEMA.

Table 3.B.1: Northern Herbigs continuum data parameters, flux measurements, and mass estimates observed with NOEMA.

Name	Spat.res. ($''$)	rms mJy beam^{-1}	Flux (mJy)	Dust mass ($M_\oplus$)
BH Cep	1.05×0.80 (31°)	0.34	<1.0	<1.5
BO Cep	1.00×0.82 (67°)	0.33	25.7	59±6
SV Cep	0.98×0.80 (73°)	0.37	5.4	6.7±0.7
HD 200775	1.05×0.81 (54°)	0.49	10.7	4.0±0.4
XY Per	1.07×0.64 (10°)	0.73	15.5	16±1.6

distance estimate) in both north and south direction, and a large tail extending to the north-east ($\sim 10''$, Okamoto et al. 2009). We do not resolve the continuum emission with a beam of $1.1'' \times 0.8''$, and thus also do not see any of these structures. Lastly, for BH Cep we determined an upper limit on the dust mass of 1.5 $M_\oplus$ which is higher than some of the detection made by ALMA (Stapper et al. 2022).

3.C   Figures for the $J = 3 - 2$ transition

Figure 3.C.1 presents the data and models for the $J = 3 - 2$ transition, similar to Fig. 3.5. The two disks plotted are HD 135344B and HD 290764. Figures 3.C.2 and 3.C.3 are the same as Figs. 3.8 and 3.13 respectively but for the $J = 3 - 2$ transition.
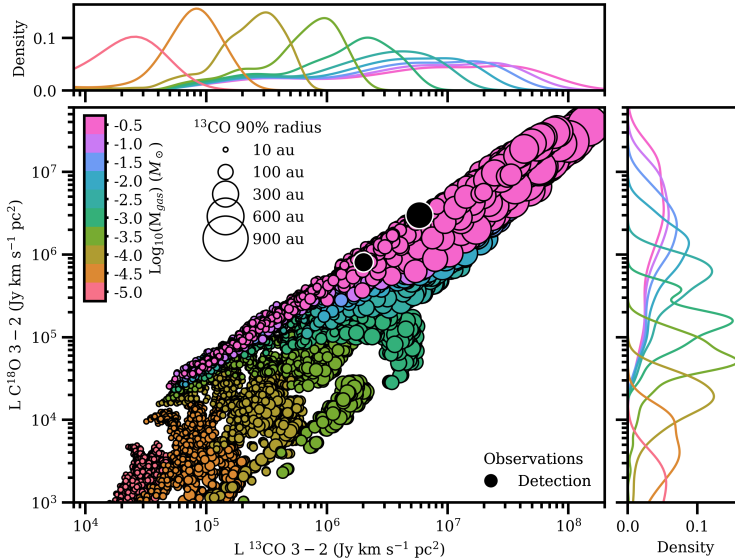
Figure 3.C.1: Same as Figure 3.5, but for the $J = 3 - 2$ transition.
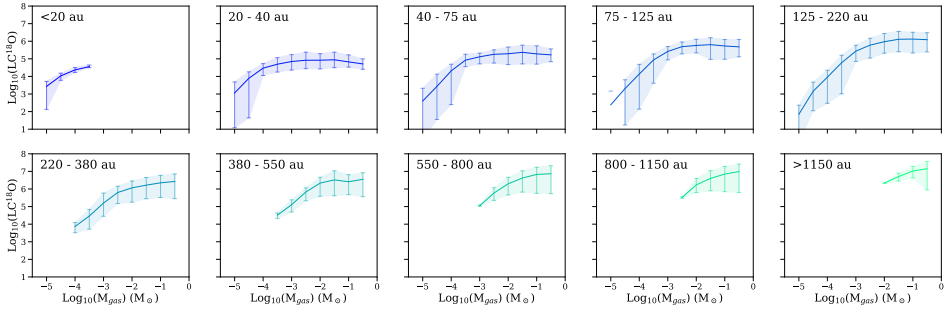
Figure 3.C.2: Same as Figure 3.8, but for the $J = 3 - 2$ transition.
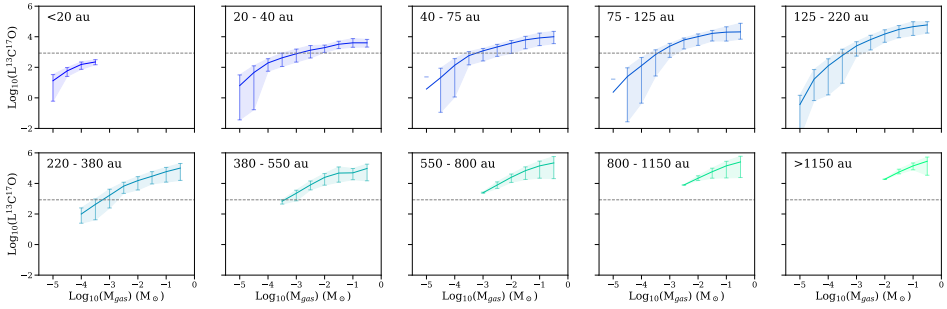
Figure 3.C.3: Same as Figure 3.13, but for the $J = 3 - 2$ transition.

3.D   Parameter overview plots

This appendix presents plots showing in which direction the parameters from Table 3.3 change the ^{13}CO and C^{18}O luminosities, similar to Fig. 3.6. Figures 3.D.1 to 3.D.4 are the same as Fig. 3.6, but for the other R_c values used. Similarly, Figures 3.D.5 and 3.D.6 are the same as Fig. 3.6, but for the other γ values. Lastly, Figures 3.D.7 to 3.D.13 show the same figures but for the $J = 3 - 2$ transition.
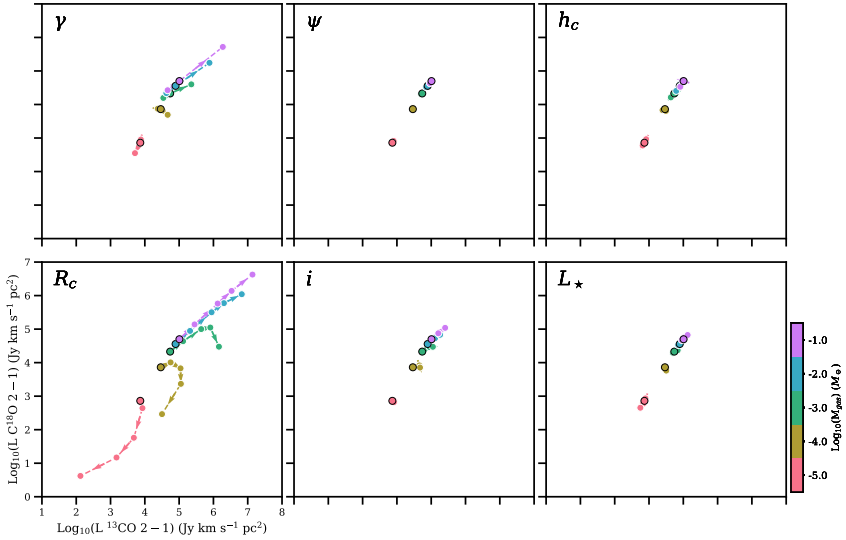
Figure 3.D.1: Same as Fig. 3.6, but with $R_c = 5$ au
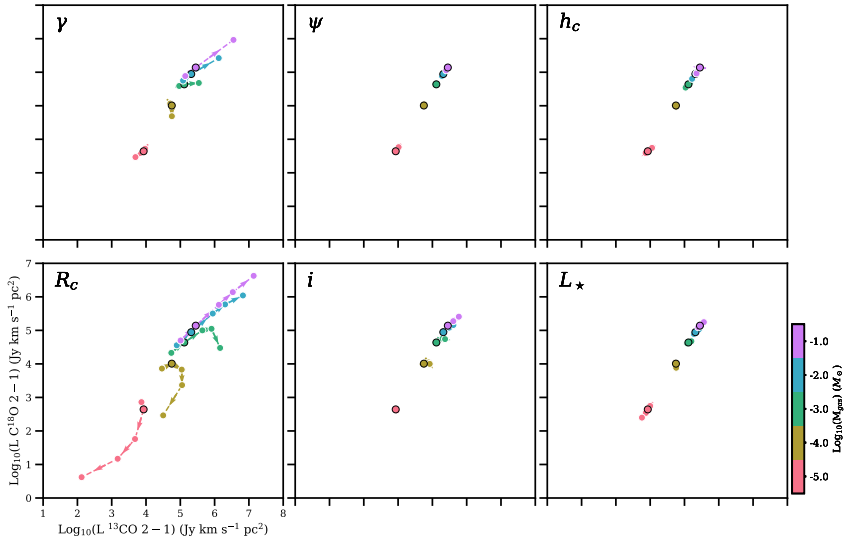
Figure 3.D.2: Same as Fig. 3.6, but with $R_c = 10$ au
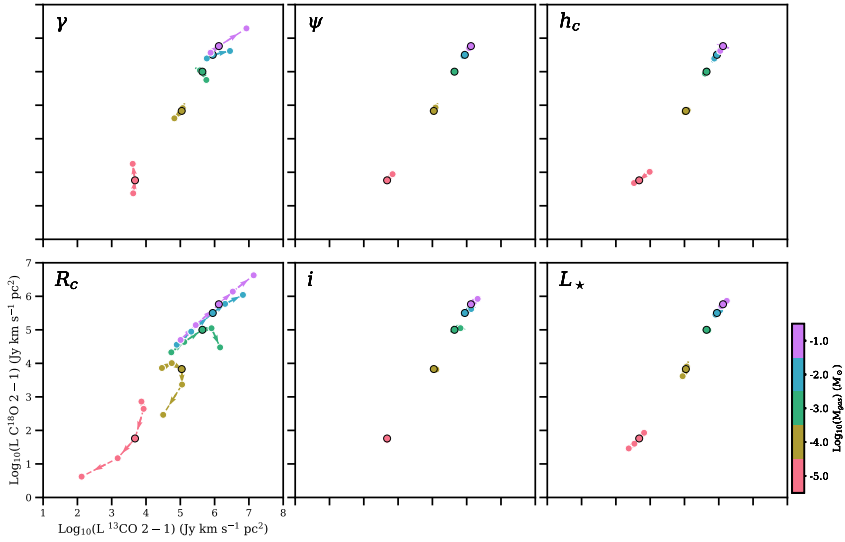
Figure 3.D.3: Same as Fig. 3.6, but with $R_c = 30$ au
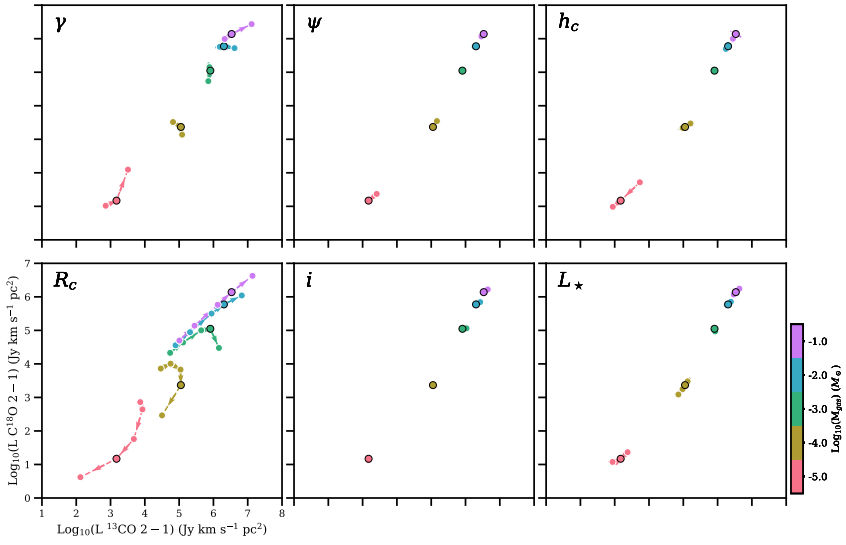
Figure 3.D.4: Same as Fig. 3.6, but with $R_c = 60$ au
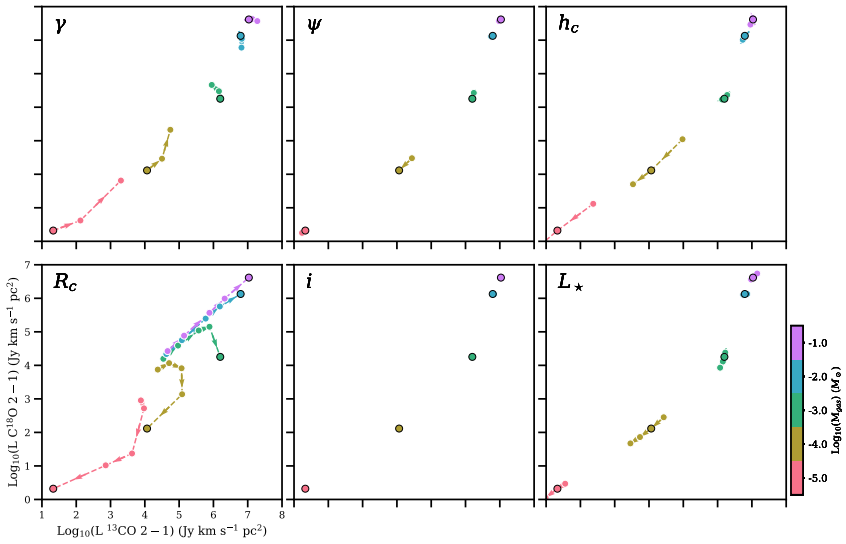
Figure 3.D.5: Same as Fig. 3.6, but with $\gamma = 0.4$
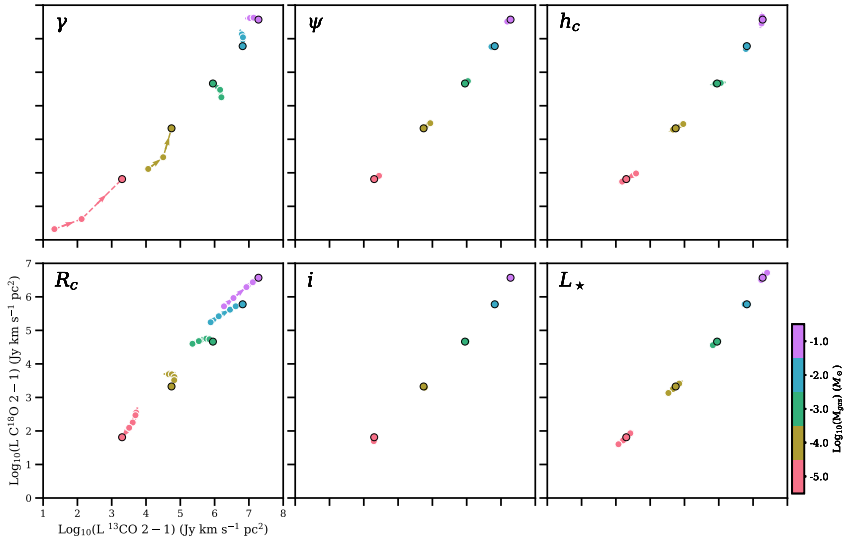
Figure 3.D.6: Same as Fig. 3.6, but with $\gamma = 1.5$
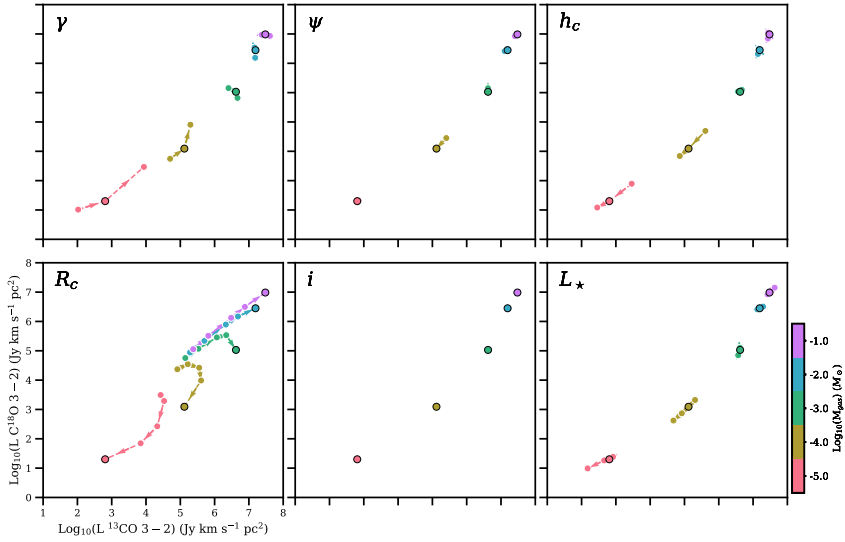
Figure 3.D.7: Same as Fig. 3.6, but with the $J = 3 - 2$ transition.
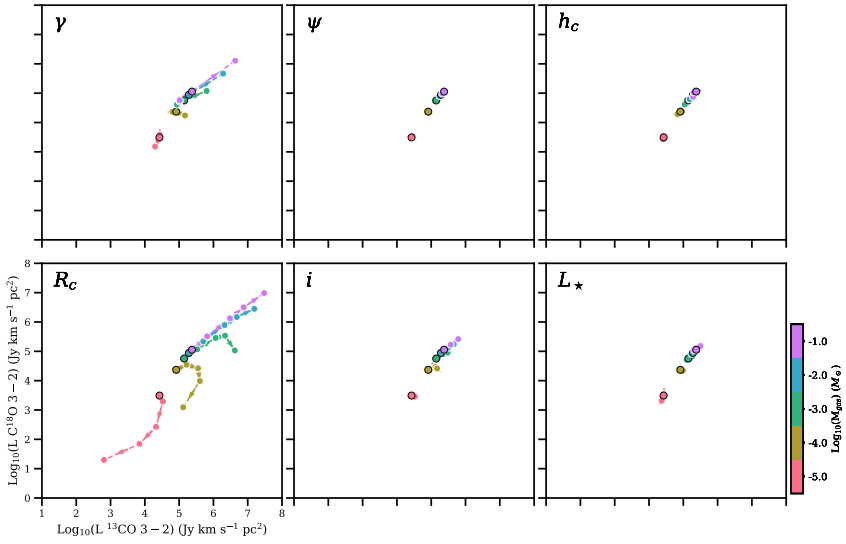
Figure 3.D.8: Same as Fig. 3.D.7, but with $R_c = 5$ au
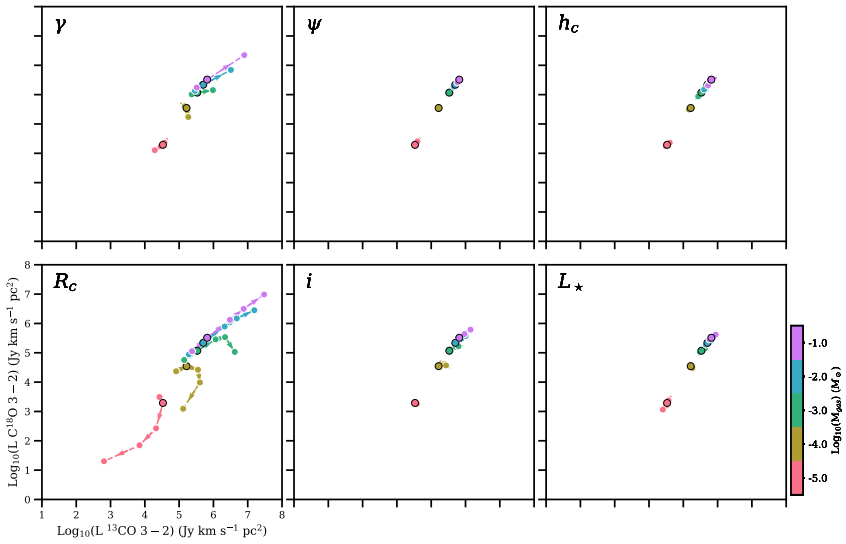
Figure 3.D.9: Same as Fig. 3.D.7, but with $R_c = 10$ au
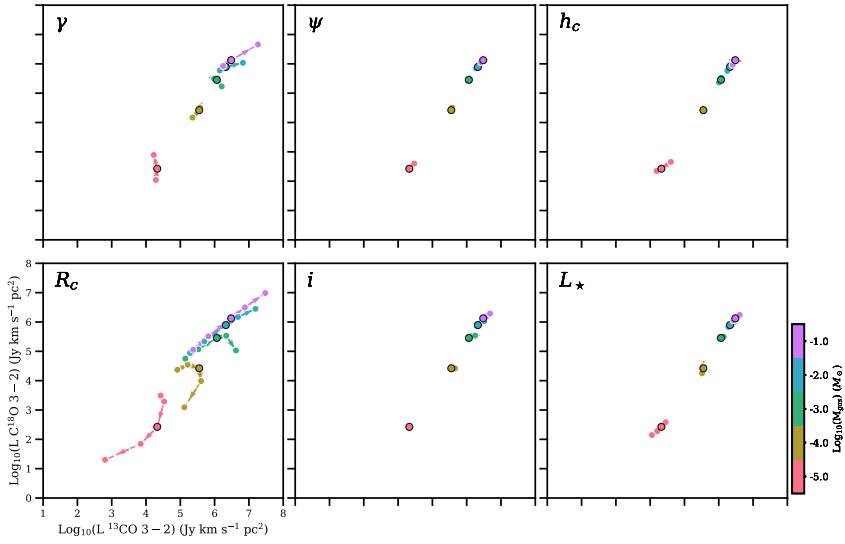
Figure 3.D.10: Same as Fig. 3.D.7, but with $R_c = 30$ au
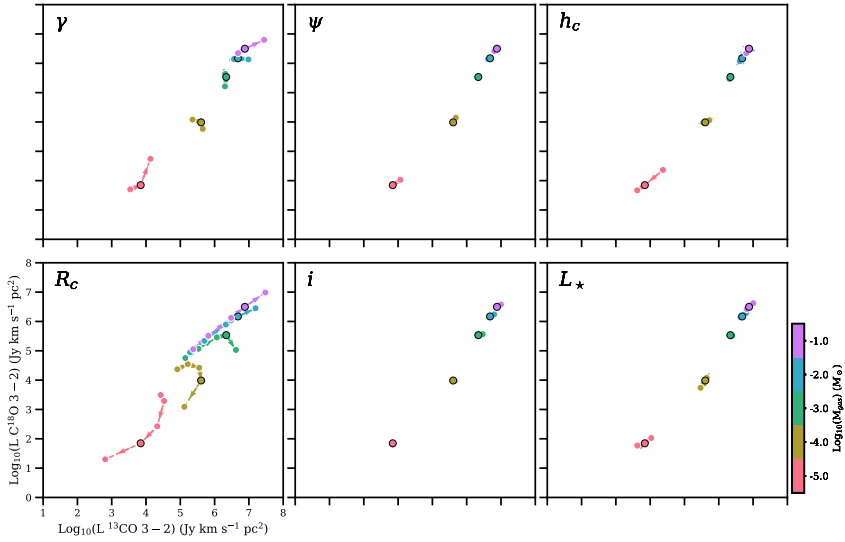
Figure 3.D.11: Same as Fig. 3.D.7, but with $R_c = 60$ au
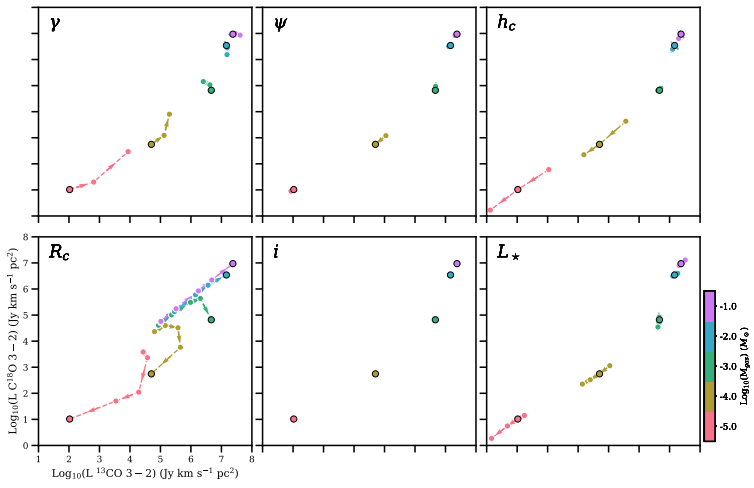
Figure 3.D.12: Same as Fig. 3.D.7, but with $\gamma = 0.4$
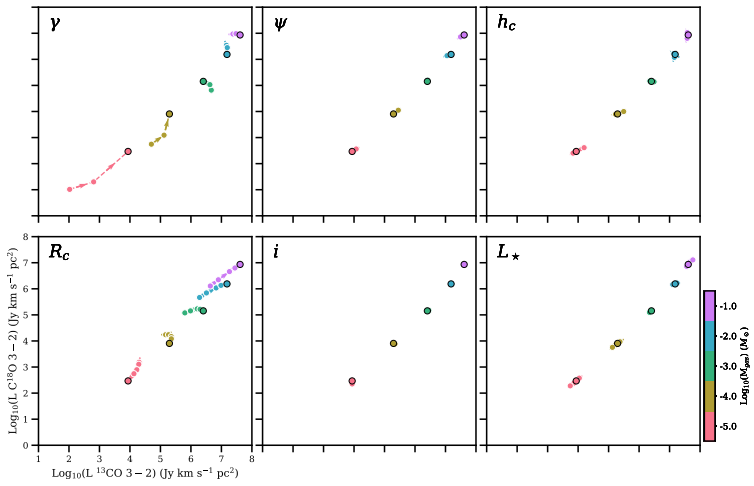
Figure 3.D.13: Same as Fig. 3.D.7, but with $\gamma = 1.5$

3.E   Disk masses

Table 3.E.1 presents the mean disk masses and range in possible disk masses based on our models for all Herbig disks presented in this work.

Table 3.E.1: Gas mass range and average values of the Herbig disk gas masses together with the resulting gas-to-dust ratio when combined with the dust masses from Stapper et al. (2022) and the dust masses from Table 3.B.1.

Name	$\text{Log}_{10}(\Delta M_{\text{g}})$ $(M_\odot)$	$\text{Log}_{10}(\bar{M}_{\text{g}})$ $(\text{M}_\odot)$	$\Delta_{g/d}$
AB Aur	$>$-0.5	-0.75	5010
AK Sco	$-3.5 - -0.5$	-2.64	124
BH Cep	$<$-0.5	-3.98	$>$23
BO Cep	$-3.0 - -0.5$	-1.67	122
CQ Tau	$-2.5 - -1.0$	-1.90	95
HD 9672	$-4.5 - -3.5$	-3.99	271
HD 31648	$-1.25 - -0.75$	-1.00	470
HD 34282	$-1.5 - -0.5$	-0.91	474
HD 36112	$-2.25 - -1.75$	-2.00	177
HD 58647	$<$-4.0	-4.73	6
HD 97048	$-1.5 - -0.5$	-1.00	214
HD 100453	$-2.5 - -0.5$	-1.50	603
HD 100546	$-2.0 - -0.5$	-1.50	277
HD 104237	$-3.0 - -0.5$	-1.62	745
HD 135344B	$-2.5 - -1.0$	-1.68	199
HD 139614	$-2.5 - -0.5$	-1.59	205
HD 141569	$-3.25 - -2.75$	-3.00	933
HD 142527	$>$-0.5	-0.83	228
HD 142666	$-2.5 - -0.5$	-1.50	420
HD 163296	$-1.25 - -0.75$	-1.00	714
HD 169142	$-2.0 - -0.5$	-1.25	818
HD 176386	$<$-3.5	-4.70	$>$112
HD 200775	$<$-0.5	-3.92	10
HD 290764	$-1.5 - -0.5$	-1.00	369
HR 5999	$<$-4.0	-4.73	2
KK Oph	$<$-0.5	-3.95	2
MWC 297	$<$-0.5	-4.14	$<$1
SV Cep	$<$-0.5	-3.96	5

Table 3.E.1: Continued.

Name	$\mathrm{Log}_{10}(\Delta \mathrm{M_g})$ $(M_\odot)$	$\mathrm{Log}_{10}(M_\mathrm{g})$ $(\mathrm{M}_\odot)$	$\Delta_{g/d}$
TY CrA	<-3.5	-4.68	68
V718 Sco	-2.5 − -0.5	-1.44	1022
V892 Tau	-3.0 − -0.5	-2.40	17
XY Per	<-0.5	-3.84	3
Z CMa	<-2.5	-4.61	<1

Chapter 4

A complete Herbig disk mass survey in Orion

L. M. Stapper, M. R. Hogerheijde, E. F. van Dishoeck, A. S. Booth,
S. L. Grant, S. E. van Terwisga

Abstract

Context: Disks around intermediate mass stars called Herbig disks are the formation sites of giant exoplanets. Obtaining a complete inventory of these disks will therefore give insights into giant planet formation. However, until now no complete disk survey has been done on Herbig disks in a single star-forming region.

Aims: This work aims to obtain the first complete survey of Herbig disks. Orion is the only nearby region with a significant number of Herbig disks (N=35) to carry out such a survey. The resulting dust mass distribution is compared to other dust mass distributions of disks around proto- and pre-main sequence stars in Orion. In addition we ascertain if previous ALMA observations have been biased towards the most massive and brightest Herbig disks.

Methods: Using new NOEMA observations of 25 Herbig disks, in combination with ALMA archival data of 10 Herbig disks, results in a complete sample of all know Herbig disks in Orion. Using *uv*-plane analysis for the NOEMA observed disks, and literature values of the ALMA observed disks, we obtain the dust masses of all Herbig disks and obtain a cumulative dust mass distribution. Additionally, six disks with new CO isotopologues detections are presented, one of which is detected in $C^{17}O$. We calculate the external ultraviolet (UV) irradiance on each disk and compare the dust mass to it.

Results: We find a median disk dust mass of 11.7 $M_{\oplus}$ for the Herbig disks. Comparing the Herbig disks in Orion to previous surveys for mainly T Tauri disks in Orion, we find that while $\sim 50\%$ of the Herbig disks have a mass higher than 10 $M_{\oplus}$, this is at most 25% for the T Tauri disks. This difference is especially striking when considering that the Herbig disks are around a factor of two older than the T Tauri disks. Comparing to the Herbig disks observed with ALMA from a previous study, no significant difference is found between the distributions. We find a steeper (slope of -5.2) relationship between the dust mass and external UV irradiation compared to that of the T Tauri disks (slope of -1.3). Comparing our results to a recent SPHERE survey of disks in Orion, we see that the Herbig disks present the largest and brightest disks and have structures indicative of gas-giant formation.

Conclusions: Herbig disks are on average more massive compared to T Tauri disks. This work shows the importance of complete samples, giving rise to the need of a complete survey of the Herbig disk population.

4.1   Introduction

Herbig disks are disks around pre-main sequence stars with spectral types of B, A, and F, and stellar masses of 1.5-10 M$_\odot$ with Hα indicating ongoing accretion (Herbig 1960; Brittain et al. 2023). These disks are the prime formation site of giant exoplanets: directly imaged exoplanets are often found around early spectral type stars (Marois et al. 2008, 2010; Lagrange et al. 2010), and exoplanet population studies show that the occurrence rate of massive exoplanets is highest around intermediate mass stars (e.g., Johnson et al. 2010; Nielsen et al. 2019). Recent work by Stapper et al. (2022) has shown that the mean mass of Herbig disks is higher compared to disks around lower mass T Tauri stars. The interpretation of these higher disk fluxes are still being discussed: either as a consequence of massive exoplanets forming in these disks stopping radial drift and keeping the emitting area of the dust large (Stapper et al. 2022), and/or high dust masses causing massive exoplanets to form in these disks (e.g., Guzmán-Díaz et al. 2023). Regardless of interpretation, massive exoplanets are likely forming in these disks.

Some of the most well-known protoplanetary disks are Herbig disk. These millimeter-bright disks display many different types of structures, and are therefore especially favored for in-depth morphological (e.g., Andrews et al. 2018a), kinematical (Pinte et al. 2018b, 2019; Izquierdo et al. 2022), and chemical studies (e.g., Öberg et al. 2021; Booth et al. 2024). Stapper et al. (2022) compiled all ALMA data available of Herbig disks within 450 pc, including these well-studied disks. They found a clear increase in the mean dust mass compared to disks in the Lupus and Upper Sco star-forming regions, which primarily consist of T Tauri stars, showing that the stellar mass - disk mass relationship extends to the intermediate mass regime. Still, both Herbig and T Tauri disks span the same range of masses, although their distributions are skewed to different averages. Since the T Tauri samples are complete and the Herbig sample of Stapper et al. (2022) is constructed from Herbig disks studied in a variety of ALMA projects (still 64% complete including all nearby star-forming regions), the question remains if the ALMA coverage of Herbig disks is biased toward well-known and 'interesting' objects with higher disk masses.

Orion ($\sim$300–475 pc, Großschedl et al. 2018) is the closest star-forming complex with enough pre-main-sequence stars to harbor a sizeable number of Herbig Ae/Be stars. Many population studies have been done in different parts of Orion, tracing different star-formation environments from tranquil regions to more UV-dominated regions. In the σ Orionis cluster, an intermediate aged region of 3 Myr old, the disk dust masses were found to depend strongly on the distance to the O9 star at its center (Ansdell et al. 2017). Only 12% of their disks were more than 10 M$_\oplus$ in mass. Furthermore, CO was only detected in disks more than 1.5 pc separated from the O-star. On the other hand, the disks in the older λ Orionis cluster of 5 Myr have not been significantly impacted by the massive stars or the supernova which occurred in the cluster (Ansdell et al. 2020). Interestingly, there is one significant outlier, HD 245185 which is a Herbig disk, which has a more than an order of magnitude higher disk mass than any of the other disks in this region. The younger (0.5 Myr) NGC 2024 cluster was surveyed by van Terwisga et al.
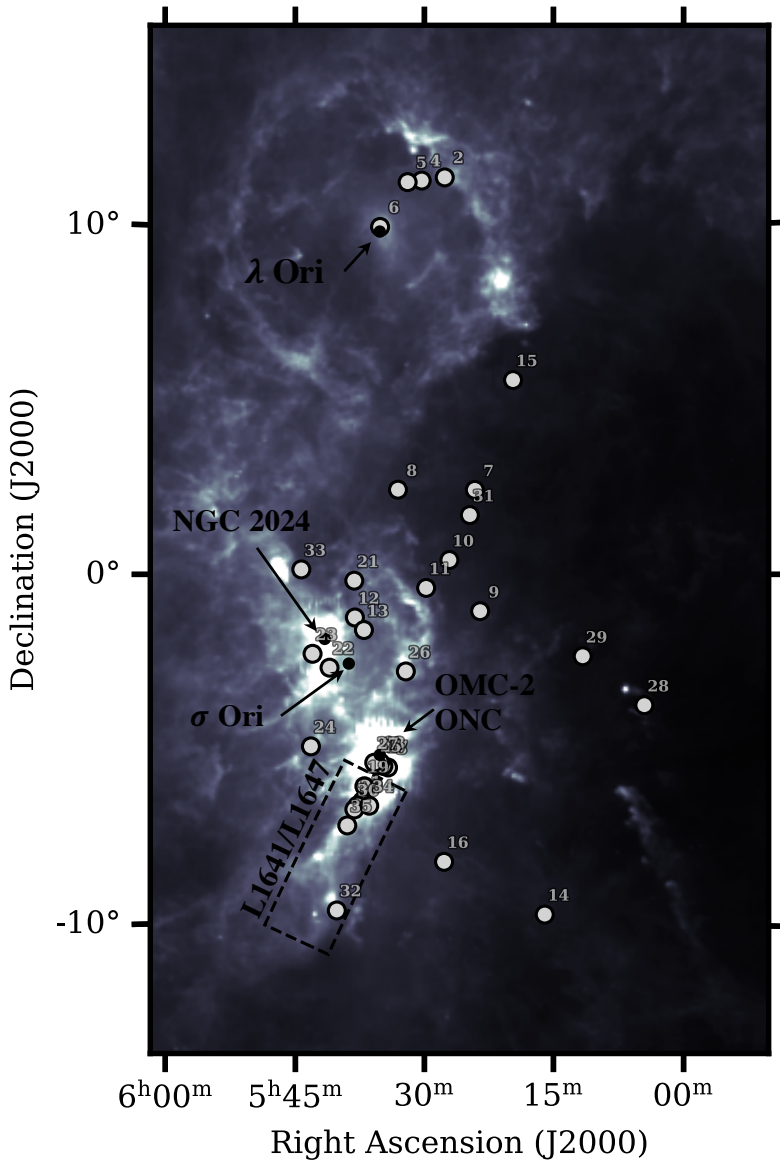
Figure 4.1: Positions on the sky of the Herbig disk sample used in this work shown as the gray markers. The numbers next to the markers correspond to the numbers in Table 4.1. The background is an IRAS 100μm image (Neugebauer et al. 1984). The positions of six disk surveys have been indicated as well: σ Ori (Ansdell et al. 2017), ONC (Eisner et al. 2018), OMC-2 (van Terwisga et al. 2019), λ Ori (Ansdell et al. 2020), NGC 2024 (van Terwisga et al. 2020), and L1641/L1647 (SODA, van Terwisga et al. 2022).

(2020). This cluster consists of two populations, the eastern population is shielded from FUV irradiation and is similar to other isolated regions, while the western population is older and may be affected by the FUV irradiation. Other younger clusters such as the Orion Nebula Cluster and Orion Molecular Cloud-2 have been surveyed as well (Eisner et al. 2018; van Terwisga et al. 2019), and even class 0 and I surveys have been done (Tobin et al. 2020). Lastly, the largest population study of disks to date, consisting of 873 disks, has been done in the L1641 and L1647 regions of the Orion A cloud (SODA, van Terwisga et al. 2022, for L1641 also see Grant et al. 2021).

The plethora of population studies available in Orion gives a solid basis for a comparison between T Tauri disks and Herbig disks. In this work we present new Northern Extended Millimeter Array (NOEMA) observations of all Herbig disks in Orion. Section 4.2 shows how the targets were selected, the NOEMA data were reduced, and the dust masses were obtained. In Section 4.3 the resulting dust mass distribution is presented and compared to distributions of other proto- and pre-main sequence stars in Orion, in addition CO spectra are presented. In Section 4.4.1 the dust mass distribution is compared to the one of ALMA from Stapper et al. (2022). The impact of external UV irradiation on the dust masses is determined in Section 4.4.2, and a comparison to scattered light is made in Section 4.4.3. Our results are summarized in Section 4.5.

4.2   Data selection & reduction

In this work we present the results of observations done with the Northern Extended Millimeter Array (NOEMA), with project number S22AU (PI: S. Grant). The disks observed with NOEMA were selected as follows. Using the boundaries of Orion as given in Zari et al. (2017), we selected all Herbig disks in Orion based on the compilations of Vioque et al. (2018) and Guzmán-Díaz et al. (2021). From this, we obtained a total of 35 Herbig disks located in the Orion star-forming region (see for their positions in Orion Fig 4.1, the numbers correspond to the numbers in Fig. 4.1). Of these 35 disks, ten have existing ALMA interferometric data available (see Stapper et al. 2022 and van Terwisga et al. 2022, as well as the annotated disks in Table 4.1). For one of these ten (V1012 Ori) we obtained publicly available ALMA archival[1] product data (PI: C. Ginski, 2021.1.01705.S). The remaining 25 disks were observed with NOEMA on 2022 December 7 and 30, on 2022 December 17, and on 2023 October 7. Figure 4.1 shows that the targets are spread over the complete constellation.

The observations were done in the C configuration. The observations made on 2022 December 17 and November 30 (setup 1) have baselines ranging from 20 to 309 meters with one antenna (#7) at projected long baselines ranging from 985 to 1397 meters. On 2022 December 7 and 2023 October 7 (setup 2), the baselines range from 20 to 321 meter. Hence, at 210 GHz the largest angular scale the data are sensitive to is $\sim 15''$, and a restoring beam of $\sim 1''$ is obtained. The wide-band correlator PolyFiX was tuned such that the lower side-band (LSB) and upper

---

[1]https://almascience.eso.org/aq/

Table 4.1: Stellar parameters, G_0, measured flux, and derived dust mass of the Orion sample used in this work.

Nr.	Name	RA (h:m:s)	Dec (deg:m:s)	Dist. (pc)	$M_\star$ ($M_\odot$)	$L_\star$ ($L_\odot$)	Sp.Tp.	$\mathrm{Log}_{10}(G_0)$	Flux (mJy)	M_{dust} ($M_\oplus$)
1.	BF Ori*	05:37:13.3	-06:35:01.0	378	1.9	13	A2	1.87	0.8	1.1±0.1
2.	CO Ori	05:27:38.3	+11:25:39.0	395	2.3	23	F3	0.09	1.5	2.4±0.5
3.	HBC 442	05:34:14.2	-05:36:54.0	383	2.0	10	F8	2.66	4.0	7.8±1.6
4.	HD 244314	05:30:19.0	+11:20:20.0	398	2.1	19	A2	0.18	5.9	10.2±2.0
5.	HD 244604	05:31:57.3	+11:17:41.0	398	2.2	34	A2	0.27	4.4	6.5±1.3
6.	HD 245185*	05:35:09.6	+10:01:51.0	410	2.2	30	B9	3.19	34.6	37.5±3.8
7.	HD 287823	05:24:08.0	+02:27:47.0	343	1.8	12	A4	1.31	8.0	11.7±2.3
8.	HD 288012	05:33:04.8	+02:28:10.0	341	<1.9	14	A2	1.75	<1.4	<5.8
9.	HD 290380	05:23:31.0	-01:04:24.0	343	1.6	6	F5	1.09	10.6	18.6±3.7
10.	HD 290409	05:27:05.5	+00:25:08.0	404	2.2	25	B9	0.90	10.1	16.8±3.4
11.	HD 290500	05:29:48.1	-00:23:43.0	402	1.9	13	A2	1.45	11.9	23.7±4.7
12.	HD 290764*	05:38:05.3	-01:15:22.0	397	2.0	22	A5	1.71	210.1	91.2±9.1
13.	HD 290770	05:37:02.4	-01:37:21.0	393	2.6	55	B8	1.70	3.5	4.4±0.9
14.	HD 34282*	05:16:00.5	-09:48:35.0	306	<1.9	14	A0	0.05	99.0	86.7±8.7
15.	HD 34700	05:19:41.4	+05:38:43.0	347	2.6	23	F8	0.02	8.1	10.2±2.0
16.	HD 35929	05:27:42.8	-08:19:39.0	377	3.5	93	A9	0.73	<0.7	<2.0
17.	HD 36917	05:34:47.0	-05:34:15.0	445	4.4	407	B8	2.86	<0.8	<2.3
18.	HD 36982	05:35:09.8	-05:27:53.0	404	<6.4	1349	B2	3.76	<0.8	<1.3
19.	HD 37258*	05:36:59.3	-06:09:16.0	377	2.3	26	A0	2.30	1.8	2.1±0.2
20.	HD 37357*	05:37:47.1	-06:42:30.0	465	2.8	87	B9	2.01	2.9	3.8±0.4
21.	HD 37371	05:38:09.9	-00:11:01.0	405	3.1	100	B8	2.36	<0.6	<2.0
22.	HD 37806	05:41:02.3	-02:43:01.0	397	3.5	200	B8	1.90	3.4	3.1±0.6
23.	HD 38087	05:43:00.6	-02:18:45.0	373	4.2	347	B5	1.79	<0.6	<1.2

Table 4.1: Continued.

Nr.	Name	RA (h:m:s)	Dec (deg:m:s)	Dist. (pc)	$M_\star$ ($M_\odot$)	$L_\star$ ($L_\odot$)	Sp.Tp.	$\mathrm{Log_{10}}(G_0)$	Flux (mJy)	M_{dust} ($M_\oplus$)
24.	HD 38120	05:43:11.9	-04:59:50.0	381	2.8	71	B8	0.13	31.9	35.6±7.1
25.	NV Ori	05:35:31.4	-05:33:09.0	384	2.1	59	F0	3.22	4.0	4.8±1.0
26.	RY Ori	05:32:09.9	-02:49:47.0	347	1.6	6	F4	0.64	10.6	19.1±3.8
27.	T Ori	05:35:50.5	-05:28:35.0	399	2.5	59	A0	3.25	1.5	1.9±0.4
28.	UX Ori	05:04:30.0	-03:47:14.0	320	1.9	13	A3	0.29	20.2	25.2±5.0
29.	V1012 Ori	05:11:36.5	-02:22:48.5	386	1.3	6	A3	0.08	26.4	47.8±4.8
30.	V1787 Ori*	05:38:09.3	-06:49:17.0	394	2.1	28	A3	1.47	14.8	18.2±1.8
31.	V346 Ori	05:24:42.8	+01:43:48.0	336	1.6	7	A7	2.32	15.3	24.8±5.0
32.	V350 Ori	05:40:11.8	-09:42:11.0	391	<1.9	9	A1	0.27	4.4	9.1±1.8
33.	V351 Ori	05:44:18.8	+00:08:40.0	323	2.0	21	A7	0.18	69.4	77.4±15.5
34.	V380 Ori*	05:36:25.4	-06:42:58.0	374	2.8	95	B9	1.84	6.2	5.1±0.5
35.	V599 Ori*	05:38:58.6	-07:16:46.0	401	2.1	31	A4	0.60	55.9	69.0±6.9

Notes. For the disks with an asterisk the fluxes have been taken from Stapper et al. (2022, 2024) and van Terwisga et al. (2022). In addition to the fluxes there is an absolute calibration error, which is 10% for ALMA, and 20% for NOEMA. Except for the UV irradiance G_0, continuum flux, and inferred dust mass which we derive in this work, all parameters are taken from Guzmán-Díaz et al. (2021), see this paper for their corresponding uncertainties. For V1012 Ori, the parameters are taken from Vioque et al. (2018), and the continuum flux is determined from the ALMA pipeline product data. HD 290764 is ALMA Band 7 data.

side-band (USB) ranged from 203.7 to 211.8 GHz and 219.2 to 227.3 GHz respectively with a channel width of 2 MHz (~ 2.7 km s^{-1}). In addition, thirteen high resolution spectral windows with a width of 62.5 kHz (~ 86 m s^{-1}) where centered on molecular emission lines such as the $J = 2 - 1$ transition of the CO isotopologues ^{13}CO, C^{18}O, and C^{17}O, and other molecules such as CN and H$_2$CO.

The NOEMA data were calibrated using the standard pipeline calibration using the `CLIC` program of the Grenoble Image and Line Data Analysis Software (`GILDAS`[2]). For setup 1 the phase rms threshold was set to 55°, and the seeing threshold, normally applied to long baseline observations, was not included as only one antenna was at long baselines. For setup 2 the phase rms threshold was set to the default value of 70°. The calibrators used for setup 1 were 2200+420, LkHα 101, 0923+392, and 2010+723 for the passband calibration, and 0458-020 and J0542-0913 were used for the phase and amplitude calibration. All calibrators were used for the flux calibration. The calibrators for setup 2 were LkHα 101 and 3C84, which were used for the bandpass calibration, and J0509+056 was used for the phase and amplitude calibration. All calibrators were used for the flux calibration. Due to the reduced phase rms threshold for setup 1, 10% of the data taken on 2022 November 30 were flagged, while 2% was flagged for the data taken on 2022 December 17. The weather during observing setup 2 on 2022 November 7 was particularly bad, increasing to a precipitable water vapor of 5 mm by the end of the observations. Due to this, 43% of the data are flagged. For the observations made on 2023 October 7 nothing was flagged. The on-source integration times ranged from 15 to 30 minutes. After the calibration was done, the data were exported to `uvfits` files to be further analyzed.

The data were analyzed using the `Common Astronomy Software Applications` (CASA) application version 5.8.0 (McMullin et al. 2007). To obtain the integrated fluxes in continuum, the LSB and USB were both combined to make a continuum measurement set. This Gaussian is fitted using the `uvmodelfit` task in CASA after changing the phase-center to be on the target using the `fixvis` task. As all detections are unresolved, fitting a Gaussian to the visibilities is therefore a good approximation of the observations. From this fit the total flux is obtained. For the non-detections, assuming the emission is coming from a singe beam, three times the rms noise from the empty image was used. For the remaining ten Herbig disks with existing ALMA data, we use the published fluxes as presented in Stapper et al. (2022) and van Terwisga et al. (2022), and for V1012 Ori we apply the same method as Stapper et al. (2022) on ALMA archive product data.

To obtain the dust masses, we use the same assumptions as other works, see for details Stapper et al. (2022). The flux and dust mass can be related via

$$M_{\mathrm{dust}} = \frac{F_\nu d^2}{\kappa_\nu B_\nu(T_{\mathrm{dust}})}, \qquad (4.1)$$

under the assumption of optical thin emission (Hildebrand 1983). Here, the dust opacity is κ_ν, the distance is d, and B_ν is the value of the Planck curve at a dust temperature of T_{dust}. The dust opacity is estimated as a power-law of the form

---

[2]`http://www.iram.fr/IRAMFR/GILDAS`

$\kappa_\nu \propto \nu^\beta$, such that it equals $10 \text{ cm}^2 \text{ g}^{-1}$ at a frequency of 1000 GHz (Beckwith et al. 1990). The power-law index β is assumed to be equal to 1. To obtain an estimate of the temperature of the dust in Herbig disks we scale the dust temperature T_{dust} using the approach of Andrews et al. (2013) via

$$T_{dust} = 25 \text{ K} \times \left(\frac{L_\star}{L_\odot} \right)^{1/4} . \tag{4.2}$$

For the error on the dust masses we use the recommended absolute flux calibration error of 20% for NOEMA, and 10% for ALMA.

4.3   Results

4.3.1   Dust mass distribution

Using the `lifelines` package (Davidson-Pilon et al. 2021) we obtain the cumulative distribution of the Herbig disks in Orion following Stapper et al. (2022). The cumulative distribution is presented in the left panel of Figure 4.2, where it is compared to the cumulative dust mass distributions of four regions in Orion (see Fig. 4.1 for their positions in Orion): NGC 2024 (0.5 Myr, van Terwisga et al. 2020), L1641/L1647 (SODA, 1-3 Myr, van Terwisga et al. 2022), σ Ori (3 Myr, Ansdell et al. 2017), and λ Ori (5 Myr, Ansdell et al. 2020).

The dust masses of the Herbig disks range from 91 $M_\oplus$ for HD 290764 down to < 1.2 $M_\oplus$ for HD 38087. For HD 288012, the disk around the secondary is detected with a flux of 16.5 mJy, corresponding to a disk mass of 65 $M_\oplus$, while for the disk around the Herbig star an upper limit of < 1.4 $M_\oplus$ is found. The median of the disk masses is 11.7 $M_\oplus$ with a standard deviation of 26 $M_\oplus$, excluding the upper limits.
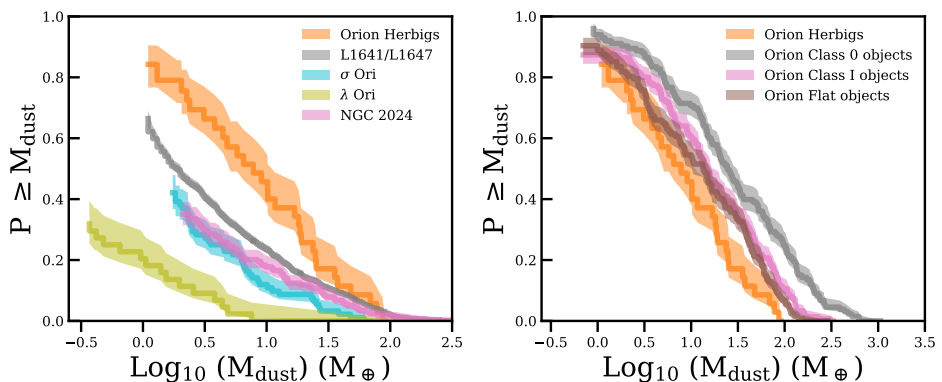
Figure 4.2: The Orion Herbig disk dust mass distribution compared to other disk surveys done in Orion. The other surveys are: NGC 2024 (van Terwisga et al. 2020), L1641/L1647 (SODA, van Terwisga et al. 2022), σ Ori (Ansdell et al. 2017), λ Ori (Ansdell et al. 2020), and VANDAM (Tobin et al. 2020).

As noted in Stapper et al. (2022), we also find that Herbig disks are more massive than T Tauri disks. As the left panel of Fig. 4.2 shows, while the most massive disks are not necessarily part of the Herbig disk population, the number of more massive disks, i.e., disks with a mass more than 10 $M_\oplus$, is at around 50% for the Herbig disks. For the other regions this is $\sim 25\%$ or lower.

This difference in mass is especially evident when comparing the Herbig disk ages to the ages of the surveyed regions. Based on isochrones from pre-main sequence evolutionary tracks, the median age of the Herbig disks in Orion, after removing upper limits, is 5.1±4.1 Myr (Guzmán-Díaz et al. 2021). The ages range from a minimum age of 0.5 Myr to a maximum age of 17 Myr. NGC 2024, the youngest region, is less massive than the Herbig disks; $\sim 20\%$ of the population is more massive than 10 $M_\oplus$, see Fig. 4.2. Even splitting the NGC 2024 region in its two populations (the younger east, and older west population), the younger population has a dust mass distribution up to $\sim 30\%$ at 10 $M_\oplus$, still lower than what is found for the Herbig disks.

The difference is even more stark when comparing the dust masses of the oldest region, λ Ori, to those of the Herbig disks. All but one disk has a mass below 10 $M_\oplus$. This disk is HD 245185, which is in the 90th percentile of our dust masses[3]. Regions impacted by external irradiation, such as the disks in σ Ori (Ansdell et al. 2017; Maucó et al. 2023), show lower disk masses compared to the Herbig disks as well.

In the Orion A and B clouds the class 0, I and flat spectrum objects have been part of the VANDAM survey (Tobin et al. 2020), allowing for a comparison to the Herbig disks. This comparison is shown in the right panel of Fig. 4.2. The dust masses were determined by scaling the dust temperature by the bolometric luminosity of the objects, similar to eq. (4.2) but with 43 K at 1 $L_\odot$, instead of 25 K. Tobin et al. (2020) found median dust masses of 25.7, 15.6, and 13.8 $M_\oplus$ for the class 0, I, and flat spectrum objects respectively. Though lower disk masses are found when including the disk temperature from radiative transfer (Sheehan et al. 2022). The Class 0 objects are clearly more massive than the Herbig disks, with the median disk mass a factor of ~ 2.5 higher than for the Herbig disks. The Orion Flat spectrum objects have a remarkably similar dust mass distribution to the Herbig disks.

4.3.2   Gas observations

The NOEMA observations also covered the ^{13}CO, C^{18}O, and C^{17}O $J = 2 - 1$ emission lines. To obtain the spectra of these CO isotopologues, first the phase center was aligned on-target using the `fixvis` task, after which the `plotms` task was used to export the measured visibility spectra averaged over time, baseline, and scans. The spectra have been binned by a factor of ten, resulting in a ~ 0.9 km s^{-1} resolution.

Figure 4.3 presents the detected ^{13}CO, C^{18}O, and C^{17}O spectra of six disks. For these six disks we detect ^{13}CO emission at a peak signal-to-noise of 6 and higher.

---

[3]We adopt a lower disk mass compared to Ansdell et al. (2020) by using a higher disk temperature, 59 K instead of 20 K.

For only two disks we also detect $C^{18}O$. In V351 Ori, even $C^{17}O$ is detected. For an additional two disks, T Ori and HD 36982, foreground cloud emission in the form of large scale emission is detected.
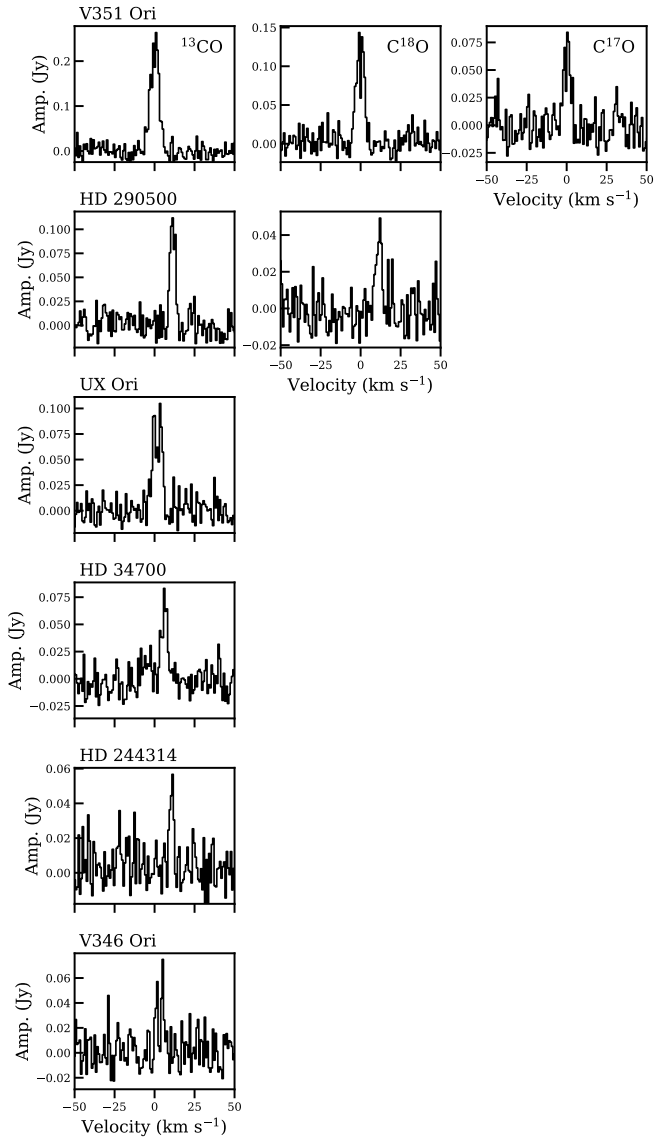
Figure 4.3: Spectra of the disks in which ^{13}CO, $C^{18}O$, or $C^{17}O$ are detected. The spectra are centered on the frequencies of the emission lines and are binned to 1 km s^{-1}.

4.4   Discussion

4.4.1   Comparison to the ALMA Herbig disks

Figure 4.4 compares the obtained cumulative distribution of the Herbig disks in
Orion to the distribution of the with all-sky survey of Herbig disks with ALMA
of Stapper et al. (2022) combined with the extra sources observed with NOEMA
from Stapper et al. (2024). The detection rate of the Herbig disks in Orion is
similar to what was found for the sample analyzed by Stapper et al. (2022). Out
of the 35 disks in the Orion sample, 6 are not detected, resulting in a 83% detection
rate. For the sample of Stapper et al. (2022) 2 out of 36 disks were not detected.
However, the ALMA data are more sensitive, and at the NOEMA sensitivity the
same detection rate of 83% would have been obtained for the sample of Stapper
et al. (2022). Indeed, the cumulative distributions shown in Fig. 4.4 have the same
completeness at a disk mass of ~ 1 $M_\oplus$.

The main difference between the two dust mass cumulative distributions is
at the high end of the distribution. Mostly the higher mass disks are missing
in the Orion sample when compared to the sample of Stapper et al. (2022). To
test whether the dust distributions come from a the same population, we use
two tests, the `lifelines` `logrank_test` and the Kolmogorov-Smirnov test from
`SciPy` (Virtanen et al. 2020). These tests test if the Orion distribution is different
from the all-sky ALMA distribution, the logrank test also takes upper limits into
account. We find p-values for the distributions of p=0.26 (logrank) and p=0.32
(KS), and therefore cannot reject the null hypothesis of both distributions being
sampled from the same distribution. However, in the Orion population, massive
disks such as HD 97048 and HD 142527 (156 $M_\oplus$ and 215 $M_\oplus$ respectively, Stapper
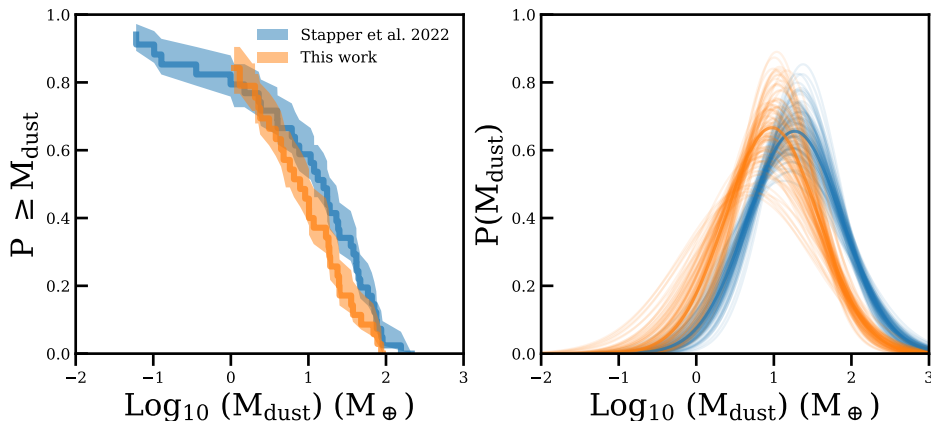
Figure 4.4: Comparison of the Herbig sample in Orion of this work with the Herbig
disks analyzed in Stapper et al. (2022) and Stapper et al. (2024). The left panel
present the cumulative distributions. The right panel shows the fitted log-normal
distributions.

et al. 2022) are missing. Adding these two massive disks to the Orion population results in p-values of 0.83 (logrank) and 0.50 (KS), suggesting that the difference is mainly driven by missing higher mass disks. This furthermore suggests that the ALMA all-sky coverage may have been slightly biased toward including the most massive disks, and shows that a complete all-sky survey is warranted.

A lognormal distribution is fitted through the cumulative distributions, following previous works (Williams et al. 2019; Stapper et al. 2022, 2024), to obtain probability density distributions. These distributions are shown in the right panel of Fig. 4.4. The mean value of the distributions are $\text{Log}_{10}(M_{\text{dust}}(M_{\oplus}))=0.94^{+0.06}_{-0.07}$ and $1.27^{+0.05}_{-0.05}$ for the Orion sample and the sample of Stapper et al. (2022) respectively. The width of the distributions are the same, $0.59^{+0.07}_{-0.06}$ and $0.61^{+0.06}_{-0.06}$ respectively. There is a clear overlap between the two distributions, further substantiating that the distributions are not significantly different.

Summarizing, we find no significant difference in the distribution of the dust masses of the Herbig disks in Orion compared to the distribution of Stapper et al. (2022).

4.4.2   Impact of UV on Herbig disk masses

Orion contains a large number of massive young stars which contribute to the far ultraviolet (FUV) external irradiation field, which influences the amount of mass present in the disk by triggering photoevaporative winds. Figure 4.5 shows the external ionizing stars as the blue shaded stars and the corresponding FUV impact on the Herbig disks as the purple to yellow shaded circles in terms of G_0 (1.6×10^{-3} erg cm^{-2} s^{-1}, Habing 1968). The Herbig disks with a blue edge have also been detected with NOEMA in at least ^{13}CO. For HD 34282 ^{13}CO and C^{18}O have been detected with ALMA (Stapper et al. 2024), and for HD 245185 and V1012 Ori ^{12}CO is very bright and detected with ALMA (Stapper et al. 2024).

The ionizing stars were found, following van Terwisga & Hacar (2023), by querying `Simbad`[4] for stars with spectral types earlier than A0 within the region on the sky as shown in Figs. 4.1 and 4.5. The distances to the stars were limited to 300-475 pc, and as the uncertainties on these distances can be fairly large only projected distances are used. The FUV luminosities of these stars were then computed by using BHAC-15 isochrones (Baraffe et al. 2015) and integrating model spectra (Castelli & Kurucz 2003) between 911.6 and 2066 Å. As was done by van Terwisga & Hacar (2023), no stars beyond a projected distance of 10 pc from a given Herbig disk were taken into account, but interstellar extinction was not included otherwise. The minimum UV irradiation was set at 1 G_0. The resulting values of G_0 are shown in Fig. 4.5, and compared to the dust masses in Fig. 4.6; disks with CO detections are indicated as in Fig. 4.5.

Figure 4.6 presents the dust mass as a function of UV irradiation. By binning the dust masses in logarithmically spaced bins in UV irradiation, we can assess whether there is a trend between the two variables. The solid black line is using the mean value of each bin, the dashed black line is using the median per bin. The

---

[4]`http://simbad.u-strasbg.fr/simbad/`
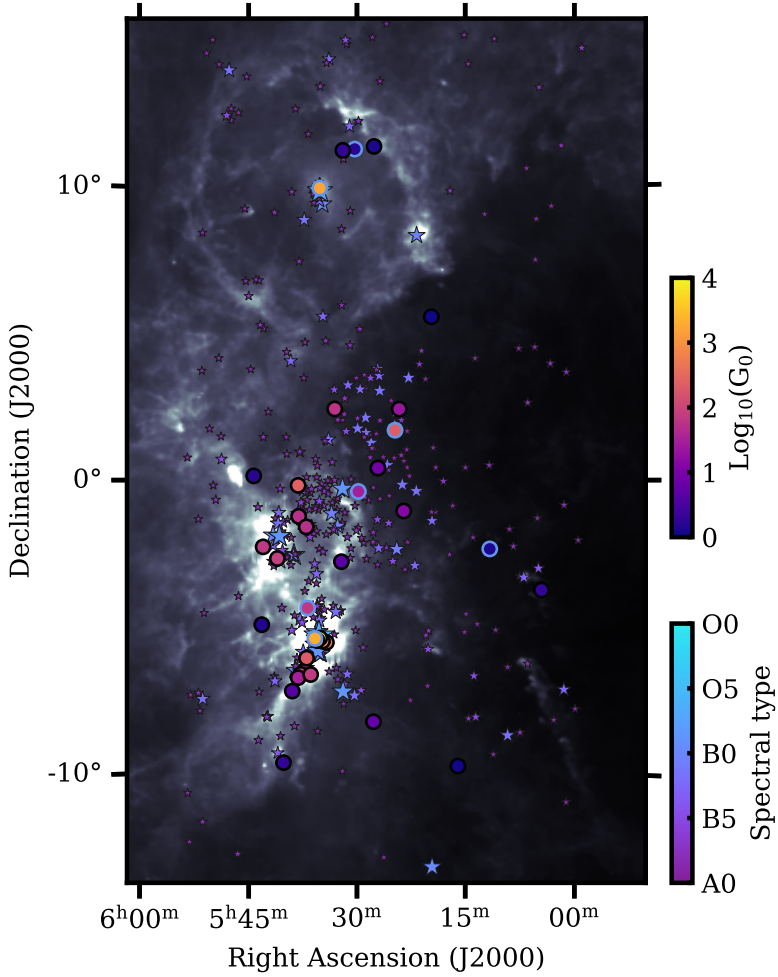
Figure 4.5: Similar to Fig. 4.1, but now the FUV irradiation in G_0 is shown as the color of the Herbig disk markers. O and B type stars are plotted as the stars, where the color (and size) indicates their spectral type. The Herbig disk with a blue edge have also been detected with NOEMA in at least ^{13}CO. For HD 34282 ^{13}CO and C^{18}O have been detected with ALMA, and for HD 245185 and V1012 Ori ^{12}CO is very bright and detected with ALMA (Stapper et al. 2024).
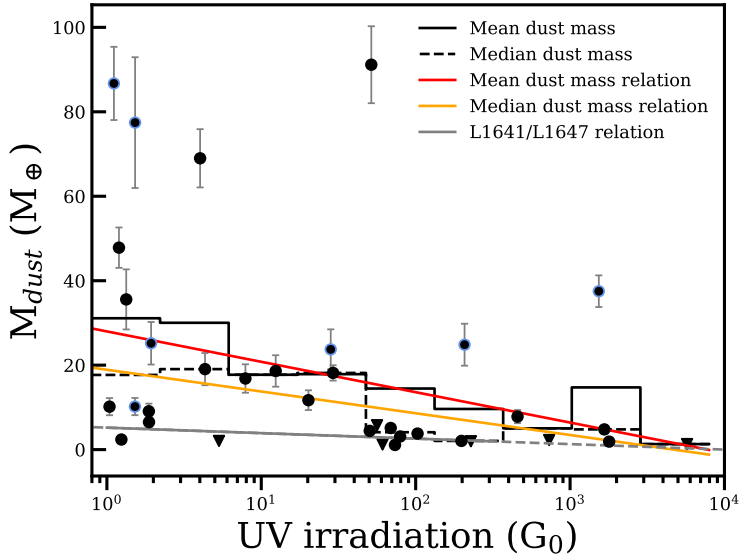
Figure 4.6: The external UV irradiation plotted against the dust mass of the Herbig disks. Histograms binning the dust masses are shown, either using the mean or median dust mass in each bin. A relationship is fitted through these binned data. The relationship found for L1641/L1647 is shown as the gray line (van Terwisga & Hacar 2023). The region over which this line was fitted is solid, while the dashed line is extrapolated. The blue outlines indicate disks in which CO is detected (see Fig. 4.3, or Stapper et al. 2024).

gray line in Fig. 4.6 is the relationship between the dust mass and UV irradiation found for L1641/L1647 (van Terwisga & Hacar 2023).

Based on Fig. 4.6, there is a trend with a decrease in dust mass for an increase in UV irradiation for Herbig disks. Especially the mean binned dust masses clearly decrease with an increase in UV irradiance. Using the median disk mass to remove the influence of outliers, the trend is still visible. Fitting a linear relationship through the binned data using the `curve_fit` routine from `SciPy` results in the red and orange relationships shown in Fig. 4.6. For the mean dust masses we find $M_{\mathrm{dust}} = -7.2\pm1.1\times \log_{10}(F_{\mathrm{uv}}/G_0)+28.0\pm2.5$, and for the median dust masses we find $M_{\mathrm{dust}} = -5.2\pm1.0\times \log_{10}(F_{\mathrm{uv}}/G_0)+18.9\pm2.3$. We find a steeper relationship compared to that of L1641/L1647 which has a slope of $-1.3^{+0.14}_{-0.13}$ (van Terwisga & Hacar 2023).

There are disks with dust masses higher than 10 $M_\oplus$ for all bins, except at the highest UV irradiation. Furthermore, CO is detected over all UV irradiation values traced, which is a tracer of the UV irradiance as well. For some of the disks with the strongest UV irradiance, we still clearly detect CO emission. The UV irradiation increases the temperature of the disk both in the dust and the gas, which is used to explain the bright CO emission seen in irradiated T Tauri disks due to less freeze-out (Boyden & Eisner 2020; Ballering et al. 2023). But for Herbig

disks the star dominates: using eq. (2) from Ballering et al. 2023, the Herbig disk needs to be within (a projected distance of) ~ 0.3 pc of an O-star (which none of our disks are) for the temperature set by UV irradiation to dominate over the temperature set by the stellar luminosity (see eq. (4.2)). Especially HD 245185 is of note, for which strong ^{12}CO emission has been detected with ALMA (Ansdell et al. 2020), even though it has one of the highest irradiances of the sample used in our work. This might be indicative of a chance alignment, and that the Herbig disk is actually further away from the O-star than it seems. Placing HD 245185 at the same distance as the shell seen around λ Ori (Figs. 4.1, 4.5), results in a distance of ~ 20 pc, instead of less than 1 pc. This would decrease the irradiance to negligible values of around 2-4 G_0, aligning the disk mass with the seen trend. The other high disk masses might therefore also be chance alignments. Still, disks likely need to be close to the O-star for their chemistry to be affected by UV irradiation (Ramírez-Tannus et al. 2023; Díaz-Berríos et al. 2024).

4.4.3   Comparison to scattered-light data

Recently Valegard et al. (2024) published a survey of disks in Orion observed in scattered light imaging with SPHERE/VLT. This survey was done as part of the DESTINYS program (recent papers include Garufi et al. 2024; Ginski et al. 2024; Valegard et al. 2024). The survey consists of 23 stars in Orion with spectral types ranging from A0 to K6. Out of the 23 disks 10 have a detection of a disk, and four of these have a clearly resolved disk.

Out to Orion only few disks are possible to resolve with SPHERE. In the sample of Valegard et al. (2024), four disks are resolved: HD 294260, V1012 Ori, V351 Ori, and V599 Ori. Out of these four disks, three are Herbig disks and some of the more massive disks in our sample. HD 294260 is a intermediate mass T Tauri (IMTT) star, which are precursors of Herbig stars (Valegård et al. 2021). The disk around IMTT stars show similar characteristics as the disks around Herbig stars, with the same dust mass distribution (Stapper et al. subm.). The dust mass of HD 294260 is found to be 74.4$\pm$7.9 M$_{\oplus}$ (Stapper et al. subm.). Other disks resolved with scattered-light imaging in Orion include HD 34282 (de Boer et al. 2021) and HD 290764 (Ohta et al. 2016). All of these disks are around intermediate mass stars.

Some of these disks also show clear signs of asymmetries in the polarized scattered light. V351 Ori shows multiple asymmetric structures (Wagner et al. 2020; Valegard et al. 2024), in particular arc-like structures in the outer ring of the disk. V599 Ori has indications of a spiral arm, the inner disk is brighter in the southeast and the outer disk in the northwest (Valegard et al. 2024). These types of structures are generally explained by giant planets residing in these disks (see for an overview Bae et al. 2023). As around intermediate mass stars giant exoplanet formation is highest (e.g., Johnson et al. 2007, 2010; Nielsen et al. 2019), the fact the massive and largest disks with substructures found around intermediate mass disks could be related to this. As Stapper et al. (2022) and others (e.g., Maaskant et al. 2013) proposed, the evolution of Herbig disks is likely significantly influenced by these giant exoplanets, which can keep the disk large and bright. A similar hy-

pothesis was put forward by Ansdell et al. (2020) for the HD 245185 disk, which is by an order of magnitude the most massive disk in λ Orionis. The host star of the HD 245185 disk was found to also be depleted in refractory elements, suggesting giant planet formation occurring in this disk (Kama et al. 2015; Guzmán-Díaz et al. 2023). Similarly, V599 Ori was also found to be depleted in refractory elements (Guzmán-Díaz et al. 2023). While these large disks are not lacking around T Tauri disks (e.g., V1094 Sco van Terwisga et al. 2018, IM Lup (Andrews et al. 2018a), Sz 98 Ansdell et al. 2016), they do seem to be more common around Herbig disks.

4.5   Conclusion

In this paper we present the first complete survey of Herbig disks in a single region. We present new NOEMA observations of 25 Herbig disks which, together with 10 archival ALMA observations, cover all Herbig disks in Orion. Based on these observations we conclude the following:

1. The Herbig disks in Orion are found to have a median dust disk mass of 11.7 $M_\oplus$, ranging from 91 $M_\oplus$ down to an upper limit of < 1.2 $M_\oplus$.

2. Comparing the Herbig disks in Orion to previous surveys done in Orion, we find a higher mean dust disk mass compared to the T Tauri disks. While for Herbig disks 50% of the disks have masses higher than 10 $M_\oplus$, for T Tauri disks this is 25% or lower. This difference is especially apparent when considering that the Herbig disks have a median age of 5.1 Myr, while the star-forming regions in Orion are as young as 0.5 Myr.

3. There are no significant differences between the dust mass distribution of the Orion Herbig disk population and those observed with ALMA across the sky (Stapper et al. 2022). The only difference appears due to the lack of a few individual objects with particularly large disk masses (beyond ~ 150 $M_\oplus$), that are absent from the Orion sample.

4. Herbig disks show a steeper trend between disk dust mass and UV irradiation compared to T Tauri disks. A slope of -5.2 is found, compared to 1.3 for T Tauri disks.

5. The largest disks in the recent SPHERE survey of disks in Orion of Valegard et al. (2024) are Herbig disks and some of the most massive disks in our sample, likely relating to giant exoplanet formation occurring in these disks.

This work has shown the importance of complete studies of Herbig disks. As we are going towards more complete and better defined samples of Herbig stars, we should push for complete millimeter observations of the Herbig disk population.

PART II

Evolution and structure of
Herbig disks

The $\dot{M}$–M_{disk} relationship for Herbig Ae/Be stars: a lifetime problem for disks with low masses?

S. L. Grant, L. M. Stapper, M. R. Hogerheijde, E. F. van Dishoeck,
S. Brittain, M. Vioque

Abstract

The accretion of material from protoplanetary disks onto their central stars is a fundamental process in the evolution of these systems and a key diagnostic in constraining the disk lifetime. We analyze the relationship between the stellar accretion rate and the disk mass in 32 intermediate-mass Herbig Ae/Be systems and compare them to their lower-mass counterparts, T Tauri stars. We find that the $\dot{M}$–M_{disk} relationship for Herbig Ae/Be stars is largely flat at $\sim 10^{-7}$ $M_\odot$ yr^{-1} across over three orders of magnitude in dust mass. While most of the sample follows the T Tauri trend, a subset of objects with high accretion rates and low dust masses are identified. These outliers (12 out of 32 sources) have an inferred disk lifetime of less than 0.01 Myr and are dominated by objects with low infrared excess. This outlier sample is likely identified in part by the bias in classifying Herbig Ae/Be stars, which requires evidence of accretion that can only be reliably measured above a rate of $\sim 10^{-9}$ $M_\odot$ yr^{-1} for these spectral types. If the disk masses are not underestimated and the accretion rates are not overestimated, this implies that these disks may be on the verge of dispersal, which may be due to efficient radial drift of material or outer disk depletion by photoevaporation and/or truncation by companions. This outlier sample likely represents a small subset of the larger young, intermediate-mass stellar population, the majority of which would have already stopped accreting and cleared their disks.

5.1   Introduction

Circumstellar disks are the birthplaces of planets and those planets must form in the first several million years of the disk lifetime before the disk dissipates. It is then important to understand how disks evolve and to characterize how that evolution impacts planet formation and vice versa. The rate at which material is being accreted onto the star from the disk and the disk mass are two key parameters in assessing the evolutionary state of a system. These two diagnostics probe different regions in the disk: the accretion rate traces the innermost star-disk connection and the disk mass traces the mass reservoir at tens to hundreds of au.

Despite the contrasting scales that the accretion rate ($\dot{M}$) and disk mass ($M_{\rm disk}$) probe, it has been predicted that the two quantities should be related and can give an estimate of the disk lifetime, $t_{\rm disk} = M_{\rm disk}/\dot{M}$ (e.g. Hartmann et al. 1998; Jones et al. 2012; Lodato et al. 2017; Rosotti et al. 2017; Sellek et al. 2020; Manara et al. 2022). The transfer of material inward from the outer disk can be affected by a variety of factors, including the formation of pressure traps, stellar irradiation and photoevaporation, MHD disk winds, and the presence of giant planets and companions (e.g., Jones et al. 2012; Rosotti et al. 2017; Tabone et al. 2022b; Zagaria et al. 2022). Deviations from the nominal $\dot{M}$–$M_{\rm disk}$ relationship can then indicate the presence of one or more of these processes.

Recent observational efforts conducted at optical and near-infrared wavelengths paired with the numerous outer disk surveys, particularly with ALMA, have led to large populations of disks with both $\dot{M}$ and $M_{\rm dust}$ measurements (Mendigutía et al. 2012; Manara et al. 2016, 2020; Ansdell et al. 2017; Mulders et al. 2017; Grant et al. 2021; Testi et al. 2022; Fiorellino et al. 2022). However, these surveys have greatly favored low-mass T Tauri stars, with the exception of Mendigutía et al. (2012) which was carried out before ALMA was operational. The more massive Herbig Ae/Be stars, by comparison, lack homogeneous (sub-)millimeter observations (Stapper et al. 2022), while they are well-covered in surveys focusing on accretion signatures (e.g., Donehew & Brittain 2011; Fairlamb et al. 2015, 2017; Grant et al. 2022; Vioque et al. 2022). The disks around these intermediate-mass stars are thought to form giant exoplanets more efficiently than low-mass stars (Johnson et al. 2010; Reffert et al. 2015). Indeed, van der Marel & Mulders (2021) use disk properties to tentatively point to a connection between stellar mass and giant planet formation. Therefore, it is essential to understand disk evolution and planet formation in the disks around intermediate-mass stars. In this work, we take these two key disk diagnostics, $\dot{M}$ and $M_{\rm disk}$, to study the $\dot{M}$–$M_{\rm disk}$ relationship in a sample of 32 Herbig Ae/Be objects.

5.2   Sample, mass accretion rates, and dust masses

5.2.1   Sample

Our sample is compiled from the ALMA-observed sample of Stapper et al. (2022), which provides the dust masses used in this work. Their sample consists of the

Table 5.1: Properties of our sample. Accretion rates with [a] come from Wichittanakom et al. (2020), [d] from Garcia Lopez et al. (2006), and the rest are from Grant et al. (2022). Groups marked with [b] are from Guzmán-Díaz et al. (2021), [c] from Boersma et al. (2009), and the rest are from Grant et al. (2022). Dust masses are from Stapper et al. (2022). Binary information is from the compilation in Vioque et al. (2018).

Source	RA	Dec	M_* $(M_\odot)$	$\log_{10}(L_*)$ $(L_\odot)$	Age (Myr)	$\log_{10}(\dot{M})$ $(M_\odot/\mathrm{yr})$	M_{dust} $(M_\oplus)$	Group	Binary
AB Aur	04:55:45.9	+30:33:04	$2.152^{+0.359}_{-0.214}$	$1.61^{+0.19}_{-0.21}$	$4.05^{+1.43}_{-1.49}$	-6.13 ± 0.27 [a]	11.8 ± 1.2	I	Yes
AK Sco	16:54:44.8	-36:53:19	$1.401^{+0.070}_{-0.070}$	$0.62^{+0.03}_{-0.01}$	$8.382^{+1.72}_{-0.42}$	<-8.06	6.1 ± 0.6	II	Yes
BF Ori	05:37:13.3	-06:35:01	$1.807^{+0.090}_{-0.090}$	$1.29^{+0.06}_{-0.05}$	$6.38^{+0.32}_{-0.46}$	-7.28 ± 0.39	1.1 ± 0.1	II	
CQ Tau	05:35:58.5	+24:44:54	$1.468^{+0.189}_{-0.109}$	$0.87^{+0.18}_{-0.12}$	$8.898^{+2.80}_{-2.52}$	<-8.33	44.2 ± 4.8	I	Yes
HD 100453	11:33:05.5	-54:19:29	$1.251^{+0.063}_{-0.063}$	$0.79^{+0.02}_{-0.00}$	$6.528^{+0.45}_{-0.49}$	-8.32 ± 0.51	17.5 ± 1.8	I	Yes
HD 100546	11:33:25.3	-70:11:41	$2.055^{+0.103}_{-0.123}$	$1.37^{+0.07}_{-0.05}$	$5.48^{+1.41}_{-0.77}$	-6.95 ± 0.36	38 ± 3.9	I	
HD 104237	12:00:04.9	-78:11:35	$1.849^{+0.092}_{-0.092}$	$1.33^{+0.04}_{-0.01}$	$5.48^{+0.27}_{-0.4}$	-6.43 ± 0.34	10.5 ± 1.1	II	Yes
HD 135344B	15:15:48.4	-37:09:16	$1.432^{+0.072}_{-0.072}$	$0.79^{+0.03}_{-0.04}$	$8.927^{+0.45}_{-0.91}$	<-8.15	35.2 ± 3.8	I	Yes
HD 139614	15:40:46.4	-42:29:54	$1.481^{+0.074}_{-0.074}$	$0.77^{+0.03}_{-0.01}$	$14.49^{+1.41}_{-3.60}$	-8.14 ± 1.03	41.7 ± 4.3	I	
HD 141569	15:49:57.7	-03:55:17	$1.860^{+0.093}_{-0.093}$	$1.22^{+0.03}_{-0.03}$	$8.616^{+11.38}_{-1.19}$	-7.76 ± 0.65	0.36 ± 0.04	II	Yes
HD 142527	15:56:41.9	-42:19:24	$1.613^{+0.124}_{-0.081}$	$0.96^{+0.03}_{-0.00}$	$6.627^{+0.33}_{-1.55}$	<-7.29	214.9 ± 22.1	I	Yes
HD 142666	15:56:40.0	-22:01:40	$1.493^{+0.075}_{-0.075}$	$0.94^{+0.04}_{-0.05}$	$9.33^{+0.77}_{-0.47}$	-7.63 ± 1.26	25.1 ± 2.6	II	
HD 163296	17:56:21.3	-21:57:22	$1.833^{+0.092}_{-0.092}$	$1.20^{+0.06}_{-0.03}$	$7.598^{+1.05}_{-1.22}$	-7.27 ± 0.75	46.7 ± 5	II	
HD 169142	18:24:29.8	-29:46:50	$2.000^{+0.131}_{-0.128}$	$1.31^{+0.12}_{-0.22}$	$8.984^{+11.02}_{-3.90}$	-7.09 ± 0.21 [a]	22.9 ± 2.4	I [b]	
HD 176386	19:01:38.9	-36:53:27	$2.299^{+0.143}_{-0.299}$	$1.58^{+0.12}_{-0.22}$	$4.05^{+15.95}_{-0.57}$	-7.08 ± 0.2 [a]	<0.06	II [c]	Yes
HD 245185	05:35:09.6	+10:01:51	$1.923^{+0.177}_{-0.096}$	$1.29^{+0.13}_{-0.10}$	$7.643^{+12.36}_{-2.56}$	-6.85 ± 0.36	41.5 ± 7.6	I	Yes
HD 290764	05:38:05.3	-01:15:22	$1.691^{+0.128}_{-0.085}$	$1.18^{+0.09}_{-0.09}$	$6.89^{+0.54}_{-1.41}$	-7.0 ± 0.39	90.3 ± 11.8	I	
HD 31648	04:58:46.3	+29:50:37	$1.779^{+0.131}_{-0.089}$	$1.27^{+0.14}_{-0.05}$	$6.201^{+0.31}_{-1.12}$	-6.57 ± 0.17 [a]	70.9 ± 7.7	II [b]	
HD 34282	05:16:00.5	-09:48:35	$1.450^{+0.072}_{-0.072}$	$0.98^{+0.05}_{-0.04}$	$6.54^{+2.41}_{-0.63}$	-7.5 ± 0.73	86.8 ± 9.7	I	Yes
HD 36112	05:30:27.5	+19:25:57	$1.564^{+0.108}_{-0.108}$	$1.04^{+0.12}_{-0.08}$	$8.289^{+0.41}_{-1.40}$	-7.32 ± 0.4	18.8 ± 2	I	Yes
HD 37258	05:36:59.3	-06:09:16	$1.881^{+0.136}_{-0.108}$	$1.24^{+0.12}_{-0.10}$	$7.929^{+12.07}_{-2.45}$	-6.98 ± 0.37	2.4 ± 0.4	II	Yes
HD 53367	07:04:25.5	-10:27:16	12^{+4}_{-}	$3.13^{+0.23}_{-0.17}$	$0.08^{+0.08}_{-0.08}$	-6.97 ± 0.45	<0.05	I	Yes

Table 5.1: Continued.

Source	RA	Dec	M_* ($M_\odot$)	$\log_{10}(L_*)$ ($L_\odot$)	Age (Myr)	$\log_{10}(\dot{M})$ ($M_\odot/\mathrm{yr}$)	M_{dust} ($M_\oplus$)	Group	Binary
HD 58647	07:25:56.1	-14:10:44	$3.867^{+0.333}_{-0.193}$	$2.44^{+0.11}_{-0.09}$	$0.8372^{+0.12}_{-0.18}$	-5.84 ± 0.31	1 ± 0.1	II	Yes
HD 9672	01:34:37.9	-15:40:35	$1.810^{+0.090}_{-0.090}$	$1.17^{+0.09}_{-0.02}$	$6.89^{+0.34}_{-0.51}$	-7.8 ± 1.0 [a]	0.13 ± 0.01	II [b]	
HD 97048	11:08:03.2	-77:39:17	$2.252^{+0.113}_{-0.135}$	$1.54^{+0.07}_{-0.06}$	$4.37^{+1.11}_{-0.32}$	-6.49 ± 0.34	155.9 ± 16	I	Yes
HR 5999	16:08:34.3	-39:06:19	$2.432^{+0.122}_{-0.122}$	$1.72^{+0.05}_{-0.04}$	$2.729^{+0.26}_{-0.35}$	-6.0 ± 0.11 [a]	4 ± 0.4	II [b]	Yes
MWC 297	18:27:39.5	-03:49:52	$16.901^{+1.868}_{-1.215}$	$4.59^{+0.12}_{-0.12}$	$0.02754^{+0.006}_{-0.006}$	<-5.89	65.7 ± 9.6	I	Yes
TY CrA	19:01:40.8	-36:52:34	$2.063^{+0.223}_{-0.190}$	$1.41^{+0.14}_{-0.23}$	$6.38^{+13.62}_{-2.01}$	<-8.31 [d]	0.10 ± 0.01	I [b]	Yes
V1787 Ori	05:38:09.3	-06:49:17	$1.659^{+0.094}_{-0.083}$	$1.15^{+0.11}_{-0.09}$	$7.43^{+0.59}_{-1.05}$	-7.17 ± 0.38	24.2 ± 2.9	II	
V599 Ori	05:38:58.6	-07:16:46	$2.029^{+0.101}_{-0.101}$	$1.44^{+0.06}_{-0.06}$	$4.289^{+0.42}_{-0.54}$	-6.71 ± 0.37	75 ± 8.6	I	
V718 Sco	16:13:11.6	-22:29:07	$1.605^{+0.080}_{-0.080}$	$0.90^{+0.05}_{-0.04}$	$9.804^{+2.80}_{-0.49}$	-7.49 ± 0.23 [a]	11.9 ± 1.3	II [b]	Yes
VV Ser	18:28:47.9	+00:08:40	$2.892^{+0.145}_{-0.145}$	$1.95^{+0.10}_{-0.08}$	$2.77^{+8.13}_{-0.21}$	<-6.14	2.3 ± 0.3	II	

Herbig Ae/Be systems in Vioque et al. (2018) that are within 450 pc and had available ALMA observations (see Stapper et al. 2022 for more details and notes on some excluded objects).

The stellar properties for our sample are listed in Table 5.1 and are largely from Vioque et al. (2018). Thirty-one of our 32 sources have high quality Gaia DR2 parallaxes that were used in Vioque et al. (2018), which are largely consistent with Gaia (E)DR3 (Guzmán-Díaz et al. 2021). One source, HD 53367, was in the low quality sample, and the Gaia DR3 parallax is very different from that of DR2 (parallax of 0.8199±0.2114 milliarcseconds in DR3 and 7.7682±0.7854 milliarcseconds in DR2). We keep this source in our sample, using the stellar parameters based on the Gaia DR2 data, but we urge caution in interpreting the results for this source and we do not include it in fits to the $\dot{M}$–$M_{\rm disk}$ relationship that we present in Section 5.3. The stellar masses range from 1.3 to 16.9 $M_\odot$, but 29 of our 32 sources have stellar masses less than 3 $M_\odot$. Our sample represents a slightly older population, with 27 of our sources having ages greater than 3 Myr. The Meeus et al. (2001) Group determinations, that are determined from the spectral energy distributions (SEDs) and are thought to reflect the dust disk structure (e.g., Meeus et al. 2001; van Boekel et al. 2005; Maaskant et al. 2013; Garufi et al. 2017; Stapper et al. 2022), are largely from the SED analysis of Grant et al. (2022) and Guzmán-Díaz et al. (2021). Our sample is nearly evenly split between Group I (17) and Group II (15) disks.

5.2.2   Mass accretion rates

The accretion rates for our sample come from the works of Grant et al. (2022), Wichittanakom et al. (2020), and Garcia Lopez et al. (2006). Grant et al. (2022) use Brγ observations to derive $L_{\rm Br\gamma}$ which is then converted to an accretion luminosity using the relationship from Fairlamb et al. (2017). Similarly, Wichittanakom et al. (2020) do the same, except using Hα instead of Brγ. Hα and Brγ have a similar spread in the empirical relationship between $L_{\rm line}$ and $L_{\rm acc}$ and are both robust tracers of accretion, even if the line is not generated in the accretion columns (e.g., Mendigutía et al. 2015). For one object, TY CrA, we use the accretion rate from Garcia Lopez et al. (2006). For this target, the Brγ line is in absorption that is mostly consistent with the photosphere, therefore there is only an upper limit on the accretion rate and we do not include it in the $\dot{M}$–$M_{\rm disk}$ fits that we discuss in the rest of the paper.

The median accretion rate in our sample is $\log_{10}(\dot{M}) = -7.09$ (M$_\odot$ yr^{-1}), not including upper limits, with a median log error of 0.37. Both sources of the accretion rate measurements rely on the assumption that magnetospheric accretion is the dominant mechanism in these sources. However, the Herbig Ae/Be stellar mass/effective temperature range is thought to be the regime where magnetospheric accretion may break down to boundary layer accretion due to the weak stellar magnetic fields (e.g., Vink et al. 2002; Donehew & Brittain 2011; Mendigutía et al. 2011; Cauley & Johns-Krull 2014; Wichittanakom et al. 2020; Grant et al. 2022). Based on the findings of Wichittanakom et al. (2020), Grant et al. (2022), and Vioque et al. (2022), the accretion mechanism change may occur at the $\sim$4

$M_\odot$ boundary and only two stars in our sample above this boundary, HD 53367 and MWC 297.

We have no targets with an accretion rate detection below 10^{-9} $M_\odot$ yr^{-1}. One of the criteria needed for Herbig Ae/Be classification is the presence of an accretion tracer, frequently H I lines in emission (e.g., Herbig 1960; The et al. 1994). The use of these lines in identifying Herbig Ae/Be stars is complicated by the fact that these stars have photospheric absorption at those lines and that the depths of the photospheric absorption depends on the stellar effective temperature (Joner & Hintz 2015; Fairlamb et al. 2017). The lower limit on the detectable accretion rate varies with spectral type, the ability to characterize the photosphere, and the measurement method. For example, the lower limit on the measurement of the accretion rate from the veiling of the Balmer jump in the near ultraviolet (NUV) ranges from a few times 10^{-9} $M_\odot$ yr^{-1} for 2 $M_\odot$ Herbig stars to about 10^{-6} $M_\odot$ yr^{-1} for 7 $M_\odot$ Herbig stars (see Figure 5 in Sicilia-Aguilar et al. 2016). If one assumes that the calibration of line luminosity and accretion luminosity inferred from the NUV excess is valid for lower accretion rates, then it is possible to infer lower levels of accretion from spectroscopy of those lines. Fairlamb et al. (2015) also highlight the changing lower accretion limits based on stellar effective temperature (see their Figure 9). From Sicilia-Aguilar et al. (2016) and Fairlamb et al. (2015), an accretion rate of $\sim 10^{-9}$ $M_\odot$ yr^{-1} is generally the lower limit for the lowest stellar mass objects in the Herbig Ae/Be classification. The accretion rate values in this work are all above this level, including the outlier objects that are discussed in Section 5.3. We discuss the lack of low accretion rate objects in more detail in Section 5.4.2.

5.2.3 Dust masses

The dust masses in this work were determined in Stapper et al. (2022) using archival ALMA observations. The spatial resolution in these observations ranges from $0.02''$ to $1.84''$. Our sample is evenly split between resolved and unresolved disks, although more Group I disks are resolved (11/17) than Group II (5/15). The average spatial resolution for the Group I disks is $0.''37$, while the average is $0.''88$ for the Group II disks. The disk integrated millimeter fluxes were converted to dust masses using a dust temperature that is scaled by the stellar luminosity (Andrews et al. 2013). The adopted dust opacities, κ_ν were determined by a power-law such that $\kappa_\nu = 10$ cm^{2}g^{-1} at 1000 GHz (Beckwith et al. 1990) and scales with an index of 1. In this work we assume that the disk mass is 100 times the dust mass, however, we discuss the implications of this assumption in Section 5.4.1.

5.3   Results

The $\dot{M}-M_{\mathrm{disk}}$ relationship for our Herbig Ae/Be sample is presented in Figure 5.1. We fit the Herbig Ae/Be $\dot{M}-M_{\mathrm{disk}}$ relationship using the method from Kelly (2007)[1], taking errors on $\dot{M}$ and M_{disk} and upper limits into account (Testi et al.

---

[1]`https://linmix.readthedocs.io`
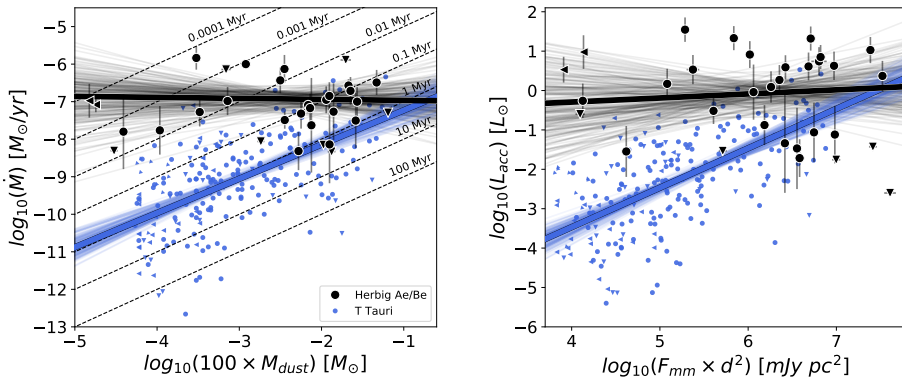
Figure 5.1: Left: The $\dot{M}$–M_{disk} relationship for our sample of Herbig Ae/Be stars (black points) and the T Tauri stars from Testi et al. (2022) (blue points). We have excluded the few sources in the Testi et al. (2022) sample that have $M_* > 1.5\ M_\odot$. The black line is the best fit for the Herbig Ae/Be sample and the blue line is the best fit for the T Tauri sample. The thin black lines and thin blue lines are 200 samples of the posterior for the fits to the Herbig Ae/Be and T Tauri points, respectively. Upper limits on the dust mass are shown as leftward facing triangles and upper limits on the accretion rate are shown as downward facing triangles. If both the accretion rate and dust mass measurements are upper limits, the triangle points to the lower left. The dotted gray lines show different disk lifetimes. The Herbig Ae/Be disks are outliers above the already large scatter seen for the lower mass stars. Right: The relationship between the accretion luminosity and the millimeter flux (normalized by the distance).

2022; Fiorellino et al. 2022). We find that the $\dot{M}$–M_{disk} relationship in our Herbig Ae/Be sample is $\log_{10}(\dot{M})$=(-0.03 ± 0.21)$\log_{10}(M_{\mathrm{disk}})$+(-6.99 ± 0.52), a mostly flat relationship over three orders of magnitude in dust mass. This $\dot{M}$–M_{disk} relationship is drastically different from that of low-mass systems, in particular the large sample compiled and analyzed by Testi et al. (2022) (Figure 5.1). At the highest disk masses, the Herbig Ae/Be sample largely overlaps with the T Tauri population, although at the higher end of the accretion rate range. However, at the low disk mass end, the Herbig Ae/Be objects lie at and well above the upper end of the T Tauri star accretion rate distribution. The flat relationship that we find for our sample is likely influenced by the fact that Herbig Ae/Be stars require accretion signatures to be classified as such and generally accretion cannot be measured below $\sim 10^{-9}\ \mathrm{M_\odot\ yr^{-1}}$ in intermediate-mass stars. Therefore we lack objects with low accretion rates that may steepen the relationship for intermediate-mass stars in general. While this lower limit is important to keep in mind when interpreting the Herbig Ae/Be $\dot{M}$–M_{disk} relationship, the flatness of the observed relationship highlights the objects with high accretion rates and low dust masses as clear outliers.

Also shown in Figure 5.1 is the relationship between the accretion luminosity and the millimeter flux (normalized by the distance) and the same flat trend is
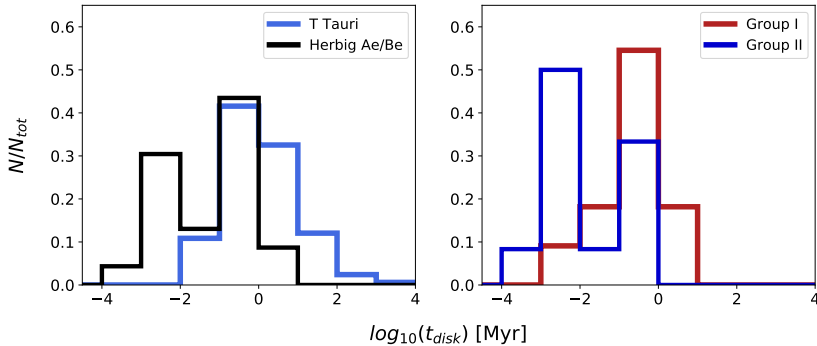
Figure 5.2: Left: The t_{disk} distribution for T Tauri disks from Testi et al. (2022) (blue) and our Herbig Ae/Be sample (black). We have removed any targets from the Testi et al. (2022) sample that have $M_* > 1.5\ M_\odot$. Objects with upper limits on $\dot{M}$ or M_{disk} are not included. A two-sample Kolmogorov-Smirnov test returns a p-value of 2.7×10^{-7}, indicating that the distributions are drawn from different populations. Right: The t_{disk} distribution for Group I disks (red) and Group II disks (blue). A two-sample Kolmogorov-Smirnov test returns a p-value of 0.02, indicating that the distributions may be drawn from different populations.

present for the Herbig Ae/Be stars, while the T Tauri stars again show a steeper relationship. The fact that these more "direct" quantities show the same relationship indicates that any assumptions going into the determination of the accretion rate and the disk mass (e.g., the dust temperature, magnetospheric accretion being the only source of emission used in determining the accretion rates, etc.) are not the root cause of the flat $\dot{M}$–M_{disk} relationship for the Herbig Ae/Be sample.

The inferred disk lifetime, $t_{\mathrm{disk}} = M_{\mathrm{disk}}/\dot{M}$, is a good measure of how much a given disk deviates from the relationship seen for the T Tauri disks, which cluster around the $t_{\mathrm{disk}} \sim 1$ Myr line. The low disk mass objects in our sample have accretion rates that indicate that the disk will be depleted on much shorter timescales, with 12 of our 32 disks having inferred disk lifetimes of less than 10,000 years (0.01 Myr). We show the distribution of t_{disk} in Figure 5.2, comparing the T Tauri sample of Testi et al. (2022) to our sample of Herbig Ae/Be sources. A two-sample Kolmogorov-Smirnoff test (Virtanen et al. 2020) returns a p-value of 2.7×10^{-7}, indicating that the T Tauri and Herbig Ae/Be samples are drawn from different populations. Figure 5.2 also shows the Herbig Ae/Be distribution when broken into Group I and Group II sources, showing that the Group II sources are clearly bimodal, while the Group I distribution is unimodal. A two-sample Kolmogorov-Smirnoff test (Virtanen et al. 2020) returns a p-value of 0.02, indicating that the distributions may be drawn from different populations. We show the $\dot{M}$–M_{disk} relationship broken up into Group I and Group II objects in Figure 5.3.

In the Appendix we discuss each of the 12 low disk mass sources that stand out in the $\dot{M}$–M_{disk} relationship. In particular, we compare our $\dot{M}$ and M_{disk} values to previous values in the literature. We find that our accretion rate val-

ues are consistent with those in the literature, subject to differences in accretion determination and variability. In contrast, our disk masses tend to be lower, due to a combination of higher resolution observations, which reduce the amount of contamination from nearby sources/cloud emission, and higher dust temperatures. For instance, this population of high accretion rate, low disk mass objects was not seen in the $\dot{M}-M_{\mathrm{disk}}$ analysis of Mendigutía et al. (2012), which found that the $\dot{M}-M_{\mathrm{disk}}$ relationship for Herbig Ae/Be stars was in line with that of the T Tauri stars. Nine of our objects overlap with their sample and we have compared the accretion rates and dust masses used in each work. Their accretion rates are within an order of magnitude of ours and are evenly split between being higher and lower than our values. The Stapper et al. (2022) disk mass values are lower than those in Mendigutía et al. (2012) in 6 sources (one has a higher value in our work, one is an upper limit in Mendigutía et al. 2012, and one has no disk mass determination in Mendigutía et al. 2012 due to a lack of millimeter flux). This is due to two differences: 1) the millimeter fluxes from ALMA used by Stapper et al. (2022) are lower in 6 out of 7 targets, likely due to higher angular resolution observations which suffer less from contamination, and 2) higher dust temperatures used by Stapper et al. (2022). The dust temperatures in Stapper et al. (2022) were determined by scaling by the stellar luminosity while the temperatures in Mendigutía et al. (2012) were determined from graybody fits to photometry at wavelengths longer than 350 μm. We note that if we adopt a uniform dust temperature of 20 K, as is commonly done for lower-mass stars, the disk lifetimes increase, but not enough to remove the low-inferred disk lifetimes, with all 12 low disk mass sources having disk lifetimes still less than 0.1 Myr. See the Appendix for further comparison of various disk mass determinations in the literature for these 12 targets.

5.4 Discussion

In this sample of Herbig Ae/Be objects, we find that the $\dot{M}-M_{\mathrm{disk}}$ relationship is relatively flat. While the majority of objects fall along the nominal, steep $\dot{M}-M_{\mathrm{disk}}$ relationship of the T Tauri stars, the relationship in our sample is being affected by a subset of objects appearing to have accretion rates inconsistent with their disk masses, such that the disks have a very short inferred lifetime. This outlier sample is likely present due to the biases in Herbig Ae/Be classification, which are limited to objects with accretion rates above $\sim 10^{-9}$ $M_{\odot}$ yr^{-1}. Here we focus on these short lifetime "outlier" objects, first to discuss factors that would move these targets into the nominal $\dot{M}-M_{\mathrm{disk}}$ regime, and second how to explain these targets if their disk masses and accretion rates are not under- and overestimated, respectively.

5.4.1 Factors that would move the outliers into the general spread

Here, we consider the possibility that either the accretion rates or the dust masses for the low-lifetime objects may be over and under estimated, respectively.

- Optical depth: In the scenario where Group II disks are undergoing efficient radial drift, the dust disks will be compact and may be optically thick at millimeter wavelengths which would then lead us to underestimate the dust, and therefore disk, masses (Stapper et al. 2022; Liu et al. 2022). Modeling efforts, paired with observations at centimeter wavelengths which may be optically thin if the millimeter wavelengths are not, are needed to establish if optically thick emission is the cause of the low disk mass determinations. However, based on the gas masses available for some of these objects (next point), it is unlikely that this is the case for all of these sources.

- Gas mass: We are inferring a disk mass based on a gas-to-dust mass ratio of 100. If the true gas-to-dust mass ratio is higher, then our "low-mass" disks may be high enough to move the objects to the right enough in the $\dot{M}-M_{\mathrm{disk}}$ plane to make the relationship more consistent with what is seen for lower mass stars (e.g., Sellek et al. 2020). Note that the same problem may exist for low-mass stars, even when taking into account the freeze-out of common gas tracers (e.g., Miotello et al. 2023). We find gas mass or gas-to-dust mass ratios available in the literature for 11 of our 32 objects (van der Marel et al. 2016; Boehler et al. 2017; Miley et al. 2018; Yen et al. 2018; Kama et al. 2020; Rivière-Marichalar et al. 2022). Of these, 5 are upper limits which are above, and therefore consistent with, the disk masses that we use here. There are 4 objects for which the gas mass, or gas-to-dust mass ratios, are below the values inferred from the dust continuum. Finally, two objects have gas masses that are above what we assume here, neither of which changes the disk lifetime substantially. Further discussion of gas masses for the low dust mass, high accretion rate objects is given in the Appendix (Additionally, Stapper et al. in prep will provide a detailed analysis of the gas tracers for this sample). Further careful analysis of gas observations of the disks around Herbig Ae/Be stars is needed to determine the true disk mass, in particular, using gas tracers that are themselves optically thin (Booth et al. 2019). With these gas masses, we would then be able to determine whether the "low-mass" disks are really on the verge of dissipation or whether there is still a large gas reservoir.

- Disk winds: There is evidence that disk winds contribute to the Brγ line that is largely used to derive the accretion rates in this work (e.g., Kraus et al. 2008; Kurosawa et al. 2016; Hone et al. 2019; Wojtczak et al. 2022). If this is the case, then a given accretion rate used here may be artificially inflated. If we instead take accretion rates determined using ultraviolet observations from Donehew & Brittain (2011), Mendigutía et al. (2011), and Fairlamb et al. (2015), which are unaffected by any contribution from a disk wind, the mismatch in slope between T Tauri stars and the Herbig Ae/Be objects is even larger. For example, Mendigutía et al. (2011) use the Balmer discontinuity and find an accretion rate of 1.45×10^{-5} M$_\odot$ yr^{-1} for HD 58647, a factor of 10 higher than the value we use that was determined from Brγ. On the other hand, Brittain et al. (2007) found an accretion rate of 3.5×10^{-7} M$_\odot$ yr^{-1} using Brγ. Despite the discrepancies in the accretion rate, none of

these values solve the short lifetime implied for this disk which has a dust mass of 1 ± 0.1 $M_\oplus$. With the Brittain et al. (2007) accretion rate the disk lifetime is 860 years, with the Grant et al. (2022) accretion rate adopted here it is 206 years, and with the Balmer discontinuity accretion rate from Mendigutía et al. (2011) it is only 21 years.

To summarize, if all of the outlier Group II disks are extremely optically thick, have gas-to-dust ratios that are much larger than the standard interstellar medium value of 100, or have disk winds that contribute significantly to the accretion tracers used to determine the accretion rate, these objects could really be in the nominal disk lifetime regime. While this needs to be investigated further, literature values of the gas mass and accretion rates determined from ultraviolet observations, which do not suffer from contributions from disk winds, indicate that the trends we are seeing are robust.

5.4.2   Making sense of the outliers

If the mass accretion rates, dust masses, and gas-to-dust ratios are not wildly off due to the factors discussed above, how might we explain this low-lifetime population of disks? Either these sources are rapidly depleting their disks and we are observing them just as they are about to dissipate, or we are witnessing these sources undergoing variable accretion and happen to be catching them at a point of high accretion that will then decrease before the disk is fully dissipated. We explore these options here.

The low disk lifetime objects are predominantly Group II disks. Our understanding of what these group classifications means has evolved significantly with additional observations and analysis since the classification by Meeus et al. (2001). Maaskant et al. (2013), Garufi et al. (2017), and Stapper et al. (2022) all find evidence for large cavities in the disks of Group I objects. Additionally, Stapper et al. (2022) find that the Group I disks have higher dust masses than Group II disks, with Group II disks potentially unable to form giant planets at large radii, resulting in efficient radial drift and compact disks. This agrees with the interpretation of Kama et al. (2015) and Guzmán-Díaz et al. (2023), who found that refractory elements were depleted in the photospheres of Group I objects relative to Group II disks, suggesting dust trapping in Group I disks by giant planets. The dust mass difference is the source of the difference in the $\dot{M}-M_{\mathrm{disk}}$ relationship, as the accretion rates have been found to be consistent between Group I and II systems (Mendigutía et al. 2012; Banzatti et al. 2018; Grant et al. 2022).

If we apply the interpretations of Group I and Group II disks as being gapped and potentially hosting giant planets at large radii vs. being unable to form giant planets at large radii and thus having radially compact disks, then the difference in the $\dot{M}-M_{\mathrm{disk}}$ relationship becomes more clear (Figure 5.3). In this scenario Group I disks form giant planets, clearing large gaps in the gas and dust and are surrounded by dust rings at large radii (see the ALMA continuum images in Figure 5.3). If Group II disks are not able to form giant planets, then they are unable to trap gas or dust in the outer disk, resulting in a rapid inflow of material to the inner disk which maintains a high accretion rate. It is unclear
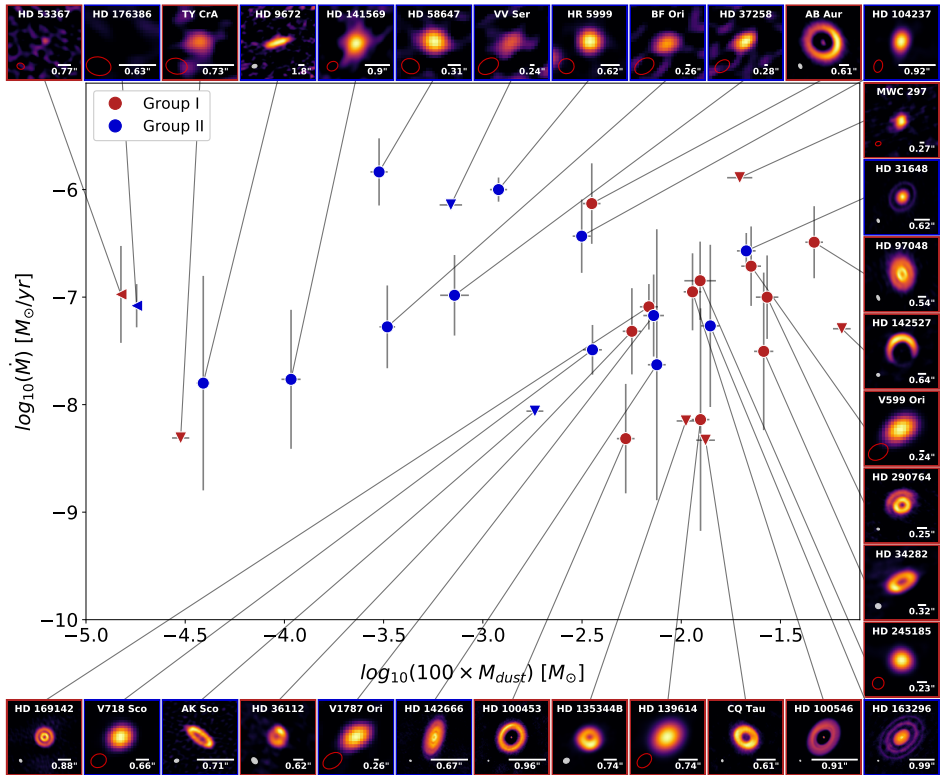
Figure 5.3: The $\dot{M}$–M_{disk} relationship for the Herbig Ae/Be stars broken up by group classification (Group I sources in red and Group II sources in blue). Upper limits are the same as in Figure 5.1. ALMA continuum images from Stapper et al. (2022) are shown for each object with a 100 au scale bar and the beam at the bottom of each image. If the disk is unresolved in the ALMA observations, the beam is shown in red.

when these systems will then begin to decrease in accretion rate and how rapid that decrease is. This would result in radially compact dust disks for the Group II sources, but higher resolution observations are needed to confirm, as none of the low disk lifetime (<0.01 Myr) Group II disks are currently resolved (Figure 5.3). The Group II disks have an average spatial resolution in the ALMA observations of 0.″88, compared to 0.″37 for the Group I disks. Additionally, comparing the gas and dust radii will be crucial for determining if efficient radial drift can explain these systems (e.g., Trapman et al. 2019; Toci et al. 2021).

Other factors that can result in the low disk masses for these objects could come from outer disk depletion from photoevaporation and/or due to multiplicity. If these objects are close to nearby massive stars, the extreme irradiation environments can strip away material, leaving the outer disk depleted (e.g., Mann et al. 2014; Ansdell et al. 2017; Eisner et al. 2018; Winter et al. 2018). Multiplicity has also been shown to impact outer disk evolution, resulting in truncation of the disk (Manara et al. 2019b; Panić et al. 2021; Zagaria et al. 2022). If any companions are massive stars themselves, then these disks may doubly suffer from truncation and photoevaporation.

Twenty of the 32 objects in our sample are known binaries, however, the fraction could be higher given the limited surveys that have searched for multiple systems. To identify the binaries in this sample, we use the binary information from Vioque et al. (2018), largely collected from Leinert et al. (1997), Baines et al. (2006), and Wheelwright et al. (2010). There are two interesting examples in our sample to study of the effects of multiplicity and photoevaporation: the TY CrA/HD 176386 and HR 5999/HR 6000 systems. TY CrA is in a close triple, if not quadruple, system (e.g., Vaňko et al. 2013), and is close to HD 176386, another target in our sample which has a low inferred disk lifetime, and is also a binary. The second example comes from HR 5999, which is itself a binary and is 45″ ($\sim$7000 au at a distance of 158 pc) to HR 6000, an early A-type star with no evidence for a disk (Stelzer et al. 2009). The low disk masses of these systems may be due to photoevaporation and/or truncation from their companions. High spatial resolution observations, in both the gas and dust, paired with photoevaporation and dynamic truncation models (e.g., Rosotti & Clarke 2018) will help to distinguish the effects of binarity and photoevaporation in these multiple systems.

If these disks are on the verge of dissipation, why do we see them at all? Either these disks are going through an accretion outburst such that despite their low disk masses, we are still able to classify them as Herbig Ae/Be stars, or these high accretion rate, low disk mass objects make up only a small portion of the young, intermediate-mass young stellar object population.

The fact that low $\dot{M}$ targets are not in our sample is not surprising: Herbig Ae/Be stars are, in part, identified due to the presence of accretion-tracing lines, namely H I lines in emission (e.g., Herbig 1960; The et al. 1994). In practice, only a handful of Herbig Ae/Be stars have rates lower than 1×10^{-8} M$_\odot$ yr^{-1} (7/267 in the sample of Vioque et al. 2022, 10/102 in the sample of Grant et al. 2022). Mooley et al. (2013) searched for such objects in the Taurus star forming region. These authors identify three B-type stars and two A-type stars that are probable members. They identify two other stars that are plausible members. Thus, half

of the A and B stars in this star-forming region do not show obvious signatures of accretion. Iglesias et al. (2023) use a volume-limited sample (out to 300 pc) and find that only six out of 134 targets in their sample of young, intermediate-mass stars ($1.5 \leq M_* \leq 3.5\ M_\odot$) show the accretion signatures needed to designate them as Herbig Ae/Be stars. These results suggest that there is a significant population of A and B stars in our volume (out to 450 pc) that are analogous to the weak lined T Tauri stars. Therefore, the sample of Herbig Ae/Be objects studied in this work may not be representative of the intermediate-mass young stellar object population as a whole, with most of these objects already having dissipated their disks, and thus not meeting the criteria for Herbig Ae/Be objects. Despite this bias, HD 9672 (49 Cet) in our sample is potentially at an intermediate stage, as it has been characterized in different works as a debris disk (Zuckerman & Song 2012), albeit one with a large CO gas content (e.g., Moór et al. 2019; Higuchi et al. 2020), and as a Herbig Ae system (Vioque et al. 2018). Similarly, HD 141569 in our sample, has been considered a "hybrid" disk in the transition phase between a protoplanetary disk and a debris disk (Augereau & Papaloizou 2004; Miley et al. 2018; Di Folco et al. 2020; Gravity Collaboration et al. 2021; Iglesias et al. 2023). These targets may represent the bridge between protoplanetary and debris disks.

The short disk lifetimes inferred in this work have relied on the assumption that the accretion rate is constant in time. However, young stars are known to be variable, with wide-ranging timescales for variability (see the recent review by Fischer et al. 2022). If these low-lifetime targets are undergoing a period of high accretion that will not last, then the disks may not deplete on the short timescales inferred. This has been seen to impact T Tauri stars (Claes et al. 2022), however this variability may not be enough to explain the spread in the accretion rates measured for T Tauri stars (Manara et al. 2022). How this variability might be different for higher mass objects, if it is different at all, is unclear (see the discussion on this topic for Herbig Ae/Be objects in Brittain et al. 2023). Characterizing variability in Herbig Ae/Be objects, and putting them into context with young, diskless A and B stars will be crucial for determining whether the low-lifetime population seen here are simply a subset of the larger population that are undergoing periods of strong accretion and thus are included in Herbig Ae/Be samples.

5.5   Summary and conclusions

We analyze a sample of 32 Herbig Ae/Be objects (1.3 to 16.9 $M_\odot$) to determine the relationship between the accretion rate and the dust disk masses. We find the following:

1. The mass accretion rate is roughly constant with disk mass, as probed by the dust mass, for Herbig Ae/Be stars ($\dot{M} \sim 10^{-7}\ M_\odot\ \mathrm{yr}^{-1}$). This is significantly different from the steeper relationship found for T Tauri stars, likely due in part to the biases in classifying stars as Herbig Ae/Bes. While $\sim$two-thirds of the sample follows the $\dot{M}-M_{\mathrm{disk}}$ relationship of the T Tauri stars, one-third has high accretion rates relative to their dust masses.

2. T Tauri stars and Herbig Ae/Be systems show very different disk lifetime ($t_{\mathrm{disk}} = M_{\mathrm{disk}}/\dot{M}$) distributions, with $\sim$30-40% of the Herbig Ae/Be sample having disk lifetimes shorter than 0.01 Myr, with this population being dominated by Group II disks (identified by low infrared excesses).

3. If the disk masses are underestimated (due to optical depth effects or a higher-than-expected gas-to-dust mass ratio) or the accretion rates are overestimated (due to contributions to the accretion tracers by winds), the outlier objects may actually reside in the nominal $\dot{M}$–M_{disk} relationship. However, based on values of the disk gas mass measurements and accretion tracers that cannot be contaminated by winds from the literature, it is unlikely this is the cause of all of the low lifetime disks we are observing.

4. Unless these objects have extreme variability, the outlier disks are on the verge of dissipation. This may be due to efficient radial drift for Group II objects that may not be able to trap material in the outer disk like Group I disks, photoevaporation, and/or truncation of the outer disk due to multiplicity, all of which can result in low disk masses.

5. We have no low disk mass, low accretion rate objects in our Herbig Ae/Be sample, highlighting the bias in identifying these objects, which require accretion signatures and infrared excesses to be considered as such. In particular, the inability to measure accretion rates below $\sim 10^{-9}$ $\mathrm{M_\odot\,yr^{-1}}$ in these spectral types limits our ability to characterize the $\dot{M}$–M_{disk} relationship during the last stages of disk evolution in young, intermediate-mass systems.

Further work is needed to characterize the high accretion rate, low dust mass sample. Future high-resolution ALMA observations of these disks are needed to determine whether these disks are compact. Additionally, the sample of Herbig Ae/Be systems with ALMA observations should be expanded, which would allow us to determine whether the low inferred disk lifetime objects constitute only a small fraction of Herbig Ae/Be systems or whether this population is substantial. Finally, to better understand disk evolution around intermediate-mass stars we should also characterize the precursors of Herbig Ae/Be stars, intermediate-mass T Tauri stars, and their descendants, debris disks, to understand how disks move through this plane from formation to dissipation.

Appendix

In this section, we compare the $\dot{M}$ and M_{disk} values that we use in this work to previous values in the literature for all of the objects with an inferred disk lifetime less than 0.01 Myr. In general, we find that high spatial resolution (sub-)millimeter observations are needed to properly determine the disk dust masses, especially for targets with nearby companions which may contaminate low-resolution observations.

- AB Aur
  Guzmán-Díaz et al. (2021) find that AB Aur has a disk mass of 0.009±0.002 $M_\odot$, assuming a gas-to-dust ratio of 100, using a variety of (sub-)millimeter observations. This is within a factor of three of our value of 0.0035 $M_\odot$ (M_{dust}=11.8 $M_\oplus$). Rivière-Marichalar et al. (2022) find that the gas-to-dust mass ratio varies in the disk of AB Aur, from ∼10-40. Therefore, the disk mass is likely to be lower than what we use here, resulting in an even lower disk lifetime than we infer.

  There are several values of the accretion rate for AB Aur in the literature: $\log_{10}(\dot{M})$=–6.85 ($M_\odot$ yr^{-1}) (Garcia Lopez et al. 2006), $\log_{10}(\dot{M})$=-7.74 ($M_\odot$ yr^{-1}) (Donehew & Brittain 2011), $\log_{10}(\dot{M})$=-6.90 ($M_\odot$ yr^{-1}) (Salyk et al. 2013), and $\log_{10}(\dot{M})$=-6.13 ($M_\odot$ yr^{-1}) (Wichittanakom et al. 2020). We adopt the value from Wichittanakom et al. (2020).

- HD 104237
  Guzmán-Díaz et al. (2021) find a disk mass of 0.008±0.002 $M_\odot$ for HD 104237, a factor of less than three larger than our value of 0.003 $M_\odot$ (M_{dust}=10.5 $M_\oplus$). The Guzmán-Díaz et al. (2021) disk mass is based on 1.27 mm observations from Henning et al. (1994) using the 15 m SEST telescope with a resolution of 23″, which would contain several additional sources in the beam. The ALMA observations are not high enough resolution to resolve the disk, but a companion is observed in the continuum, indicating that we are resolving out some, if not all, sources of additional contamination. Kama et al. (2020) using HD observations from *Herschel*/PACS observations find a gas-to-dust mass ratio of ≤300.

  HD 104237 hosts a binary pair at the center of the circumbinary disk. This has resulted in interesting work on the nature of the inner disk in this system. Garcia et al. (2013) find that Brγ is variable, with the line equivalent width changing by a factor of 2 depending on the binary interaction, however Garcia Lopez et al. (2006) find an accretion rate of $\log_{10}(\dot{M})$=–7.45 ($M_\odot$ yr^{-1}), one order of magnitude lower than the value we use here.

- HD 37258

  van Terwisga et al. (2022) find a dust mass of 8.9±0.41 $M_{\oplus}$ for HD 37258, relative to the one derived by Stapper et al. (2022) of 2.4±0.4 $M_{\oplus}$. These measurements are from the same ALMA observations (2019.1.01813.S, PI: S. van Terwisga), but the fluxes derived are slightly different and the dust temperatures are different, with van Terwisga et al. (2022) assuming T_{dust}=20 K and Stapper et al. (2022) using T_{dust}=51 K, derived from the stellar luminosity.

  Fairlamb et al. (2015) find an accretion rate of $\log_{10}(\dot{M})$=-6.98 ($M_{\odot}$ yr^{-1}), the same value as found by Grant et al. (2022).

- BF Ori

  Guzmán-Díaz et al. (2021) report a disk mass of 0.005±0.002 $M_{\odot}$ for BF Ori using observations from the IRAM 30 m telescope presented in Natta et al. (1997). This is 15 times higher than our adopted value from ALMA observations of 3.3×10^{-4} $M_{\odot}$ (M_{dust}=1.1 $M_{\oplus}$). This is due to two reasons, the first is that the IRAM observations have a main beam width of 11″, which likely suffer from contamination compared to the ALMA observations which have a beam of 1.″49×1.″03. The ALMA observations are still not high enough resolution to resolve the disk, but are high enough to minimize contamination from nearby objects and cloud contamination. The second contributing factor is the choice of dust temperature, with Guzmán-Díaz et al. (2021) using a temperature of 25 K and Stapper et al. (2022) using a value of 58 K.

  Several works have reported accretion rates for BF Ori: $\log_{10}(\dot{M})$=-7.06 ($M_{\odot}$ yr^{-1}) (Donehew & Brittain 2011), $\log_{10}(\dot{M})$<-8.0 ($M_{\odot}$ yr^{-1}) (Mendigutía et al. 2011), $\log_{10}(\dot{M})$=-6.65 ($M_{\odot}$ yr^{-1}) (Fairlamb et al. 2015), and $\log_{10}(\dot{M})$=-7.28 (Grant et al. 2022; adopted here). The Donehew & Brittain (2011), Mendigutía et al. (2011), and Fairlamb et al. (2015) values are all determined using the Balmer excess, which are 0.22, 0.0, and 0.15 mag, for each of those works, respectively. BF Ori is known to exhibit UX Ori-type behavior (e.g., Shenavrin et al. 2012), with photometric variability in the visual and infrared, therefore we adopt the most recent measurement for the accretion rate, which is within the spread of the previous measurements.

- HR 5999

  Guzmán-Díaz et al. (2021) find a disk mass of 0.008±2.19×10^{-4} $M_{\odot}$, using observations from SCUBA (Sandell et al. 2011) and SMA (Meeus et al. 2012), in comparison to the disk mass we adopt here of 0.0012 $M_{\odot}$. The derived fluxes are quite similar with Meeus et al. (2012) deriving a 1.3 mm flux of 34.3±0.9 mJy and Stapper et al. (2022) deriving a flux of 26.5 mJy. A companion is seen in the ALMA continuum observations which is well-resolved from HR 5999. Yen et al. (2018) used ^{13}CO and C^{18}O ALMA observations, paired with models from Miotello et al. (2016), to determine a gas mass of $6^{+7.2}_{-3.2}$×10^{-5} $M_{\odot}$ for HR 5999, which is 20 times lower than our estimate from the dust mass. This gas mass value, when taken with

an accretion rate of $\log_{10}(\dot{M})$=-6.0 ($M_\odot$ yr^{-1}), results in an inferred disk lifetime of only 60 years.

Wichittanakom et al. (2020) re-derived the accretion rate for HR 5999 from the observations of Fairlamb et al. (2015, 2017) with updated stellar parameters, finding an accretion rate of $\log_{10}(\dot{M})$=-6.0 ($M_\odot$ yr^{-1}), compared to the accretion rate by Fairlamb et al. (2015) of $\log_{10}(\dot{M})$=-6.25 ($M_\odot$ yr^{-1}). We adopt the accretion rate from Wichittanakom et al. (2020).

- VV Ser
  Guzmán-Díaz et al. (2021) determine a disk mass of $9.54\times10^{-4}\pm2.730\times10^{-4}$ $M_\odot$ for VV Ser using observations from the Plateau de Bure Interferometer (Alonso-Albi et al. 2008; Boissier et al. 2011) with a beam of $1.''7\times0.''8$ at 1.3 mm. This matches well with our derived disk mass of 6.9×10^{-4} $M_\odot$ (2.3 $M_\oplus$ in dust mass). Pontoppidan et al. (2007) found that the mass of the small dust grains is only $\sim$0.03 $M_\oplus$.

  Mendigutía et al. (2011) find a Balmer jump (0.54 mag) that is inconsistent with magnetospheric accretion models, however Donehew & Brittain (2011) find a Balmer jump of 0.16 mag, which is within the range of magnetospheric models run by Mendigutía et al. (2011). Garcia Lopez et al. (2016) find that several H I lines, including Brγ, are variable, with Brγ likely to originate in a disk wind. The models used in that work assume an accretion rate of 3.3×10^{-7} $M_\odot$ yr^{-1}. With these discrepant measurements, it is unclear whether the accretion mechanism is variable, if magnetospheric accretion is taking place in this object, and if so, how much of the Brγ line is generated from magnetospheric accretion. However, while the accretion mechanism may be unclear, the accretion rate is likely to be high, given the high Balmer jump observed in both Mendigutía et al. (2011) and Donehew & Brittain (2011). We note that Donehew & Brittain (2011) find an accretion rate of $\log_{10}(\dot{M})$=-7.49 ($M_\odot$ yr^{-1}), but with a pre-Gaia distance and stellar properties. We adopt an upper limit to the accretion rate of $\log_{10}(\dot{M})$<-6.14 ($M_\odot$ yr^{-1}) from Grant et al. (2022) and do not include it in the $\dot{M}-M_{\mathrm{disk}}$ fits.

- HD 58647
  Few (sub-)millimeter observations of HD 58647 are available in the literature. We consider the ALMA observations (from Program 2018.1.00814.S), with an RMS of 0.14 mJy beam^{-1} and a beam of $0.''47\times0.''39$, and the dust mass determination of 1$\pm$0.1 $M_\oplus$ from Stapper et al. (2022) to be robust.

  In comparison to the lack of (sub-)millimeter observations, HD 58647 has several U-band and near-infrared observations. Mendigutía et al. (2011) use the Balmer discontinuity and find an accretion rate of $\log_{10}(\dot{M})$=−4.84 ($M_\odot$ yr^{-1}) for HD 58647. Using Brγ observations, Brittain et al. (2007) find an accretion rate of $\log_{10}(\dot{M})$=-6.45 ($M_\odot$ yr^{-1}), Ilee et al. (2014) find an accretion rate of $\log_{10}(\dot{M})$=-6.32 ($M_\odot$ yr^{-1}), and Grant et al. (2022) find an accretion rate of $\log_{10}(\dot{M})$=-5.84 ($M_\odot$ yr^{-1}). We adopt the latter in this work.

- HD 141569
  Miley et al. (2018) find a gas mass of 6×10^{-4} $M_\odot$ for HD 141569 using ALMA ^{13}CO (2-1) observations, a factor of 6 above our inferred disk mass of 1×10^{-4} $M_\odot$. This higher disk mass is still low enough that the inferred disk lifetime is only 0.03 Myr. Guzmán-Díaz et al. (2021) find a disk mass of 1.46×10^{-4} $M_\odot$ for HD 141569 from millimeter observations, in good agreement with the value that we adopt from Stapper et al. (2022).

  For HD 141569 several accretion rates have been determined in the literature: Garcia Lopez et al. (2006) find an accretion rate of $\log_{10}(\dot{M})$=-8.37 ($M_\odot$ yr^{-1}), Mendigutía et al. (2012) find a value of $\log_{10}(\dot{M})$=-6.89 ($M_\odot$ yr^{-1}), and Fairlamb et al. (2015) find a value of $\log_{10}(\dot{M})$=-7.65 ($M_\odot$ yr^{-1}). Grant et al. (2022) and Wichittanakom et al. (2020) update the value from Fairlamb et al. (2015) to $\log_{10}(\dot{M})$=-7.76 ($M_\odot$ yr^{-1}) and $\log_{10}(\dot{M})$=-7.23 ($M_\odot$ yr^{-1}), respectively. We adopt the value from Grant et al. (2022).

- HD 9672
  Moór et al. (2019) find a CO gas mass of 1.11×10^{-2} $M_\oplus$ (3.33×10^{-8} $M_\odot$) for HD 9672/49 Cet, however, CO may not be a good tracer of the total disk mass, in particular depending on the gas origin (e.g., Moór et al. 2019). Using the dust continuum and assuming a gas-to-dust mass ration of 100, Guzmán-Díaz et al. (2021) find a disk mass of 2.92×10^{-4} $M_\odot$ from infrared photometry from *Herschel*/PACS, a factor of seven higher than our value of 3.9×10^{-5} $M_\odot$. The ALMA observations analyzed in Stapper et al. (2022) should provide a more accurate estimate of the dust mass due to the longer wavelength observations.

  The accretion rate of $\log_{10}(\dot{M})$=-7.80 ($M_\odot$ yr^{-1}) for HD 9672 comes from Wichittanakom et al. (2020), derived from the Fiber-fed Extended Range Optical Spectrograph (FEROS, Kaufer et al. 1999) spectra from ESO Program 082.A-9011(A).

- TY CrA
  Cazzoletti et al. (2019) find a dust mass for TY CrA of 0.66 $M_\oplus$ (disk mass of 2×10^{-4} $M_\odot$, assuming a gas-to-dust mass ratio of 100), compared to that derived by Stapper et al. (2022) of 0.1 $M_\oplus$ (disk mass of 3×10^{-5} $M_\odot$, assuming a gas-to-dust mass ratio of 100), from the same dataset, largely due to the difference in dust temperature assumed. Guzmán-Díaz et al. (2021) find a disk mass of less than 0.017 $M_\odot$, from the upper limits on the millimeter flux from Henning et al. (1994) and Pezzuto et al. (1997).

  The only accretion rate in the literature that we found is that of Garcia Lopez et al. (2006), who found an accretion rate of $\log_{10}(\dot{M})$<-8.31 ($M_\odot$ yr^{-1}), based on the depth of the Brγ line, which indicated little or no accretion taking place in this object.

- HD 176386
  HD 176386 is undetected in the ALMA observation, with the continuum only present at the 1.6σ level (Stapper et al. 2022). That observation had

an RMS of 0.20 mJy/beam, meaning that the upper limit for the flux of 0.32 mJy, corresponding to a dust mass of 0.06 $M_{\oplus}$ (1.8×10^{-5} $M_{\odot}$ in total disk mass assuming a gas-to-dust ratio of 100). Guzmán-Díaz et al. (2021) used sub-millimeter observations from SCUBA (Di Francesco et al. 2008) to determine a disk mass of 0.121±0.01 $M_{\odot}$. This nearly 4 orders of magnitude difference is due to contamination in the SCUBA maps, which have a 14″ full width at half maximum in the 850 μm map used. HD 176386B is a binary companion to HD 176386 with a separation of 3.″7 (Wilking et al. 1997), and would have contributed to the flux observed in the low resolution SCUBA observations. The high resolution ALMA observations, with a beam of 0.″43×0.″32, is able to spatially distinguish the sources.

HD 176386 has several accretion rates in the literature. Garcia Lopez et al. (2006) find an accretion rate of $\log_{10}(\dot{M})$=-8.11 ($M_{\odot}$ yr^{-1}), Wichittanakom et al. (2020) find a value of $\log_{10}(\dot{M})$=-7.08 ($M_{\odot}$ yr^{-1}), and Guzmán-Díaz et al. (2021) find a value of $\log_{10}(\dot{M})$=-6.49 ($M_{\odot}$ yr^{-1}). Pogodin et al. (2012), whose X-Shooter data is the source of the Hα equivalent width used in Wichittanakom et al. (2020), conclude that magnetospheric accretion cannot be applied to this object, given that the disk may be dispersed. Given that we have stringent upper limits on the disk mass for this object, we agree that the disk may be dispersed and the accretion rate should be considered with caution. However, the Pogodin et al. (2012) absorption Hα profile for HD 176386 does show shallowing relative to a photospheric model, which may be due to accretion. We take the adapted value from Wichittanakom et al. (2020), however this value should be used with caution.

- HD 53367
  The ALMA observations analyzed in Stapper et al. (2022) (from Program 2018.1.00814.S) show that HD 53367 is only present in the continuum at the 2.4σ level with an RMS of 0.14 mJy beam^{-1}. We are not aware of other (sub-)millimeter observations of this target.

  Donehew & Brittain (2011) find an accretion rate of $\log_{10}(\dot{M})$<-7.92 ($M_{\odot}$ yr^{-1}) from a Balmer discontinuity of <0.09 mag. Fairlamb et al. (2015) find a similar Balmer discontinuity of 0.10 mag and they are unable to determine an accretion rate for this source given the very high stellar effective temperature of 29500±1000 K. The $\dot{M}$ value that we adopt here of $\log_{10}(\dot{M})$=-6.97 ($M_{\odot}$ yr^{-1}) is from Grant et al. (2022), based on strong Brγ line emission. However, given the high stellar mass and effective temperature of this object, this accretion rate should be viewed with caution. Given the low dust mass of this object, if any accretion is taking place, the disk would likely be depleted very quickly.

Chapter 6

A dichotomy in group II Herbig disks: ALMA gas disk height measurements show both shadowed large vertically extended disks and compact flat disks

L. M. Stapper, M. R. Hogerheijde, E. F. van Dishoeck, T. Paneque-Carreño

Abstract

Context: Herbig stars can be classified into group I and group II depending on the shape of the far-IR excess from the spectral energy distribution. This separation may be evolutionary and related to the vertical structure of these disks.

Aims: We aim to determine the emission height of Herbig disks and compare the resulting vertical extent of both groups.

Methods: ALMA Band 6 observations of ^{12}CO J=2-1 emission lines at sufficient velocity (~ 0.3 km s^{-1}) and spatial resolution (~ 30 au) of eight Herbig disks (four group I and four group II sources) are used to determine the emission heights from the channel maps via geometrical methods previously developed in other works.

Results: We find that all group I disks are vertically extended with a height to radius ratio of at least 0.25, and for three of the disks the gas emission profile can be traced out to 200-500 au. The group II disks are divided between MWC 480 and HD 163296 which have similar emission height profiles as the group I disks and AK Sco and HD 142666 which are very flat (not exceeding a height of 10 au over the full extent traced) and more compact (< 200 au in size). The brightness temperatures show no differences between the disks when the luminosity of the host star is accounted for.

Conclusions: Our findings agree with previous work suggesting that group I disks are vertically extended and that group II disks are either large and self-shadowed or compact. Both MWC 480 and HD 163296 could be precursors of group I disks, which we see now before a cavity has formed that would allow irradiation of the outer parts of the disk. The very flat disks AK Sco and HD 142666 could be due to significant settling because of the advanced age of these disks (~ 20 instead of < 10 Myr). These large differences in vertical structures are not reflected in the spectral energy distributions of these disks. More and deeper observations at higher spatial and velocity resolution are necessary to further characterize the Herbig sub-groups.

6.1   Introduction

Herbig Ae/Be stars (e.g., Herbig 1960; Waters & Waelkens 1998) are pre-main-sequence stars of intermediate mass and spectral type between B and mid-F. The disks around Herbig stars (hereafter Herbig disks) have been found to be larger than those around T-Tauri stars (Acke & van den Ancker 2004; van der Marel & Mulders 2021; Stapper et al. 2022). This characteristic could explain why giant planets are more common around intermediate-mass main-sequence stars (e.g., Johnson et al. 2007; Fulton et al. 2021). The potential of forming a giant planet may be linked to the group I and II spectral energy distribution (SED) character-ization of Herbig disks (Stapper et al. 2022). These two groups are based on the shape of the SED, specifically on the infrared (IR) excess (Meeus et al. 2001; Acke et al. 2009). While group II SEDs can be fitted with a single (power) law across the near–far IR wavelength range, group I SEDs require an additional blackbody component that dominates the far-IR emission. Based on these differences, group I disks are interpreted to be flaring disks (or vertically extended, i.e., increasing height with radius), while the group II disks are flat (i.e., constant height with radius) or self-shadowed (Meeus et al. 2001).

Originally, an evolutionary sequence from group I to group II was hypothesized, with grain growth and settling reducing the far-IR emission (Dullemond & Dominik 2004a,b, 2005). However, the evolution of the Herbig subgroups has been shown to be more complicated. Most, if not all, Herbig group I disks have been found to have inner cavities (Honda et al. 2012; Maaskant et al. 2013), which has given rise to the idea that the flux increase at longer wavelengths is due to an irradiated inner cavity wall. Consequently, an evolution from group I to group II was discarded, and instead, it was proposed that group II objects might eventually evolve into group I objects by means of the creation of an inner cavity (Maaskant et al. 2013; Menu et al. 2015).

However, the lack of scattered light from group II disks suggests that these disks may still be flat or self-shadowed disks (e.g., Garufi et al. 2017, 2022). This led Garufi et al. (2017) to propose that group II disks can either be self-shadowed large disks or small compact disks, which is in contrast to the group I disks, as they are all large and bright in both scattered light (Garufi et al. 2014) and millimeter observations (Stapper et al. 2022). Consequently, the question arises of whether the differences in vertical disk height are also present in the gas.

In recent years, the high velocity and spatial resolution of the Atacama Large Millimeter/submillimeter Array (ALMA) has allowed for the vertical structure of mid-inclination protoplanetary disks to be characterized (e.g., Pinte et al. 2018a; Rich et al. 2021; Law et al. 2021, 2022; Paneque-Carreño et al. 2021, 2022, 2023), increasing the variety of disks that can be studied in addition to edge-on disks (e.g., Podio et al. 2020; Villenave et al. 2020). The emission heights of different molecules (e.g., Law et al. 2021) and asymmetries in the vertical emission of CO in a disk (Paneque-Carreño et al. 2021) have been found. In this paper, we apply the technique of Pinte et al. (2018a) as implemented by Paneque-Carreño et al. (2023) on both group I and group II disks to determine the emission heights of ^{12}CO and see if there are any differences present between the two groups.

Section 6.2 presents the targets and how they were selected and imaged. Section 6.3.1 shows the extracted disk heights, and Section 6.3.2 shows the temperature maps of each disk. The results are discussed in the context of group I versus group II in Section 6.4.1 and in relation to the age of the very flat disks in Section 6.4.2. Lastly, in Section 6.5, the conclusions are summarized.

6.2 Sample selection and data reduction

In recent years, many Herbig disks have been observed with ALMA (for a recent compilation, see Stapper et al. 2022). Some of these data are deep, high-resolution observations. These data were either included in ALMA Large Programs, such as MAPS (Öberg et al. 2021) and DSHARP (Andrews et al. 2018a), or studied separately. We selected our sample based on the available data in the ALMA archive[1] (Stapper et al. 2022). To be able to determine the emission heights of a disk, the data and the disk must meet several requirements. First, an inclination of at least $30°$ is needed to reliably extract the surface emitting heights (Law et al. 2021). Second, a certain level of velocity resolution is necessary to adequately trace the isovelocity curves in the selected channels. In general, a velocity resolution of at least ~ 0.3 km s^{-1} is necessary. Lastly, sufficient spatial resolution is necessary to distinguish both the nearside and the far side of the disk (for systematics, see Pinte et al. 2018a; Paneque-Carreño et al. 2022). For our sources, this came down to ~ 30 au. To properly trace the vertical extent of the Herbig disks, we used ^{12}CO $J = 2 - 1$ observations. These requirements left us with eight data sets in total: four for group I and four for group II disks (see Table 6.1). The SEDs of these disks are shown in Appendix 6.A and clearly show the distinguishing features of both groups. We note that this technique of determining the vertical extent of the disk traces the $\tau = 1$ line rather than the scale height of the gas. Paneque-Carreño

---

[1]https://almascience.eso.org/asax/

Table 6.1: Data and stellar parameters of each Herbig disk.

Group	Herbig disk	Vel. res. (km s^{-1})	Sp. res. ($''$)	rms (mJy beam^{-1})	Project ID	Dist. (pc)	M$_\star$ (M$_\odot$)	L$_\star$ (L$_\odot$)	Age (Myr)	Inc. (°)	PA (°)
I	HD 34282	0.2	0.27	4.6	2015.1.00192.S	306.5	<1.9	14.5	<20	60	117
	HD 97048	0.3	0.46	4.2	2015.1.00192.S	184.1	2.8	64.6	4	41	3
	HD 100453	0.3	0.25	3.5	2015.1.00192.S	103.6	1.6	6.2	30	140
	HD 100546	0.2	0.24	4.2	2016.1.00344.S	108.0	2.1	21.9	8	43	139
II	AK Sco	0.3	0.15	2.5	2016.1.00204.S	139.2	1.7	5.6	8	109	51
	HD 142666	0.35	0.13	1.6	2016.1.00484.L	145.5	1.8	13.5	9	62	162
	HD 163296	0.2	0.14	0.6	2018.1.01055.L	100.6	1.9	15.5	10	46	312
	MWC 480	0.2	0.3	1.2	2018.1.01055.L	155.2	1.9	16.6	8	-32	328

Notes. The stellar parameters are taken from Guzmán-Díaz et al. (2021). The following lists where the inclinations and position angles were taken from: AK Sco, Czekala et al. (2015); HD 142666, Huang et al. (2018); HD 163296, Izquierdo et al. (2022); MWC 480, Teague et al. (2021); HD 34282, van der Plas et al. (2017b); HD 100453, Rosotti et al. (2020); HD 97048, Walsh et al. (2016); HD 100546, Pineda et al. (2019).
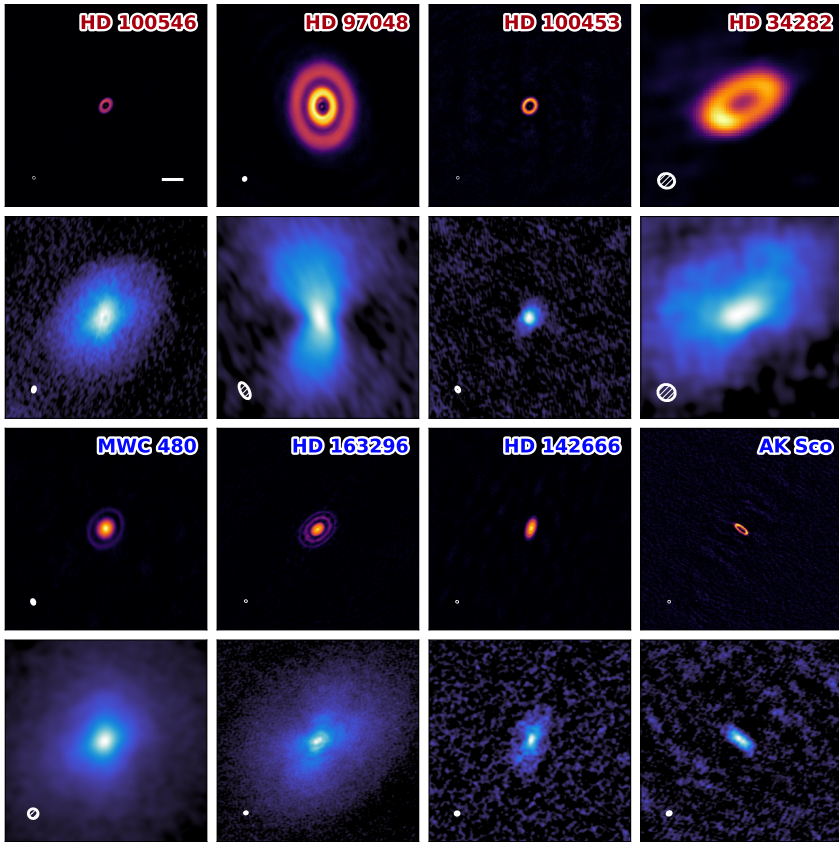
Figure 6.1: Continuum and ^{12}CO velocity integrated (moment 0) maps of the group I disks (top two rows) and group II disks (bottom two rows). Each image is 1000×1000 au in size; additionally, a bar of 100 au in size is shown in the top-left panel. In the bottom-left corner of each image, the size of the beam is shown. The moment 0 maps use a 3σ clip and only include channels with disk emission. To make the outer regions of the disks more visible, a power-law normalization was used

et al. (2023) have shown that the ratio between the traced emission height and the gas scale height is generally a factor of two to five.

To obtain well-defined upper surfaces, ^{12}CO observations toward the eight disks were used. For HD 163296 and MWC 480, the imaged ^{12}CO data sets from the MAPS Large Program were used (see Czekala et al. 2021 for the specifics on the imaging). All other data were imaged using the `Common Astronomy Software Applications` (CASA), application version 5.8.0 (McMullin et al. 2007). For all data sets, the data were either binned by a factor of two in velocity, to increase the sensitivity, or the native velocity resolution was used. After subtracting the continuum using `uvcontsub` (which was not done for the temperature maps shown in Section 6.3.2), the data were imaged using the `multiscale` algorithm. The

scales used were 0 (point source), 1, 2, 5, 10, and 15 times the size of the beam in pixels ($\sim$5 pixels). A Briggs robust weighting of 0.5 was used. For HD 142666 a uv taper of $0.08''$ was applied to increase the beam size for better extraction of the emission surface heights. These steps resulted in the image parameters listed in Table 6.1. The velocity integrated maps of ^{12}CO can be found in Fig. 6.1 together with the Band 6 or 7 continuum images of each disk.

To obtain the emitting surface heights of the ^{12}CO emission, the technique set out in Pinte et al. (2018a) was employed. Using geometric relations and assuming Keplerian rotation, the emission height can be retrieved. We used the same implementation of this technique as Paneque-Carreño et al. (2021, 2022, 2023), who made the distinction between the upper and lower emission surfaces visually through the use of hand-drawn masks with `ALFAHOR` (ALgorithm For Accurate H/R; Paneque-Carreño et al. 2023, see Appendix 6.B). This approach limits contamination between the different surfaces, resulting in a cleaner retrieval of the emission surfaces. The extracted data points were averaged in bins of 20 au in size with an uncertainty corresponding to the standard deviation of the data points in that bin. The distances used and other stellar parameters can be found in Table 6.1. The resulting hand-drawn masks and extracted points are shown in the figures of Appendix 6.B.

An exponentially tapered power law was fitted to each profile in order to easily compare between disks and other works. We followed Law et al. (2021) in using the following expression:

$$z(r) = z_0 \times \left(\frac{r}{1''}\right)^{\phi} \times \exp\left(-\left[\frac{r}{r_{\text{taper}}}\right]^{\psi}\right), \quad (6.1)$$

where z is the vertical height of the surface emission, r is the radius of the profile, and $z0$ and r_{taper} are related to the size of the disk in the vertical and radial direction, respectively. All units are in arcseconds. In order to fit Eq. (6.1), we used the `curve_fit` function from `SciPy` (Virtanen et al. 2020) to do a nonlinear least-squares fit to the retrieved binned emission surfaces. Bins with only one point were excluded. Lastly, for additional visual aid in identifying whether the disks are vertically extended or flat, Appendix 6.C presents the velocity maps of each disk.

6.3   Results

6.3.1   Disk heights

The continuum and the ^{12}CO line observations presented in Figure 6.1 already show a large variety of structures and sizes regarding the disks in this work. Both HD 97048 and HD 34282 each show a large dust and gas disk extent. The dark regions in the ^{12}CO observations of HD 97048 are due to foreground cloud absorption. For the group I disks, all disks except HD 100453 are large in gas. Among the group II disks, HD 142666 and AK Sco are smaller compared to the other

disks. The continuum of all the disks shows substructure, and half of the disks show a single dust ring, while the others show multiple rings.

Figure 6.2 presents the extracted height profiles for the eight disks. The top four panels show the group I disks, and the bottom four panels show the group II disks. In general, the heights of most of the disks are at a $z/r \sim 0.25$. All group I disks have a z/r of at least 0.25, either in large parts of the disk, such
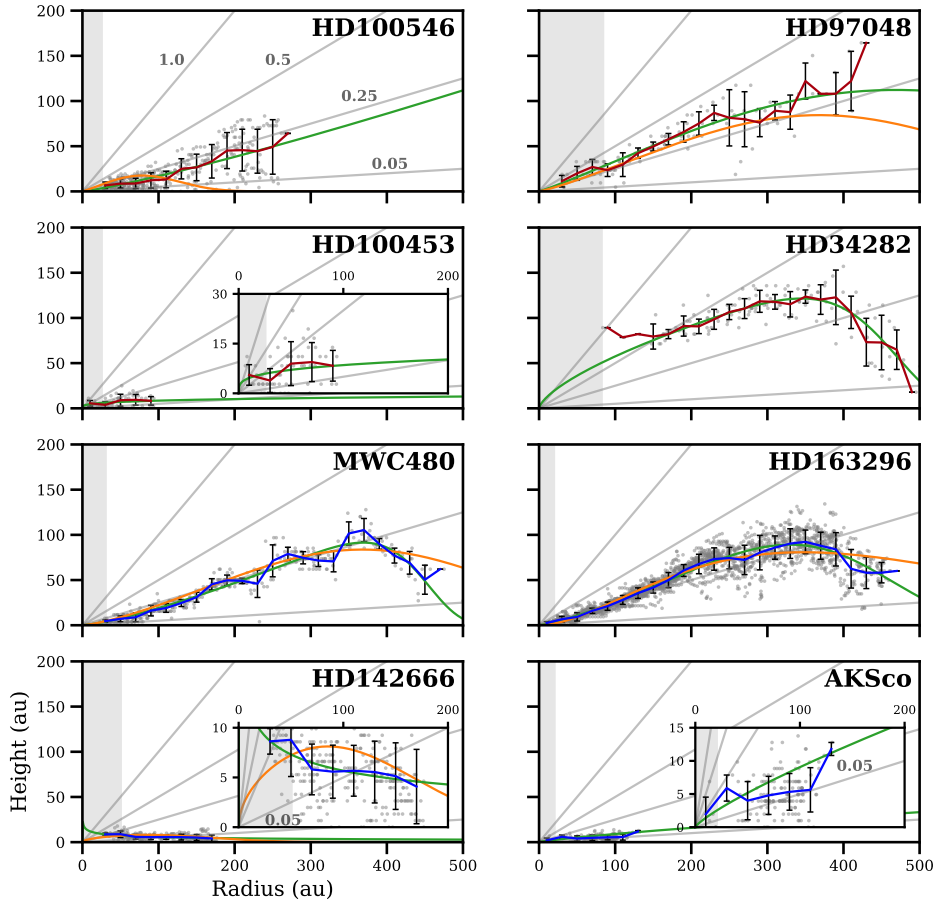
Figure 6.2: Height profiles of the group I disks (top four panels) and group II disks (bottom four panels). The gray lines indicate the 1.0, 0.5, 0.25, and 0.05 height to radius ratios. The gray scatter is the extracted points from the channel maps, and the line shows the mean value of the scatter in bins of 20 au in size. The error bars indicate the standard deviation of the scatter in each bin. The fitted profiles are shown as green lines and are compared to the orange profiles from Law et al. (2021) for HD 163296 and MWC 480, Law et al. (2022) for HD 142666 and HD 100546, and Rich et al. (2021) for HD 97048. The gray-shaded regions indicate the size of the major axis of the beam.

as HD 100546 or HD 97048, or at small radii only (HD 100453). MWC 480 and HD 163296 belong to group II and are vertically very similar to the group I disks. Both disks have a $z/r \sim 0.25$ and have gas disk sizes of around 500 au. In contrast, AK Sco and HD 142666 are flat and relatively small, only going out to 200 au. We will now discuss each disk separately.

While having similar or worse spatial resolution compared to the other disks, HD 34282 is limited by the resolution of the data, as its source was the farthest away (306.5 pc; see Guzmán-Díaz et al. 2021 or Table 6.1). For the inner 100 au, the far sides and the near sides of the disk cannot be separated from each other, making it impossible to sample the emission height at these radii (see Fig. 6.B.4). The part that is well sampled shows a vertically extended disk going as high as $z/r \sim 0.5$. In the case of HD 34282, the tapered power-law fit shows that at small radii the disk could go above $z/r \sim 0.5$, which is higher than what is found in most disks (e.g., Law et al. 2022).

In our sample, HD 97048 is also a high vertically extended disk, with a z/r out to 0.33. Although we did not probe the turnover at the large radii seen in many of the disks, we found that the emission originates from higher z/r regions in comparison to what Rich et al. (2021) found. While the inner region is again limited by the spatial resolution of the data, the profile is above a z/r of 0.25 at regions close to the mid-plane. The z/r values close to the mid-plane of the best fit correspond well with those of Rich et al. (2021), while the outer regions mainly contribute to the difference between the two fits. The data lack samples at lower velocities close to the system velocity (see Fig. 6.C.1 in Appendix 6.C) due to foreground cloud absorption, which reduces the number of sampled heights in Fig. 6.2. For HD 100546, we were able to probe the emission heights to a larger radius than what was found by Law et al. (2022). However, no clear turnover was detected at these larger radii up to where we sampled the surface. The disk clearly follows a $z/r \sim 0.25$.

When fitting the exponentially tapered power law to the height profiles of MWC 480 and HD 163296, we found a steeper drop-off at large radii compared to what Law et al. (2021) found. This difference was due to our ability to better separate the lower and upper emission surfaces by drawing masks, which would have otherwise contaminated the overall inferred profile. At smaller separations, our relations agree with what Law et al. (2021) found, while due to a better sampling at larger separations, the relations start to differ at larger radii, resulting in a steeper drop.

For HD 142666, we found a very flat disk, similar to the disk height found by Law et al. (2022), but there are differences at small radii. In addition to HD 142666, we found a second very flat disk: AK Sco. Both of these disks are also the smallest disks in the sample of this work.

6.3.2   Disk temperatures

One would expect that these large differences in the height of the emitting layer would be reflected in the temperature of the emitting gas. To examine whether this is indeed the case, temperature maps of the disks were made, see Fig. 6.3. These
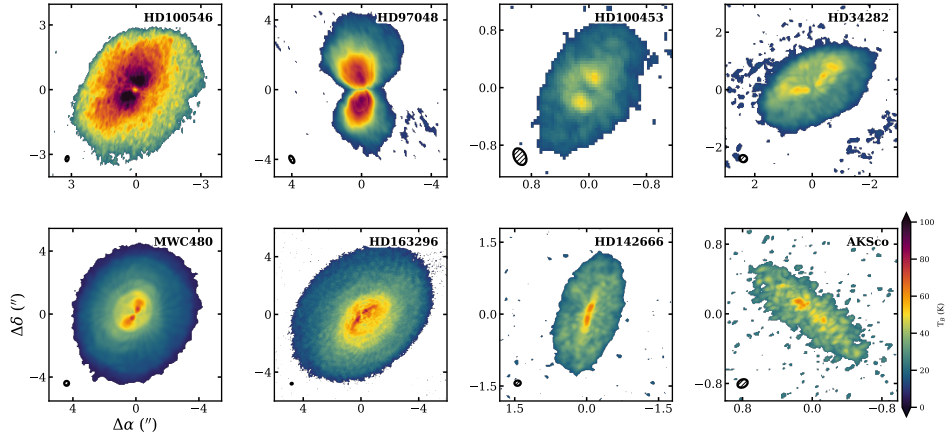
Figure 6.3: Temperature maps of the eight disks, determined using the Planck law. The top and bottom rows show the group I and II disks, respectively. Each image is clipped at an S/N of 3. The size of the beam is shown in the bottom-left corner.

maps were made with `bettermoments` using a clip of $3\times$S/N and the full Planck expression. A radial cut along the disks' major axes that follows the projected fitted height profiles of the temperature maps can be found in the left column of Fig. 6.4. Each disk shows a decrease in temperature close to the star due to beam dilution, as the emitting region shrinks and no longer fills the beam (e.g., Leemker et al. 2022). Also, for HD 142666, the relatively low velocity resolution can lower the inferred temperature by underresolving the line. Both Figs. 6.3 and 6.4 show large differences between temperatures of individual disks. However, no clear trend is present between the group I and group II sources, and there are disks from both groups that show very similar temperature profiles. For example, HD 100453, AK Sco, and HD 142666 are relatively cold, and HD 34282, HD 163296, and MWC 480 are relatively warm. The only clear outliers are HD 100546 and HD 97048, which are much warmer in the region out to 450 au compared to the other disks.

We might expect that these differences in temperature are due to the relative vertical extent of the disks. The right column of Fig. 6.4 shows radial cuts of the temperature maps where the temperature is scaled by the stellar luminosity as $\sim (L_\star/L_\odot)^{1/4}$ (following the dust temperature scaling presented in Andrews et al. 2013). This scaling removes the effect of the central star on the temperature of the disk. As presented in Table 6.1, both HD 100546 and HD 97048 are the most luminous stars in our sample and, compared to the less luminous stars, significantly increased the relative disk temperatures. When the scaling is applied, the relative disk temperatures become noticeably more similar. Most notably, the temperature profile of HD 97048 becomes almost identical to the profiles of HD 34282, MWC 480, and HD 163296. Consequently, the disk temperatures are as one would expect for their luminosity and size. Hence, we do not find a difference
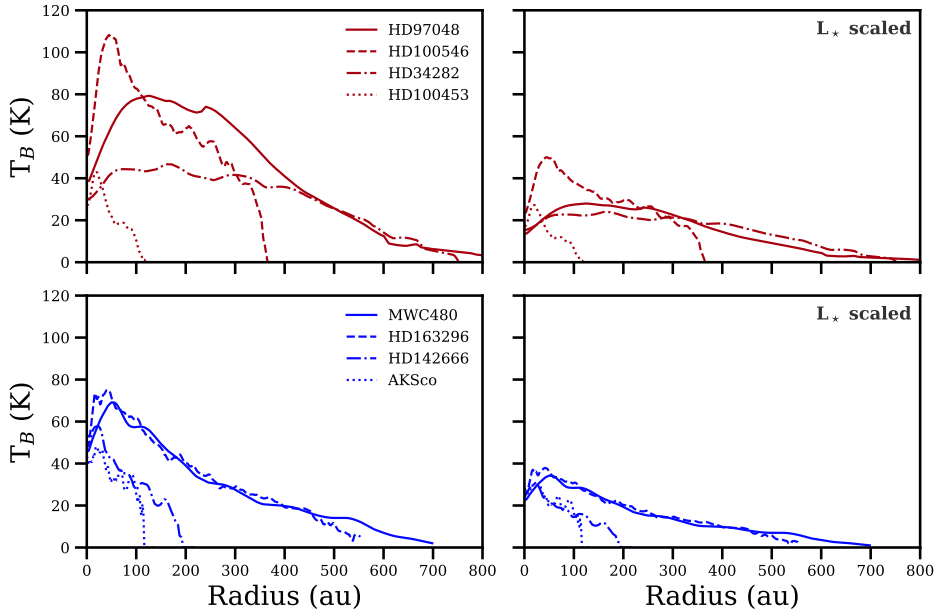
Figure 6.4: Radial cuts of the temperature maps in Fig. 6.3 along the major axes of the disks and the projected emission surface fit shown in Fig. 6.2. The radial cuts are colored by group: group I (red, top row) and group II (blue, bottom row). The legend is ordered by stellar luminosity. The right panels show the temperature scaled by the stellar luminosity as $T \sim (L_\star/L_\odot)^{1/4}$ from Andrews et al. (2013).

in temperature between the group I and group II sources despite differences in vertical extent.

Fedele et al. (2016) modeled Herbig Ae disks based on Herschel/HIFI high-J CO line profiles and determined the radial gas temperature structure for, among others, different vertically extended disks. They found that for a z/r between 0.01 and 0.3, the gas temperature is independent of the vertical extent of the disk and that the differences only start in higher layers probed by (very) high-J CO lines. Given that our ^{12}CO emission surfaces are from $z/r \sim 0.3$ and lower, our results fall in line with these models.

6.4 Discussion

6.4.1 Group I versus group II

The different Herbig disk groups were originally interpreted as group I being made up of flaring disks and group II being made up of flat or self-shadowed disks, with an evolution from group I to group II via dust settling. As outlined in Section 6.1, this view has become more complicated. Based on scattered light imaging, Garufi et al. (2017) proposed that group II disks can be divided into objects with large,

shadowed disks and objects with small disks. Both result in a low far-IR flux. The shadowed disks could evolve into group I disks by creating an inner cavity, thus removing the part of the disk casting the shadow. Recent studies have shown a high occurrence rate of cavities in group I disks, in both gas and dust (e.g., Menu et al. 2015; van der Plas et al. 2015).

Most group I disks are large vertically extended disks. For the disks in group II, there is a clear difference between two sets of disks (e.g., MWC 480 and HD 163296 versus HD 142666 and AK Sco). The former are indistinguishable from the group I disks in our sample regarding both their size and the vertical extent of the disk, while the latter are more compact and flat.

These two sets of disks coincide with the proposed distinction between compact and self-shadowed disks within group II by Garufi et al. (2017). The analogous height profiles of MWC 480 and HD 163296 compared to the group I disks suggest that they are precursors of the group I disks, as Garufi et al. (2017) suggest for HD 163296. These disks are shadowed due to an inner disk that keeps the outer regions cool, which results in a group II SED. Once a cavity forms, the shadowing disappears, and a group I disk is formed. Throughout this evolution, the height profile of the disk stays the same. The puzzling aspect is that a higher temperature should result in a more vertically extended disk, but this was not observed. So there may be a (unrelated) trend occurring at the same time that results in a flatter disk that counteracts the effect of the larger illumination. The two flatter disks in our sample are also the most compact, and such a flat disk also result in a group II SED.

Hence, two types of group II disks can be distinguished. On the one hand are the disks that will eventually evolve into group I disks with very similar radial and vertical structures but with an inner disk that shadows the outer disk. And on the other hand are disks that are very flat and never develop an inner cavity that would expose the outer disk to heating.

We note that no differences between the vertically extended but shadowed and vertically flat disks are present in the SEDs of the group II disks (see Appendix 6.A). As shown in Garufi et al. (2017, 2022), in general, multiple tracers are necessary to fully characterize a Herbig disk, one of which is the ability to spatially resolve the disk.

6.4.2   Old flat group II disks

Both AK Sco and HD 142666 are very flat disks compared to the other disks in our sample. What could cause such a flat disk?

The ages of these disks are not well determined and have a significant range of possible values. In Table 6.1 for instance, an age of 7.8 Myr is cited for AK Sco (Guzmán-Díaz et al. 2021). However, others give ranges of values from lower limits, from 12 Myr (Garufi et al. 2022) to 18 Myr (Czekala et al. 2015). While not present in this work due to too low spectral resolution observations, HD 9672 (or 49 Ceti) is a group II Herbig disk but is also considered to be a debris disk (e.g., Moór et al. 2019). The secondary dust in the debris disk, which is expected to have a low-scale height, could cause the group II classification. At the advanced

age of these disks, the PAHs and small dust grains in the higher regions of the disk may have been removed. This in turn would lower the gas temperature and decrease the gas scale height. Hence, while they are not debris disks, the flat disks AK Sco and HD 142666 may have had significantly more evolution (dust settling and thus a decrease of the gas scale height) than one would assume based on the ages mentioned in Table 6.1.

6.5   Conclusion

In this work we determined the emission heights of eight Herbig disks, four group I disks (HD 100546, HD 97048, HD 100453, and HD 34282) and four group II disks (MWC 480, HD 163296, HD 142666, and AK Sco), following the classification of Meeus et al. (2001). With these emission heights, we tested the interpretation that group I disks are vertically extended irradiated disks and group II disks are self-shadowed or flat disks. The following conclusions have been made:

1. All but one of the group I disks are large (>200 au) and have $z/r \sim 0.25$. The exception is HD 100453, which has the same z/r as the other group I disks but is traced to a smaller radii.

2. Two of the group II disks (MWC 480 and HD 163296) have emission height profiles that are indistinguishable from those of the group I disks.

3. There are two very flat disks among the group II disks (HD 142666 and AK Sco). The emission heights of these very flat disks are below 10 au over the full extent of the traced disk (out to 200 au).

4. The temperatures reveal no significant differences between the disks when scaled based on the luminosity of the star despite differences in vertical extent.

5. Our findings correspond with the proposed scenario of Garufi et al. (2017), where some group II disks are self-shadowed and will evolve into a group I disk by forming a cavity that causes the outer disk to be irradiated (MWC 480 and HD 163296), while other group II disks are small and flat (AK Sco and HD 142666).

6. No significant differences are present between the SEDs of the flat and the vertically extended group II disks. Hence, resolved observations play a key role in fully characterizing the different Herbig disk populations.

The small source sample of only four objects in each SED group with available ALMA data of sufficient quality shows that more observations of sufficient S/N and resolution, both spatial and kinematic, are needed. Future studies with a larger sample must be done in order to place our reported dichotomy in gas disk heights on a firm statistical footing.

Acknowledgements

Appendix

6.A   Spectral energy distributions

Figure 6.A.1 presents the SEDs of the eight Herbig disks. The main distinction between the group I and group II disks is clear: group I disks have extra emission at mid-far IR wavelengths, while group II disks only decrease in emission with increasing wavelength.
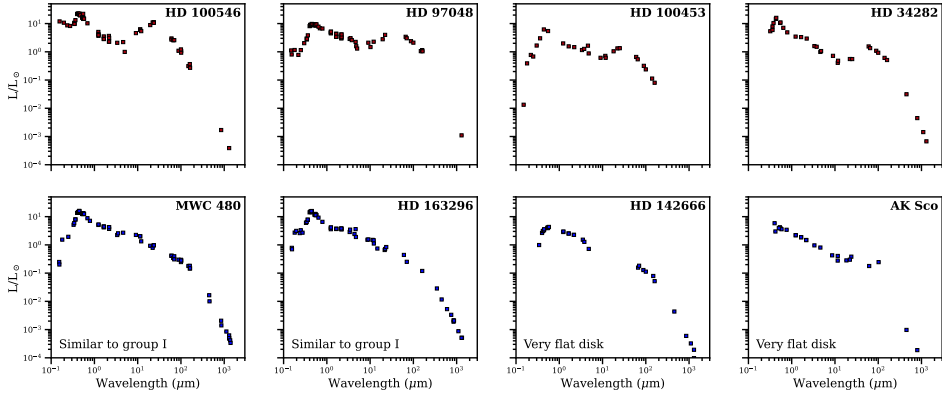

Figure 6.A.1: Spectral energy distributions (SEDs) of the eight disks. The top and bottom rows show the SEDs of the group I and group II sources, respectively. The SEDs of HD 100546, HD 97048, MWC 480, HD 163296, and HD 142666 are from the DIANA project (Woitke et al. 2019). The SEDs of HD 100453 and HD 34282 are from Khalafinejad et al. (2016). Lastly, the SED of AK Sco is compiled from the following sources: Hip (1997); Hindsley & Harrington (1994); Zacharias et al. (2004); Gaia Collaboration et al. (2023); Ishihara et al. (2010); Cutri & et al. (2012); Jensen et al. (1996). The SEDs of HD 100453, HD 34282, and AK Sco have been dereddened using the `Astropy` affiliated package `dust_extinction` with $R_V = 3.1$ (Bessell 1979) and a visual extinction (A_V) from Guzmán-Díaz et al. (2021).

6.B   Channel maps

Figures 6.B.1 to 6.B.8 show the ^{12}CO $J = 2 - 1$ channel maps used in this work together with the hand-drawn masks. The masks have been made by carefully identifying the emitting regions visually. We did not use the central channels nor the first and last channels because a horizontal extent and a separation between the far side and the nearside is necessary to extract the heights.
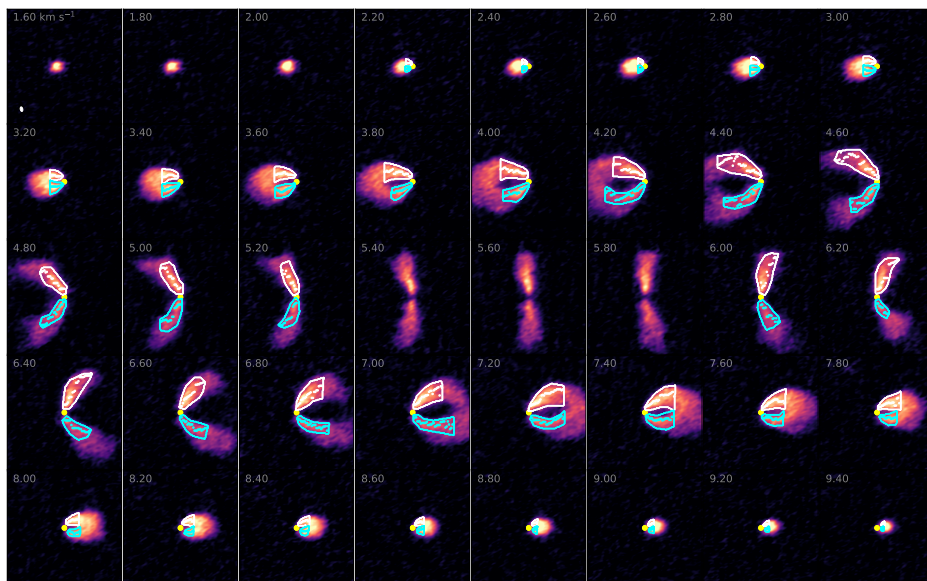
Figure 6.B.1: ^{12}CO channel maps of HD 100546. The white and blue lines show the outlines of the hand-drawn masks of the far sides and the nearside, respectively. The white and blue scatter show the corresponding extracted points. The yellow circle denotes the position of the star. To make the fainter parts more visible, a power-law normalization was used. On each panel, the channel velocity in km s^{-1} is indicated in the top-left corner. The beam size is shown in the bottom-left corner of the first panel.
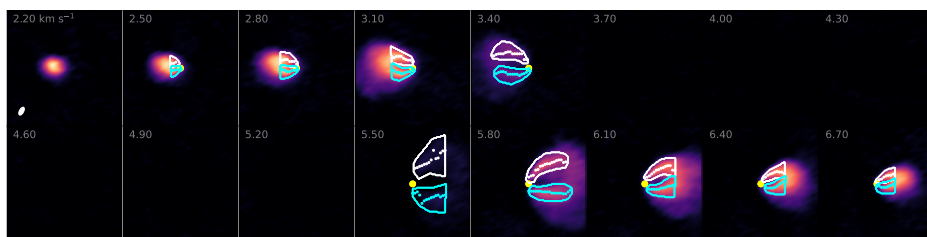
Figure 6.B.2: Similar to Fig. 6.B.1, but for HD 97048.
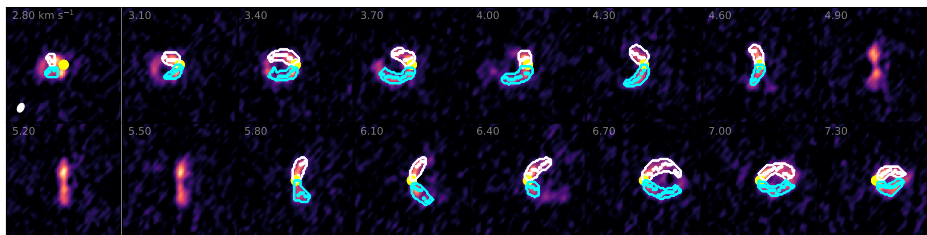
Figure 6.B.3: Similar to Fig. 6.B.1, but for HD 100453.
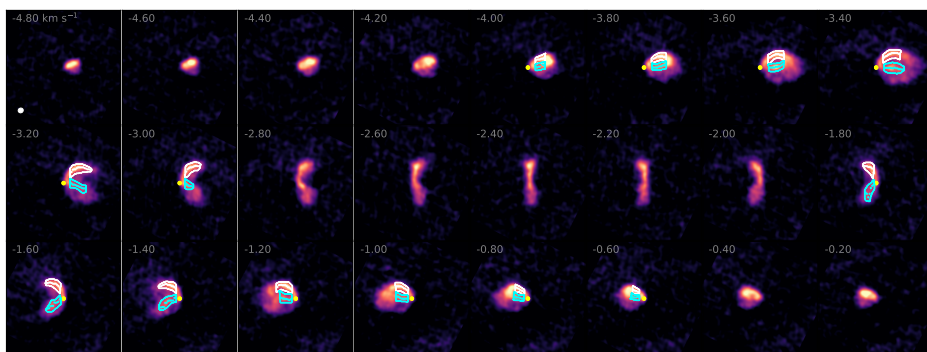
Figure 6.B.4: Similar to Fig. 6.B.1, but for HD 34282.
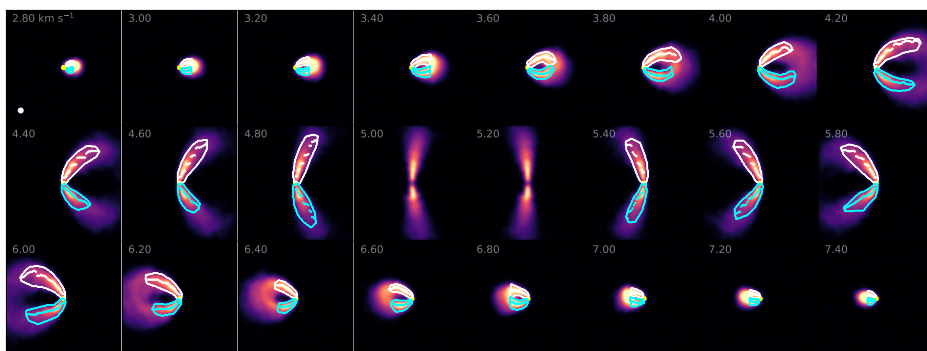
Figure 6.B.5: Similar to Fig. 6.B.1, but for MWC 480.
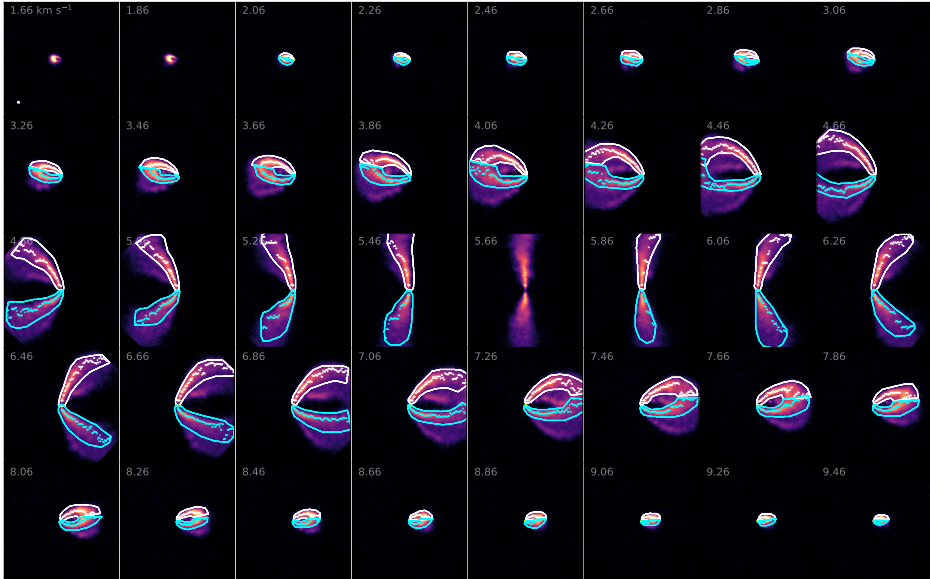
Figure 6.B.6: Similar to Fig. 6.B.1, but for HD 163296.
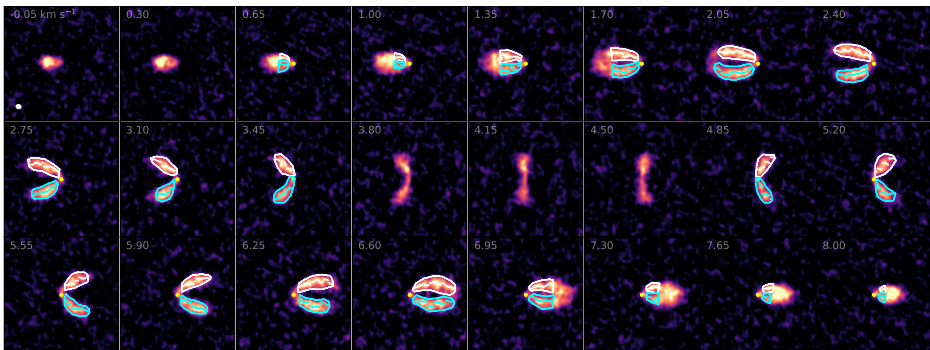
Figure 6.B.7: Similar to Fig. 6.B.1, but for HD 142666.
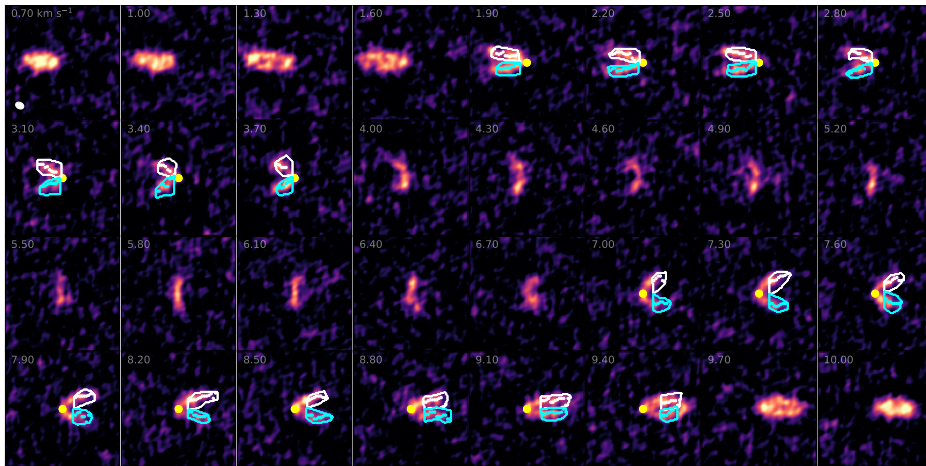
Figure 6.B.8: Similar to Fig. 6.B.1, but for AK Sco.

6.C   Velocity maps

Fig. 6.C.1 shows the moment 1 maps of the disks made with `bettermoments` (Teague et al. 2018) clipped at an S/N of 3. In these figures, the alignment of the redshifted and blueshifted sides provide an additional indication of how vertically extended a disk is. At high enough inclinations, the largest velocities at a particular separation curve with the vertical height of the disk. Hence, if the redshifted and blueshifted sides are aligned opposite to each other, the disk is flat, as seen in the HD 142666 and AK Sco disks. In contrast, a v shape indicates a vertically extended disk, as seen in HD 34282 and HD 163296.
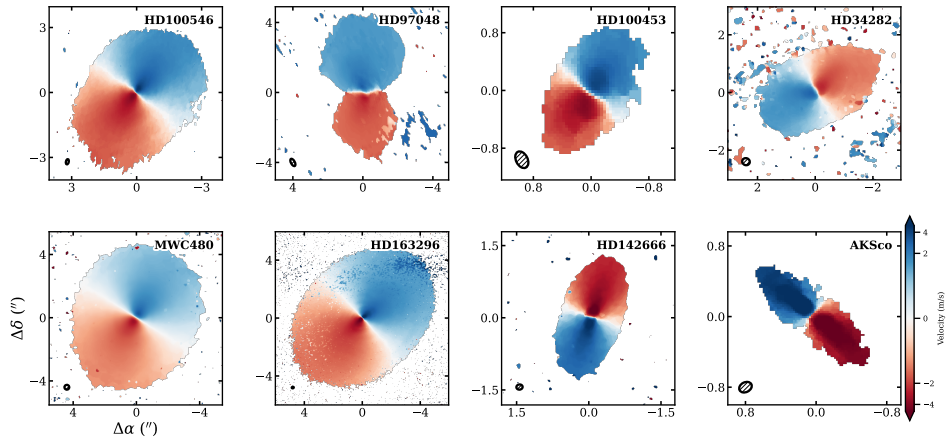
Figure 6.C.1: Moment one (intensity weighted average velocity) maps of the eight disks. The top and bottom rows show the group I and II disks, respectively. The color bar is centered on their respective system velocities. Each map is clipped at an S/N of 3. The size of the beam is shown in the bottom-right corner.

Intermediate mass T Tauri disk masses and a comparison to their Herbig disk descendants

L. M. Stapper, M. R. Hogerheijde, E. F. van Dishoeck, M. Vioque, J. P. Williams, C. Ginski

Abstract

Context: Herbig disks are the prime sites for the formation of massive exoplanets, so looking into the precursors of these disks can give us clues in planet formation timescales. The precursors of Herbig stars are called Intermediate Mass T Tauri (IMTT) stars, which have spectral types later than F, but stellar masses between 1.5 and 5 $M_\odot$, and will eventually become Herbig stars with spectral types of A and B.

Aims: The aim of this work is to obtain the dust and gas masses and radii of all IMTT disks with ALMA archival data. The obtained disk masses are then compared to Herbig disks and T Tauri disks and the obtained disks sizes to those of Herbig disks.

Methods: ALMA Band 6 and 7 archival data are obtained for 34 IMTT disks with continuum observations, 32 of which have at least ^{12}CO, ^{13}CO, or C^{18}O observations although most of them at quite shallow integrations. The disk integrated flux together with the stellar parameters and distances are used to obtain a total disk dust mass. Using thermochemical Dust And LInes (DALI) models from previous work, we additionally obtain gas masses of some of the IMTT disks based on the CO isotopologues. From the disk masses and sizes cumulative distributions are obtained.

Results: The IMTT disks in this study have the same dust mass and radius distributions as Herbig disks. No differences in dust mass are found for group I versus group II disks, in contrast to Herbig disks. The disks for which a gas mass could be determined show similar high mass disks as for the Herbig disks. Comparing the disk dust and gas mass distributions to the mass distribution of exoplanets shows that there also is not enough dust mass in disks around intermediate mass stars to form the massive exoplanets. On the other hand there is more than enough gas to form the atmospheres of exoplanets.

Conclusions: We conclude that the sampled IMTT disk population is almost indistinguishable compared to Herbig disks, as their disk masses are the same, even though these are younger objects. Based on this, we conclude that planet formation is already well on its way in these objects, and thus planet formation should start early on in the lifetime of Herbig disks. Combined with our findings on the group I and group II disks, we conclude that most disks around intermediate mass pre-main sequence stars converge quickly to small disks unless prevented by a massive exoplanet.

7.1   Introduction

Herbig disks are planet-forming disks around pre main-sequence stars called Herbig stars characterized by spectral types of B, A, and F, and stellar masses of 1.5 $M_\odot$ to 10 $M_\odot$ (e.g., Herbig 1960; Brittain et al. 2023). These disks are the precursors of famous directly imaged planetary systems such as HR 8799 (Marois et al. 2008, 2010), β Pic (Lagrange et al. 2010), and 51 Eri (Chauvin et al. 2017), and host some of the first kinematically detected planets (Pinte et al. 2018b; Izquierdo et al. 2023). How these planets have formed is not known, but we do know from exoplanet statistics that the prevalence of giant planets is highest around intermediate mass stars (e.g., Johnson et al. 2007, 2010; Nielsen et al. 2019; Fulton et al. 2021). Comparing dust structures and planet occurrence rates indeed shows a positive correlation between the two, and an increase in the prevalence of dust structures with stellar mass (van der Marel & Mulders 2021). Hence, Herbig disks are an important piece of the planet formation puzzle.

However, Herbig disks are generally quite old (a median age of 6 Myr for Herbig Ae stars, Vioque et al. 2018), many showing structures indicative of planet formation making these some of the most famous and best investigated disks (e.g., HD 100546, HD 163296, MWC 480; Fedele et al. 2017; Teague et al. 2018; Öberg et al. 2021; Booth et al. 2023a). Planets may already form early on in the lifetime of the disk, as there is an apparent lack of solids in class II disks to form the observed family of giant exoplanets (Manara et al. 2018; Tychoniec et al. 2020), and structures are already visible in earlier stages (ALMA Partnership et al. 2015; Segura-Cox et al. 2020). While the recent ALMA large program eDisk (Ohashi et al. 2023) does not show as many substructures in class 0 and class I objects as expected, possibly because these structures have not formed yet or high continuum optical depth, planetesimals, i.e., planets' building blocks, are likely to already form in these younger objects (e.g., Drążkowska & Dullemond 2018). Hence, these younger objects can still give us insights into planet formation timescales.

In total around 380 Herbig stars are known (Vioque et al. 2018; Wichittanakom et al. 2020; Guzmán-Díaz et al. 2021; Vioque et al. 2022). In addition, around 1500 more Herbig candidates have been identified by Vioque et al. (2020), so the total population size is expected to be much larger. A recent compilation of all available ALMA archival data out to Orion has shown that these Herbig disks are more massive in dust mass than the disks around their lower stellar mass counterparts called T Tauri stars (Stapper et al. 2022). This could naturally result in the higher prevalence of giant exoplanets around higher mass stars (e.g., Johnson et al. 2010). Moreover, work by Stapper et al. (2024) indicates that the Herbig disks are much warmer compared to T Tauri disks, causing less CO freeze-out and reprocessing in Herbig disks, consistent with thermo-chemical models (Bosman et al. 2018). This makes CO a viable mass tracer in Herbig disks. However, due to the relatively horizontal pre main-sequence evolutionary tracks in the Hertzsprung-Russell diagram, there are intermediate mass objects which were not part of the analysis of Stapper et al. (2022, 2024) which have the same stellar mass as Herbig stars but a spectral type later than F. These are called Intermediate mass T Tauri (IMTT) stars, the precursors of Herbig stars with spectral types of F to K3 and stellar

masses between 1.5 and 5 $M_\odot$ (Calvet et al. 2004; Valegård et al. 2021). Valegård et al. (2021) has compiled a sample of 49 IMTTs based on optical photometry. All stars within 500 pc with spectral types ranging from F0 to K3, and with a stellar luminosity of at least 2.1 $L_\odot$ (i.e., $M_\star \geq 1.5\ M_\odot$) were selected. The resulting sample, while not as young as class I objects, has a median age of 4 Myr, ranging from 0.3 Myr to 9 Myr, based on isochrones. We note that, like the Herbig disks, the IMTT disks are likely biased towards the high accretors and brightest disks (see, e.g., Figure 1 of Grant et al. 2023). A millimeter study into this sample will give insight into the evolution of the dust and gas around these intermediate mass objects.

A significant fraction of the IMTTs compiled by Valegård et al. (2021) has ALMA millimeter observations. In this work we compile the available ALMA data and compare the obtained dust masses to previous works of Herbig disks (Stapper et al. 2022, hereafter S22), and gas masses to Herbig disks (Stapper et al. 2024, hereafter S24), and to T Tauri disks (e.g., Ansdell et al. 2016, 2017; Barenfeld et al. 2016; van Terwisga et al. 2020, 2022; Manara et al. 2023).

In Section 7.2 the data selection and reduction procedures are set out. In Section 7.3 we explore if new models are needed compared to the DALI (Bruderer et al. 2012; Bruderer 2013) thermochemical models run for Herbig disks in S24, which can then be used to determine the gas masses from the CO observations. In Section 7.4 we show the resulting continuum and gas images in §7.4.1, obtain a dust mass and dust radius distribution and compare these to previous works in §7.4.2, and obtain the gas masses and radii in §7.4.3 and compare these to previous works. We discuss these results in Section 7.5, in the context of the Meeus et al. (2001) groups and the evolution of disks around intermediate mass stars in §7.5.1, and discuss the implications on planet formation around intermediate mass stars in §7.5.2. Lastly, Section 7.6 summarizes our conclusions.

7.2   Data selection & reduction

Using the IMTTs from Valegård et al. (2021), we obtained all publicly available Band 6 and Band 7 data on the ALMA archive[1] containing continuum, ^{12}CO, ^{13}CO, and C^{18}O observations. There is some overlap between the Herbig disks and IMTTs from Vioque et al. (2018) and Valegård et al. (2021), the former have been used in S22 for Herbig dust masses. These are AK Sco, HD 135344B, HD 142527, and HD 142666, see Table 7.1 for their spectral types. We use the data of these objects as presented in both S22 and S24. Additionally we include recently made public ALMA data from the DESTINYS program (e.g., Garufi et al. 2024, Ginski et al. 2024, Valegard et al. 2024) with project code 2021.1.01705.S (P.I.: C. Ginski), and not yet published data with project code 2022.1.01155.S (P.I.: M. Vioque), and ACA data with project codes 2021.2.00005.S and 2022.1.01460.S (both P.I.: J. Williams). The resulting sample of IMTTs has a range of spectral types ranging from A8 to K4. The histograms presented in Fig. 7.1 show that this range in spectral types overlaps with the late spectral type Herbig stars and

---

[1]`https://almascience.eso.org/asax/`
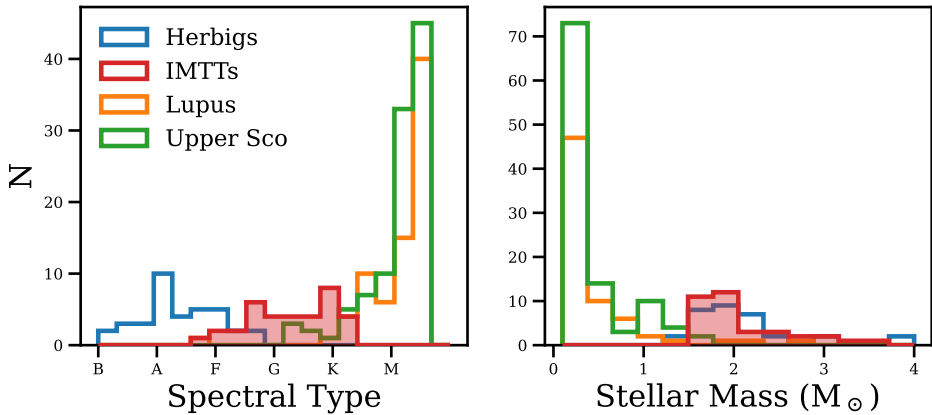
Figure 7.1: Histogram of the spectral types (left panel) and stellar masses (right panel) of the IMTTs in this work (from Valegård et al. 2021) compared to the Herbig star sample of S22 and references therein, and the surveys of Lupus (Ansdell et al. 2016) and Upper Sco (Barenfeld et al. 2016).

the early spectral type T Tauri stars, but that the range in stellar masses is the same as that of the Herbig stars. Also, see Figure 1 of Valegård et al. (2021) for a comparison of IMTT stars and Herbig stars on an Hertzsprung-Russell diagram.

The observing details of the unpublished data can be found in Table 7.3. In general the integration times are of the order of minutes, ranging from 1.4 minutes to 7.5 minutes. The data were taken in 2022 and 2023, almost all within a year of each other. As project 2021.1.01705.S only covers continuum and the ^{12}CO line, we supplement the data with other projects, where possible, to include the ^{13}CO and C^{18}O lines. Specifically for HD 34700 and PDS 277 only the ^{13}CO and C^{18}O data from 2021.2.00005.S are taken, as the ^{12}CO and continuum data are taken from the more sensitive observations of the 12m array.

The 12-m array data were phase self-calibrated based on the continuum data for multiple rounds up until the peak signal-to-noise did not improve compared to the previous round. This increased the peak signal-to-noise (S/N) of 12 of our targets (AK Sco, CR Cha, HD 135344 B, HD 142527, HD 294260, HT Lup, PDS 156, PDS 277, RY Tau, SR 21, SU Aur, and UX Tau). In most cases one to three rounds were done, beginning with a solution interval at "inf", then decreasing by factors of two, which increases the signal-to-noise ratio by a factor of 1.7 on average. After phase calibration, a single round of amplitude calibration was done as well, which was only applied to SU Aur. The resulting calibration table was applied to the line spectral windows by using the `applycal` task. For the ACA data no self-calibration was done. In this work we only use for T Tau the continuum data, and refer for the CO data to Rota et al. (2022).

Table 7.1: Source parameters used to calculate the dust masses, for Keplerian masking, and the obtained dust and gas radii.

Name	RA (h:m:s)	Dec (deg:m:s)	Dist. (pc)	$M_\star$ ($M_\odot$)	$L_\star$ ($L_\odot$)	Sp.Tp.	Group	V_{sys} (km s^{-1})	V_{int} (km s^{-1})	inc (°)	PA (°)	Ref.
AK Sco	16:54:44.8	-36:53:19.0	140	1.52	6.94	F5	I	5.4	2.5	109	128	1, a
Ass ChaT2-21	11:06:15.3	-77:21:56.7	165	2.09	10.37	G5	debris	–	–	–	–	2
Ass ChaT2-54	11:12:42.6	-77:22:22.9	203	1.92	5.03	G8	debris	–	–	–	–	3
BE Ori	05:37:00.1	-06:33:27.3	392	1.86	7.95	G3	II	–	–	–	–	2
Brun 656	05:35:21.3	-05:12:12.7	467	2.72	27.4	G2	debris	–	–	–	–	2
CO Ori	05:27:38.2	+11:25:39.1	400	2.97	43.82	F7	II	–	–	–	–	4
CR Cha	10:59:06.9	-77:01:40.3	186	1.62	3.72	K4	II	5.2	2.5	31	-36	5, b
CV Cha	11:12:27.6	-76:44:22.3	192	1.85	4.63	K0	II	–	–	–	–	2
DI Cha	11:07:20.6	-77:38:07.3	190	1.95	9.82	G2	II	–	–	–	–	2
GW Ori	05:29:08.4	+11:52:12.7	398	3.02	35.47	G5	I	13.8	2.5	37	176	6, c
Haro 1-6	16:26:03.0	-24:23:36.6	134	2.04	12.78	G1	I	–	–	–	–	2
HBC 442	05:34:14.2	-05:36:54.2	382	1.9	13.2	F8	II	–	–	–	–	7
HBC 502	05:46:07.9	-00:11:56.9	411	2.01	10.71	K3	I	–	–	–	–	2
HD 34700	05:19:41.4	+05:38:42.8	353	2.46	24.34	G0	I	5.1	4.5	0	0	2
HD 35929	05:27:42.8	-08:19:38.5	384	3.25	80.78	F2	II	–	–	–	–	8
HD 135344B	15:15:48.4	-37:09:16.4	135	1.5	8.09	F8	I	7.1	1.5	10	-62	2, d
HD 142527	15:56:41.9	-42:19:23.7	157	2.06	19.31	F6	I	3.6	1.5	27	26	9, e
HD 142666	15:56:40.0	-22:01:40.4	148	1.62	11.81	A8	II	4.1	1.5	62	18	2, f
HD 144432	16:06:57.9	-27:43:10.1	155	1.64	12.5	A9	II	–	–	–	–	10
HD 288313	05:54:03.0	+01:40:22.1	418	3.47	38.47	K2	–	–	–	–	–	2
HD 294260	05:36:51.3	-04:25:40.0	407	1.68	8.74	G1	II	12.0	2.5	0	0	11
HQ Tau	04:35:47.3	+22:50:21.4	158	1.85	4.63	K0	II	–	–	–	–	2
HT Lup	15:45:12.8	-34:17:31.0	154	1.8	5.95	K3	II	5.4	2.5	48	14	2, g
LkHA 310	05:47:11.0	+00:19:14.8	422	1.87	6.8	G6	I	–	–	–	–	2
LkHA 330	03:45:48.3	+32:24:11.8	308	1.93	14.39	F7	I	9.0	0.8	28	-49	2, h
PDS 156	18:27:26.1	-04:34:47.6	398	2.61	21.12	G5	II	13.0	2.5	0	0	2
PDS 277	08:23:11.8	-39:07:01.5	343	1.59	9.68	F3	I	1.6	2.5	0	0	2

Table 7.1: Continued.

Name	RA (h:m:s)	Dec (deg:m:s)	Dist. (pc)	$M_\star$ ($M_\odot$)	$L_\star$ ($L_\odot$)	Sp.Tp.	Group	V_{sys} (km s^{-1})	V_{int} (km s^{-1})	inc (°)	PA (°)	Ref.
PR Ori	05:36:24.8	-06:17:30.6	408	2.5	10.83	K1	I/II	–	–	–	–	2
RY Ori	05:32:09.9	-02:49:46.8	365	1.69	9.01	F7	II	–	–	–	–	7
RY Tau	04:21:57.4	+28:26:35.1	134	1.69	11.97	K1	II	6.6	2.5	65	-23	6, i
EM* SR 21	16:27:10.3	-24:19:13.1	138	1.64	7.03	G1	I	2.75	2.5	15	-16	12, j
SU Aur	04:56:00.4	+30:34:01.1	158	2.22	12.75	G4	I	5.8	1.5	53	123	2, k
SW Ori	05:34:15.8	-06:36:04.7	376	1.51	3.28	G8	I	–	–	–	–	2
T Tau	04:21:59.4	+19:32:06.2	144	1.94	8.88	K0	I	–	–	–	–	6
UX Tau	04:30:04.0	+18:13:49.2	139	2.34	8.91	G8	I	5.4	2.5	40	-167	2, 1

Notes. Object coordinates, distances, stellar masses and luminosities, and groups are taken from Valegård et al. (2021) and references therein. See Valegård et al. (2021) for the uncertainties on these values. The spectral types are taken from: (1) Houk (1982), (2) Valegård et al. (2021), (3) Daemgen et al. (2013), (4) Mora et al. (2001), (5) Torres et al. (2006), (6) Herbig (1977), (7) Manoj et al. (2006), (8) Houk & Swift (1999), (9) Houk (1978), (10) Houk (1982), (11) Rydgren & Vrba (1984), (12) Suárez et al. (2006). The inclinations and position angles are taken from: (a) Czekala et al. (2015), (b) Kim et al. (2020), (c) Bi et al. (2020), (d) Cazzoletti et al. (2019), (e) Kataoka et al. (2016), (f) Huang et al. (2018), (g) Kurtovic et al. (2018), (h) Pinilla et al. (2022a), (i) Long et al. (2018), (j) Pérez et al. (2014), (k) Ginski et al. (2021), (l) Francis & van der Marel (2020). For the disks with a zero degree inclination and position angle a mask was applied, but no inclination and position angle values were found in the literature.

Table 7.2: Continuum and line fluxes, dust and gas radii, and resulting dust and gas masses.

Name	Continuum Flux (mJy)	$R_{dust,\,68\%}$ (au)	$R_{dust,\,90\%}$ (au)	^{12}CO Flux (Jy km s^{-1})	$R_{gas,\,68\%}$ (au)	$R_{gas,\,90\%}$ (au)
AK Sco	26.14	42±2	53±2	2.18±0.05	78±4	114±5
Ass ChaT2-21	<1.21*	–	–	<0.29*	–	–
Ass ChaT2-54	<3.16*	–	–	<0.89*	–	–
BE Ori	0.94	<286	<373	<0.33	–	–
Brun 656	<1.68	–	–	–	–	–
CO Ori	<7.78	–	–	<2.09	–	–
CR Cha	139.47	63±3	88±3	2.22±0.04	158±27	249±27
CV Cha	56.70*	<76	<119	–	–	–
DI Cha	23.76*	<73	<100	–	–	–
GW Ori	200.33	287±12	382±12	51.54±0.06	782±16	1033±16
Haro 1-6	3.22	<108	<155	<0.88	–	–
HBC 442	<9.29	–	–	<2.41	–	–
HBC 502	<4.57	–	–	–	–	–
HD 34700	10.51	<189	<244	6.65±0.06	301±38	421±38
HD 35929	0.22	<12	<17	<0.04	–	–
HD 135344B	539.69*	81±10	109±10	20.07±0.18*	158±10	219±10
HD 142527	1048.15	208±9	236±9	27.14±0.10	542±30	793±30
HD 142666	118.55	40±1	52±1	4.05±0.03	136±6	186±6
HD 144432	44.92	<587	<856	<2.25	–	–
HD 288313	1.03	<99	<166	<0.15	–	–
HD 294260	41.53	<123	<181	1.72±0.03	<233	<348
HQ Tau	3.94	<22	<30	–	–	–
HT Lup	62.54	19±1	25±1	4.78±0.04	111±2	141±2
LkHA 310	14.55	<109	<157	<0.18	–	–
LkHA 330	52.33	123±5	141±5	2.00±0.12	219±23	337±54
PDS 156	9.94	<90	<129	0.35±0.03	<164	<273
PDS 277	39.48	<114	<168	0.62±0.04	<217	<322
PR Ori	21.82	<344	<510	–	–	–
RY Ori	<22.49	–	–	<2.58	–	–
RY Tau	207.91	51±1	65±1	7.89±0.20	171±7	237±10
SR 21	88.20	61±3	69±3	0.53±0.02	28±4	35±4
SU Aur	16.73	<58	<100	13.52±0.13	255±11	346±11
SW Ori	7.46	<285	<396	<0.38	–	–
T Tau	171.62	16±1	22±1	–	–	–
UX Tau	64.54	49±7	64±7	8.46±0.12	216±9	453±24

Table 7.2: Continued.

^{13}CO Flux (Jy km s^{-1})	$R_{gas,\,68\%}$ (au)	$R_{gas,\,90\%}$ (au)	$C^{18}O$ Flux (Jy km s^{-1})	$R_{gas,\,68\%}$ (au)	$R_{gas,\,90\%}$ (au)	M_{dust} ($M_{\oplus}$)	$\mathrm{Log}_{10}(M_{gas})$ ($M_{\odot}$)
0.68±0.04	66±6	97±18	0.27±0.02	52±5	69±11	6.0±0.6	-2.6±1.2
–	–	–	–	–	–	<0.1	–
<5.06*	–	–	<5.20*	–	–	<0.5	–
<0.39	–	–	<0.31	–	–	1.7±0.2	–
–	–	–	–	–	–	<3.0	–
<2.51	–	–	<1.85	–	–	<10.7	–
0.74±0.05	150±28	233±111	0.29±0.02	139±28	201±28	69.7±7.0	-1.7±0.8
<4.99 *	–	–	<4.51*	–	–	10.4±1.0	–
<4.48*	–	–	<1.80*	–	–	3.4±0.3	–
6.30±0.07	578±16	808±19	1.30±0.03	419±16	561±21	241.8±27.3	-1.1±0.4
<0.99	–	–	<0.44	–	–	0.6±0.1	–
<2.58	–	–	<2.42	–	–	<16.2	–
–	–	–	–	–	–	<7.9	–
<1.20	–	–	<0.91	–	–	10.7±1.1	–
<0.04	–	–	<0.03	–	–	0.23±0.03	–
8.86±0.08*	119±9	171±9	3.55±0.08*	86±9	125±9	35.8±3.7	-1.7±0.4
11.88±0.07	334±31	491±31	3.91±0.04	271±31	368±31	231.2±23.4	-0.8±0.2
1.51±0.06	<182	<260	0.64±0.04	<164	<236	26.0±2.6	-1.5±0.7
<1.59	–	–	<1.21	–	–	13.1±1.3	–
<0.18	–	–	<0.16	–	–	1.6±0.2	–
–	–	–	–	–	–	74.4±7.9	–
<0.18	–	–	<0.13	–	–	1.6±0.2	–
<0.24	–	–	<0.18	–	–	18.0±1.8	–
<0.16	–	–	<0.15	–	–	36.7±4.2	–
1.48±0.08	194±14	261±29	0.63±0.04	117±7	143±12	47.2±5.3	-1.2±0.5
<0.06	–	–	<0.05	–	–	16.2±1.7	–
<0.72	–	–	<0.67	–	–	48.8±5.0	–
–	–	–	–	–	–	41.7±4.3	–
<2.50	–	–	<2.16	–	–	<40.0	–
2.16±0.13	132±13	228±33	<0.10	–	–	37.1±23.9	–
0.50±0.02	31±4	42±4	0.38±0.02	34±4	47±4	23.8±2.4	-1.2±0.6
0.91±0.13	211±65	320±141	–	–	–	4.9±0.5	–
–	–	–	<0.34	–	–	15.7±1.6	–
–	–	–	–	–	–	47.3±4.8	–
2.10±0.06	94±9	152±13	0.96±0.04	82±9	132±20	13.7±1.4	-1.4±0.6

Table 7.3: Observing details of the unpublished data.

Project Code	P.I.	Name	Date	Int. Time (min.)	Calibrators	Array
2021.1.01705.S	C. Ginski	HD 294260	21/08/22, 02/09/22	2.6	J0423-0120, J0532-0307	12m
		HD 34700	21/08/22	1.4	J0423-0120, J0527+0331	12m
		PDS 277	31/08/22	2.4	J1037-2934, J0828-3731	12m
2022.1.01155.S	M. Vioque	HD 288313 A	06/04/23, 15/06/23	7.3	J0423-0120, J0541-0541	12m
		LkHα 310	06/04/23, 15/06/23	7.5	J0423-0120, J0541-0541	12m
		PDS 156	09/04/23	3.7	J1924-2914, J1851+0035	12m
2021.2.00005.S	J. Williams	CO Ori	01/06/23	4.0	J0423-0120, J0532+0732	ACA
		HD 34700	01/06/23	7.4	J0423-0120, J0532+0732	ACA
		HBC 442	03/07/23	3.4	J0423-0120, J0501-0159	ACA
		RY Ori	03/07/23	3.4	J0423-0120, J0501-0159	ACA
		PDS 277	28/08/22, 06/09/22	7.4	J0538-4405, J0854+2006, J0501-0159	ACA
2022.1.01460.S	J. Williams	HD 144432	24/05/23	4.9	J1924-2914, J1554-2704	ACA

Notes. For the resulting spatial and velocity resolution, and the rms noise see Table 7.A.1.

For the continuum data, the imaging was done using multifrequency synthesis. The spectral lines were imaged after subtracting the continuum using `uvcontsub`. Different velocity resolutions were used depending on the dataset. For the imaging we used `multiscale` using 0 (point source), 1, 2, 5, 10 and 15 times the size of the beam in pixels (~ 5 pixels) as the size of the scales. Similar to S24, the last three scales were only used if the disk morphology allowed for it. Lastly, for the mosaic data of Brun 656 and HBC 502, we use the product data from the archive. See Table 7.A.1 for the resulting data parameters.

To obtain the integrated fluxes, we use the same method as described in S22 and S24 which uses an increasing aperture size to ascertain what the maximum amount of disk integrated flux is. This method also returns a size of the disk. The found fluxes and sizes are presented in Table 7.2.

To obtain the dust masses, we again follow S22, using the following relationship (Hildebrand 1983) to directly relate the continuum emission to the dust mass, assuming optically thin emission,

$$M_{\text{dust}} = \frac{F_\nu d^2}{\kappa_\nu B_\nu(T_{\text{dust}})}. \tag{7.1}$$

Here, F_ν is the continuum flux as emitted by the dust in the disk at a distance d to the object, and κ_ν is the dust opacity at a given frequency (Beckwith et al. 1990). $B_\nu(T_{\text{dust}})$ is the value of the Planck function at a given dust temperature T_{dust}. The dust temperature is given by the relationship of Andrews et al. (2013), which scales the dust temperature by the stellar luminosity in solar luminosities via

$$T_{\text{dust}} = 25 \text{ K} \times \left(\frac{L_\star}{L_\odot}\right)^{1/4}. \tag{7.2}$$

7.3   Model setup

For the modeling of the CO isotopologues, we use the `DALI` grid for Herbig disks presented in S24. `DALI` (Bruderer et al. 2012; Bruderer 2013) is a thermo-chemical code which takes heating, cooling, and chemical processes into account and uses
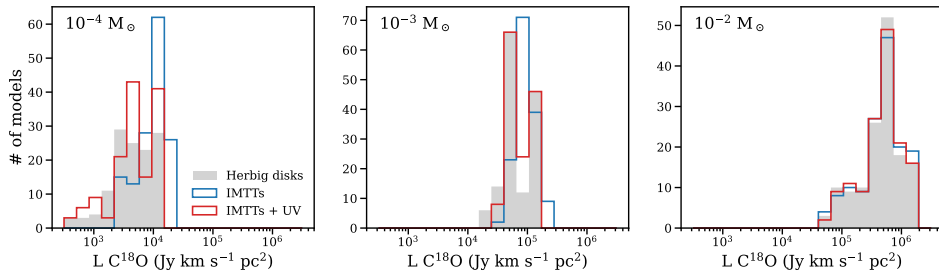
Figure 7.2: Histogram of the disk integrated $C^{18}O$ luminosities of models run by the thermochemical code DALI for three different disk masses, as indicated in the top left of each panel. A comparison is done between the models used by S24 (gray), and models for which the stellar effective temperature has been lowered to an IMTT appropriate value either with (red) or without (blue) accretion UV added. The lower effective temperature of the IMTT star increases the $C^{18}O$ luminosity for the lowest mass disks compared to the Herbig disk models, as there is less UV emission and therefore less photodissociation of CO. Adding the accretion UV increases the photodissociation of CO, moving the $C^{18}O$ luminosity back to Herbig disk levels.

these to solve for the gas and dust thermal structure of the disk. The models used by S24 use the CO isotopologue chemistry network of Miotello et al. (2016), which includes isotope-selective photodissociation, fractionation reactions, self-shielding, and freeze-out.

T Tauri stars have lower effective temperatures compared to Herbig stars resulting in less UV emission in the former compared to the latter. Therefore, UV emission from accretion is added to the stellar spectrum for T Tauri stars (e.g. Miotello et al. 2014, 2016), as accretion contributes significantly to the overall UV budget. This is in contrast to Herbig stars, for which the accretion UV is not significant compared to the UV photons already emitted by the star itself (Miotello et al. 2016). In the case of IMTTs however, while having higher luminosities compared to T Tauri stars, accretion UV could still add significant amounts of UV to the overall spectrum.

To test this, we compare the grid of models from S24 to two smaller grids of models with an effective stellar temperature of 5500 K and luminosity of 10 $L_\odot$ for IMTT disks, excluding the largest disk models from S24. One grid has accretion UV added and one grid does not. The accretion luminosity is set as 1.5 $L_\odot$, the median value from the works of Calvet et al. (2004), from modeling at wavelengths > 2000 Å, and Wichittanakom et al. (2020), from Hα emission. The accretion was added to the stellar spectrum with a blackbody at 10^4 K. The addition of the accretion UV results in $L_{uv}/L_{bol} = 7.8 \times 10^{-2}$, compared to $L_{uv}/L_{bol} = 3.2 \times 10^{-2}$ without. Figure 7.2 compares the resulting disk integrated $C^{18}O$ luminosities of both grids to the Herbig disk grid from S24, raytraced at a distance of 100 pc. Each panel presents a different gas mass, from 10^{-4} to 10^{-2} solar masses. The lower effective temperature of the IMTT stars decreases the UV luminosity compared to Herbig stars, which increases the $C^{18}O$ luminosity of the disk for the

lowest disk masses due to a decrease in photo-dissociation of CO. As the CO gas becomes optically thin self-shielding becomes less efficient. For the highest disk mass considered in Fig. 7.2 the disk integrated $C^{18}O$ luminosity is very similar to that of the Herbig disks. When including the accretion UV, the $C^{18}O$ luminosity compensates for the decrease in UV emission due to the lower effective temperature, effectively moving the distribution back again to that of the Herbig disks. Hence, we use the same models in this work as was done in S24.

7.4   Results

7.4.1   Continuum and gas images

Figure 7.3 presents the continuum images of all IMTTs observed with ALMA. Similar to the observations of Herbig disks in S22, there is a large variety of sizes and structures visible in our set of IMTT observations. The majority of disks are unresolved, but all disks which are resolved exhibit transitional disk features or multiple rings. In total, 11 disks have resolved observations showing structures, out of the 26 detected disks, this is 42%. This is lower compared to the fraction found by S24, which was 60% (15/25), which is likely due to the lower spatial resolution of the data available in our work. All disks which are also classified as Herbig disks are part of the resolved disks, removing these disks lowers the amount of resolved disks even more, showing a clear lack of deep observations towards IMTT disks. Apart from disks with resolved structures, there are three unresolved disks which are noteworthy. For HD 35929 the data give strong constraints on the size of the dust disk, less than 41 au, while still being unresolved. This may only be free-free emission (for more on free-free emission, see e.g., Rota et al. 2024). Also SU Aur and HD 34700, which show extended asymmetric emission in the dust, while the main disk is unresolved. Particularly SU Aur is famous for its large arm in CO due to late-stage infall, which could be related to this asymmetry (Ginski et al. 2021).

There are also multiple stellar systems present in our sample. HD 288313 in particular is a complex system of at least three components (Reipurth et al. 2010). The disk around the A component (the Herbig star) is quite faint in the continuum emission, while one of the other components has a peak flux an order of magnitude higher. HT Lup is a triple system, with all three components having clear millimeter continuum emission (Kurtovic et al. 2018). The A component around the Herbig star has the largest disk. In Fig. 7.3, the B component is also visible, while the C component is outside of the field of view. Lastly, T Tau is a triple stellar system (Köhler et al. 2016).

The moment zero maps of disks for which at least one of the three CO isotopologues are detected are presented in Figure 7.4. If one of the isotopologues is detected, the other non-detections are also shown by integrating over the same velocity range as is done for the detected isotopologue. If a panel is empty, no observations of that particular isotopologue are available.

Again, a large variety in structures can be seen. In particular cavities are visible in three of our disks in both ^{13}CO and $C^{18}O$: HD 135344B, LkHα 330, and
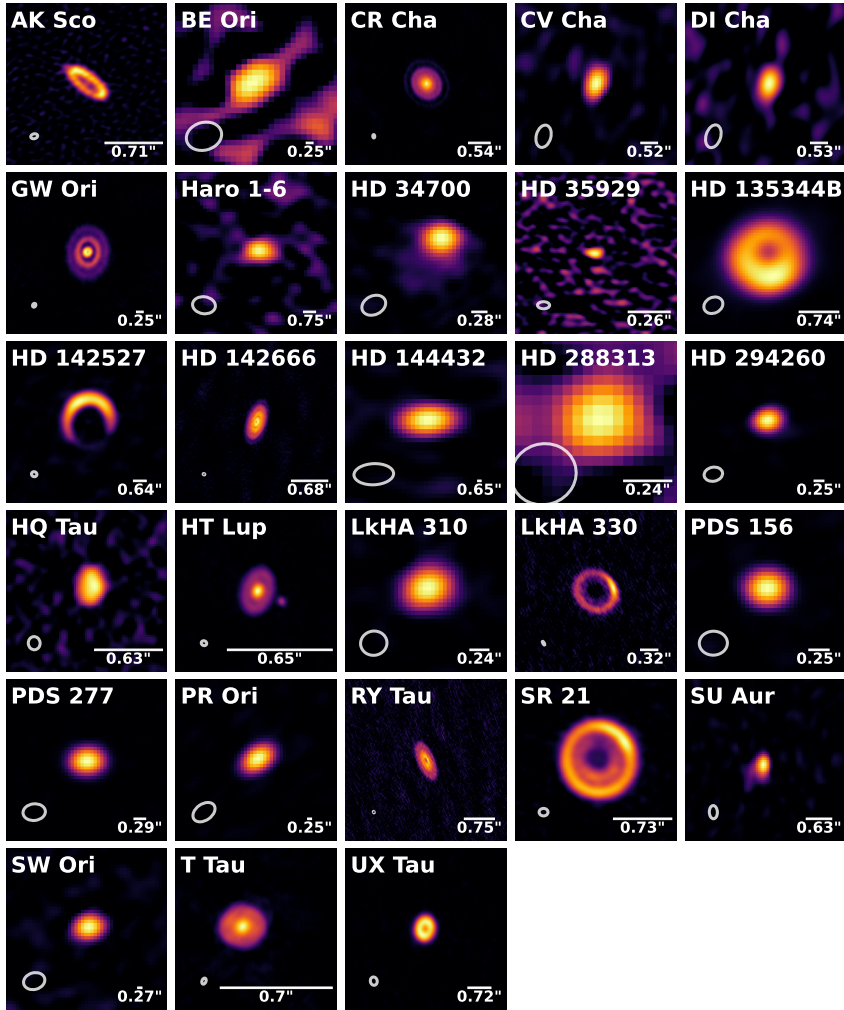
Figure 7.3: Continuum images of Intermediate Mass T Tauri disks with a detection, using a sinh stretch. The size of the image is indicated by the bar of size 100 au on the bottom right of each panel with below the angular size. The beam size is shown as the ellipse on the bottom left of each panel.

HD 142527 (see for more on these disks e.g., van der Marel et al. 2015; Brown et al. 2008; Pinilla et al. 2022a; Temmink et al. 2023). This is indicative of deep cavities, where these molecules become optically thin. Apart from cavities other structures are visible as well, in particular envelopes and streamers. These potential streamers and envelopes can be seen in the ^{12}CO emission of GW Ori, T Tau (Rota et al. 2022), and SU Aur (Ginski et al. 2021). We note that streamers are not present in the sample of Herbig disks, anecdotally showing that the IMTT disks are indeed younger compared to the Herbig disks. HT Lup has large unresolved structures
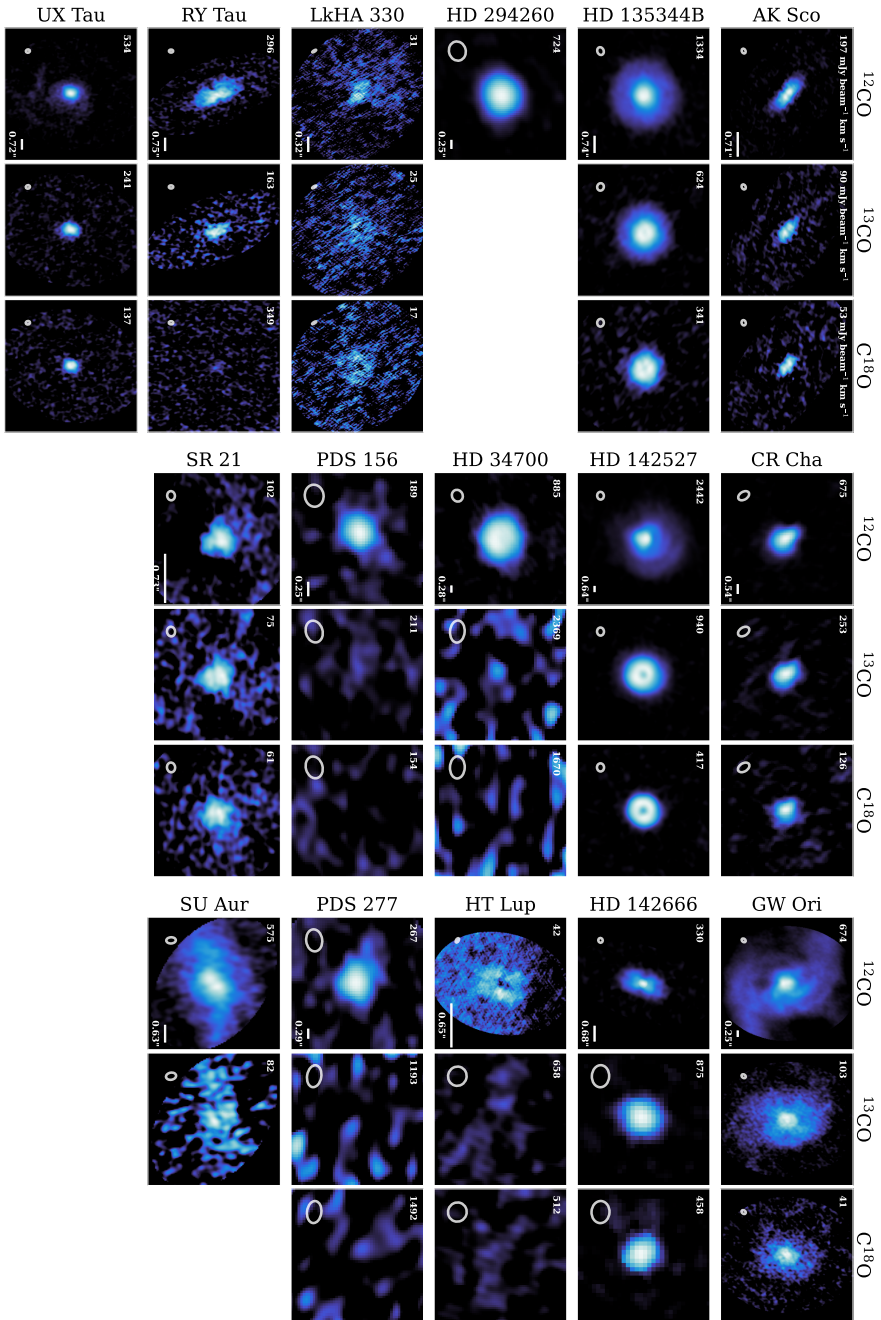
Figure 7.4: ^{12}CO, ^{13}CO, and $C^{18}O$ velocity integrated-intensity maps as obtained with Keplerian masking for all IMTTs which have a detection in at least one of the three isotopologues. An empty panel indicates that no observations are available of that particular isotopologue.

visible by large fringe patterns in the observations, and strong continuum absorption in the center of the disk (see the cavity-like appearance in Fig. 7.4). Other disks with absorption include SR 21 in particular, with strong absorption features on the south-western side of the disk resulting in an asymmetric appearance in ^{12}CO.

7.4.2   Dust masses and radii

Following S22 we can obtain cumulative distributions from the dust masses using the `lifelines` package (Davidson-Pilon et al. 2021), together with the probability distributions by fitting a log-normal distribution, see the left and right panel of Fig. 7.5 respectively. In addition, the cumulative distribution of the Herbig disks from S22, and the distributions of the disks in Lupus (Ansdell et al. 2016) and Upper Sco (Barenfeld et al. 2016) are also shown.

The distributions of the Herbig dust masses and the IMTT dust masses stand out as very similar. At around 60 $M_{\oplus}$ the IMTT distribution does slightly dip below the Herbig distribution, but is still within the shaded region indicating the 1σ confidence interval. Using a Kolmogorov-Smirnov test using `scipy` (Virtanen et al. 2020), we can assess whether the distributions are sampled from the same underlying distribution. We obtain a p-value of 0.962, indicating that we can accept the null hypothesis and that both distributions have the same underlying dust mass distribution.

Following S22, we can obtain the probability distributions by fitting a log-
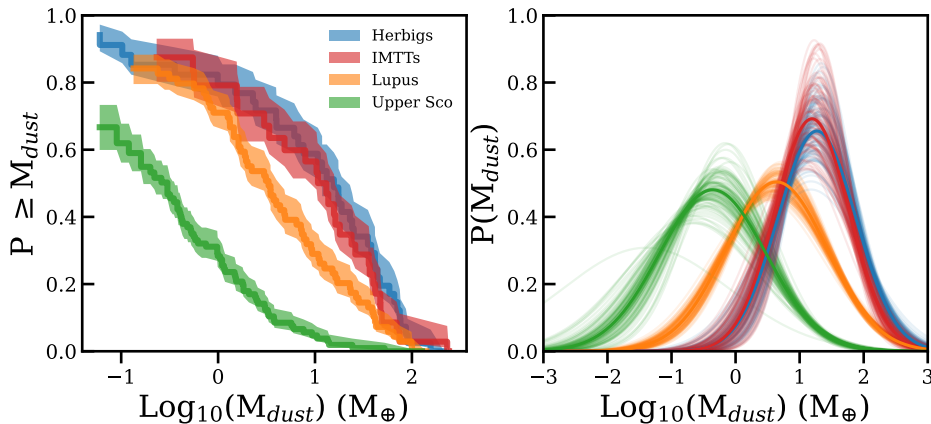
Figure 7.5: Dust mass distributions of the IMTTs, Herbig disks (Stapper et al. 2022), disks in Lupus (Ansdell et al. 2016), and disks in Upper Sco (Barenfeld et al. 2016). The left panel shows the cumulative distributions, with the shaded region indicating the 1σ confidence interval. The right panel presents the probability distributions obtained by fitting a log-normal distribution to the cumulative distributions using a bootstrapping method. This figure shows a clear similarity between the IMTT and Herbig dust mass distributions.
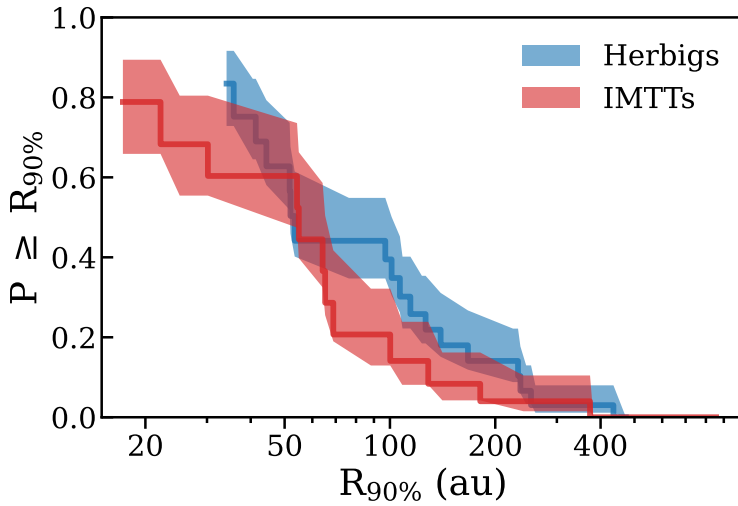
Figure 7.6: Cumulative distributions of the 90% dust radii of the Herbig disks (S24) and of the IMTTs. Both samples have a similar radius distribution.

normal distribution to the cumulative distributions using a bootstrapping method with 10^5 samples. These fits result in the probability distributions shown in the right panel of Figure 7.5. The resulting distributions show a clear overlap between the Herbig disks and IMTTs. Table 7.4 shows the resulting means and standard deviations of the distributions. We include the dust masses of five Herbig disks observed with NOEMA from S24, hence the slight difference in obtained parameters for the Herbig disk dust mass distribution compared to the one in S22. Both the mean and the standard deviation of the Herbig disks and IMTTs fall within the given uncertainty intervals. Hence, further supporting the similarities between the two distributions.

Figure 7.6 presents the cumulative distributions of the $R_{90\%}$ dust radii for the IMTT disks and for the Herbig disks (S24). The radii are very similar between the two populations, as was also the case for the dust masses. The largest IMTT disk in our sample is the disk of GW Ori, with a 90% radius of 382 au. The other resolved disks range from 236 au down to 25 au with a median of 69 au. Again using a Kolmogorov-Smirnov test, we can test the null hypothesis of both distributions being sampled from the same populations. Indeed, we cannot reject this null hypothesis based on the resulting p-value of 0.860 . Hence,the two distributions can be sampled from the same underlying population.

7.4.3   Gas masses and radii

In this section we compare the disk integrated luminosities of the ^{13}CO and C^{18}O isotopologues to the DALI models obtained by S24. This is shown in Figure 7.7. In the left panel, the $J = 2 - 1$ transition is shown, while the right panel shows

Table 7.4: Log-normal distribution fit results for the dust mass cumulative distributions shown in Fig. 7.5. The M_{dust} parameters are given in $\log_{10}(M/M_{\oplus})$.

	μ	σ
Herbigs	$1.27^{+0.05}_{-0.05}$	$0.61^{+0.06}_{-0.06}$
IMTTs	$1.19^{+0.06}_{-0.07}$	$0.58^{+0.09}_{-0.08}$
Lupus	$0.64^{+0.04}_{-0.05}$	$0.79^{+0.05}_{-0.04}$
Upper Sco	$-0.36^{+0.11}_{-0.14}$	$0.83^{+0.09}_{-0.07}$

the $J = 3 - 2$ transition of the CO isotopologues. The observations are given as the black markers. The radius of both the observations and the disk models are indicated by the size of the markers. The radius is traced by the ^{13}CO 90% radius.

Comparing the observed and modeled ^{13}CO and C^{18}O luminosities as shown in Fig. 7.7, it is clear that for the detected disks, most are in the optically thick regime similar to the Herbig disks, as the smallest disks are on the bottom left, while the largest disks are on the top right. See S24 for more details.

For the disks in which the CO isotopologues are detected, we obtain the disk mass after selecting models based on the disk and stellar parameters in Table 7.1 (see S24 for details on this selection process). Apart from RY Tau, for which only a C^{18}O upper limit was found but ^{13}CO was detected, all disks show gas-to-dust ratios of at least the ISM value of 100 or higher. This is in line with the findings for the Herbig disks in S24. Importantly, while the upper limits for the Herbig disks with non-detections of ^{13}CO and C^{18}O were constraining enough to obtain a limit on the disk mass, the upper limits obtained for the IMTT disks are not. Hence, most have upper limits of the maximum disk mass in the model grid. The obtained gas masses are in general slightly lower compared to the Herbig disks, see
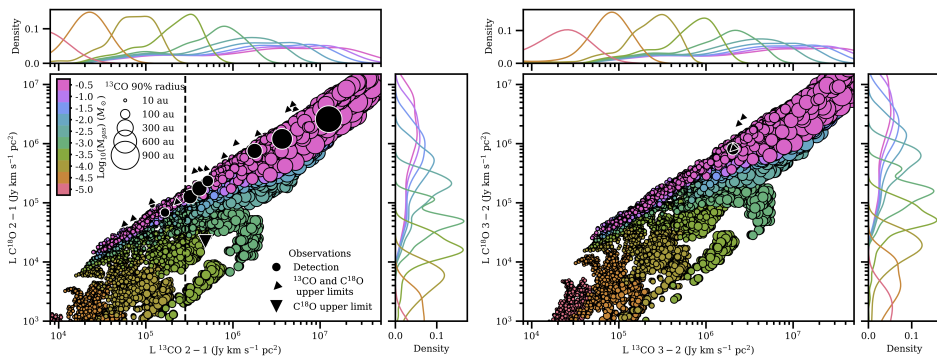
Figure 7.7: ^{13}CO and C^{18}O disk integrated luminosities for transitions $J = 2 - 1$ (left panel) and $J = 3 - 2$ (right panel). The colors correspond to the DALI models from S24, while the black markers correspond to the observations. The vertical line in the left panel indicates the ^{13}CO luminosity of SU Aur, as no C^{18}O observations are available.
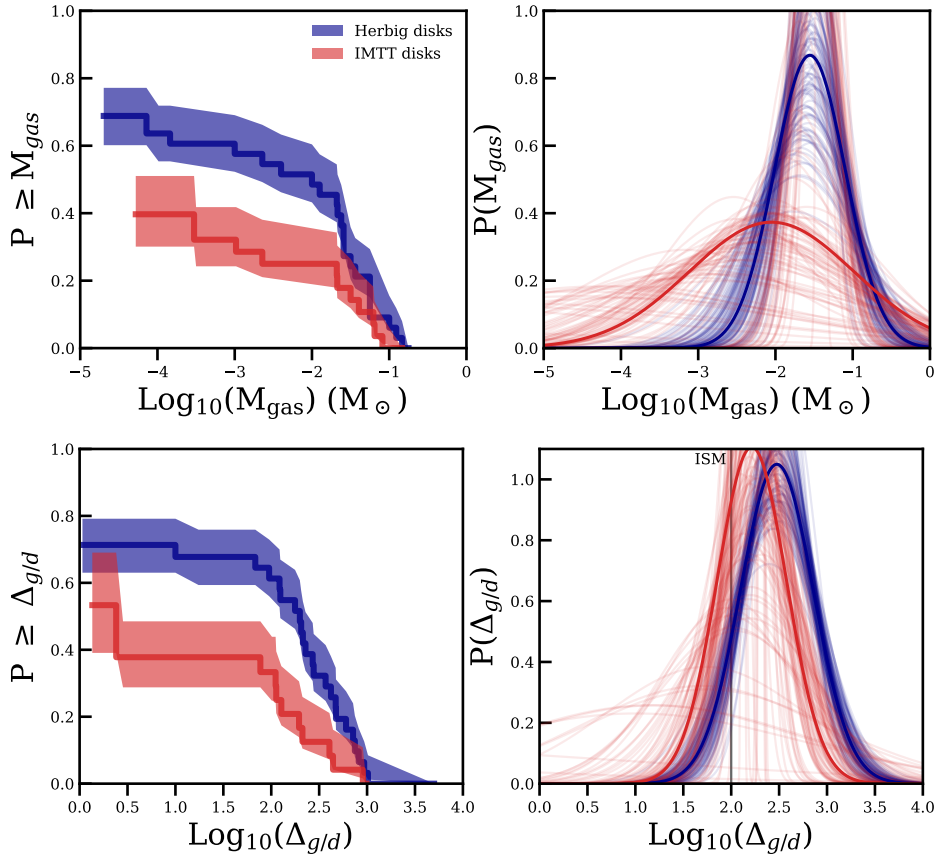
Figure 7.8: The resulting gas masses obtained from the models of S24 are shown in the top row. The Herbig disks are shown in blue, while the distribution of the IMTT disks is shown in red. Combining the gas distributions with the dust mass distributions in Fig. 7.5 results in the gas-to-dust ratio distributions in the bottom row.

Figure 7.8. The distribution is wider going towards lower gas masses compared to the Herbig disks.

Combining the gas and dust mass distributions of the IMTT and Herbig disks from Figs. 7.5 and 7.8, we obtain two similar gas-to-dust ratio distributions in the bottom row of Fig. 7.8. The distribution of the IMTT disks seems to be slightly lower. However, the difference in the mean gas-to-dust ratio might be pushed down due to the many upper limits in the IMTT sample. Hence, we conclude that there is no indication of the IMTT gas-to-dust ratios being different when compared to the Herbig disks.

The dust and gas ^{12}CO 90% radii are presented in Fig. 7.9, in which the radii are compared to those of the Herbig disks (S22 and S24). The dust radial
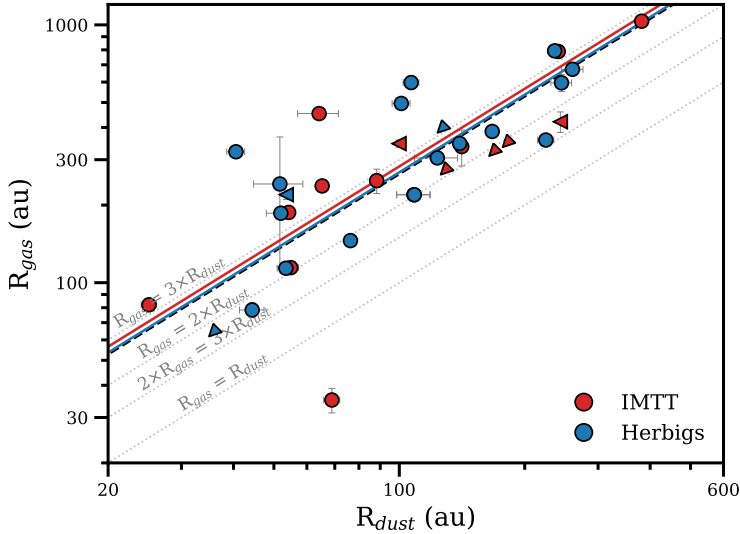
Figure 7.9: Dust and gas 90% radii of the IMTT disks (red) and Herbig disks
(blue). The fitted relation between the two parameters is shown as the solid lines.
The relationship is the same for both Herbig and IMTT disks. In yellow the region
is shown where the difference between the dust and gas radii cannot be explained
by optical depth effects only (Trapman et al. 2019). The dashed black line is a fit
through the IMTT disks excluding SR 21, GW Ori, HT Lup, and SU Aur.

drift dominated limit from Trapman et al. (2019) is also shown, which indicates
the region where optical depth effects cannot solely account for the difference seen
between the gas and dust radius, hence radial drift is needed. Fitting a relationship
through the scatter of the resolved disks we find a ratio of 2.8±0.2 between the gas
and dust radius for the IMTT disks. This is the same compared to the ratio of the
Herbig disks of 2.7±0.2 within the uncertainties. We note that for multiple IMTT
disks the ^{12}CO radius is rather difficult to determine. GW Ori has large spiral-like
structures on the north and south side of the disk. As this is not the case for the
^{13}CO disk, the ^{12}CO disk is likely measured to be larger. HT Lup has foreground
contamination, but the disk is visible in ^{12}CO. The radius size measurement is
therefore set by visual inspection. SR 21 has absorption on the south side of the
disk, reducing the size of the ^{12}CO disk. Still, for the other two isotopologues the
disk is not found to be large, the CO isotopologues are only peaking inside the
cavity of this transition disk. This results in a smaller gas disk size compared to
the dust disk size. Lastly, due to the infalling streamer, the size of the disk of
^{12}CO is also difficult to determine. Removing these four disks results in a gas to
dust radius ratio of 2.6±0.3, again the same as that for the Herbig disks.

Table 7.5: Log-normal distribution fit results for the dust mass cumulative distributions shown in Fig. 7.10. The M_{dust} parameters are given in $\log_{10}(M/M_\oplus)$.

	μ	σ
Group I	$1.38^{+0.13}_{-0.25}$	$0.41^{+0.23}_{-0.15}$
Group II	$1.15^{+0.08}_{-0.15}$	$0.35^{+0.19}_{-0.14}$

7.5   Discussion

7.5.1   Evolution of Herbig disks

As IMTTs are the precursors of Herbig stars, the fact that the disk dust radii and masses are the same may be unexpected. As the IMTTs are younger, an evolution towards smaller less massive disks due to dust evolutionary processes is expected. As proposed in S22, the stopping of radial drift due to massive exoplanets can explain the large difference seen in the mass and size of Herbig disks when compared to T Tauri disks. As no difference in the radius or the dust mass is found between the Herbig disks and the IMTT disks, this may indicate that massive exoplanets have already formed in the IMTT disks stopping radial drift, resulting in a higher inferred disk mass. As both the radii and dust mass distributions are indistinguishable for both IMTTs and Herbigs, this implies that planets are forming early in their lifetime, dominating the (dust) evolution of these disks, giving very similar results. Furthermore, by selecting stars with infrared excess with masses between 1.5 and 3.5 solar masses within 300 pc, Iglesias et al. (2023) found that most of these pre-main sequence intermediate mass stars are already evolved towards the debris disk stage in less than 10 Myr (though the lack of accretion in these stars may indicate that these disks are older). The main difference between these stars and the Herbig stars is that for Herbig stars emission lines are necessary to be classified as one. Given the stark similarities between Herbig and IMTT disks, this separation into full disks and debris disks should happen early on in the disk lifetime, and might highly depend on planet formation happening in these disks.

In S22, a dust mass dichotomy was found between the group I and group II disks as defined by Meeus et al. (2001). In particular the distribution of dust masses of the group II disks was very similar to the dust mass distribution of the disks in Lupus (Ansdell et al. 2016). On the other hand, the group I disks were more massive. Moreover, in contrast to the mostly full disks of the group II disks, group I disks were found to have large inner cavities. As Valegård et al. (2021) has classified the IMTTs into group I and group II based on the Meeus et al. (2001) classification, we can ascertain if the same differences between the two groups are found.

Figure 7.10 presents the two cumulative mass distributions in the left panel, with the fitted log-normal probability distributions in the right panel. The results from this fit can be found in Table 7.5. We do not find a clear difference between the two populations, which was found for the Herbig disks (S22). However, we
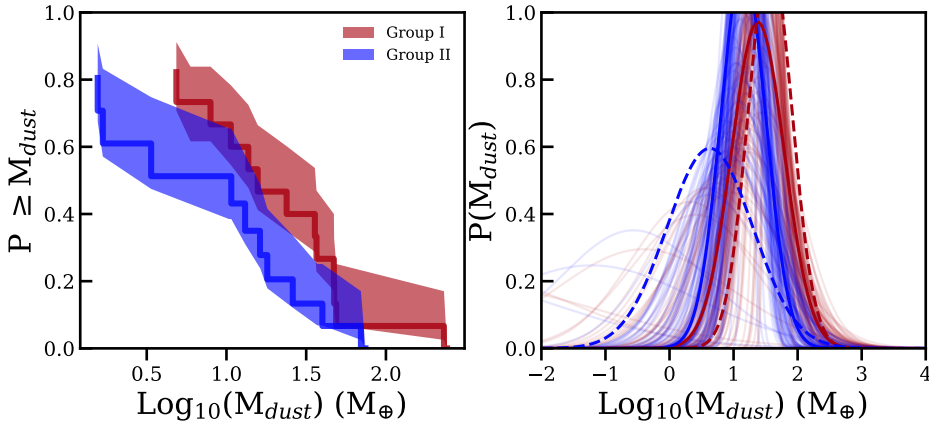
Figure 7.10: Dust cumulative distributions of the group I and group II disks. There is no significant difference, in contrast to what is found for the Herbig disks (S22). The dotted distributions in the right panel are the dust mass distributions for the Herbig disks from S22.

do note that the maximum and minimum dust masses are indeed lower for the group II disks compared to the group I disks. Comparing the distributions in the left panel of Fig. 7.10 with the distributions presented by S22, the mean dust mass of the group I disks is the same, the main difference is in the group II disks.

As was noted by Honda et al. (2012), Maaskant et al. (2013), and S22, group I disks tend to be transitional disks, having large inner cavities, while group II disks tend to have full disks. With the IMTTs this is the case as well. For the resolved disks, the group I disks indeed show cavities (AK Sco, SR 21, HD 135344B, HD 142527, LkHα 330, and UX Tau), and the group II disks indeed have full disks (CR Cha, GW Ori, HD 142666, HT Lup, and RY Tau). We note that the classification of AK Sco by Valegård et al. (2021) is group I, while it is classified as group II by Guzmán-Díaz et al. (2021) as used by S22. Hence, the ALMA observations are of particular necessity to characterize the disk. The difference in mass and morphology between the group I and group II disks was interpreted by S22 as the group I disks forming massive exoplanets which create an inner cavity by stopping radial drift, while the group II disks most of the solid mass drifts inwards reducing the total inferred disk mass. As there is no difference in the inferred dust mass for the group I disks when comparing the Herbig disks with the IMTT disks, no evolution has happened in these particular disks, which is expected if the radial drift has stopped. On the other hand, the group II Herbig disks have lower disk masses than the group II IMTT disks, which is expected if the radial drift has not been stopped in the disk. So, most disks around intermediate-mass pre-main sequence stars converge quickly to small/compact disks unless prevented by a massive exoplanet. This should occur well before the age of the IMTT disks, i.e., 5 Myr. We are mainly tracing the survivors of this process, as a large fraction of the pre-main sequence intermediate mass stars are like those of Iglesias et al.

(2023).

This hypothesis is also supported by observations of metallicities of the Herbig stars themselves (Kama et al. 2015; Guzmán-Díaz et al. 2023). Stars with a group I disk generally have lower metallicities compared to the group II disks, which is associated with the presence of massive exoplanets accreting the refractory elements and stopping the radial drift of the dust inwards. Brittain et al. (2023) point out that there is evidence that the opacities and temperatures of the dust are not the same between the two groups (Woitke et al. 2019). Group I disks tend to have smaller grains compared to group II disks, resulting in a higher inferred disk mass in the former compared to the latter. That no differences between the group I and group II disks are found in Fig. 7.10 might be an effect of similar dust populations in the younger IMTT disks and that this differentiates when evolving towards a Herbig disk. This must be further investigated using longer wavelength observations.

Lastly, recent work by Vioque et al. (2023) has shown that intermediate-mass young stellar objects become significantly less clustered with time. Hence, the IMTT disks are expected to be more clustered than Herbig stars. Given the fact that we do not find significant differences between both populations might indicate that the environment does not play a major role in the evolution of disks around intermediate mass stars. Due to the disk being stronger bound to the star, in combination with a higher disk mass, external UV irradiation is not as impactful as it would be for disks around lower mass stars (e.g., Haworth et al. 2018, 2023). However, a study dedicated to the effect of UV radiation on Herbig disks is needed to investigate this further.

7.5.2 Planet formation around intermediate mass stars

The dust masses of planet-forming disks have been directly compared to the solid mass of massive exoplanets in planetary systems by Tychoniec et al. (2020). They found a clear discrepancy between class II disks and the masses present in massive exoplanets, which would not be able to form. Even when taking into account observational biases this discrepancy would only not be a problem when the formation efficiency would be 100% (Mulders et al. 2021), which is likely not the case (see for an overview Drążkowska et al. 2023). As this comparison only has been done based on the dust mass inferred from continuum observations, this section will also directly compare the exoplanetary masses to the gas masses we found in the disks around intermediate mass stars. Moreover, we also include observational biases into the distribution.

To obtain an updated exoplanet mass distribution, we use the NASA exoplanet archive[2], and select all confirmed exoplanets. Following Tychoniec et al. (2020), we set no detection method and use both the planet mass M_p and minimum planet mass $M_p \sin(i)$ in our distribution. To obtain a distribution for the intermediate mass stars, we only include the planets around stars with a minimum mass of 1.5 $M_\odot$. To obtain a distribution taking the observational biases into account, we use the work of Wolthoff et al. (2022), who determined giant exoplanet occurrence

---

[2]https://exoplanetarchive.ipac.caltech.edu

rates around stars with masses higher than 0.8 $M\odot$. Based on this work, we normalize the distribution to 1.3% for planetary masses higher than 9 $M_{\rm jup}$, to 5.7% for masses higher than 2.7 $M_{\rm jup}$ and to 15.8% for the complete distribution. We note that planets with a period ranging from 80 to 3600 days are used here, so there are differences in the scales traced by planets and disks. Following Tychoniec et al. (2020), the total planetary mass includes both the core mass and the atmosphere, so we use the relationship from Thorngren et al. (2016) to obtain a heavy-element mass of the planet, and we assume that this is the dust mass necessary to form the planet. The total gas (atmosphere) mass is then simply the difference between the planetary mass and the heavy-element mass of the planet. After the core and atmosphere masses, all planetary systems belonging to the same star are combined into a single mass. The number of stars hosting at least one giant planet is 10.7% (Wolthoff et al. 2022), hence we again normalize the distribution so that it adds up to 10.7%. The resulting distribution is shown in the left panel of Fig. 7.11.

Figure 7.11 also shows the dust mass and gas mass distributions after combining the data of our work with the dust masses from S22 and the gas masses from S24, after removing the duplicate disks from the sample of our work. The tail end of dust mass distribution of the disks is similar to the dust masses necessary to build the exoplanetary systems. However, an efficiency of 100% is necessary. This is in
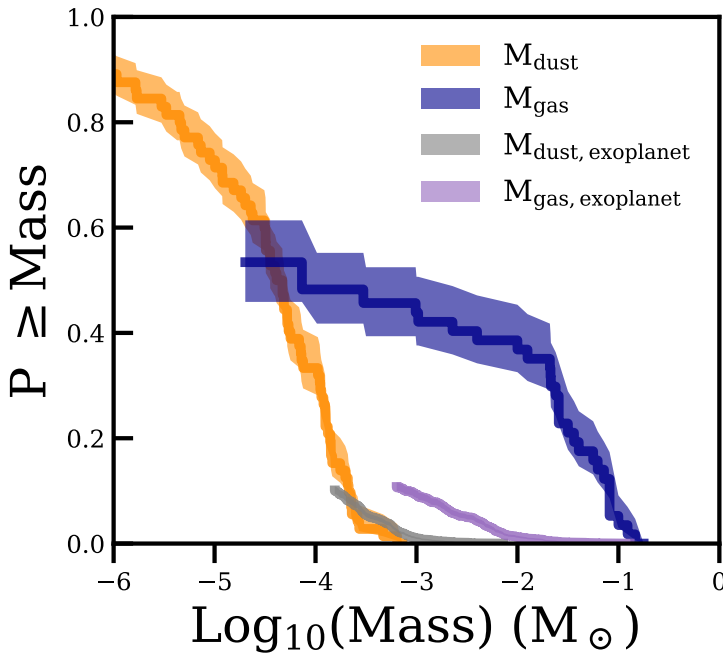
Figure 7.11: Comparing the dust and gas mass cumulative distributions of the disks around intermediate mass (IMTT disks + Herbig disks) with a dust and gas mass distribution of exoplanets.

line with what Mulders et al. (2021) finds. Comparing the exoplanet dust mass distribution with the disk gas mass distribution, assuming a gas-to-dust ratio of 100, the lower mass planets may be less of a problem to still form. Still, it is clear that the cores of the massive exoplanets should already have formed in these systems. This is in line with the previous discussion, as these exoplanets are thought to have a big impact on the evolution of disks around intermediate mass stars.

Comparing the gas mass distributions, there still is more than enough gas mass available in the disks to form the exoplanet atmosphere. For a large fraction of the population there is at least one or two orders of magnitude difference in the mass available in the disks compared to what is necessary to form the exoplanets. Hence, planet envelope accretion might still be ongoing, while the cores of the planets have already been formed.

7.6   Conclusion

In this work we analyze the continuum, ^{12}CO, ^{13}CO, and C^{18}O emission of 35 Intermediate Mass T Tauri (IMTT) disks, all being ALMA archival data. The obtained dust masses and radii are compared to those of Herbig disks (Stapper et al. 2022), and T Tauri disks (Barenfeld et al. 2016; Ansdell et al. 2016). From our results the following can be concluded:

1. IMTT disks have both the same dust mass distribution and dust radius distribution as Herbig disks.

2. The gas mass of IMTT disks is possibly slightly lower than that of Herbig disks, but this is likely due to the lack in sensitivity of the available CO isotopologue observations in the archive to obtain meaningful gas mass limits. Deeper observations of IMTT disks are urgently needed.

3. The gas radii are the same as that of the Herbig disks. Compared to the dust radii, the same ratio between the two is found as for the Herbig disks.

4. Dividing the IMTT disks into group I (rising FIR slope) and group II (decreasing FIR slope) disks reveals no significant difference regarding the dust mass. This is in stark contrast to what is found for Herbig disks, for which the inferred dust mass in the group II disks is lower than for the group I disks. This difference between the Herbig group I and group II disks might be indicative of different evolutionary scenarios happening in these two groups. Group I disks staying the same due to a massive exoplanet stopping radial drift, while the group II disks rapidly shrink over time due to radial drift decreasing the inferred disk mass.

5. As the mass and sizes of IMTT disks are the same as for Herbig disks, planet formation has already started in these disks, shaping their formation, and subsequent evolution towards Herbig disks. Most disks around intermediate-mass pre-main sequence stars converge quickly to small disks

unless prevented by a massive exoplanet. We are mainly tracing the survivors of this process, as most pre-main sequence intermediate mass stars are debris disks.

6. Comparing the disk dust mass distributions to the amount of dust mass in massive exoplanets, it is clear that the cores of the exoplanets already need to have formed, as there is not enough dust mass present in the disks. However, comparing the disk gas mass distributions to the mass in planetary envelopes, there is more than an order of magnitude difference. This indicates that while the core of the exoplanets have already been formed, they are likely still accreting their envelope.

IMTTs are an important class of objects for understanding planet formation and would benefit from targeted, high resolution deep imaging observations with ALMA in the future.

Appendix

7.A Datasets used

In Table 7.A.1 the project codes of the used data sets are listed together with their spatial and velocity resolution and the (line-free) rms noise.

Table 7.A.1: Data sets and corresponding parameters for each IMTT disk. The rms noise is for an empty channel at the given velocity resolution with units mJy beam^{-1}. The ^{13}CO, C^{18}O, and project code columns continue on the next page.

Name	Continuum Spat.res. ($''$)	rms	^{12}CO Spat.res. ($''$)	Vel.res. (km s^{-1})	rms
AK Sco	0.09 × 0.06 (-76°)	0.05	0.15 × 0.11 (-63°)	1.00	3.55
Ass ChaT2-21	0.48 × 0.31 (1°)	0.39	0.55 × 0.38 (-3°)	0.42	23.27
Ass ChaT2-54	0.76 × 0.40 (45°)	0.87	0.81 × 0.43 (45°)	0.40	75.75
BE Ori	1.33 × 1.03 (-75°)	0.31	1.60 × 1.19 (-73°)	0.20	44.40
Brun 656	0.94 × 0.66 (-69°)	0.83			
CO Ori	7.08 × 4.83 (84°)	1.78	7.62 × 5.21 (78°)	0.20	282.44
CR Cha	0.08 × 0.05 (5°)	0.02	0.72 × 0.47 (32°)	0.20	10.57
CV Cha	0.71 × 0.45 (-15°)	3.70			
DI Cha	0.73 × 0.45 (-18°)	3.35			
GW Ori	0.15 × 0.12 (-29°)	0.08	0.20 × 0.15 (-37°)	0.20	5.85
Haro 1-6	1.42 × 1.06 (83°)	0.54	1.58 × 1.19 (86°)	0.20	101.78
HBC 442	7.79 × 4.38 (83°)	2.11	8.23 × 4.90 (81°)	0.20	308.71
HBC 502	1.77 × 1.06 (-80°)	5.50			
HD 34700	0.46 × 0.35 (-64°)	0.19	0.54 × 0.48 (-63°)	0.63	10.05
HD 35929	0.08 × 0.04 (89°)	0.03	0.11 × 0.06 (-62°)	0.20	4.86
HD 135344B	0.37 × 0.29 (-63°)	0.98	0.36 × 0.29 (-68°)	0.20	29.59
HD 142527	0.27 × 0.24 (69°)	0.76	0.93 × 0.81 (-85°)	0.20	16.11
HD 142666	0.03 × 0.02 (65°)	0.03	0.21 × 0.20 (-70°)	0.32	5.83
HD 144432	7.39 × 3.94 (-87°)	1.89	7.53 × 4.12 (-88°)	1.50	92.27
HD 288313	0.33 × 0.30 (-72°)	0.25	0.39 × 0.36 (-65°)	0.64	10.16
HD 294260	0.46 × 0.35 (-79°)	0.22	0.58 × 0.51 (-75°)	0.63	7.87
HQ Tau	0.12 × 0.11 (6°)	0.12			
HT Lup	0.03 × 0.03 (68°)	0.02	0.07 × 0.04 (57°)	0.32	1.25
LkHA 310	0.33 × 0.30 (-81°)	0.17	0.40 × 0.36 (-70°)	0.64	12.13
LkHA 330	0.08 × 0.03 (30°)	0.02	0.10 × 0.03 (32°)	1.50	1.26
PDS 156	0.35 × 0.30 (-87°)	0.15	0.41 × 0.35 (-82°)	0.63	11.79
PDS 277	0.56 × 0.41 (-84°)	0.24	0.70 × 0.51 (-83°)	0.63	12.28
PR Ori	1.52 × 1.01 (-55°)	0.70			
RY Ori	7.76 × 4.47 (86°)	2.16	8.35 × 5.03 (83°)	0.20	308.84
RY Tau	0.04 × 0.02 (27°)	0.05			
			0.25 × 0.18 (-1°)	0.70	15.36
SR 21	0.11 × 0.09 (90°)	0.09	0.14 × 0.12 (-83°)	0.35	7.01
SU Aur	0.33 × 0.20 (2°)	0.19	0.36 × 0.23 (3°)	0.40	14.81
SW Ori	1.34 × 1.03 (-74°)	0.31	1.61 × 1.18 (-73°)	0.20	44.77
T Tau	0.04 × 0.03 (-21°)	0.08			
UX Tau	0.26 × 0.21 (12°)	0.08	0.30 × 0.25 (10°)	0.32	8.44

Table 7.A.1: Continued.

^{13}CO			C^{18}O			
Spat.res. ($''$)	Vel.res. (km s^{-1})	rms	Spat.res. ($''$)	Vel.res. (km s^{-1})	rms	Project codes
0.16 × 0.12 (-63°)	1.00	3.97	0.16 × 0.13 (-75°)	1.00	2.50	2016.1.00204.S
						2012.1.00313.S*
0.74 × 0.56 (-42°)	0.40	435.53	0.76 × 0.47 (-14°)	0.40	429.18	2013.1.01075.S*
1.75 × 1.25 (-69°)	0.20	46.02	1.75 × 1.26 (-71°)	0.20	39.70	2019.1.00951.S
						2017.1.01353.S
7.86 × 5.43 (81°)	0.20	284.19	7.87 × 5.47 (83°)	0.20	225.54	2021.2.00005.S
0.75 × 0.49 (33°)	0.20	12.06	0.76 × 0.49 (32°)	0.20	8.70	2017.1.00286.S
0.73 × 0.56 (-44°)	0.20	542.70	0.75 × 0.48 (-14°)	0.20	544.64	2013.1.00437.S*
0.70 × 0.48 (-7°)	0.30	300.56	0.69 × 0.48 (-8°)	0.30	513.42	2013.1.00437.S*
0.21 × 0.16 (-36°)	0.20	6.75	0.21 × 0.15 (-37°)	0.20	4.77	2017.1.00286.S
1.65 × 1.24 (86°)	0.20	110.71	1.65 × 1.23 (84°)	0.20	62.65	2016.1.00545.S
8.54 × 5.04 (80°)	0.20	312.10	8.57 × 5.17 (80°)	0.20	271.11	2021.2.00005.S
						2016.1.01338.S
						2021.1.01705.S
7.75 × 5.12 (85°)	0.20	296.24	7.77 × 5.20 (88°)	0.20	227.99	2021.2.00005.S
0.11 × 0.07 (-69°)	0.35	3.21	0.11 × 0.07 (-71°)	0.35	2.62	2021.1.00854.S
						2012.1.00870.S*
0.34 × 0.30 (75°)	0.20	19.06	0.35 × 0.30 (84°)	0.20	25.93	2012.1.00158.S*
0.97 × 0.84 (-87°)	0.20	16.76	0.98 × 0.85 (-88°)	0.20	11.76	2015.1.01353.S
						2016.1.00484.L
1.05 × 0.82 (87°)	0.20	42.43	1.04 × 0.85 (87°)	0.20	27.06	2015.1.01600.S
7.98 × 4.37 (-90°)	1.50	67.76	8.01 × 4.38 (-90°)	1.50	54.38	2022.1.01460.S
0.42 × 0.39 (-69°)	0.66	11.89	0.42 × 0.39 (-68°)	0.67	10.09	2022.1.01155.S
						2021.1.01705.S
0.15 × 0.13 (0°)	0.20	20.81	0.15 × 0.14 (4°)	0.20	15.78	2016.1.01164.S
						2016.1.00484.L
0.29 × 0.28 (74°)	0.40	33.54	0.29 × 0.28 (70°)	0.40	24.82	2015.1.00222.S
0.43 × 0.39 (-71°)	0.66	10.22	0.42 × 0.38 (-70°)	0.67	9.48	2022.1.01155.S
0.10 × 0.03 (31°)	1.50	1.33	0.11 × 0.03 (31°)	1.50	1.18	2018.1.01302.S
0.49 × 0.37 (-74°)	0.66	11.59	0.49 × 0.37 (-75°)	0.67	10.47	2022.1.01155.S
						2021.1.01705.S
7.13 × 4.58 (81°)	0.20	209.84	7.09 × 4.59 (83°)	0.20	188.04	2021.2.00005.S
						2019.1.01813.S
8.66 × 5.15 (83°)	0.20	312.46	8.68 × 5.28 (82°)	0.20	263.91	2021.2.00005.S
						2017.1.01460.S
0.26 × 0.19 (0°)	0.70	13.61	0.27 × 0.19 (0°)	0.70	9.91	2013.1.00498.S
0.15 × 0.12 (-83°)	0.35	7.37	0.15 × 0.12 (-82°)	0.35	5.68	2018.1.00689.S
0.38 × 0.27 (10°)	0.40	16.69				2013.1.00426.S
1.75 × 1.25 (-69°)	0.20	45.80	1.76 × 1.26 (-70°)	0.20	40.45	2019.1.00951.S
						2019.1.00703.S
0.31 × 0.26 (13°)	0.66	6.19	0.32 × 0.26 (12°)	0.67	4.71	2013.1.00498.S

Bibliography

1997, ESA Special Publication, Vol. 1200, The HIPPARCOS and TYCHO catalogues. Astrometric and photometric star catalogues derived from the ESA HIPPARCOS Space Astrometry Mission

Acke, B., Min, M., van den Ancker, M. E., et al. 2009, A&A, 502, L17

Acke, B. & van den Ancker, M. E. 2004, A&A, 426, 151

Agúndez, M., Roueff, E., Le Petit, F., & Le Bourlot, J. 2018, A&A, 616, A19

Aikawa, Y., van Zadelhoff, G. J., van Dishoeck, E. F., & Herbst, E. 2002, A&A, 386, 622

Alcalá, J. M., Natta, A., Manara, C. F., et al. 2014, A&A, 561, A2

Alecian, E., Wade, G. A., Catala, C., et al. 2013, MNRAS, 429, 1001

ALMA Partnership, Brogan, C. L., Pérez, L. M., et al. 2015, ApJ, 808, L3

Alonso-Albi, T., Fuente, A., Bachiller, R., et al. 2008, ApJ, 680, 1289

Alonso-Albi, T., Fuente, A., Bachiller, R., et al. 2009, A&A, 497, 117

Anderson, A. R., Williams, J. P., van der Marel, N., et al. 2022, ApJ, 938, 55

Andre, P., Ward-Thompson, D., & Barsony, M. 1993, ApJ, 406, 122

Andrews, S. M. 2020, ARA&A, 58, 483

Andrews, S. M., Huang, J., Pérez, L. M., et al. 2018a, ApJ, 869, L41

Andrews, S. M., Rosenfeld, K. A., Kraus, A. L., & Wilner, D. J. 2013, ApJ, 771, 129

Andrews, S. M., Terrell, M., Tripathi, A., et al. 2018b, ApJ, 865, 157

Andrews, S. M. & Williams, J. P. 2005, ApJ, 631, 1134

Andrews, S. M., Wilner, D. J., Espaillat, C., et al. 2011, ApJ, 732, 42

Andrews, S. M., Wilner, D. J., Hughes, A. M., Qi, C., & Dullemond, C. P. 2010, ApJ, 723, 1241

Ansdell, M., Haworth, T. J., Williams, J. P., et al. 2020, AJ, 160, 248

Ansdell, M., Williams, J. P., Manara, C. F., et al. 2017, AJ, 153, 240

Ansdell, M., Williams, J. P., Trapman, L., et al. 2018, ApJ, 859, 21

Ansdell, M., Williams, J. P., van der Marel, N., et al. 2016, ApJ, 828, 46

Astropy Collaboration, Price-Whelan, A. M., Sipőcz, B. M., et al. 2018, AJ, 156, 123

Astropy Collaboration, Robitaille, T. P., Tollerud, E. J., et al. 2013, A&A, 558, A33

Augereau, J. C. & Papaloizou, J. C. B. 2004, A&A, 414, 1153

Bae, J., Isella, A., Zhu, Z., et al. 2023, in Astronomical Society of the Pacific Conference Series, Vol. 534, Protostars and Planets VII, ed. S. Inutsuka, Y. Aikawa, T. Muto, K. Tomida, & M. Tamura, 423

Bae, J., Teague, R., Andrews, S. M., et al. 2022, ApJ, 934, L20

Bae, J., Zhu, Z., & Hartmann, L. 2017, ApJ, 850, 201

Baines, D., Oudmaijer, R. D., Porter, J. M., & Pozzo, M. 2006, MNRAS, 367, 737

Balbus, S. A. & Hawley, J. F. 1991, ApJ, 376, 214

Ballering, N. P., Cleeves, L. I., Haworth, T. J., et al. 2023, ApJ, 954, 127

Ballering, N. P. & Eisner, J. A. 2019, AJ, 157, 144

Bally, J. 2016, ARA&A, 54, 491

Banzatti, A., Garufi, A., Kama, M., et al. 2018, A&A, 609, L2

Baraffe, I., Homeier, D., Allard, F., & Chabrier, G. 2015, A&A, 577, A42

Barenfeld, S. A., Carpenter, J. M., Ricci, L., & Isella, A. 2016, ApJ, 827, 142

Barenfeld, S. A., Carpenter, J. M., Sargent, A. I., Isella, A., & Ricci, L. 2017, ApJ, 851, 85

Bastian, N., Covey, K. R., & Meyer, M. R. 2010, ARA&A, 48, 339

Beckwith, S. V. W., Sargent, A. I., Chini, R. S., & Guesten, R. 1990, AJ, 99, 924

Benisty, M., Bae, J., Facchini, S., et al. 2021, ApJ, 916, L2

Benisty, M., Dominik, C., Follette, K., et al. 2023, in Astronomical Society of the Pacific Conference Series, Vol. 534, Protostars and Planets VII, ed. S. Inutsuka, Y. Aikawa, T. Muto, K. Tomida, & M. Tamura, 605

Benisty, M., Stolker, T., Pohl, A., et al. 2017, A&A, 597, A42

Benson, P. J. & Myers, P. C. 1989, ApJS, 71, 89

Bergin, E. A., Cleeves, L. I., Gorti, U., et al. 2013, Nature, 493, 644

Bessell, M. S. 1979, PASP, 91, 589

Bessell, M. S. & Eggen, O. J. 1972, ApJ, 177, 209

Bi, J., van der Marel, N., Dong, R., et al. 2020, ApJ, 895, L18

Birnstiel, T., Dullemond, C. P., & Brauer, F. 2010, A&A, 513, A79

Bisschop, S. E., Fraser, H. J., Öberg, K. I., van Dishoeck, E. F., & Schlemmer, S. 2006, A&A, 449, 1297

Boehler, Y., Weaver, E., Isella, A., et al. 2017, ApJ, 840, 60

Boersma, C., Peeters, E., Martín-Hernández, N. L., et al. 2009, A&A, 502, 175

Bohlin, R. C., Savage, B. D., & Drake, J. F. 1978, ApJ, 224, 132

Boissier, J., Alonso-Albi, T., Fuente, A., et al. 2011, A&A, 531, A50

Booth, A. S. & Ilee, J. D. 2020, MNRAS, 493, L108

Booth, A. S., Ilee, J. D., Walsh, C., et al. 2023a, A&A, 669, A53

Booth, A. S., Law, C. J., Temmink, M., Leemker, M., & Macias, E. 2023b, arXiv e-prints, arXiv:2308.07910

Booth, A. S., Leemker, M., van Dishoeck, E. F., et al. 2024, arXiv e-prints, arXiv:2402.04001

Booth, A. S., Tabone, B., Ilee, J. D., et al. 2021, ApJS, 257, 16

Booth, A. S., Walsh, C., Ilee, J. D., et al. 2019, ApJ, 882, L31

Booth, R. A., Meru, F., Lee, M. H., & Clarke, C. J. 2018, MNRAS, 475, 167

Bosman, A. D., Walsh, C., & van Dishoeck, E. F. 2018, A&A, 618, A182

Boss, A. P. 1997, Science, 276, 1836

Boyden, R. D. & Eisner, J. A. 2020, ApJ, 894, 74

Brittain, S. D., Kamp, I., Meeus, G., Oudmaijer, R. D., & Waters, L. B. F. M. 2023, Space Sci. Rev., 219, 7

Brittain, S. D., Simon, T., Najita, J. R., & Rettig, T. W. 2007, ApJ, 659, 685

Brown, J. M., Blake, G. A., Qi, C., Dullemond, C. P., & Wilner, D. J. 2008, ApJ, 675, L109

Bruderer, S. 2013, A&A, 559, A46

Bruderer, S., van der Marel, N., van Dishoeck, E. F., & van Kempen, T. A. 2014, A&A, 562, A26

Bruderer, S., van Dishoeck, E. F., Doty, S. D., & Herczeg, G. J. 2012, A&A, 541, A91

Calvet, N., Muzerolle, J., Briceño, C., et al. 2004, AJ, 128, 1294

Carmona, A., van den Ancker, M. E., Audard, M., et al. 2010, A&A, 517, A67

Carmona, A., van den Ancker, M. E., & Henning, T. 2007, A&A, 464, 687

Carney, M. T., Fedele, D., Hogerheijde, M. R., et al. 2018, A&A, 614, A106

Carpenter, J. M., Ricci, L., & Isella, A. 2014, ApJ, 787, 42

Castelli, F. & Kurucz, R. L. 2003, in Modelling of Stellar Atmospheres, ed. N. Piskunov, W. W. Weiss, & D. F. Gray, Vol. 210, A20

Cataldi, G., Aikawa, Y., Iwasaki, K., et al. 2023, arXiv e-prints, arXiv:2305.12093

Cauley, P. W. & Johns-Krull, C. M. 2014, ApJ, 797, 112

Cazzoletti, P., Manara, C. F., Baobab Liu, H., et al. 2019, A&A, 626, A11

Cazzoletti, P., van Dishoeck, E. F., Pinilla, P., et al. 2018, A&A, 619, A161

Chauvin, G., Desidera, S., Lagrange, A. M., et al. 2017, A&A, 605, L9

Chen, P. S., Shan, H. G., & Zhang, P. 2016, New Astronomy, 44, 1

Chen, X. P., Henning, T., van Boekel, R., & Grady, C. A. 2006, A&A, 445, 331

Cieza, L. A., González-Ruilova, C., Hales, A. S., et al. 2021, MNRAS, 501, 2934

Cieza, L. A., Ruíz-Rodríguez, D., Hales, A., et al. 2019, MNRAS, 482, 698

Claes, R. A. B., Manara, C. F., Garcia-Lopez, R., et al. 2022, A&A, 664, L7

Claudi, R., Maire, A. L., Mesa, D., et al. 2019, A&A, 622, A96

Cleeves, L. I., Öberg, K. I., Wilner, D. J., et al. 2016, ApJ, 832, 110

Codella, C., Cabrit, S., Gueth, F., et al. 2014, A&A, 568, L5

Coulson, I. M. & Walther, D. M. 1995, MNRAS, 274, 977

Covino, E., Terranegra, L., Vittone, A. A., & Russo, G. 1984, AJ, 89, 1868

Currie, T., Lawson, K., Schneider, G., et al. 2022, Nature Astronomy, 6, 751

Cutri, R. M. & et al. 2012, VizieR Online Data Catalog, II/311

Czekala, I., Andrews, S. M., Jensen, E. L. N., et al. 2015, ApJ, 806, 154

Czekala, I., Loomis, R. A., Teague, R., et al. 2021, ApJS, 257, 2

Daemgen, S., Petr-Gotzens, M. G., Correia, S., et al. 2013, A&A, 554, A43

Davidson-Pilon, C., Kalderstam, J., Jacobson, N., et al. 2021, CamDavidson-Pilon/lifelines: 0.25.10

de Boer, J., Ginski, C., Chauvin, G., et al. 2021, A&A, 649, A25

de Gregorio-Monsalvo, I., Ménard, F., Dent, W., et al. 2013, A&A, 557, A133

Deng, D., Ruaud, M., Gorti, U., & Pascucci, I. 2023, ApJ, 954, 165

Di Folco, E., Péricaud, J., Dutrey, A., et al. 2020, A&A, 635, A94

Di Francesco, J., Johnstone, D., Kirk, H., MacKenzie, T., & Ledwosinska, E. 2008, ApJS, 175, 277

Díaz-Berríos, J. K., Guzmán, V. V., Walsh, C., et al. 2024, arXiv e-prints, arXiv:2405.00615

Doering, R. L., Meixner, M., Holfeltz, S. T., et al. 2007, AJ, 133, 2122

Donehew, B. & Brittain, S. 2011, AJ, 141, 46

Dong, R., Liu, S.-y., Eisner, J., et al. 2018, ApJ, 860, 124

Draine, B. T. 2006, ApJ, 636, 1114

Draine, B. T. & Li, A. 2007, ApJ, 657, 810

Drew, J. E., Busfield, G., Hoare, M. G., et al. 1997, MNRAS, 286, 538

Drążkowska, J., Bitsch, B., Lambrechts, M., et al. 2023, in Astronomical Society of the Pacific Conference Series, Vol. 534, Protostars and Planets VII, ed. S. Inutsuka, Y. Aikawa, T. Muto, K. Tomida, & M. Tamura, 717

Drążkowska, J. & Dullemond, C. P. 2018, A&A, 614, A62

Du, F., Bergin, E. A., & Hogerheijde, M. R. 2015, ApJ, 807, L32

Dullemond, C. P. & Dominik, C. 2004a, A&A, 417, 159

Dullemond, C. P. & Dominik, C. 2004b, A&A, 421, 1075

Dullemond, C. P. & Dominik, C. 2005, A&A, 434, 971

Dullemond, C. P., Dominik, C., & Natta, A. 2001, ApJ, 560, 957

Dullemond, C. P., Juhasz, A., Pohl, A., et al. 2012, RADMC-3D: A multi-purpose radiative transfer tool, Astrophysics Source Code Library, record ascl:1202.015

Eisner, J. A., Arce, H. G., Ballering, N. P., et al. 2018, ApJ, 860, 77

Eisner, J. A., Bally, J. M., Ginsburg, A., & Sheehan, P. D. 2016, ApJ, 826, 16

Endres, C. P., Schlemmer, S., Schilke, P., Stutzki, J., & Müller, H. S. P. 2016, Journal of Molecular Spectroscopy, 327, 95

Facchini, S., Birnstiel, T., Bruderer, S., & van Dishoeck, E. F. 2017, A&A, 605, A16

Fairlamb, J. R., Oudmaijer, R. D., Mendigutía, I., Ilee, J. D., & van den Ancker, M. E. 2015, MNRAS, 453, 976

Fairlamb, J. R., Oudmaijer, R. D., Mendigutia, I., Ilee, J. D., & van den Ancker, M. E. 2017, MNRAS, 464, 4721

Fedele, D., Carney, M., Hogerheijde, M. R., et al. 2017, A&A, 600, A72

Fedele, D., Toci, C., Maud, L., & Lodato, G. 2021, A&A, 651, A90

Fedele, D., van Dishoeck, E. F., Kama, M., Bruderer, S., & Hogerheijde, M. R. 2016, A&A, 591, A95

Fiorellino, E., Tychoniec, Ł., Manara, C. F., et al. 2022, ApJ, 937, L9

Fischer, W. J., Hillenbrand, L. A., Herczeg, G. J., et al. 2022, arXiv e-prints, arXiv:2203.11257

Flaherty, K., Hughes, A. M., Simon, J. B., et al. 2020, ApJ, 895, 109

Flaherty, K. M., Hughes, A. M., Rosenfeld, K. A., et al. 2015, ApJ, 813, 99

Folsom, C. P., Bagnulo, S., Wade, G. A., et al. 2012, MNRAS, 422, 2072

Francis, L. & van der Marel, N. 2020, ApJ, 892, 111

Fukagawa, M., Hayashi, M., Tamura, M., et al. 2004, ApJ, 605, L53

Fukagawa, M., Tamura, M., Itoh, Y., et al. 2006, ApJ, 636, L153

Fulton, B. J., Rosenthal, L. J., Hirsch, L. A., et al. 2021, ApJS, 255, 14

Gaia Collaboration, Brown, A. G. A., Vallenari, A., et al. 2018a, A&A, 616, A1

Gaia Collaboration, Brown, A. G. A., Vallenari, A., et al. 2018b, A&A, 616, A1

Gaia Collaboration, Brown, A. G. A., Vallenari, A., et al. 2021, A&A, 649, A1

Gaia Collaboration, Prusti, T., de Bruijne, J. H. J., et al. 2016, A&A, 595, A1

Gaia Collaboration, Vallenari, A., Brown, A. G. A., et al. 2023, A&A, 674, A1

Garcia, P. J. V., Benisty, M., Dougados, C., et al. 2013, MNRAS, 430, 1839

Garcia, P. J. V., Thiébaut, E., & Bacon, R. 1999, A&A, 346, 892

Garcia Lopez, R., Kurosawa, R., Caratti o Garatti, A., et al. 2016, MNRAS, 456, 156

Garcia Lopez, R., Natta, A., Testi, L., & Habart, E. 2006, A&A, 459, 837

Garg, H., Pinte, C., Christiaens, V., et al. 2021, MNRAS, 504, 782

Garufi, A., Dominik, C., Ginski, C., et al. 2022, A&A, 658, A137

Garufi, A., Ginski, C., van Holstein, R. G., et al. 2024, arXiv e-prints, arXiv:2403.02158

Garufi, A., Meeus, G., Benisty, M., et al. 2017, A&A, 603, A21

Garufi, A., Quanz, S. P., Schmid, H. M., et al. 2014, A&A, 568, A40

Ginski, C., Facchini, S., Huang, J., et al. 2021, ApJ, 908, L25

Ginski, C., Garufi, A., Benisty, M., et al. 2024, arXiv e-prints, arXiv:2403.02149

Ginski, C., Tazaki, R., Dominik, C., & Stolker, T. 2023, ApJ, 953, 92

Grant, S. L., Espaillat, C. C., Brittain, S., Scott-Joseph, C., & Calvet, N. 2022, ApJ, 926, 229

Grant, S. L., Espaillat, C. C., Wendeborn, J., et al. 2021, ApJ, 913, 123

Grant, S. L., Stapper, L. M., Hogerheijde, M. R., et al. 2023, AJ, 166, 147

Gravity Collaboration, Ganci, V., Labadie, L., et al. 2021, A&A, 655, A112

Gray, R. O. & Corbally, C. J. 1998, AJ, 116, 2530

Gray, R. O., Corbally, C. J., Garrison, R. F., et al. 2006, AJ, 132, 161

Gray, R. O., Riggs, Q. S., Koen, C., et al. 2017, AJ, 154, 31

Greene, T. P., Wilking, B. A., Andre, P., Young, E. T., & Lada, C. J. 1994, ApJ, 434, 614

Großschedl, J. E., Alves, J., Meingast, S., et al. 2018, A&A, 619, A106

Guilloteau, S. & Dutrey, A. 1998, A&A, 339, 467

Guzmán-Díaz, J., Mendigutía, I., Montesinos, B., et al. 2021, A&A, 650, A182

Guzmán-Díaz, J., Montesinos, B., Mendigutía, I., et al. 2023, A&A, 671, A140

Habing, H. J. 1968, Bull. Astron. Inst. Netherlands, 19, 421

Haffert, S. Y., Bohn, A. J., de Boer, J., et al. 2019, Nature Astronomy, 3, 749

Haisch, Karl E., J., Lada, E. A., & Lada, C. J. 2001, ApJ, 553, L153

Hammond, I., Christiaens, V., Price, D. J., et al. 2023, MNRAS, 522, L51

Harris, C. R., Millman, K. J., van der Walt, S. J., et al. 2020, Nature, 585, 357

Harris, R. J., Andrews, S. M., Wilner, D. J., & Kraus, A. L. 2012, ApJ, 751, 115

Hartmann, L., Calvet, N., Gullbring, E., & D'Alessio, P. 1998, ApJ, 495, 385

Hartmann, L., Herczeg, G., & Calvet, N. 2016, ARA&A, 54, 135

Hartmann, L., Kenyon, S. J., Hewett, R., et al. 1989, ApJ, 338, 1001

Haworth, T. J., Clarke, C. J., Rahman, W., Winter, A. J., & Facchini, S. 2018, MNRAS, 481, 452

Haworth, T. J., Coleman, G. A. L., Qiao, L., Sellek, A. D., & Askari, K. 2023, MNRAS, 526, 4315

Hendler, N., Pascucci, I., Pinilla, P., et al. 2020, ApJ, 895, 126

Henning, T., Launhardt, R., Steinacker, J., & Thamm, E. 1994, A&A, 291, 546

Herbig, G. H. 1960, ApJS, 4, 337

Herbig, G. H. 1977, ApJ, 214, 747

Higuchi, A. E., Kóspál, Á., Moór, A., Nomura, H., & Yamamoto, S. 2020, ApJ, 905, 122

Hildebrand, R. H. 1983, QJRAS, 24, 267

Hillenbrand, L. A. 2005, arXiv e-prints, astro

Hindsley, R. B. & Harrington, R. S. 1994, AJ, 107, 280

Honda, M., Maaskant, K., Okamoto, Y. K., et al. 2012, ApJ, 752, 143

Hone, E., Kraus, S., Davies, C. L., et al. 2019, A&A, 623, A38

Houk, N. 1978, Michigan catalogue of two-dimensional spectral types for the HD stars

Houk, N. 1982, Michigan Catalogue of Two-dimensional Spectral Types for the HD stars. Volume_3. Declinations -40_f0 to -26_f0.

Houk, N. & Smith-Moore, M. 1988, Michigan Catalogue of Two-dimensional Spectral Types for the HD Stars. Volume 4, Declinations -26°.0 to -12°.0., Vol. 4

Houk, N. & Swift, C. 1999, Michigan Spectral Survey, 5, 0

Hsu, W.-H., Hartmann, L., Allen, L., et al. 2013, ApJ, 764, 114

Hu, X., Li, Z.-Y., Zhu, Z., & Yang, C.-C. 2022, MNRAS, 516, 2006

Huang, J., Andrews, S. M., Dullemond, C. P., et al. 2018, ApJ, 869, L42

Hubrig, S., Carroll, T. A., Scholler, M., & Ilyin, I. 2015, MNRAS, 449, L118

Hughes, A. M., Duchêne, G., & Matthews, B. C. 2018, ARA&A, 56, 541

Hughes, A. M., Lieman-Sifry, J., Flaherty, K. M., et al. 2017, ApJ, 839, 86

Hughes, A. M., Wilner, D. J., Andrews, S. M., Qi, C., & Hogerheijde, M. R. 2011, ApJ, 727, 85

Hughes, A. M., Wilner, D. J., Kamp, I., & Hogerheijde, M. R. 2008, ApJ, 681, 626

Hunter, J. D. 2007, Computing in Science & Engineering, 9, 90

Ida, S. & Lin, D. N. C. 2004, ApJ, 604, 388

Iglesias, D. P., Panić, O., van den Ancker, M., et al. 2023, MNRAS, 519, 3958

Ilee, J. D., Fairlamb, J., Oudmaijer, R. D., et al. 2014, MNRAS, 445, 3723

Ilee, J. D., Hall, C., Walsh, C., et al. 2020, MNRAS, 498, 5116

Irvine, N. J. & Houk, N. 1977, PASP, 89, 347

Isella, A., Guidi, G., Testi, L., et al. 2016, Phys. Rev. Lett., 117, 251101

Isella, A., Natta, A., Wilner, D., Carpenter, J. M., & Testi, L. 2010, ApJ, 725, 1735

Ishihara, D., Onaka, T., Kataza, H., et al. 2010, A&A, 514, A1

Izquierdo, A. F., Facchini, S., Rosotti, G. P., van Dishoeck, E. F., & Testi, L. 2022, ApJ, 928, 2

Izquierdo, A. F., Testi, L., Facchini, S., et al. 2023, A&A, 674, A113

Jaschek, C., Jaschek, M., Andrillat, Y., & Egret, D. 1991, A&A, 252, 229

Jensen, E. L. N., Mathieu, R. D., & Fuller, G. A. 1996, ApJ, 458, 312

Jiang, H., Macías, E., Guerra-Alvarado, O. M., & Carrasco-González, C. 2024, A&A, 682, A32

Johansen, A., Blum, J., Tanaka, H., et al. 2014, in Protostars and Planets VI, ed. H. Beuther, R. S. Klessen, C. P. Dullemond, & T. Henning, 547–570

Johansen, A. & Lambrechts, M. 2017, Annual Review of Earth and Planetary Sciences, 45, 359

Johnson, J. A., Aller, K. M., Howard, A. W., & Crepp, J. R. 2010, PASP, 122, 905

Johnson, J. A., Butler, R. P., Marcy, G. W., et al. 2007, ApJ, 670, 833

Joner, M. D. & Hintz, E. G. 2015, AJ, 150, 204

Jones, M. G., Pringle, J. E., & Alexander, R. D. 2012, MNRAS, 419, 925

Jonkheid, B., Dullemond, C. P., Hogerheijde, M. R., & van Dishoeck, E. F. 2007, A&A, 463, 203

Juhász, A., Bouwman, J., Henning, T., et al. 2010, ApJ, 721, 431

Kaeufer, T., Woitke, P., Min, M., Kamp, I., & Pinte, C. 2023, arXiv e-prints, arXiv:2302.04629

Kama, M., Bruderer, S., van Dishoeck, E. F., et al. 2016, A&A, 592, A83

Kama, M., Folsom, C. P., & Pinilla, P. 2015, A&A, 582, L10

Kama, M., Trapman, L., Fedele, D., et al. 2020, A&A, 634, A88

Kamp, I., Tilling, I., Woitke, P., Thi, W. F., & Hogerheijde, M. 2010, A&A, 510, A18

Kataoka, A., Tsukagoshi, T., Momose, M., et al. 2016, ApJ, 831, L12

Kaufer, A., Stahl, O., Tubbesing, S., et al. 1999, The Messenger, 95, 8

Kelly, B. C. 2007, ApJ, 665, 1489

Keppler, M., Benisty, M., Müller, A., et al. 2018, A&A, 617, A44

Khalafinejad, S., Maaskant, K. M., Mariñas, N., & Tielens, A. G. G. M. 2016, A&A, 587, A62

Kim, S., Takahashi, S., Nomura, H., et al. 2020, ApJ, 888, 72

Klaassen, P. D., Juhasz, A., Mathews, G. S., et al. 2013, A&A, 555, A73

Köhler, R., Kasper, M., Herbst, T. M., Ratzka, T., & Bertrang, G. H. M. 2016, A&A, 587, A35

Kokubo, E. & Ida, S. 1996, ICARUS, 123, 180

Koresko, C. D., Beckwith, S. V. W., Ghez, A. M., Matthews, K., & Neugebauer, G. 1991, AJ, 102, 2073

Kratter, K. & Lodato, G. 2016, ARA&A, 54, 271

Kratter, K. M., Murray-Clay, R. A., & Youdin, A. N. 2010, ApJ, 710, 1375

Kraus, S., Hofmann, K. H., Benisty, M., et al. 2008, A&A, 489, 1157

Kraus, S., Hofmann, K. H., Malbet, F., et al. 2009, A&A, 508, 787

Kraus, S., Kreplin, A., Fukugawa, M., et al. 2017, ApJ, 848, L11

Krijt, S., Schwarz, K. R., Bergin, E. A., & Ciesla, F. J. 2018, ApJ, 864, 78

Krolikowski, D. M., Kraus, A. L., & Rizzuto, A. C. 2021, AJ, 162, 110

Kroupa, P. 2001, MNRAS, 322, 231

Kurosawa, R., Kreplin, A., Weigelt, G., et al. 2016, MNRAS, 457, 2236

Kurtovic, N. T., Pérez, L. M., Benisty, M., et al. 2018, ApJ, 869, L44

Lacour, S., Biller, B., Cheetham, A., et al. 2016, A&A, 590, A90

Lacy, J. H., Knacke, R., Geballe, T. R., & Tokunaga, A. T. 1994, ApJ, 428, L69

Lada, C. J. 1987, in Star Forming Regions, ed. M. Peimbert & J. Jugaku, Vol. 115, 1

Lagrange, A. M., Bonnefoy, M., Chauvin, G., et al. 2010, Science, 329, 57

Lambrechts, M., Morbidelli, A., Jacobson, S. A., et al. 2019, A&A, 627, A83

Law, C. J., Crystian, S., Teague, R., et al. 2022, ApJ, 932, 114

Law, C. J., Teague, R., Loomis, R. A., et al. 2021, ApJS, 257, 4

Law, C. J., Teague, R., Öberg, K. I., et al. 2023, ApJ, 948, 60

Leemker, M., Booth, A. S., van Dishoeck, E. F., et al. 2022, A&A, 663, A23

Leemker, M., van't Hoff, M. L. R., Trapman, L., et al. 2021, A&A, 646, A3

Leinert, C., Richichi, A., & Haas, M. 1997, A&A, 318, 472

Lesur, G., Flock, M., Ercolano, B., et al. 2023, in Astronomical Society of the Pacific Conference Series, Vol. 534, Protostars and Planets VII, ed. S. Inutsuka, Y. Aikawa, T. Muto, K. Tomida, & M. Tamura, 465

Levenhagen, R. S. & Leister, N. V. 2006, MNRAS, 371, 252

Lieman-Sifry, J., Hughes, A. M., Carpenter, J. M., et al. 2016, ApJ, 828, 25

Lissauer, J. J. 1993, ARA&A, 31, 129

Liu, S.-F., Jin, S., Li, S., Isella, A., & Li, H. 2018, ApJ, 857, 87

Liu, Y., Dipierro, G., Ragusa, E., et al. 2019, A&A, 622, A75

Liu, Y., Linz, H., Fang, M., et al. 2022, A&A, 668, A175

Lodato, G., Scardoni, C. E., Manara, C. F., & Testi, L. 2017, MNRAS, 472, 4700

Long, F., Andrews, S. M., Vega, J., et al. 2021, ApJ, 915, 131

Long, F., Herczeg, G. J., Pascucci, I., et al. 2017, ApJ, 844, 99

Long, F., Pinilla, P., Herczeg, G. J., et al. 2018, ApJ, 869, 17

Loomis, R. A., Cleeves, L. I., Öberg, K. I., et al. 2018, ApJ, 859, 131

Loomis, R. A., Öberg, K. I., Andrews, S. M., et al. 2020, ApJ, 893, 101

Lynden-Bell, D. & Pringle, J. E. 1974, MNRAS, 168, 603

Maaskant, K. M., Honda, M., Waters, L. B. F. M., et al. 2013, A&A, 555, A64

Malfait, K., Bogaert, E., & Waelkens, C. 1998, A&A, 331, 211

Manara, C. F., Ansdell, M., Rosotti, G. P., et al. 2022, arXiv e-prints, arXiv:2203.09930

Manara, C. F., Ansdell, M., Rosotti, G. P., et al. 2023, in Astronomical Society of the Pacific Conference Series, Vol. 534, Protostars and Planets VII, ed. S. Inutsuka, Y. Aikawa, T. Muto, K. Tomida, & M. Tamura, 539

Manara, C. F., Morbidelli, A., & Guillot, T. 2018, A&A, 618, L3

Manara, C. F., Mordasini, C., Testi, L., et al. 2019a, A&A, 631, L2

Manara, C. F., Natta, A., Rosotti, G. P., et al. 2020, A&A, 639, A58

Manara, C. F., Rosotti, G., Testi, L., et al. 2016, A&A, 591, L3

Manara, C. F., Tazzari, M., Long, F., et al. 2019b, A&A, 628, A95

Mann, R. K., Di Francesco, J., Johnstone, D., et al. 2014, ApJ, 784, 82

Manoj, P., Bhatt, H. C., Maheswar, G., & Muneer, S. 2006, ApJ, 653, 657

Manoj, P., Ho, P. T. P., Ohashi, N., et al. 2007, ApJ, 667, L187

Marois, C., Macintosh, B., Barman, T., et al. 2008, Science, 322, 1348

Marois, C., Zuckerman, B., Konopacky, Q. M., Macintosh, B., & Barman, T. 2010, Nature, 468, 1080

Matrà, L., Panić, O., Wyatt, M. C., & Dent, W. R. F. 2015, MNRAS, 447, 3936

Maucó, K., Manara, C. F., Ansdell, M., et al. 2023, A&A, 679, A82

McClure, M. K., Bergin, E. A., Cleeves, L. I., et al. 2016, ApJ, 831, 167

McMullin, J. P., Waters, B., Schiebel, D., Young, W., & Golap, K. 2007, in Astronomical Society of the Pacific Conference Series, Vol. 376, Astronomical Data Analysis Software and Systems XVI, ed. R. A. Shaw, F. Hill, & D. J. Bell, 127

Meeus, G., Montesinos, B., Mendigutía, I., et al. 2012, A&A, 544, A78

Meeus, G., Waters, L. B. F. M., Bouwman, J., et al. 2001, A&A, 365, 476

Mendigutía, I. 2020, Galaxies, 8, 39

Mendigutía, I., Calvet, N., Montesinos, B., et al. 2011, A&A, 535, A99

Mendigutía, I., Mora, A., Montesinos, B., et al. 2012, A&A, 543, A59

Mendigutía, I., Oudmaijer, R. D., Rigliaco, E., et al. 2015, MNRAS, 452, 2837

Menu, J., van Boekel, R., Henning, T., et al. 2015, A&A, 581, A107

Michel, A., van der Marel, N., & Matthews, B. 2021, arXiv e-prints, arXiv:2104.05894

Miley, J. M., Panić, O., Wyatt, M., & Kennedy, G. M. 2018, A&A, 615, L10

Miotello, A., Bruderer, S., & van Dishoeck, E. F. 2014, A&A, 572, A96

Miotello, A., Kamp, I., Birnstiel, T., Cleeves, L. C., & Kataoka, A. 2023, in Astronomical Society of the Pacific Conference Series, Vol. 534, Protostars and Planets VII, ed. S. Inutsuka, Y. Aikawa, T. Muto, K. Tomida, & M. Tamura, 501

Miotello, A., Rosotti, G., Ansdell, M., et al. 2021, A&A, 651, A48

Miotello, A., van Dishoeck, E. F., Kama, M., & Bruderer, S. 2016, A&A, 594, A85

Miotello, A., van Dishoeck, E. F., Williams, J. P., et al. 2017, A&A, 599, A113

Mooley, K., Hillenbrand, L., Rebull, L., Padgett, D., & Knapp, G. 2013, ApJ, 771, 110

Moór, A., Curé, M., Kóspál, Á., et al. 2017, ApJ, 849, 123

Moór, A., Kóspál, Á., Ábrahám, P., & Pawellek, N. 2020, in Origins: From the Protosun to the First Steps of Life, ed. B. G. Elmegreen, L. V. Tóth, & M. Güdel, Vol. 345, 349–350

Moór, A., Kral, Q., Ábrahám, P., et al. 2019, ApJ, 884, 108

Mora, A., Merín, B., Solano, E., et al. 2001, A&A, 378, 116

Mordasini, C., Alibert, Y., Benz, W., Klahr, H., & Henning, T. 2012, A&A, 541, A97

Morgan, W. W., Keenan, P. C., & Kellman, E. 1943, An atlas of stellar spectra, with an outline of spectral classification

Mulders, G. D., Pascucci, I., & Apai, D. 2015, ApJ, 814, 130

Mulders, G. D., Pascucci, I., Ciesla, F. J., & Fernandes, R. B. 2021, ApJ, 920, 66

Mulders, G. D., Pascucci, I., Manara, C. F., et al. 2017, ApJ, 847, 31

Murillo, N. M., Lai, S.-P., Bruderer, S., Harsono, D., & van Dishoeck, E. F. 2013, A&A, 560, A103

Muro-Arena, G. A., Benisty, M., Ginski, C., et al. 2020, A&A, 635, A121

Najita, J. R. & Kenyon, S. J. 2014, MNRAS, 445, 3315

Natta, A., Grinin, V. P., Mannings, V., & Ungerechts, H. 1997, ApJ, 491, 885

Natta, A., Testi, L., Neri, R., Shepherd, D. S., & Wilner, D. J. 2004, A&A, 416, 179

Nelson, R. P., Gressel, O., & Umurhan, O. M. 2013, MNRAS, 435, 2610

Neugebauer, G., Habing, H. J., van Duinen, R., et al. 1984, ApJ, 278, L1

Nielsen, E. L., De Rosa, R. J., Macintosh, B., et al. 2019, AJ, 158, 13

Öberg, K. I. & Bergin, E. A. 2021, Phys. Rep., 893, 1

Öberg, K. I., Guzmán, V. V., Walsh, C., et al. 2021, ApJS, 257, 1

Ohashi, N., Tobin, J. J., Jørgensen, J. K., et al. 2023, ApJ, 951, 8

Ohta, Y., Fukagawa, M., Sitko, M. L., et al. 2016, PASJ, 68, 53

Okamoto, Y. K., Kataza, H., Honda, M., et al. 2009, ApJ, 706, 665

Ormel, C. W. 2017, in Astrophysics and Space Science Library, Vol. 445, Formation, Evolution, and Dynamics of Young Solar Systems, ed. M. Pessah & O. Gressel, 197

pandas development team, T. 2020, pandas-dev/pandas: Pandas

Paneque-Carreño, T., Izquierdo, A. F., Teague, R., et al. 2024, A&A, 684, A174

Paneque-Carreño, T., Miotello, A., van Dishoeck, E. F., et al. 2022, arXiv e-prints, arXiv:2207.08827

Paneque-Carreño, T., Miotello, A., van Dishoeck, E. F., et al. 2023, A&A, 669, A126

Paneque-Carreño, T., Pérez, L. M., Benisty, M., et al. 2021, ApJ, 914, 88

Panić, O., Haworth, T. J., Petr-Gotzens, M. G., et al. 2021, MNRAS, 501, 4317

Pascucci, I., Cabrit, S., Edwards, S., et al. 2022, arXiv e-prints, arXiv:2203.10068

Pascucci, I., Testi, L., Herczeg, G. J., et al. 2016, ApJ, 831, 125

Pecaut, M. J. & Mamajek, E. E. 2016, MNRAS, 461, 794

Pegues, J., Öberg, K. I., Qi, C., et al. 2023, ApJ, 948, 57

Pérez, L. M., Carpenter, J. M., Andrews, S. M., et al. 2016, Science, 353, 1519

Pérez, L. M., Isella, A., Carpenter, J. M., & Chandler, C. J. 2014, ApJ, 783, L13

Pezzuto, S., Strafella, F., & Lorenzetti, D. 1997, ApJ, 485, 290

Pineda, J. E., Szulágyi, J., Quanz, S. P., et al. 2019, ApJ, 871, 48

Pinilla, P., Benisty, M., Kurtovic, N. T., et al. 2022a, A&A, 665, A128

Pinilla, P., Garufi, A., & Gárate, M. 2022b, A&A, 662, L8

Pinilla, P., Pascucci, I., & Marino, S. 2020, A&A, 635, A105

Pinte, C., Harries, T. J., Min, M., et al. 2009, A&A, 498, 967

Pinte, C., Ménard, F., Duchêne, G., & Bastien, P. 2006, A&A, 459, 797

Pinte, C., Ménard, F., Duchêne, G., et al. 2018a, A&A, 609, A47

Pinte, C., Price, D. J., Ménard, F., et al. 2018b, ApJ, 860, L13

Pinte, C., van der Plas, G., Ménard, F., et al. 2019, Nature Astronomy, 3, 1109

Poblete, P. P., Calcino, J., Cuello, N., et al. 2020, MNRAS, 496, 2362

Podio, L., Garufi, A., Codella, C., et al. 2020, A&A, 642, L7

Pogodin, M. A., Hubrig, S., Yudin, R. V., et al. 2012, Astronomische Nachrichten, 333, 594

Pogodin, M. A., Malanushenko, V. P., Kozlova, O. V., Tarasova, T. N., & Franco, G. A. P. 2006, A&A, 452, 551

Pollack, J. B., Hubickyj, O., Bodenheimer, P., et al. 1996, ICARUS, 124, 62

Pontoppidan, K. M., Dullemond, C. P., Blake, G. A., et al. 2007, ApJ, 656, 980

Quanz, S. P., Amara, A., Meyer, M. R., et al. 2015, ApJ, 807, 64

Quanz, S. P., Avenhaus, H., Buenzli, E., et al. 2013, ApJ, 766, L2

Ramírez-Tannus, M. C., Bik, A., Cuijpers, L., et al. 2023, ApJ, 958, L30

Reffert, S., Bergmann, C., Quirrenbach, A., Trifonov, T., & Künstler, A. 2015, A&A, 574, A116

Reipurth, B., Herbig, G., & Aspin, C. 2010, AJ, 139, 1668

Ricci, L., Testi, L., Natta, A., & Brooks, K. J. 2010, A&A, 521, A66

Rich, E. A., Teague, R., Monnier, J. D., et al. 2021, ApJ, 913, 138

Richards, A. M. S., Moravec, E., Etoka, S., et al. 2022, arXiv e-prints, arXiv:2207.05591

Rigliaco, E., Gratton, R., Mesa, D., et al. 2019, A&A, 632, A18

Rivière-Marichalar, P., Fuente, A., Esplugues, G., et al. 2022, arXiv e-prints, arXiv:2207.06716

Rosotti, G. P., Benisty, M., Juhász, A., et al. 2020, MNRAS, 491, 1335

Rosotti, G. P. & Clarke, C. J. 2018, MNRAS, 473, 5630

Rosotti, G. P., Clarke, C. J., Manara, C. F., & Facchini, S. 2017, MNRAS, 468, 1631

Rota, A. A., Manara, C. F., Miotello, A., et al. 2022, A&A, 662, A121

Rota, A. A., Meijerhof, J. D., van der Marel, N., et al. 2024, arXiv e-prints, arXiv:2401.05798

Rubinstein, A. E., Macías, E., Espaillat, C. C., et al. 2018, ApJ, 860, 7

Ruíz-Rodríguez, D., Cieza, L. A., Williams, J. P., et al. 2018, MNRAS, 478, 3674

Rydgren, A. E. & Vrba, F. J. 1984, AJ, 89, 399

Salinas, V. N., Hogerheijde, M. R., Mathews, G. S., et al. 2017, A&A, 606, A125

Salyk, C., Herczeg, G. J., Brown, J. M., et al. 2013, ApJ, 769, 21

Sanchis, E., Testi, L., Natta, A., et al. 2021, A&A, 649, A19

Sanchis, E., Testi, L., Natta, A., et al. 2020, A&A, 633, A114

Sandell, G., Weintraub, D. A., & Hamidouche, M. 2011, ApJ, 727, 26

Schöier, F. L., van der Tak, F. F. S., van Dishoeck, E. F., & Black, J. H. 2005, A&A, 432, 369

Schwarz, K. R., Bergin, E. A., Cleeves, L. I., et al. 2016, ApJ, 823, 91

Segura-Cox, D. M., Schmiedeke, A., Pineda, J. E., et al. 2020, Nature, 586, 228

Sellek, A. D., Booth, R. A., & Clarke, C. J. 2020, MNRAS, 498, 2845

Shakura, N. I. & Sunyaev, R. A. 1973, A&A, 24, 337

Sheehan, P. D. & Eisner, J. A. 2018, ApJ, 857, 18

Sheehan, P. D., Tobin, J. J., Looney, L. W., & Megeath, S. T. 2022, ApJ, 929, 76

Shenavrin, V. I., Grinin, V. P., Rostopchina-Shakhovskaja, A. N., Demidova, T. V., & Shakhovskoi, D. N. 2012, Astronomy Reports, 56, 379

Sicilia-Aguilar, A., Banzatti, A., Carmona, A., et al. 2016, PASA, 33, e059

Sierra, A., Pérez, L. M., Zhang, K., et al. 2021, ApJS, 257, 14

Sitko, M. L., Day, A. N., Kimes, R. L., et al. 2012, ApJ, 745, 29

Skiff, B. A. 2014, VizieR Online Data Catalog, B/mk

Snell, R. L., Loren, R. B., & Plambeck, R. L. 1980, ApJ, 239, L17

Spezzi, L., Alcalá, J. M., Covino, E., et al. 2008, ApJ, 680, 1295

Stapper, L. M., Hogerheijde, M. R., van Dishoeck, E. F., et al. 2024, A&A, 682, A149

Stapper, L. M., Hogerheijde, M. R., van Dishoeck, E. F., & Mentel, R. 2022, A&A, 658, A112

Stapper, L. M., Hogerheijde, M. R., van Dishoeck, E. F., & Paneque-Carreño, T. 2023, A&A, 669, A158

Stelzer, B., Robrade, J., Schmitt, J. H. M. M., & Bouvier, J. 2009, A&A, 493, 1109

Stolker, T., Dominik, C., Avenhaus, H., et al. 2016, A&A, 595, A113

Sturm, J. A., Booth, A. S., McClure, M. K., Leemker, M., & van Dishoeck, E. F. 2023, A&A, 670, A12

Sturm, J. A., McClure, M. K., Harsono, D., et al. 2022, A&A, 660, A126

Suárez, O., García-Lario, P., Manchado, A., et al. 2006, A&A, 458, 173

Tabone, B., Rosotti, G. P., Cridland, A. J., Armitage, P. J., & Lodato, G. 2022a, MNRAS, 512, 2290

Tabone, B., Rosotti, G. P., Lodato, G., et al. 2022b, MNRAS, 512, L74

Tang, Y.-W., Guilloteau, S., Dutrey, A., et al. 2017, ApJ, 840, 32

Tang, Y. W., Guilloteau, S., Piétu, V., et al. 2012, A&A, 547, A84

Tazaki, R., Ginski, C., & Dominik, C. 2023, ApJ, 944, L43

Tazzari, M., Clarke, C. J., Testi, L., et al. 2021, MNRAS[arXiv:2010.02249]

Tazzari, M., Testi, L., Ercolano, B., et al. 2016, A&A, 588, A53

Tazzari, M., Testi, L., Natta, A., et al. 2017, A&A, 606, A88

Teague, R., Bae, J., Aikawa, Y., et al. 2021, ApJS, 257, 18

Teague, R., Bae, J., Bergin, E. A., Birnstiel, T., & Foreman-Mackey, D. 2018, ApJ, 860, L12

Temmink, M., Booth, A. S., van der Marel, N., & van Dishoeck, E. F. 2023, arXiv e-prints, arXiv:2304.06382

Testi, L., Birnstiel, T., Ricci, L., et al. 2014, in Protostars and Planets VI, ed. H. Beuther, R. S. Klessen, C. P. Dullemond, & T. Henning, 339

Testi, L., Natta, A., Manara, C. F., et al. 2022, A&A, 663, A98

The, P. S., de Winter, D., & Perez, M. R. 1994, A&AS, 104, 315

Thomas, S. J., van der Bliek, N. S., Rodgers, B., Doppmann, G., & Bouvier, J. 2007, in Binary Stars as Critical Tools & Tests in Contemporary Astrophysics, ed. W. I. Hartkopf, P. Harmanec, & E. F. Guinan, Vol. 240, 250–253

Thorngren, D. P., Fortney, J. J., Murray-Clay, R. A., & Lopez, E. D. 2016, ApJ, 831, 64

Tilling, I., Woitke, P., Meeus, G., et al. 2012, A&A, 538, A20

Tisserand, P., Clayton, G. C., Welch, D. L., et al. 2013, A&A, 551, A77

Tjin A Djie, H. R. E., van den Ancker, M. E., Blondel, P. F. C., et al. 2001, MNRAS, 325, 1441

Tobin, J. J., Hartmann, L., Chiang, H.-F., et al. 2012, Nature, 492, 83

Tobin, J. J., Sheehan, P. D., Megeath, S. T., et al. 2020, ApJ, 890, 130

Toci, C., Rosotti, G., Lodato, G., Testi, L., & Trapman, L. 2021, MNRAS, 507, 818

Torres, C. A. O., Quast, G. R., da Silva, L., et al. 2006, A&A, 460, 695

Trapman, L., Ansdell, M., Hogerheijde, M. R., et al. 2020, A&A, 638, A38

Trapman, L., Facchini, S., Hogerheijde, M. R., van Dishoeck, E. F., & Bruderer, S. 2019, A&A, 629, A79

Trapman, L., Miotello, A., Kama, M., van Dishoeck, E. F., & Bruderer, S. 2017, A&A, 605, A69

Trapman, L., Rosotti, G., Zhang, K., & Tabone, B. 2023, ApJ, 954, 41

Trapman, L., Tabone, B., Rosotti, G., & Zhang, K. 2022, ApJ, 926, 61

Tripathi, A., Andrews, S. M., Birnstiel, T., & Wilner, D. J. 2017, ApJ, 845, 44

Tsiganis, K., Gomes, R., Morbidelli, A., & Levison, H. F. 2005, Nature, 435, 459

Tychoniec, Ł., Manara, C. F., Rosotti, G. P., et al. 2020, A&A, 640, A19

Ubeira Gabellini, M. G., Miotello, A., Facchini, S., et al. 2019, MNRAS, 486, 4638

Valegard, P. G., Ginski, C., Derkink, A., et al. 2024, arXiv e-prints, arXiv:2403.02156

Valegård, P. G., Waters, L. B. F. M., & Dominik, C. 2021, A&A, 652, A133

van Boekel, R., Min, M., Waters, L. B. F. M., et al. 2005, A&A, 437, 189

van den Ancker, M. E., Blondel, P. F. C., Tjin A Djie, H. R. E., et al. 2004, MNRAS, 349, 1516

van der Marel, N., Cazzoletti, P., Pinilla, P., & Garufi, A. 2016, ApJ, 832, 178

van der Marel, N. & Mulders, G. D. 2021, AJ, 162, 28

van der Marel, N., van Dishoeck, E. F., Bruderer, S., et al. 2013, Science, 340, 1199

van der Marel, N., van Dishoeck, E. F., Bruderer, S., Pérez, L., & Isella, A. 2015, A&A, 579, A106

van der Marel, N., Williams, J. P., Ansdell, M., et al. 2018, ApJ, 854, 177

van der Plas, G., Ménard, F., Canovas, H., et al. 2017a, A&A, 607, A55

van der Plas, G., Ménard, F., Ward-Duong, K., et al. 2016, ApJ, 819, 102

van der Plas, G., van den Ancker, M. E., Waters, L. B. F. M., & Dominik, C. 2015, A&A, 574, A75

van der Plas, G., Wright, C. M., Ménard, F., et al. 2017b, A&A, 597, A32

van der Velden, E. 2020, The Journal of Open Source Software, 5, 2004

van Kempen, T. A., Green, J. D., Evans, N. J., et al. 2010, A&A, 518, L128

van Terwisga, S. E. & Hacar, A. 2023, A&A, 673, L2

van Terwisga, S. E., Hacar, A., & van Dishoeck, E. F. 2019, A&A, 628, A85

van Terwisga, S. E., Hacar, A., van Dishoeck, E. F., Oonk, R., & Portegies Zwart, S. 2022, A&A, 661, A53

van Terwisga, S. E., van Dishoeck, E. F., Ansdell, M., et al. 2018, A&A, 616, A88

van Terwisga, S. E., van Dishoeck, E. F., Mann, R. K., et al. 2020, A&A, 640, A27

Vaňko, M., Eiff, M. A.-v., Pribulla, T., et al. 2013, MNRAS, 431, 2230

Vieira, S. L. A., Corradi, W. J. B., Alencar, S. H. P., et al. 2003, AJ, 126, 2971

Vigan, A., Fontanive, C., Meyer, M., et al. 2021, A&A, 651, A72

Villenave, M., Ménard, F., Dent, W. R. F., et al. 2021, A&A, 653, A46

Villenave, M., Ménard, F., Dent, W. R. F., et al. 2020, A&A, 642, A164

Villenave, M., Stapelfeldt, K. R., Duchêne, G., et al. 2022, ApJ, 930, 11

Vink, J. S., Drew, J. E., Harries, T. J., & Oudmaijer, R. D. 2002, MNRAS, 337, 356

Vioque, M., Cavieres, M., Pantaleoni González, M., et al. 2023, AJ, 166, 183

Vioque, M., Oudmaijer, R. D., Baines, D., Mendigutía, I., & Pérez-Martínez, R. 2018, A&A, 620, A128

Vioque, M., Oudmaijer, R. D., Schreiner, M., et al. 2020, A&A, 638, A21

Vioque, M., Oudmaijer, R. D., Wichittanakom, C., et al. 2022, ApJ, 930, 39

Virtanen, P., Gommers, R., Oliphant, T. E., et al. 2020, Nature Methods, 17, 261

Visser, R., van Dishoeck, E. F., & Black, J. H. 2009, A&A, 503, 323

Visser, R. G. & Ormel, C. W. 2016, A&A, 586, A66

Wagner, K., Stone, J., Dong, R., et al. 2020, AJ, 159, 252

Walsh, C., Juhász, A., Meeus, G., et al. 2016, ApJ, 831, 200

Walsh, C., Juhász, A., Pinilla, P., et al. 2014, ApJ, 791, L6

Waskom, M. L. 2021, Journal of Open Source Software, 6, 3021

Waters, L. B. F. M. & Waelkens, C. 1998, ARA&A, 36, 233

Wheelwright, H. E., Oudmaijer, R. D., & Goodwin, S. P. 2010, MNRAS, 401, 1199

White, J. A. & Boley, A. C. 2018, ApJ, 859, 103

White, J. A., Boley, A. C., Hughes, A. M., et al. 2016, ApJ, 829, 6

Whitney, B. A., Clayton, G. C., Schulte-Ladbeck, R. E., et al. 1993, ApJ, 417, 687

Wichittanakom, C., Oudmaijer, R. D., Fairlamb, J. R., et al. 2020, MNRAS, 493, 234

Wilking, B. A., McCaughrean, M. J., Burton, M. G., et al. 1997, AJ, 114, 2029

Williams, J. P. & Best, W. M. J. 2014, ApJ, 788, 59

Williams, J. P., Cieza, L., Hales, A., et al. 2019, ApJ, 875, L9

Williams, J. P. & Cieza, L. A. 2011, ARA&A, 49, 67

Wilson, T. L. & Rood, R. 1994, ARA&A, 32, 191

Winter, A. J., Clarke, C. J., Rosotti, G., et al. 2018, MNRAS, 478, 2700

Wittenmyer, R. A., Butler, R. P., Horner, J., et al. 2020, MNRAS, 491, 5248

Woitke, P., Kamp, I., Antonellini, S., et al. 2019, PASP, 131, 064301

Woitke, P., Kamp, I., & Thi, W. F. 2009, A&A, 501, 383

Wojtczak, J. A., Labadie, L., Perraut, K., et al. 2022, arXiv e-prints, arXiv:2210.13095

Wölfer, L., Facchini, S., Kurtovic, N. T., et al. 2021, A&A, 648, A19

Wölfer, L., Facchini, S., van der Marel, N., et al. 2023, A&A, 670, A154

Wolthoff, V., Reffert, S., Quirrenbach, A., et al. 2022, A&A, 661, A63

Xin, Z., Espaillat, C. C., Rilinger, A. M., Ribas, Á., & Macías, E. 2023, ApJ, 942, 4

Yang, B., Stancil, P. C., Balakrishnan, N., & Forrey, R. C. 2010, ApJ, 718, 1062

Yen, H.-W., Koch, P. M., Manara, C. F., Miotello, A., & Testi, L. 2018, A&A, 616, A100

Youdin, A. N. & Goodman, J. 2005, ApJ, 620, 459

Yu, H., Teague, R., Bae, J., & Öberg, K. 2021, ApJ, 920, L33

Yu, S.-Y., Ho, L. C., & Zhu, Z. 2019, ApJ, 877, 100

Zacharias, N., Monet, D. G., Levine, S. E., et al. 2004, in American Astronomical Society Meeting Abstracts, Vol. 205, American Astronomical Society Meeting Abstracts, 48.15

Zagaria, F., Clarke, C. J., Rosotti, G. P., & Manara, C. F. 2022, MNRAS, 512, 3538

Zari, E., Brown, A. G. A., de Bruijne, J., Manara, C. F., & de Zeeuw, P. T. 2017, A&A, 608, A148

Zhang, K., Booth, A. S., Law, C. J., et al. 2021, ApJS, 257, 5

Zhang, K., Bosman, A. D., & Bergin, E. A. 2020a, ApJ, 891, L16

Zhang, K., Schwarz, K. R., & Bergin, E. A. 2020b, ApJ, 891, L17

Zhang, S., Zhu, Z., Huang, J., et al. 2018, ApJ, 869, L47

Zhu, Z., Nelson, R. P., Dong, R., Espaillat, C., & Hartmann, L. 2012, ApJ, 755, 6

Zhu, Z., Zhang, S., Jiang, Y.-F., et al. 2019, ApJ, 877, L18

Zormpas, A., Birnstiel, T., Rosotti, G. P., & Andrews, S. M. 2022, A&A, 661, A66

Zsom, A., Ormel, C. W., Güttler, C., Blum, J., & Dullemond, C. P. 2010, A&A, 513, A57

Zuckerman, B., Forveille, T., & Kastner, J. H. 1995, Nature, 373, 494

Zuckerman, B. & Song, I. 2012, ApJ, 758, 77

Nederlandse samenvatting

Planeten spelen al sinds mensenheugenis een belangrijke rol in onze cultuur. Van hoofdrollen in mythologieën van over de hele wereld, tot het helpen met het nemen van onze eerste stappen om het heelal om ons heen te begrijpen. Sinds de dagen van Copernicus, Galileo en Kepler is onze kennis over planeten al enorm toegenomen. Niet alleen kunnen we nu ruimtesondes naar planeten toe sturen, we hebben nu ook planeten die rond andere sterren draaien ontdekt. Sinds de eerste exoplaneet was gevonden in 1995 is er een heuse exoplaneet revolutie gaande: er zijn al meer dan 5500 exoplaneten gevonden. Deze planeten verschillen enorm van elkaar. Sommige planeten zijn zwaarder en groter dan Jupiter, maar zitten dichterbij hun ster dan Mercurius om de zon. Zo een planeet wordt een 'hete Jupiter' genoemd en heeft typisch een omloopstijd van maar enkele Aardse dagen. Aan het andere uiteinde zijn er planeten die heel ver weg van hun ster staan, op honderden keren de afstand van de aarde tot de zon[3]. Om zo een grote diversiteit aan planeten te kunnen begrijpen moeten we gaan kijken naar hoe die planeten worden gemaakt. Hiervoor hebben we grote telescopen nodig, zowel op aarde als in de ruimte. Onder andere de Atacama Large (sub)millimeter Array (ALMA) in Chili en de James Webb Space Telescope (JWST) worden op dit moment druk gebruikt om onze kennis op het gebied van planeetformatie te vergroten (zie figuur 1). Planeetformatie blijft nog steeds een ingewikkelde puzzel, waar nog veel stukjes van missen, maar we hebben de afgelopen jaren aanzienlijke vooruitgang geboekt in ons begrip ervan.

Ster- en planeetformatie

Voordat een planeet heeft kunnen ontstaan zijn er al honderden miljoenen jaren voorbij gegaan. Figuur 2 laat de verschillende stadia zien die doorlopen moeten worden voordat een ster met planeten eromheen is ontstaan. Het begint met een grote interstellaire wolk die tientallen lichtjaren groot kan zijn, en bestaat voornamelijk uit gas en een beetje stof (ongeveer 1%). Die wolk zal, na bijvoorbeeld onstabiel te zijn gemaakt door een supernova in de buurt, door de zwaartekracht ineen vallen naar de plekken met de hoogste dichtheid (zie figuur 2a). Doordat de wolk een klein beetje beweegt, zal de ineenvallende materie gaan ronddraaien

---
[3]Een astronomische eenheid, of ae.

Figuur 1: Een protoster in de absorptienevel L1527 in het sterrenbeeld de Stier (Taurus) zoals gezien door de James Webb Ruimtetelescoop. De wolk waaruit de protoster ontstaat valt op de ster via een protoplanetaire schijf. Boven en onder die schijf is het interstellaire medium weg geblazen doordat de ster ook materiaal van zich af werpt. Bron: NASA, ESA, CSA en STScI

door behoud van impulsmoment, zoals een kunstschaatser die een pirouette maakt sneller zal ronddraaien als de armen worden ingetrokken (zie figuur 2b). Uiteindelijk ontstaat er een accretieschijf waarlangs de materie op de protoster valt (zie figuur 2c), dit is te zien als de langwerpige schaduw in het midden van Figuur 1. De wolk waaruit de ster ontstaat zal langzaam opgaan in de ster of schijf, of worden weggeblazen door straalstromen die van de ster afkomen. Uiteindelijk blijft er een jonge ster met een zogenaamde protoplanetaire, of planeet vormende, schijf over (zie figuur 2d). De materie in de schijf zal uiteindelijk in planeten of op de ster terechtkomen, of worden weggeblazen door een sterrenwind. Een zogenaamde
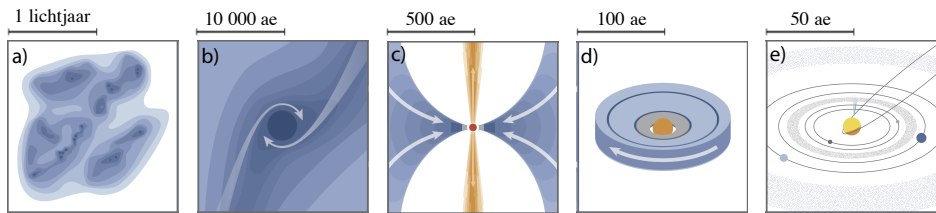
Figuur 2: De verschillende stadia van ster- en planeetformatie. Een gas wolk (a) valt ineen door de zwaartekracht (b), en een protoster ontstaat die gevoed wordt door de wolk eromheen (c). Een protoplanetaire schijf ontstaat (d), waaruit een planetenstelsel zal ontstaan (e). Bron: Öberg & Bergin (2021).

puinschijf blijft over. In deze schijf is planeetformatie nog ver van afgelopen: jonge planeten kunnen nog van plek wisselen en er zijn puinschijven gevonden met een hoop tweede generatie stof en gas, wat waarschijnlijk is vrijgekomen door botsingen tussen overgebleven brokstukken.

Protoplanetaire schijven

De focus van dit proefschrift ligt op protoplanetaire schijven, de schijven van stof en gas rond jonge sterren die planeten maken. In deze schijven beïnvloeden vele processen de evolutie van zowel het gas als het stof. Het stof begint ter grootte van een paar micrometer en moet uiteindelijk groeien tot planeten van duizenden kilometers in diameter. Vele hindernissen moeten hiervoor worden overwonnen en veel is nog onbekend. We weten in elk geval dat het kleine stof meebeweegt met het gas, maar dat grotere stofdeeltjes dat niet doen. Doordat het gas iets trager rond de ster draaid dan de grotere stofdeeltjes zullen die een tegenwind ervaren wat ervoor zorgt dat het stof richting de ster beweegt. Deze beweging moet worden gestopt, wat waarschijnlijk gebeurt door structuren die in de schijf ontstaan, zie het linker paneel van figuur 3. Als er eenmaal genoeg stofdeeltjes aaneen zijn geklonterd zal er ook gas worden vastgehouden en ontstaan er grote planeten zoals Jupiter, zie het linker paneel van figuur 3.

Dankzij de grote hoeveelheid data dat nu beschikbaar is door demografische studies van schijven in verschillende stervormingsgebieden kunnen nu ook vergelijkingen worden gedaan tussen protoplanetaire schijven en exoplaneten. Uit deze demografische studies blijkt dat de hoeveelheid materiaal dat beschikbaar is hand in hand gaat met de massa van de ster. Hoe zwaarder de ster, hoe meer massa er in de schijf eromheen zit. Verder lijkt de massa ook van de grootte van de schijf af te hangen, wat mogelijk komt door structuren in de schijf.

Doordat lage massa sterren, die ook wel T Tauri sterren worden genoemd met een massa van minder dan 1.5 keer die van de zon, vaker voorkomen bestaat het grootste deel van deze demografische studies uit deze lage massa sterren. Hierdoor weten we veel minder over wat er gebeurt rond zwaardere sterren. De focus van dit proefschrift ligt daarom op de schijven rond de zogenaamde Herbig sterren.
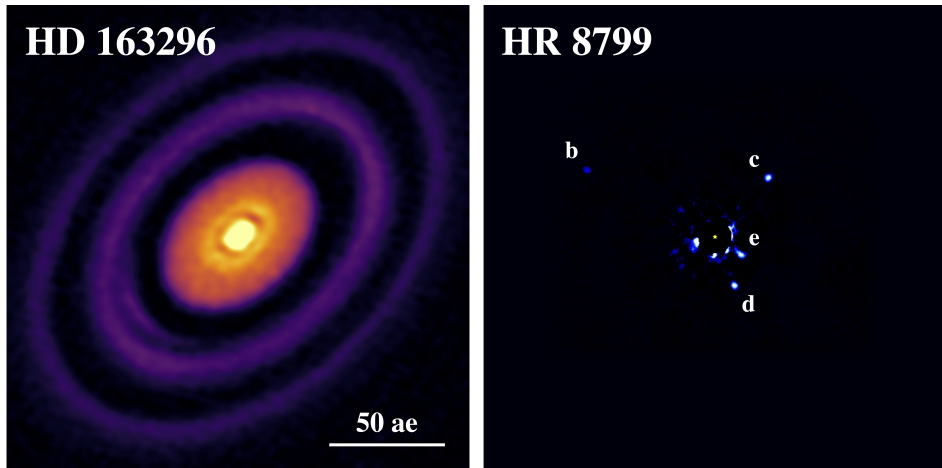
Figuur 3: Links wordt een waarneming van de Herbig schijf HD 163296 (Andrews et al. 2018b) gemaakt met de ALMA telescoop getoond. Rechts is een waarneming van het planetenstelsel HR 8799 wat uit vier planeten (b tot en met e) elk met een massa van ongeveer 7 keer de massa van Jupiter bestaat (Marois et al. 2008, 2010). De grootte van beide objecten is hetzelfde, misschien zien we in het figuur links wel de geboorte van een planetenstelsel zoals dat van HR 8799.

Dit zijn middelzware jonge sterren met massa's tussen de 2 en 8 keer die van de zon. Uit exoplaneet studies blijkt dat hoe vaak zware planeten voorkomen afhangt van de massa van de ster en dat dit het hoogste is rond middelzware sterren. Veel direct geobserveerde planeten (zoals in figuur 3) zijn ook rond dit soort sterren gevonden. Het is daarom belangrijk om een systematisch onderzoek te doen naar de schijven rond de voorlopers van deze sterren, de Herbig sterren.

Dit proefschrift

Dit proefschrift focust op de massa en structuur, zowel in het gas en het stof, van schijven rond Herbig sterren. Deze Herbig schijven worden vergeleken met schijven rond de T Tauri sterren, om te zien wat de verschillen zijn. De hoeveelheid massa die beschikbaar is en de mogelijke correlatie met de structuren die zichtbaar zijn zegt veel over de mogelijkheid om planeten in deze schijven te vormen.

Hoofdstuk 2 focust op de massa van het stof in Herbig schijven. Alle data van Herbig schijven geobserveerd met de ALMA telescoop is verzameld, tot en met de Orion nevel op ongeveer 1500 lichtjaar. De stofmassa is bepaald met behulp van de ALMA data en vergeleken met T Tauri schijven in twee andere stervormingsgebieden, Lupus (Wolf) dat maar 1-3 miljoen jaar oud is en Scorpius (Schorpioen) dat 5-11 miljoen jaar oud is. Vergeleken met de stofmassa beschikbaar in de schijven van de T Tauri sterren in Lupus en Scorpius zijn Herbig schijven respectievelijk een factor 3 tot 7 keer zwaarder. Dit grote verschil is vooral opmerkelijk als je je bedenkt dat de leeftijd van de Herbig schijven hetzelfde is als die van Scorpius

Verder zijn de schijven rond Herbig sterren ook significant groter dan de T Tauri schijven. Dit is waarschijnlijk gerelateerd aan het feit dat reuzenplaneten vaak rond middelzware sterren worden gevonden. Deze planeten stoppen het naar binnen drijven van de stofdeeltjes, waardoor het emissie oppervlak groter is en er dus een hogere stofmassa wordt gevonden. Dit is in tegenstelling tot de T Tauri schijven, waar dit proces pas op veel kortere afstanden tot de ster wordt gestopt.

De stofmassa is maar een klein gedeelte van de totale massa. De gasmassa is daarom belangrijk om te bepalen om het ontstaan van planeten goed te kunnen begrijpen, wat in hoofdstuk 3 wordt gedaan. De meerderheid van het gas bestaat uit H_2, maar dat is moeilijk te observeren. Daarom wordt vaak naar het op-een-na meest voorkomende molecuul gebruikt: koolstofmonoxide (CO). Omdat dit molecuul veel voorkomt is het nog steeds moeilijk om de hele schijf te kunnen zien doordat het ondoorzichtig is, daarom wordt vaak naar de minder voorkomende varianten van koolstofmonoxide gekeken ^{13}CO en C^{18}O. Alle beschikbare ALMA waarnemingen van deze zogenaamde isotopologen[4] van 35 Herbig schijven zijn verzameld, en met gebruik van het chemische modelleer programma DALI kan de emissiesterkte van deze stoffen worden vergeleken met modellen met een bepaalde gasmassa. De gasmassa's die hier uitkomen zijn minstens een factor 100 zwaarder vergeleken met de stofmassa's uit het vorige hoofdstuk, wat consistent is met de verhouding in het interstellaire gas. Dit is in tegenstelling tot wat er voor T Tauri schijven is gevonden, waar die gas-stof verhouding maar een factor tien is. Dit komt doordat in T Tauri schijven CO bevriest en dan wordt omgezet in andere moleculen. Maar Herbig schijven zijn warmer door de hogere lichtkracht van de ster waardoor CO niet bevriest en dus gebruikt kan worden om de gasmassa te bepalen.

Omdat de met ALMA geobserveerde Herbig schijven vooral richting de zwaarste en grootste schijven kunnen neigen, is het belangrijk om een volledige populatie te hebben om dit vertekend beeld recht te kunnen zetten. Hoofdstuk 4 presenteert het eerste volledige overzicht van alle Herbig schijven in een enkel stervormingsgebied: Orion. Met behulp van de NOEMA telescoop zijn er 25 nieuwe Herbig schijven geobserveerd, wat in combinatie met ALMA data van 10 andere schijven alle Herbig schijven in Orion zijn. De mediaan van de stofmassa's die hieruit bepaald zijn is 11.7 aardmassa's. Dit betekend dat ongeveer 50% van alle Herbig schijven zwaarder zijn dan 10 aardmassa's, wat het geval is voor minder dan 25% van de T Tauri schijven. De massaverdeling uit hoofdstuk 2 is iets vertekend richting de zwaardere schijven.

De massa van een schijf kan vergeleken worden met de hoeveelheid massa die op de ster valt (ofwel de accretie snelheid) om een idee te krijgen van hoe lang een schijf kan blijven bestaan. In hoofdstuk 5 worden de massa's uit hoofdstuk 2 vergeleken met de accretie snelheid, omdat dit voor T Tauri schijven een duidelijke relatie geeft. Voor Herbig schijven lijkt de relatie voor de zwaarste schijven overeen te komen met die van T Tauri schijven, maar voor de laagste massa schijven lijkt de accretie snelheid niet af te nemen, terwijl dit wel zo is voor de T Tauri schijven. Verschillende oplossingen worden gesuggereerd: mogelijk zijn de stofmassa's te

---

[4]Moleculen waarvan minstens een van de atomen een isotoop is, oftewel een atoom met een ander aantal neutronen maar met hetzelfde aantal protonen.

laag doordat niet al het stof te zien is, of worden de accretie snelheden overschat.

In hoofdstuk zes wordt gekeken naar de verticale hoogte van het gas in acht Herbig schijven. De groep I schijven worden van origine gezien als verticaal 'dikke' schijven, terwijl de groep II schijven dun zouden zijn. Met behulp van ALMA data is de dikte bepaald van de schijf en is gevonden dat groep II schijven inderdaad dun kunnen zijn, maar dat dat niet per se het geval hoeft te zijn. De groep II classificatie kan dan komen doordat het grootste gedeelte in de schaduw zit door een verdikking dichtbij de ster.

Herbig sterren zijn over het algemeen al redelijk oud, rond de 5 miljoen jaar. Er zijn jonge sterren die middelzware T Tauri sterren worden genoemd, die even zwaar zijn als Herbig sterren maar eruit zien als T Tauri sterren omdat de ster zelf nog niet zo warm is. Uiteindelijk zullen deze middelzware T Tauri sterren een Herbig ster worden en het is daarom belangrijk om de schijven rond deze populatie sterren te onderzoeken. Het laatste hoofdstuk, hoofdstuk 7, kijkt naar zowel de gas- en stofmassa in de schijven rond deze sterren. De massa's blijken hetzelfde te zijn als voor de Herbig schijven.

De volgende belangrijkste conclusies kunnen getrokken worden:

1. Herbig schijven zijn zwaar, zowel in het gas als het stof.

2. Reuzenplaneten hebben een grote impact op de evolutie van Herbig schijven.

3. Herbig schijven zijn zowel groter als zwaarder dan T Tauri schijven.

Toekomstperspectief

De hoofdstukken in dit proefschrift hebben laten zien dat er nog een hoop te leren valt wat betreft Herbig schijven. Het doel in de nabije toekomst is daarom ook om een volledig overzicht te krijgen van alle Herbig schijven binnen een bepaalde afstand tot de aarde. Tot nu toe zijn er al meerdere telescopen druk bezig geweest met het krijgen van data van een groot gedeelte van de Herbig populatie en dit zal binnenkort worden voltooid. Deze set van Herbig schijven zal een factor vijf groter zijn dan die uit hoofdstuk 2 en zal daarom veel inzichten in de Herbig populatie geven. Geplande upgrades aan ALMA zullen vervolg onderzoek op deze data ook gaan vermakkelijken, doordat de bandbreedte en gevoeligheid van de telescoop verbeterd zullen worden.

Directe waarnemingen van exoplaneten in schijven zal een van de hoofddoelen zijn voor de planeetformatie gemeenschap de komende jaren. Herbig schijven zullen hierin waarschijnlijk een belangrijke rol gaan spelen omdat dit de schijven zijn waarin reuzenplaneten ontstaan, die makkelijker zijn om met de huidige telescopen te detecteren. Terwijl ALMA vooral focust op de buitenste gebieden van protoplanetaire schijven, zullen de recent gelanceerde James Webb Space Telescope (JWST) en de geplande Extremely Large Telescope (ELT) in Chile een belangrijke rol spelen voor de binnenste gedeeltes van de schijven.

Wat betreft het bepalen van de massa van schijven zullen waarnemingen van nog minder veel voorkomende CO isotopologen een belangrijke eerste stap zijn

naar het nauwkeurig bepalen van de gasmassa's. Dit is al mogelijk met de ALMA telescoop. Verder zullen geplande telescopen zoals de Square Kilometer Array en de Next Generation Very Large Array, die op centimeter golflengtes observeren in plaats van millimeter zoals ALMA, inzichten geven in de distributie van centimeter stofdeeltjes.

Publications

First-author publications

1. *Constraining the gas mass of Herbig disks using CO isotopologues*
Stapper, L. M.; Hogerheijde, M. R.; van Dishoeck, E. F.; Lin, L.; Ahmadi, A.; Booth, A. S.; Grant, S. L.; Immer, K.; Leemker, M.; Pérez-Sánchez, A. F., 2024, Astronomy & Astrophysics, 682, A149.

2. *A dichotomy in group II Herbig disks. ALMA gas disk height measurements show both shadowed large vertically extended disks and compact flat disks*
Stapper, L. M.; Hogerheijde, M. R.; van Dishoeck, E. F.; Paneque-Carreño, T., 2023, Astronomy & Astrophysics, 669, A158.

3. *Iterative angular differential imaging (IADI): An exploration of recovering disk structures in scattered light with an iterative ADI approach*
Stapper, L. M.; Ginski, C., 2022, Astronomy & Astrophysics, 668, A50.

4. *The mass and size of Herbig disks as seen by ALMA*
Stapper, L. M.; Hogerheijde, M. R.; van Dishoeck, E. F.; Mentel, R., 2022, Astronomy & Astrophysics, 658, A112.

Submitted first-author publications

1. *A complete Herbig disk mass survey in Orion*
Stapper, L. M.; Hogerheijde, M. R.; van Dishoeck, E. F.; Booth, A. S.; Grant, S. L.; van Terwisga, S. E., submitted to Astronomy & Astrophysics.

2. *Intermediate mass T Tauri disk masses and a comparison to their Herbig disk descendants*
   Stapper, L. M.; Hogerheijde, M. R.; van Dishoeck, E. F.; Vioque, M.; Williams, J. P.; Ginski, C., in review at Astronomy & Astrophysics.

Co-author publications

1. *The $\dot{M}$ -M_{disk} relationship for Herbig Ae/Be stars: A lifetime problem for disks with low masses?*
   Grant, S. L.; **Stapper, L. M.**; Hogerheijde, M. R.; van Dishoeck, E. F.; Brittain, S.; Vioque, M., 2023, The Astronomical Journal, 166, 147.

2. *Disk evolution study through imaging of nearby young stars (DESTINYS): Late infall causing disk misalignment and dynamic structures in SU Aur*
   Ginski, C.; Facchini, S.; Huang, J.; Benisty, M.; Vaendel, D.; **Stapper, L. M.**; Dominik, C.; Bae, J.; Ménard, F.; Muro-Arena, G.; Hogerheijde, M. R.; McClure, M.; van Holstein, R. G.; Birnstiel, T.; Boehler, Y.; Bohn, A.; Flock, M.; Mamajek, E. E.; Manara, C. F.; Pinilla, P.; Pinte, C.; Ribas, Á., 2021, The Astrophysical Journal Letters, 908, L25.

Curriculum Vitae

I was born in Amsterdam, on the 27th of July 1997, and together with my parents and younger sister I grew up in the small village of Ouderkerk aan de Amstel, sandwiched between Amstelveen and Amsterdam. Growing up I had many different interests, from historical topics such as dinosaurs and the Middle Ages, to geology and, of course, astronomy. With two parents who read a lot, I took over this habit and read a lot too, from informative books about the history and inner workings of our universe, to fantasy books with magic. While the latter has literally the word "fantasy" in the name of the genre, the former made me fantasize about the world, and extra-solar worlds, even more. This interest only grew over the years.

After the great support and guidance at my primary school the Jan Hekman School, I chose the Keizer Karel College as my secondary school. They offered this relatively new curriculum called Technasium, which primarily focuses on doing projects by researching and designing solutions for different companies and institutions. After learning about this, it was immediately clear to me that I had to do this. In the following six years I did many different projects, from designing a new home for the penguins in Artis, to researching and digitally designing the renovation plans of Fort Uitermeer in Weesp, all the while learning about planning and tackling projects. These skills would be useful for years to come. Doing a PhD in Astronomy now, one would think that I always was good at mathematics and physics, but this mainly came to fruition in the second half of my secondary school career. While I always found those courses more interesting, only after choosing a beta-heavy curriculum of physics, biology, chemistry, and two mathematics courses, I started to excel in the exact sciences. After going to CERN during a trip in the fifth year, and getting special behind-the-scenes access, my interests into physics only grew. From that moment onward, it was clear to me that I wanted to do a related study.

Choosing a study was still difficult however. I went to the open days of many studies, from earth sciences to applied physics. But remembering my interest in astronomy, combined with my enthusiasm of physics, I started looking into the available Bachelors in that direction. Funnily enough, while going to the open day of the astronomy Bachelor's in Leiden, the car broke down and I missed almost all of the presentations planned for that day, which eventually lead me to choose for the Astronomy and Physics Bachelor's at the University of Amsterdam (UvA).

Unbeknownst to me I would go to Leiden five years later as a PhD candidate. From the beginning of the Bachelor's it was clear to me that, while still incredibly interesting, the much more heavy mathematical courses such as particle and quantum physics were not the way to go, and astronomy was where my interests really were. Specifically observational astronomy: seeing all the fascinating objects in the sky is what drove my curiosity. The first real hands-on experience with a professional telescope was during the La Palma Master's course at the UvA, in which we tried to obtain spectra to confirm the binary nature of the central star of the NGC 7008 nebula with the HERMES spectrograph on the Mercator telescope. Besides spending my time studying I also tutored secondary school students, which sparked an interest into science outreach resulting in me presenting with a mobile planetarium at primary and secondary schools for a little more than a year until the COVID pandemic hit. Going from fine grades in secondary school, to better grades in my Bachelor's, I finally found my place at the Astronomy and Astrophysics track of the Master's Physics and Astronomy in Amsterdam, and graduated Cum Laude.

Over the years at UvA I mainly became interested into the exoplanetary sciences, and did my Bachelor's thesis on observing exoplanets with high-resolution spectroscopy around stellar-flare active dwarf stars together with Jayne Birkby. During my Master's, I considered doing an extra year due to the many interesting courses available, but eventually changed this decision which resulted in me choosing a Master's project relatively late. One of the still available projects was one with Christian Ginski and Carsten Dominik, on directly observing planet-forming disks in scattered light. I decided take on this challenge, which was one of the best decisions I have ever made, as not only was the project very interesting and made me excited about the early stages of exoplanets, it also led me to choose for a career in astronomy.

In 2020 I started my PhD in Leiden, supervised by Michiel Hogerheijde and Ewine van Dishoeck. While still in the middle of the COVID pandemic, I was lucky enough to thrive working on the projects on my own without any distractions. As no ALMA proposal was accepted before my arrival, my task was to obtain all of the available continuum data for a set of disks around intermediate mass stars called Herbig disks. I would repeat this exercise multiple times for different data sets over the following few years, all resulting in most of the chapters in this thesis. Over the years I also had the opportunity to write many proposals, most of which were not accepted, but eventually a proposal for the NOEMA telescope, in the French Alps, was accepted allowing me to go to Grenoble in the last year of my PhD to reduce the data. I also had ample opportunity to develop my outreach and teaching skills. I partly organized the 2021 edition of the Netherlands Astronomy Olympiad, and gave outreach presentations with a scale model of JWST. I also was the main teaching assistant of the Practical Astronomy course, which taught me much about delegating and scheduling the other TA's (with a greater or lesser degree of success), handling problems with the telescope, and grading the many reports submitted by the students. Furthermore, I supervised two Bachelor's and two Master's students together with Michiel and one also with Alice Booth. Due to the pandemic my first in-person conference was in Leicester in 2022, and over the years I have given multiple talks and posters at conferences both online and

in-person: from Protostars and Planets VII in Kyoto, to the NAC in Egmond aan Zee. I also went on a trip to many institutes around Europe in November of 2023 to search for a postdoc position. In November I will start a postdoc position in the group of Myriam Benisty at the Max Planck Instutute of Astronomy in Heidelberg.

Acknowledgements

Since the start of my PhD, I have spend around 7500 hours on this thesis[5]. Of course I could not have done this alone. Here, I would like to thank everyone who has made this possible.

First I would like to thank my supervisors, Ewine and Michiel. Ewine, thank you for the numerous meetings and discussions we had over the years. Your incredible insights and meticulous feedback have always greatly improved the projects I did during the PhD. Your drive and joy for science is truly inspiring. Michiel, thank you for the many times I walked past your office and taking the time to discuss problems and new results. Your simple yet effective insights have more than once brought my nerves back down. To both of you, thank you for the incredible time at Leiden.

Of course other people have had much input on my work as well. In particular I would like to thank Sierra. You joining the meetings online on Fridays and giving feedback and suggestions have proven to be invaluable, the culmination of which is clear from the many chapters you are part of. Thank you Alice, for the many times we have written proposals together, and spurring me on to write some for other telescopes than ALMA. Your feedback and guidance over the years have improved my own scientific and supervision skills significantly. Also, my thanks go to Aida, thank you for your help and guidance during not only the start of my PhD, for helping me understand the complex world of ALMA observations and their reduction with CASA, but also for downloading the terabytes of data. Moreover, without everyone else at Allegro I would not have been able to do this, in particular Katharina for downloading and calibrating so much data, and Andres for your help with my self-calibration questions.

By far the most time I of course spent with the amazing research group in Leiden. Ardjan and Margot, it was great having you two in the same office, I am already missing sharing it in the new building. That is not to say that I am not content with my office mates in the new building. Andrew, thanks for the already plentiful discussions we had about mundane things like the Dutch language, and of course about science. Teresa, for sharing this burden of finishing a PhD at the same time, discussing our frustrations were relieving. Thanks Yuan, for being

---

[5]Until May the 29th 2024, assuming 20 weeks of holiday and a little bit of overtime

the ever so sporadic presence in the office. Thank you Martijn for handing over the L-G telecon baton to me, and Marissa for again taking it over. And thanks to the many other great colleagues in the group over the years, Pooneh, Andres, Lisa, Logan, Milou, Nico, Giulio, Julia, Jeroen, Pranjal, Katie, and Will. Thanks for your presence and input during the many group meetings, and allowing me to schedule you for progress reports and bringing cookies. A large part of my thanks also goes towards everyone attending the planet formation group meetings, Alessia, Osmar, Sam, Shuo, Xinyu, Luna, and many others, while my attendance has been somewhat lacking the last half year, I always enjoyed the research updates and paper discussions. Also thank you Nienke, not only for planning these meetings, but also for the feedback and help at the start of my PhD. Thanks Ana for the amazing few years of me being the TA for praktische sterrenkunde, it is a great course to teach. Maite, Fedde, Luna, Zephyr, Marissa, thank you for introducing me to D&D.

All of this would also not have been possible without the initial push during my Master's by Christian. Thank you for the great project and experience writing a paper two years later, the beautiful images coming out of this work drove my passion for this field. My thanks also go to Carsten, for allowing me to join the group meetings in Amsterdam for a few more years, even after going to Leiden, and all members of these meetings, Per-Gunnar, Kevin, Ryo, Rico, and others, while mostly seeing you online, it was great to hear about your research and insights into my work.

While the beginning of the PhD did not include international collaborations, I am happy that by the end it did. Thank you Miguel, for our discussions about the Herbig star population, your feedback on my work, and your incredible openness of sharing data with me, from which many people can learn. My thanks also go to Jonathan, for sharing your data, and your feedback on my paper. Leon, Sierk, thank you for the discussions about the DALI wrapper and much more. My thanks also go towards all of the incredible people I have met during my travels, which have in part been made possible by funding from the LKBF, your kindness and inclusiveness makes me truly honored to be part of the Astronomical community.

Als laatste, papa, mama, Lisa, zonder jullie eeuwige steun en toeverlaat had ik dit nooit kunnen doen. Joris, dank je voor het aanhoren van mijn eeuwige gezeur over werk, de vele game avonden samen, en simpelweg voor het zijn van een hele goeie vriend. Margot, zonder jou was Leiden een stuk minder mooi geweest, je vermogen in het oplossen van problemen en het geven van een luisterend oor hebben mij op menig moment uit de brand geholpen. Dank jullie wel voor alle steun.